ISBN: 978-90-365-5789-4

Ultra-Narrowband Communications

MHD Zaher Mahfouz

2023

Ultra-Narrowband Communications

A Feasibility Study
For The 2.4 GHz Band

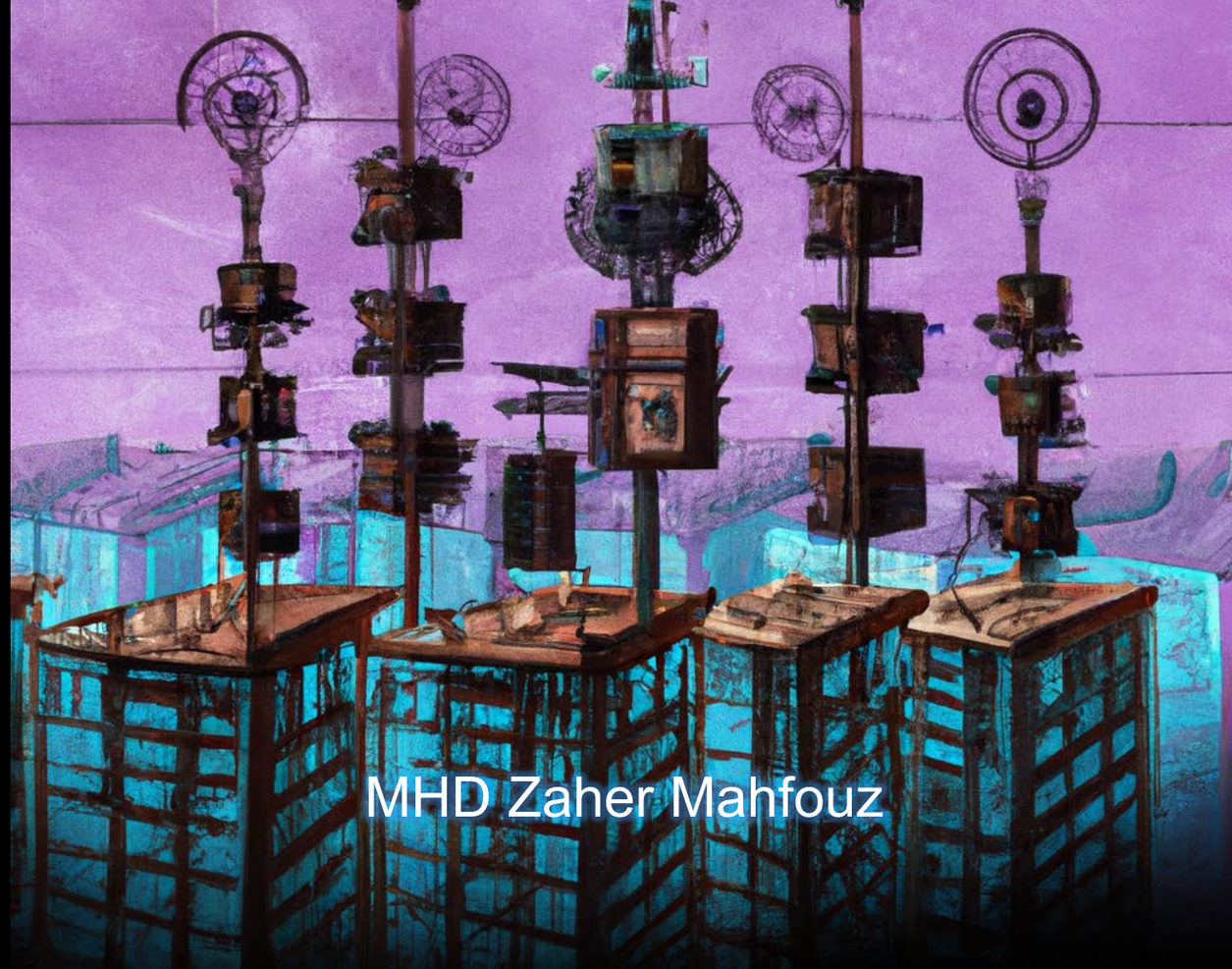

MHD Zaher Mahfouz

ULTRA-NARROWBAND COMMUNICATIONS

A FEASIBILITY STUDY FOR THE 2.4 GHZ BAND

MHD Zaher Mahfouz

ULTRA-NARROWBAND COMMUNICATIONS

A FEASIBILITY STUDY FOR THE 2.4 GHZ BAND

Dissertation

to obtain
the degree of doctor at University of Twente,
on the authority of the rector magnificus,
prof. dr. ir. A. Veldkamp,
on account of the decision of the Doctorate Board
to be publicly defended
on Friday the 29th of September 2023 at 16.45 hours

by

MHD Zaher Mahfouz

born on the 24th of July, 1987
in Damascus, Syrian Arab Republic

This dissertation has been approved by:

Promotor
prof. dr. ir. A. B. J. Kokkeler

Co-promotor
dr. A. Alayón Glazunov

Cover design: DALL-E 2
Printed by: Gildeprint
Lay-out: Novanext Overleaf
ISBN (print): 978-90-365-5789-4
ISBN (digital): 978-90-365-5790-0
DOI: 10.3990/1.9789036557900
URL: https://doi.org/10.3990/1.9789036557900

Graduation Committee:

prof. dr. J. N. Kok	University of Twente (chairman and secretary)
prof. dr. ir. A. B. J. Kokkeler	University of Twente (promotor)
dr. A. Alayón Glazunov	Linköping University (co-promotor)
prof. dr. ir. C. H. Slump	University of Twente
prof. dr. ir. G. J. Heijenk	University of Twente
prof. dr. ir. A. B. Smolders	Eindhoven University of Technology
prof. dr. V. M. Primiani	Universitá Politecnica delle Marché

UNIVERSITY OF TWENTE.

NWO
Nederlandse Organisatie voor Wetenschappelijk Onderzoek

Faculty of Electrical Engineering, Mathematics and Computer Science,
Radio Systems (RS) group

This research has been conducted within the Slow Wireless project
(project number 13769). This research is supported by
the Dutch Research Council NWO.

If you would be a real seeker after truth, it is necessary that at least once in your life you doubt, as far as possible, all things.

René Descartes

ABSTRACT

Wireless sensor networks (WSNs) have significantly transformed various industries and sectors, enabling unprecedented data collection and analysis. These networks consist of interconnected sensors that wirelessly transmit information, providing valuable insights into the environment, infrastructure, and human activities. Several types of wireless networks have emerged to address the communication requirements of different applications. Among these is the Low-Power Wide-Area Network (LPWAN), which supports long-range wireless links (hence "wide-area") for battery-based sensors (hence "low-power"). To further enhance the sustainability and functionality of WSNs, plenty of research has been conducted to develop wireless sensors that are ultra-low power, battery-less and/or biodegradable. These sensors are usually designed to operate with minimal power consumption while possibly leveraging energy harvesting techniques. As such, they pave the way for highly efficient, eco-friendly, and long-lasting wireless sensing systems, enabling a wide range of applications in areas such as smart agriculture, infrastructure management, and healthcare.

At the physical layer, different 3GPP and commercial LPWAN technologies have evolved for the past decade such as NB-IoT, LoRa, and Ultra-Narrowband (UNB). Because the majority of LPWAN applications are characterized by latency tolerance, low throughput, and low cost, the UNB signaling scheme has attracted a great deal of interest and emerged as one of the main contenders. Currently, UNB-based networks are deployed in the 868 MHz ISM band. However, the emission regulations in this license-free band severely cap the carried throughput of the sensor nodes by imposing a harsh duty-cycle limitation. Moreover, as the world embraces the on-going massive large-scale deployments of wireless sensors, a key challenge on the horizon is the current exponential growth in data traffic generated by billions of deployed sensors worldwide.

Therefore, the Slow Wireless project, within which the main scope of this thesis has been developed, explores the feasibility and the challenges of a UNB deployment in the 2.4 GHz ISM band. Compared to the 868 MHz band, the former offers a much larger bandwidth and does not have a limit on the carried throughput. As one of the work packages in the Slow Wireless project, this thesis' aims are twofold. First, it investigates the physical-layer aspects of a UNB deployment in the 2.4 GHz band in terms of energy efficiency and wireless coexistence. Second, it also aims at researching and developing a cost-effective experimental environment in which proposed solutions to the potential challenges of this deployment can be investigated.

To investigate the feasibility of a UNB deployment in the 2.4 GHz band in terms of energy efficiency, a comprehensive energy consumption model at the physical layer of a sensor node is developed for a star-topology-based WSN. Using the model, the optimal bit rates for a wide range of deployment scenarios are calculated using a

numerical example while considering several practical factors that may stem from the deployment of an energy-scavenging-powered sensor node in the 2.4 GHz band: timing-frequency accuracy, source-power limitation, and emission regulations. It is demonstrated by the outcome of the optimization process that the UNB signaling scheme is the energy-efficient/convenient solution for two WSN deployment scenarios. (*i*) The wireless link between the base station and the sensor nodes typically covers a large distance and/or frequently experiences fading/obstruction. (*ii*) It represents a convenient ultra-low-power RF solution for the WSNs whose nodes are supposed to be tiny with a very harsh peak-power consumption limitation as, e.g., in energy-scavenging-powered sensor nodes.

To investigate the feasibility of a UNB deployment in the 2.4 GHz band in terms of wireless coexistence, an empirical investigation is carried out by considering Wi-Fi networks as potential victims to the UNB interference. First, a systematic and thorough methodology is developed for the empirical investigation. The methodology is based on a worst-case interference scenario and proposes three investigation steps. The three steps assess the impact of the UNB interference on Wi-Fi links in terms of the clear-channel-assessment mechanism, the beacon delivery rate, and the transport-layer throughput, respectively. The methodology is then applied to a measurement setup to practically study the case of 100 bit/s UNB signals interfering with an IEEE 802.11n transmission in the 2.4 GHz band. Several off-the-shelf Wi-Fi devices are tested. The UNB signal is generated in two modulation schemes, namely, OOK and GMSK. Both single and multiple simultaneous UNB interferers are also considered. It is shown that OOK-based UNB signals have the least interfering impact, and that Wi-Fi pilot subcarriers are the most vulnerable to the UNB interference. Finally, to promote wireless coexistence based on the insights gained from analyzing the measurement results, 17 sub-bands are recommended for the UNB signaling scheme in the 2.4 GHz band.

A controlled experimental environment consists of an RF testing equipment, a reverberation chamber, or a combination thereof. A testing equipment is frequently utilized to simulate various propagation channel models. However, this equipment is expensive due to combined initial, maintenance, and calibration costs. Reverberation chambers have attracted an increasing interest in the over-the-air testing of wireless communications in the last couple of decades. A less-known reverberation chamber is the Vibrating Intrinsic Reverberation Chamber (VIRC), which—compared to classical reverberation chambers—is more cost effective and has a simpler structure to assemble/disassemble. Moreover, it is a more efficient environment for generating multipath conditions as well as capable of producing more uncorrelated samples. However, before the VIRC can be utilized as a versatile experimental environment (e.g., channel emulator) for the UNB signaling scheme, a relevant characterization must first be conducted on the chamber itself. Therefore, this thesis thoroughly investigates whether the VIRC can closely mimic the UNB propagation channel of the real-world environment of interest.

To utilize the VIRC as a channel emulator for the UNB signaling scheme in the 2.4 GHz band, a systematic measurement and estimation methodology is first developed for the empirical characterization of the propagation channel inside the VIRC in terms of

the first- and second-order temporal and spectral characteristics. The methodology is devised to be universal to any reverberation chamber if the mode-stirring technique is put in use. It also takes into consideration a desired estimation accuracy as well as the effect of different operating variables: carrier frequency, rotational speed of the VIRC motors, and VIRC loading condition (i.e., placing RF absorbers inside the chamber). Next, an experimental framework composed of the VIRC and its propagation channel is assembled. A thorough empirical characterization of this channel is carried out. Various channel characteristics are jointly measured and investigated with respect to the operating variables with emphasis on the 2.4 GHz band. Several mathematical models are proposed to fit the behavior of various of the measured characteristics. Moreover, the validity of the statistical method is analyzed, and the generality of the proposed models is assessed. According to the analysis of the measurement results of the VIRC, the Doppler spectrum matches the Bell model and the channel envelope histogram closely resembles the theoretical Rician distribution. Finally, given the channel characteristics of the two UNB potential deployment scenarios, it is shown that the VIRC can roughly be used as a UNB channel emulator with ascribed first- and second-order characteristics in general, but with limited emulation capability on how slow the fading can be in particular.

SAMENVATTING

Draadloze sensor netwerken (WSN's) hebben verschillende industrieën en sectoren ingrijpend veranderd, waardoor ongekende gegevensverzameling en -analyse mogelijk is. Deze netwerken bestaan uit onderling verbonden sensoren die draadloos informatie verzenden, wat waardevolle inzichten biedt in de omgeving, infrastructuur en menselijke activiteiten. Verschillende soorten draadloze netwerken zijn ontstaan om aan de communicatievereisten van verschillende toepassingen te voldoen. Een van deze netwerken is het Low-Power Wide-Area Network (LPWAN) netwerk, dat langeafstands draadloze verbindingen ondersteunt (vandaar "wide-area") voor batterij gevoede sensoren (vandaar "low-power"). Om de duurzaamheid en functionaliteit van WSN's verder te verbeteren, is er veel onderzoek gedaan naar het ontwikkelen van draadloze sensoren die een extreem laag vermogensgebruik hebben, geen batterij gebruiken en/of biologisch afbreekbaar zijn. Deze sensoren zijn meestal ontworpen om te werken met een minimaal stroomverbruik en mogelijk gebruik maken van energie-harvesting technieken. Ze banen zo de weg voor zeer efficiënte, milieuvriendelijke en draadloze meetsystemen voor langdurig gebruik, die een breed scala aan toepassingen mogelijk maken op gebieden zoals slimme landbouw, infrastructuurbeheer en gezondheidszorg.

Op de fysieke laag zijn verschillende 3GPP- en commerciële LPWAN-technologieën geëvolueerd in het afgelopen decennium, zoals NB-IoT, LoRa en Ultra-Narrowband (UNB). Omdat de meerderheid van de LPWAN-toepassingen worden gekenmerkt door tolerantie voor latency, lage throughput en lage kosten, heeft UNB- veel interesse gewekt en is het naar voren gekomen als een van de belangrijkste kandidaten voor realisatie van LPWAN technologieën. Momenteel worden UNB-gebaseerde netwerken ingezet in de 868 MHz ISM-band. De emissieregels in deze licentievrije band vormen een ernstige beperking voor de data-doorvoer van de sensor nodes door een stringente beperking van de duty-cycle. Bovendien vormt de huidige exponentiële groei van dataverkeer, gegenereerd door miljarden wereldwijd ingezette sensoren, een belangrijke uitdaging nu de wereld grootschalige draadloze sensornetwerken omarmt.

Het Slow Wireless-project waarbinnen dit proefschrift is geschreven onderzoekt daarom de haalbaarheid en uitdagingen van een UNB-implementatie in de 2,4 GHz ISM-band. Vergeleken met de 868 MHz-band biedt de laatste een veel grotere bandbreedte en kent het geen beperking op de doorvoer. Als een van de werkpakketten in het Slow Wireless-project heeft deze scriptie twee doelen. Ten eerste onderzoekt het fysieke laag aspecten van een UNB-implementatie in de 2,4 GHz-band te onderzoeken op het gebied van energie-efficiëntie en draadloze co-existentie. Daarnaast beoogt het onderzoek te doen en een kosteneffectieve experimentele omgeving te ontwikkelen waarin voorgestelde oplossingen voor de potentiële uitdagingen van deze implementatie kunnen worden onderzocht.

Om de haalbaarheid van een UNB-implementatie in de 2,4 GHz-band te onderzoeken op het gebied van energie-efficiëntie, is er een uitgebreid energieverbruiksmodel ontwikkeld voor de fysieke laag van een sensor node in een WSN gebaseerd op een ster-topologie. Met behulp van het model worden optimale bitsnelheden berekend voor een breed scala aan implementatiescenario's voor een numeriek voorbeeld, waarbij rekening wordt gehouden met verschillende praktische factoren die voortvloeien uit de implementatie van een energie-harvesting sensor node in de 2,4 GHz-band: tijd-frequentie nauwkeurigheid, vermogensbeperkingen door energie-harvesting en emissieregels. Uit de uitkomst van het optimalisatieproces blijkt dat het UNB-signaleringsschema een energiezuinige/gemakkelijke oplossing is voor twee WSN-implementatiescenario's. (i) De draadloze verbinding tussen het basisstation en de sensor nodes bestrijkt doorgaans een grote afstand en/of ondervindt frequent fading/obstructie. (ii) WSN's waarvan de nodes extreem klein moeten zijn met een zeer strikte beperking op het piekvermogen verbruik, zoals bijvoorbeeld bij energie-harvesting sensor nodes.

Om de haalbaarheid van een UNB-implementatie in de 2,4 GHz-band te onderzoeken op het gebied van draadloze co-existentie, wordt een experimenteel onderzoek uitgevoerd waarbij Wi-Fi-netwerken worden beschouwd als mogelijke slachtoffers van UNB-interferentie. Allereerst wordt een systematische en grondige methodologie ontwikkeld voor het experimentele onderzoek. De methodologie is gebaseerd op een worst-case interferentiescenario en stelt drie onderzoeksstappen voor. De drie stappen beoordelen de impact van de UNB-interferentie op Wi-Fi-verbindingen met betrekking tot het clear-channel-assessment mechanisme, de beacon delivery rate en de transportlaag-throughput. Vervolgens wordt de methodologie toegepast op een meetopstelling om een scenario met 100 bit/s UNB-signalen die interfereren met een IEEE 802.11n-transmissie in het 2,4 GHz-band te bestuderen. Verschillende commercieel beschkbare Wi-Fi-apparaten worden getest. Het UNB-signaal wordt gegenereerd in twee modulatieschema's, namelijk OOK en GMSK. Zowel enkele als meerdere gelijktijdige UNB-stoorzenders worden overwogen. Het is aangetoond dat op OOK gebaseeerde UNB signalen de minster interferentie veroorzaken en dat de Wi-Fi pilot subcarriers het meest kwetsbaar zijn voor UNB interferentie. Tot slot worden, op basis van de inzichten die zijn verkregen uit de analyse van de meetresultaten, 17 subbanden aanbevolen voor het UNB-signaleringsschema in de 2,4 GHz-band om draadloze samenwerking te bevorderen.

Een gecontroleerde experimentele omgeving bestaat uit RF-testapparatuur, een reverberation chamber of een combinatie daarvan. Testapparatuur wordt vaak gebruikt om verschillende kanaalmodellen te simuleren. Testapparatuur is echter duur vanwege de combinatie van initiële, onderhouds- en kalibratiekosten. Daarnaast zijn reverberation chambers de afgelopen decennia steeds meer in de belangstelling gekomen voor het testen van draadloze communicatie 'over-the-air'. Een minder bekende reverberation chamber is de Vibrating Intrinsic Reverberation Chamber (VIRC), die in vergelijking met klassieke reverberation chambers kosteneffectiever is en een eenvoudiger structuur heeft om in elkaar te zetten/uit elkaar te halen. Bovendien is het een efficiënter omgeving om multipad-omstandigheden te genereren en in staat om meer ongecorreleerde samples te produceren. Voordat de VIRC kan worden

gebruikt als een veelzijdige experimentele omgeving (dwz een kanaalemulator) voor het UNB-signaleringsschema, moet er eerst een effectieve karakterisering worden uitgevoerd van de reverberation chamber zelf. Dit proefschrift onderzoekt diepgaand of de VIRC het UNB kanaalmodel van een realistische omgeving nauwkeurig kan nabootsen.

Om de VIRC te gebruiken als een kanaalemulator voor het UNB-signaleringsschema in de 2,4 GHz-band, wordt eerst een systematische meet- en schattingsmethodologie ontwikkeld voor het empirisch onderzoek van het propagatiekanaal binnen de VIRC op basis van de eerste- en tweede-orde temporele en spectrale kenmerken. De methodologie is ontworpen om universeel te zijn voor elke reverberation chamber als de mode-stirring techniek wordt gebruikt. Het houdt ook rekening met de gewenste nauwkeurigheid van de schatting en het effect van verschillende operationele variabelen: draaggolffrequentie, rotatiesnelheid van de VIRC-motoren en VIRC-loading condition. Vervolgens wordt een experimenteel raamwerk samengesteld uit de VIRC- en het propagatiekanaal. Er wordt een grondige empirische karakterisering van het kanaal uitgevoerd. Diverse kanaalkenmerken worden gezamenlijk gemeten en onderzocht met betrekking tot de eerder genoemde operationele variabelen, met een nadruk op de 2,4 GHz-band. Verschillende wiskundige modellen worden voorgesteld om het gedrag van verschillende gemeten kenmerken te beschrijven. Bovendien wordt de geldigheid van de statistische methode geanalyseerd en wordt de algemene toepasbaarheid van de voorgestelde modellen beoordeeld. De analyse van de gemeten VIRC resultaten laat zien dat het Doppler spectrum overeenkomt met het Bell model en het kanaal-envelope histogram de theoretische Rice verdeling benadert. Ten slotte, gezien de kanaalkarakteristieken van de twee mogelijke UNB-implementatiescenario's, wordt aangetoond dat de VIRC ruwweg kan worden gebruikt als een UNB-kanaalemulator met toegeschreven eerste- en tweedeordekarakteristieken in het algemeen, echter wel met een beperkte emulatiecapaciteit voor trage vervaging in het bijzonder.

ACRONYMS

3GPP	3rd Generation Partnership Project
AC	anechoic chamber
AD	Anderson-Darling
AFA	adaptive-frequency-agility
AP	access point
APCO	Association of Public-Safety Communications Officials
AWGN	additive white Gaussian noise
BB	baseband
BDR	beacon delivery rate
BFSK	binary frequency-shift keying
BS	base station
CB	coherence bandwidth
CCA	clear-channel-assessment
CCA-CS	clear-channel-assessment carrier-sense
CCA-ED	clear-channel-assessment energy-detection
CDF	cumulative distribution function
CEH	channel envelope histogram
CF	carrier frequency
CLRC	classical reverberation chamber
CT	coherence time
CvM	Cramér-von Mises
DBPSK	differential binary phase-shift keying
DL	downlink
DSD	Doppler spectral density
DSSS	direct-sequence spread spectrum
DUT	device under test
EIRP	equivalent isotropic radiated power
EM	electromagnetic
EMC	electromagnetic compatibility
EMI	electromagnetic interference
ETSI	European Telecommunications Standards Institute

FCF	frequency correlation function
FHSS	frequency-hopping spread spectrum
FM	frequency modulation
FS	frequency stirring
GFSK	Gaussian frequency-shift keying
GMSK	Gaussian minimum-shift keying
GoF	goodness-of-fit
IC	initial condition
IFBW	intermediate frequency bandwidth
IoT	Internet of Things
ISM	Industrial, Scientific, and Medical
LBT	listen-before-talk
LC	loading condition
LNA	low-noise amplifier
LoS	line-of-sight
LPWAN	low-power wide-area network
LTE	long-term evolution
LUF	lowest usable frequency
MAC	media-access control
MAF	moving-average filter
MAPL	maximum allowable path loss
MCS	modulation coding scheme
MIMO	multiple-input multiple-output
MRSS	minimum received signal strength
NB	narrowband
NFAF	normalized frequency autocovariance function
NLS	nonlinear least-squares
NTAF	normalized time autocovariance function
OFDM	orthogonal frequency-division multiplexing
OOK	on-off-keying
OSI	Open Systems Interconnection
OTA	over-the-air
PA	power amplifier
PDF	probability density function
PDP	power delay profile
PER	packer error rate
PHY	physical layer
PSD	power spectral density

QoS	quality-of-service
RC	reverberation chamber
RF	radio frequency
RFI	radio-frequency interference
RP	random process
RR	rejection rate
RS	rotational speed
RSSI	received signal strength indicator
RV	random variable
Rx	receiver
SA	spectrum analyzer
SIR	signal-to-interference ratio
SISO	single-input single-output
SNR	signal-to-noise ratio
SRD	short-range device
SSB	single-sideband modulation
STA	station
TCF	time correlation function
TRx	transceiver
Tx	transmitter
UC	unstirred component
UL	uplink
ULP	ultra-low power
VIRC	Vibrating Intrinsic Reverberation Chamber
VNA	vector network analyzer
WBAN	wireless body-area network
WLAN	wireless local-area network
WPAN	wireless personal-area network
WSN	wireless sensor network

CONTENTS

1

INTRODUCTION

1.1. BACKGROUND

For the past two decades, the Internet of Things (IoT) has proved to be a key enabling technology for products and services which are gradually becoming an integral part of our daily life. This technology has the potential of changing the world socially and economically. On the social scale, services such as health monitoring and office automation will continue to impact the way humans interact with their environment in the domestic and working fields. For example, in healthcare, IoT-enabled devices can monitor patients' vital signs and send the data to healthcare providers for analysis, helping to prevent and manage chronic diseases [1]. On the economical scale, the IoT as generated an enormous number of applications in the consumer and industrial sectors. For example, in transportation, IoT-enabled vehicles can communicate with each other and with the traffic infrastructure to reduce congestion and to improve safety [2]. IoT, simply put [3], is a growing network of sensors, actuators, software and connectivity that are embedded in physical objects (e.g., vehicles and buildings), deployed in private and public places (e.g., schools and museums), and connected together—and to the Internet—through the IP protocol to collect and exchange data. According to Figure 1.1, it was estimated that 14.4-billion IoT devices (excluding smartphones, tablets, and computers) were already in use in 2022, and this number was expected to reach 27 billion by the year 2025 [4].

A trending technology that has gained renewed momentum for the past decade is the wireless sensor networks (WSNs) technology. The concept of WSNs first emerged as a military application for battlefield surveillance under the Smart Dust project which was developed at the University of California (Berkeley) and funded by the Defense Advanced Research Projects Agency (a.k.a. DARPA) [5]. Since then, the concept has attracted huge interest and has expanded enormously to result in a broad range of consumer and industrial applications [6–9]. In fact, WSNs and IoT are closely related as the former is a key component of the latter. In a typical architecture, a WSN is a scalable wireless network in which a large number of small, low-cost, and low-power sensors and/or actuators are deployed over an area of interest, sense their environment, and wirelessly transmit the sensing information on a periodic basis or

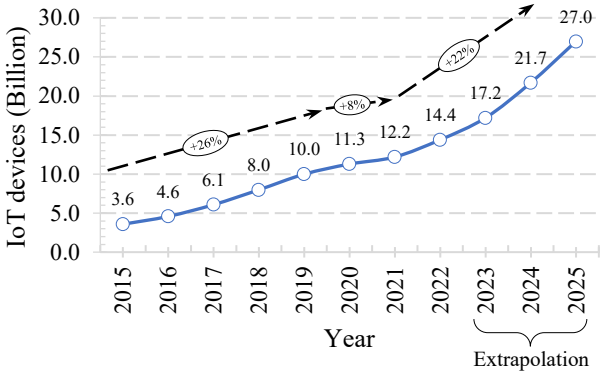

Figure 1.1: Global IoT market forecast [4].

on demand to a centralized base station (BS) for further processing and/or action [10]. Eventually, based on the processing of the collected sensing information, the actuators execute specific actions and, consequently, alter their environment in a systematic and desired manner. The utilization of wireless connectivity (i.e., WSNs) in IoT allows for the remote collection of data as well as for the automation of tasks, which improve business efficiency and, thereby, reduce operational costs.

Most IoT applications and services, such as wild-fire detection, electricity metering, livestock tracking, and dam health monitoring, are preferred to be physically deployed using wireless connectivity with a low-power budget and minimum network infrastructure [10, 13]. Therefore, as a response to such demands, researchers and engineers have developed algorithms, modulations, and media-access control (MAC) protocols to improve the performance of WSNs in terms of cost, range, and power consumption. Over the years, this has helped the emergence of a new type of WSNs commonly known as low-power wide-area networks (LPWAN). Figure 1.2 summarises the performance of LPWAN in comparison to different network technologies in terms of cost efficiency, battery lifetime, data rate, and range. In a nutshell, LPWAN networks have the following characteristics [14].

- They are made of low-cost and low-power sensor nodes which are powered by batteries with a lifetime ranging from several months up to 10 years.
- Opposed to cellular networks, their infrastructure is made of much fewer BSs that support long-range communications by providing a wireless access service to a wide coverage area of up to several tens of kilometers. This is possible because of the following two LPWAN characteristics.
- They use signaling schemes that operate at low instantaneous data rates, from few 10's kbit/s down to 100 bit/s.
- They utilize low-frequency bands, namely, sub-GHz bands.

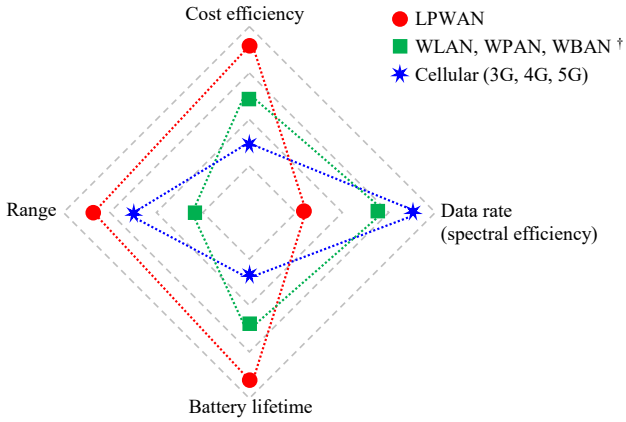

Figure 1.2: Comparative specifications of different network technologies [11, 12]. †Acronyms: WLAN (wireless local-area network), WPAN (wireless personal-area network), WBAN (wireless body-area network).

With the increasing demand for WSN applications, such as remote sensing, smart metering, precision agriculture, and environment monitoring, several LPWAN technologies and standards have been developed in the past decade. In the following, we discuss multiple technologies that have dominated the global LPWAN market.

1.2. LPWAN TECHNOLOGIES

Different standards and commercial technologies have been created and developed over the past years such as NB-IoT (NarrowBand-IoT) by 3GPP [15, 16], LoRa (Long-Range) by Semtech [17, 18], and UNB (Ultra-Narrowband) by Sigfox [19, 20]. According to Figure 1.3, NB-IoT, LoRa, and UNB are the leading LPWAN technologies in the market.

- NB-IoT uses a subset of the the 4G LTE physical-layer (PHY) after being optimized for indoor coverage and low-power devices.
- LoRa is a proprietary PHY signaling scheme based on chirp spread spectrum which is combined with a networking protocol known as LoRaWAN.
- UNB is used by several companies as a signaling scheme with an ultra-narrow bandwidth of a few 100's Hz.

Each of these technologies targets a specific type of applications and, thereby, focuses on different subsets of the following specifications [21]: cost efficiency, range, latency, battery life, and quality of service (QoS). Considering cost efficiency, NB-IoT operates in the costly licensed spectrum (i.e., high service costs), yet it has the advantage of leveraging the pre-existing cellular network infrastructure (i.e., low network roll-out costs). On the other hand, LoRa and UNB operate in the

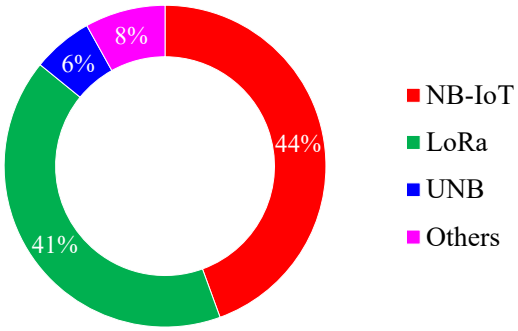

Figure 1.3: Global market share among LPWAN technologies in 2022 [4].

license-free bands, yet they need to roll out their own customized networks to extend their urban/suburban/rural coverage. Considering range and latency, UNB offers the longest range of up to 40 km [22]. However, this is at the expense of latency of 20–45 s for a two-way handshake [23, 24]. On the other hand, NB-IoT offers the shortest latency of up to 10 s [25], but at the expense of range which is limited to 10 km [22]. A flexible compromise between range and latency is possible with LoRa by virtue of its adaptive PHY [26]. In NB-IoT, the sensor nodes have to manage several tasks, namely, cell search, network coordination, handshaking, and MAC protocol [27]. Unlike Lora and UNB, these extra tasks are essential to maintain a good QoS, yet they demand additional energy which reduces the battery lifetime of an NB-IoT node. Figure 1.4 summarises the performance of the three LPWAN technologies in terms of the aforementioned specifications.

All WSN applications can be grouped into one of the following four categories: detection, metering, tracking, or monitoring [10, 13]. The majority of such applications in LPWANs is characterized by latency tolerance, low throughput, and low cost [20, 29, 30], for which UNB[1] is an attractive solution according to Figure 1.4. One example of such applications is the transfer of biometric data (e.g., glucose level) of a home patient to a cloud-connected BS [31]. In such an example, data could be transmitted regularly or on an event-triggering basis. In either case, the transfer rate could barely be up to ten times a day for a diabetic patient. Another example is an environmental monitoring network [32] in which very few packets per minute are transferred to a BS delivering information about the outdoor temperature.

In the late 1990s and early 2000s, the UNB signaling scheme was first introduced as a 12.5 kHz digital communication protocol for a simple two-way radio system. The initiative was under the APCO P25 digital standard targeted mainly for the United States public safety sector to replace the analog FM and SSB legacy schemes [33, 34]. In the early 2010s, UNB was adopted by Sigfox [19] and was later studied in the the literature as a signaling scheme for LPWANs [20, 35–43]. In the following,

[1] For this reason, from now on we focus on UNB

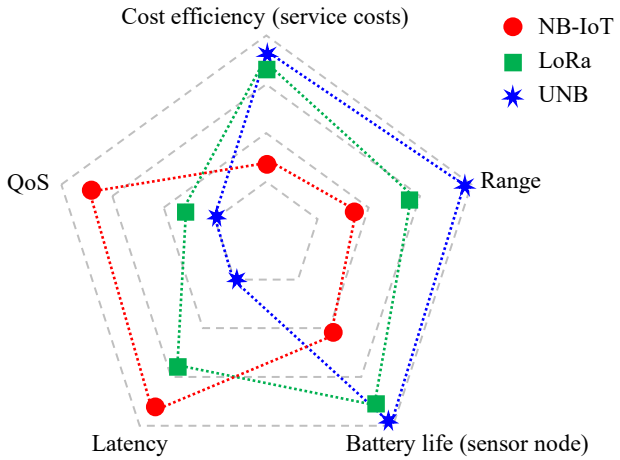

Figure 1.4: Comparative specifications of the leading LPWAN technologies [22, 28].

we introduce the concept, advantages and disadvantages related to UNB. Then we introduce the Slow Wireless project which investigates the PHY aspects of the UNB signaling scheme.

1.3. ULTRA-NARROWBAND SIGNALING SCHEME

By taking leverage of the fact that both latency tolerance and low throughput are two characteristics of the majority of LPWAN applications, the concept of UNB is thus based on two simple yet powerful ideas [21, 37–40, 44]. The first one is to make the wireless link as asymmetric as possible in terms of processing load and power consumption by shifting the burden from the sensor nodes to the BS. This is typically done by considerably reducing the instantaneous data rate while greatly simplifying the design of both the PHY and MAC layers. The second idea is to use the license-free sub-GHz bands for communications.

1.3.1. CHARACTERISTICS

Several companies currently implement the UNB signaling scheme, including Sigfox [19], Telensa [45], Weightless [46], and WAVIoT [47]. Since Sigfox dominates the UNB-based IoT market [4], we will focus on its implementation of the UNB signaling scheme in the following.

The scheme operates in the license-free Industrial, Scientific, and Medical (ISM) band of 868 MHz [21, 48]. Initially, it was only unidirectional [21], meaning that data could only be sent from the sensor nodes to the BS using an uplink (UL). Later, a downlink (DL) was introduced enabling bidirectional communications [21, 48]. Due to emission regulations [49, 50], the transmission power is upper-limited by +14 dBm and +27 dBm in the UL and the DL, respectively. Moreover, since the

listen-before-talk (LBT) and the adaptive-frequency-agility (AFA) mechanisms are not employed, there is a requirement of 1% and 10% on the duty cycle for the UL and DL, respectively. This is enforced by the emission regulations [49, 50] and, thereby, translates into an upper limit on the average data rate of 140 packets per day over the UL [21]. As opposed to NB-IoT (which utilizes orthogonal frequency-division multiplexing) and LoRa (which utilizes spread spectrum), the UNB PHY uses single-carrier modulation, namely, differential binary phase shift keying (DBPSK) and Gaussian frequency shift keying (GFSK) [21, 48]. The two signal modes of 100 bit/s and 600 bit/s are adopted for the instantaneous bit rate, resulting in an ultra-narrow occupied bandwidth of 100 Hz and 600 Hz, respectively [21, 48]. The packet payload is limited to a maximum of 12 bytes in the UL [21, 48].

The MAC layer uses a time-unslotted frequency-unslotted version of the ALOHA protocol [39], meaning that the sensor nodes can transmit data without the need for time/frequency coordination (a.k.a. rendezvous) with the BS. The communication link is always initiated by the sensor node [21, 51]. An acknowledgement packet—if requested by the node—is sent by the BS after 20–45 s [23, 24] following the piggybacking mechanism [48], meaning that the nodes only wake up from the sleep mode for sensing and transmission. The UNB network uses a star topology [21], meaning that the sensor nodes communicate directly with the BS which supports up to 1 million nodes [52]. The reason behind the latter is that Sigfox follows a non-cellular network-based approach [21], meaning that the same frequency channels are reused by all serving BSs. To improve the packet delivery rate, there are two mechanisms that are put in use by Sigfox: packet repetition (a.k.a. time and frequency diversity) and cooperative reception (a.k.a. macro-spatial diversity) [21, 53].

1.3.2. ADVANTAGES

One of the main ideas behind the UNB signaling scheme is the extremely low instantaneous data rate. This allows for the use of an extremely narrow bandwidth, which in turn provides several advantages compared to other LPWAN technologies.

- A narrower bandwidth means that the received noise is lower, resulting in a longer communication range [54].
- A signal with a narrow bandwidth effectively overpowers wideband interference and is more likely to avoid other narrowband interfering signals, resulting in interference-robust communications.
- According to the Nyquist-Shannon sampling theorem, a narrower bandwidth needs a lower sampling frequency [54], resulting in a lower power consumption by the digital circuitry due to a slower clock rate.
- Wireless signals as narrow as a few 100's Hz will certainly experience flat fading in real-world environments [55], meaning that the receiver does not need an equalizer, resulting in a lower power consumption by the digital circuitry due to a lower computational load.

- Combining an extremely low instantaneous data rate with a simple PHY design leads to a reduced complexity in terms of transceiver circuit architecture, signal processing, and antenna design. This in turn results in cheaper sensor nodes and a lower power consumption, making it an attractive option for WSN applications in which the nodes are often battery-powered and/or disposable. Moreover, considering the drive to a greener future, it is also a potentially attractive solution in which the nodes are battery-less as, e.g., in [56] and/or—most recently—biodegradable as, e.g., in [57].

The other idea behind the UNB signaling scheme is that it operates in the license-free sub-GHz band, which provides the following advantages.

- It allows for cheap service costs since there are no licensing fees or complex regulatory requirements, compared to licensed bands (as, e.g., in NB-IoT).
- Since these bands are often used for a variety of applications, there is a wide range of cheap and largely accessible components like antennas and integrated circuits that are designed and mass-produced for such bands. This makes a large-scale deployment physically doable as well as cost effective, especially in the case of aiming at developing and deploying millions of sensor nodes that use the UNB technology.

1.3.3. DISADVANTAGES

As discussed previously, the UNB signaling scheme has many advantages compared to LoRa and NB-IoT. However, it faces its own set of disadvantages (i.e., challenges and limitations) that degrade the connectivity performance [58] and limit the large-scale deployment [4].

One of the main ideas behind the UNB signaling scheme is the extremely low instantaneous data rate, which brings in several advantages, as discussed earlier. However, this very idea presents the following primary challenges that must be overcome for a successful large-scale UNB deployment.

- The Doppler effects (namely, mean Doppler shift and Doppler drift) and—more importantly—the non-idealities of the local oscillator (namely, initial frequency offset and frequency drift) can induce a significant frequency misalignment between a transmitter and a receiver. For example, typical crystal-based oscillators in the market have an accuracy of $\pm 20\,\text{ppm}$ [59], meaning that a simple and low-power UNB receiver has the overwhelming task of locating and decoding its 100 Hz designated signal at 868 MHz from a crowded bandwidth of $2 \times 868\,\text{MHz} \times 20\,\text{ppm} = 34\,\text{kHz}$ [60, 61]. This challenge has been addressed, e.g., recently in [62–65].
- In indoor/outdoor environments, the combined effect of multipath propagation of radio waves with a dynamic link and/or environment leads to a time-variant channel (a.k.a. Doppler spread and/or drift), in which the amplitude and the phase of received signals change over time. In many real-world deployments,

the bit rate of a 100 Hz UNB signal is comparable to the speed at which the channel changes [66, 67], meaning that multiple fading dips per packet are likely to happen. This phenomenon is commonly known as time-selective/fast fading, which severely degrades the received signal quality and, thereby, increases the probability of errors [38, 68–75]. To overcome this challenge, time diversity, frequency diversity, and macro-spatial diversity have been considered, e.g., in [43, 58, 76–78].

- In the case of low-density deployments, UNB signals are expected to avoid intra-network interference in the frequency domain due to their extreme-narrow bandwidth. However, collisions are most likely to occur in case of a large-scale deployment of millions of UNB sensor nodes in a single city. Moreover, due to the extended duration of a UNB packet, which can span up to two seconds, the probability of collision will even rise. This poses a challenge for UNB-based networks, as intra-network interference can result in packet losses and, thereby, a decreased overall network throughput. To address this challenge, the MAC-layer protocol of Unslotted Time-Frequency ALOHA (a.k.a. Random Frequency-Time Multiple Access) is proposed and extensively studied, e.g., in [35, 37, 39, 41, 79–82]. Moreover, the Successive Interference Cancellation technique is proposed and jointly studied with the aforementioned random-based MAC protocol in [83].

The other idea behind the UNB signaling scheme is that it operates in the license-free ISM sub-GHz band, which gives rise to the following limitations and challenges that must be addressed to ensure reliable and compliant operation.

- The emission regulations of the 868 MHz band specify limitations on the radiated power and the transmitter on-time. Depending on the utilized sub-band, the maximum effective isotropic radiated power (EIRP) should not exceed the range 14–27 dBm, and the maximum duty cycle should belong to the range 0.1%–10% [49, 50]. This poses an upper limit on the achievable communication range as well as—more importantly—on the maximum carried throughput of 140 12-byte packets per node per day [21].

- Since the 868 MHz band is shared by different WSN technologies, wireless coexistence (i.e., inter-network spectrum sharing) is inevitable. This means that the UNB signaling scheme needs to be robust against interference, while at the same time it needs to be friendly to other pre-existing technologies [40, 84, 85].

1.4. PROBLEM STATEMENT—THE SLOW WIRELESS PROJECT

UNB-based networks are deployed in the 868 MHz ISM band. However, the emission regulations in this license-free band severely cap the carried throughput of the sensor nodes by imposing a harsh duty-cycle limitation of 140 12-byte packets per node per day, according to the emission regulations [49, 50]. On the other hand,

according to the emission regulations of the 2.4 GHz ISM band [86], there is no such a limit on the carried throughput. Besides, a much larger bandwidth of a 100 MHz is available in comparison to only 7.6 MHz in the 868 MHz band.

Currently, LoRa (by Semtech [17, 87]) and RPMA (by Ingenu [88, 89]), are the only signaling schemes with a very low instantaneous bit rate that are deployed in the 2.4 GHz band. LoRa is a multi-layer protocol with a chirp spread spectrum, whereas RPMA is a full-stack protocol with a direct-sequence spread spectrum. Their wireless coexistence with respect to Wi-Fi is studied, e.g., in [90, 91]. Having said that, there is no similar deployment for UNB in the 2.4 GHz band.

Therefore, the Slow Wireless project, within which the main scope of this thesis has been developed, was initiated to investigate the feasibility of—and ultimately accomplish—a UNB[2] deployment in the 2.4 GHz license-free ISM band. In addition to the unintentional radiation from ISM equipment, this interference-rich wireless environment is heavily crowded with WLAN, WPAN, and WBAN devices and nodes. As one of three work packages in the Slow Wireless project, this thesis thus aims at investigating the physical-layer aspects of the UNB signaling scheme in the 2.4 GHz band in terms of energy efficiency and wireless coexistence. It also aims at researching and developing a cost-effective experimental environment in which proposed solutions, e.g., to the challenges of wireless coexistence and time-selective fading[3] can be investigated.

1.5. RESEARCH GOALS

Based on the aforementioned work package in the Slow Wireless project, there are three main research goals to be considered in this thesis.

1.5.1. INVESTIGATION OF UNB ENERGY EFFICIENCY

There are two popular yet contradicting views regarding optimal data rate when it comes to energy efficiency. The first one is generally circulated in the LPWAN marketing domain, indirectly indicating that a lower data rate results in a longer battery lifetime. However, this view is logically false. In fact, it misleadingly attributes the long battery lifetime (e.g., up to 10 years [14]) to the typical LPWAN characteristic of low instantaneous bit rate [20] (which is required to achieve long-range communications and/or combat strong environmental interference [92]), rather than to the extremely low carried throughput (which is enforced by emission regulations [49, 50]). The second view, on the other hand, is more factual. It implies that the optimal data rate is actually determined—among others—by the ratio of the average power consumption of the analog circuitry in the sensor nodes

[2] As mentioned in Section 1.2, UNB is a signaling scheme that is used by several companies with different PHY specifications. However, in this thesis, UNB is used as an acronym and refers to any signaling scheme with a very narrow bandwidth of a few kHz.

[3] Time-selective fading is one of several challenges that are addressed by another work package in the Slow Wireless project.

to its digital circuitry [93] (i.e., the larger the ratio, the better the energy efficiency). In semiconductor industry, since the advancement in digital chip manufacturing technology is more rapid than in analog, the average power consumption of the digital circuitry in a sensor node tends to be less than that of its analog circuitry. Thus the second view argues that a higher data rate—but up to a certain point—tends to result in a longer battery lifetime. However, this view falls short of considering the full picture. In practice, the operating data rate deviates from the optimal one because of several practical factors: size constraints of the sensor node (e.g., a potential crystal-less design and a battery peak discharge-current limitation), emission regulations (i.e., maximum EIRP and channel bandwidth), and maximum allowable path loss. Accounting for all these practical factors is not only important for achieving an energy-efficient RF solution, but—in specific deployment scenarios—it may also render some commercially available RF solutions infeasible. Therefore, the investigation of the feasibility and energy efficiency of a UNB deployment in the 2.4 GHz band is necessary.

1.5.2. INVESTIGATION OF UNB WIRELESS COEXISTENCE

An IoT sensor, which utilizes the UNB signaling scheme, would transmit packets that each fully occupies, e.g., two seconds (in the case of 200 bit/packet and 100 bit/s). Therefore, a single UNB packet in the 2.4 GHz band may cause interference to thousands of Wi-Fi packets. According to emission regulations of the 2.4 GHz band [86], narrowband[4] wireless devices that operate in the 2.4 GHz band have an upper limit of +10 dBm on the EIRP, and they "may use a Listen Before Talk (LBT) protocol with a preferred option of Adaptive Frequency Agility (AFA)" to share the spectrum along with other similar devices. However, for sensor nodes that maximally transmit −10 dBm of EIRP, "no access technique is specified", i.e., they do not have to adhere to any further rules regarding LBT or AFA mechanisms. Among WLAN, WPAN, and WBAN technologies, Wi-Fi networks are the most widespread (i.e., in homes, offices, stations, public places, and even cities with free Wi-Fi). Therefore, their desirable 24/7 uninterrupted coverage may then become subject to frequent outages caused by potential future deployments of UNB networks nearby. Regarding the resilience of Wi-Fi networks to (ultra-)narrowband interference in the 2.4 GHz band, the literature only considers the impact of single-tone jammers and the harmonics from digital clock circuits [95–101]. Moreover, these studies either do not follow a systematic/profound investigation, do not consider realistic interfering scenarios, and/or do not examine the different Wi-Fi mechanisms individually. Therefore, a systematic, profound and comprehensive investigation is lacking, which is essential to reach reliable conclusions regarding the friendly coexistence of UNB to Wi-Fi in the 2.4 GHz band.

[4] According to emission regulations [94], a narrowband signaling scheme is any modulation that does not utilize a wideband transmission technique such as spread spectrum or orthogonal frequency-division multiplexing.

1.5.3. DEVELOPMENT OF A UNB CHANNEL EMULATOR

In general, the investigation of the challenges facing a network deployment along with the corresponding proposed solutions is conducted either through RF drive/walk testing in real-world environments or through emulation-based testing in controlled experimental environments [102]. The former testing is labor intensive, time consuming, and costly [102]. Moreover, since real-world environments are not controllable, results from such testing are not repeatable [102]. On the other hand, conducting the investigation in a controlled environment guarantees the bare-minimum requirement for repeatability. A controlled experimental environment can be a radio channel emulator (i.e., RF testing equipment), a reverberation chamber (RC), or a combination thereof [103]. Radio channel emulators are frequently utilized to simulate various propagation channel models and interference conditions. However, they are expensive due to combined initial, maintenance, and calibration costs. Classical reverberation chambers (CLRCs), which were initially utilized in electromagnetic compatibility (EMC) testing [104], have attracted an increasing interest in over-the-air (OTA) testing of wireless communications in the last couple of decades [105]. A less-known RC for EMC is the Vibrating Intrinsic Reverberation Chamber (VIRC) [106]. Compared to the CLRC, the VIRC is more cost effective and has a simpler structure to assemble/disassemble [107]. Moreover, it is a more efficient environment for generating multipath conditions as well as capable of producing more uncorrelated samples [107, 108].

A future deployment of a UNB network in the 2.4 GHz band faces two major challenges: time-selective fading[5] and wireless coexistence [40, 75]. In the case of investigating the wireless coexistence between UNB and Wi-Fi networks in the VIRC, the following three requirements have to be satisfied. (*i*) Both systems should be isolated from all unintended environmental interference [109]. (*ii*) The configurations of the propagation channel inside the VIRC have to be correctly set to mimic the intended deployment scenario. *(iii)* The configurations of both systems should be accurately controlled to re-create the intended interference scenario [110]. Likewise, in the case of investigating the UNB challenge of time-selective fading in the VIRC, the two aforementioned requirements, (*i*) and (*ii*), are also necessary. Depending on which research area the VIRC is utilized in (i.e., EMC/OTA testing), a corresponding relevant characterization must first be conducted on the chamber itself before it is used in a specific application. This is to investigate the dynamic range of the chamber characteristics under interest as well as to ensure it meets the different standardization requirements. Alas, a VIRC systematic measurement and estimation methodology is lacking for OTA testing. Moreover, regarding the second requirement (*ii*), a VIRC-based channel emulator for UNB should be investigated to whether it can closely mimic the channel characteristics of the real-world environment in terms of the second-order temporal characteristics (i.e., Doppler spectrum), the second-order spectral characteristics (namely, flat fading), and the first-order characteristics (e.g., Rician distribution with different K-factors).

[5] Time-selective fading is one of several challenges that are addressed by another work package in the Slow Wireless project.

1

1.6. RESEARCH QUESTIONS

Taking the aforementioned research goals into account, the main research questions in this thesis can be formulated as follows.

1. *When it comes to feasibility in terms of energy efficiency, what are the suitable deployment scenarios for the UNB signaling scheme in the 2.4 GHz band?*
   To answer this question, various power consumption trade-offs are first identified and broken down to their "basic elements". A comprehensive energy consumption model is then developed for a conventional circuit architecture and a typical asymmetric WSN link. Next, from the perspective of energy efficiency (i.e., minimum energy consumption), optimal data rates are numerically calculated for a wide range of deployment scenarios while taking into consideration several practical factors: timing and frequency errors, emission regulations, source-power limitations, and maximum allowable path loss. Finally, based on the insights from the optimization outcome, potential deployment scenarios for the UNB signaling scheme are identified.

2. *In the case of a future deployment in the 2.4 GHz band, how friendly is the UNB signaling scheme to the IEEE 802.11-based networks (a.k.a. Wi-Fi)?*
   To answer this question, an empirical investigation is pursued. However, a systematic and thorough methodology is first developed for the investigation. Different individual Wi-Fi mechanisms[6] from PHY up to transport layer are considered. The approach of a worst-case interfering scenario is followed. The methodology is then practically applied while comprehensively considering as many UNB and Wi-Fi parameters as possible. Several off-the-shelf Wi-Fi devices are tested. Finally, based on the gained insights, recommendations are proposed to promote the friendly coexistence of the UNB signaling scheme in the 2.4 GHz band.

3. *Considering the potential deployment scenarios from the first research question, to what extent can the Vibrating Intrinsic Reverberation Chamber (VIRC) be used to emulate the wireless propagation channel that a UNB-based sensor node would experience?*
   To answer this question, a measurement and estimation methodology is first developed to systematically, thoroughly, and empirically characterize the VIRC for OTA testing in terms of the channel first- and second-order temporal and spectral characteristics. Next, a comprehensive measurement campaign and an empirical characterization and modeling of the propagation channel inside the VIRC are conducted following the developed methodology. Finally, the feasibility of a VIRC-based channel emulator for UNB-based sensor nodes is studied.

[6] Strictly speaking, Wi-Fi only defines the first two layers in the OSI (Open Systems Interconnection) model, namely, the physical layer and the data-link layer.

1.7. THESIS OUTLINE

Chapter 2, which is based on [111, 112], is dedicated to answering the first research question. The chapter presents a PHY-based optimization framework from the perspective of energy efficiency. The optimization is applied to a numerical example for a wide range of deployment scenarios, and three study cases are investigated. Next, Chapter 3, which is based on [113], is dedicated to answering the second research question. It presents an experimental study concerning the impact of UNB interference on Wi-Fi links. It also makes recommendations for the wireless coexistence between UNB and Wi-Fi networks. The next two chapters are dedicated to answering the third research question. In Chapter 4, which is based on [114], a measurement and estimation methodology for OTA testing in the VIRC is developed. Chapter 5, which is based on [115], presents an empirical characterization and modeling of the propagation channel inside the VIRC that is based on the developed methodology in the previous chapter. The feasibility of a VIRC-based channel emulator for UNB is also studied. Finally, Chapter 6 summarizes the conclusions to the research and gives recommendations for future work.

2

ENERGY EFFICIENCY

2.1. INTRODUCTION

The key aspects that drive the competition in the wireless sensor market (WSN) market are cost, size and power consumption of the sensor nodes. Fundamentally, the latter aspect is considered the most important as it essentially determines the size of the battery that must be used to power the sensor node and, thereby, the overall size of the node itself [116]. Additionally, the power consumption drastically influences the lifespan of the sensor nodes, whose batteries cannot be recharged or even replaced once they are depleted, as this would not be cost-efficient for large-scale networks. Moreover, because of size constraints in specific WSN applications, sensor nodes cannot use batteries at all, but solely depend on energy scavenging. Such nodes irregularly collect energy in minute amounts from the surrounding environment through a harvesting element in forms of ambient RF, temperature difference, light, etc. [117]. These nodes accumulate the harvested energy in a storage element, which—in the case of size constraints—is typically a supercapacitor or a thin-film battery [118]. RF modules that utilize Wi-Fi technology tend to be power hungry [119] and, thereby, are not suitable for WSNs in general, let alone to survive on energy scavenging. ZigBee and Bluetooth Low-Energy, on the other hand, have been developed as ultra-low-power (ULP) wireless technologies and, thereby, can be adopted as RF solutions for energy-scavenging-powered sensor nodes [120, 121]. However, such RF solutions require the use of physically large storage elements (e.g., ~100 μF electrolytic or ceramic capacitors) that can provide the necessary peak current (~10 mA) as well as the energy capacity. Therefore, in the case of WSN applications with miniature-size constraints, alternative RF solutions are needed.

Papotto *et al.* [122] presented a battery-less crystal-less RF-powered transceiver that supports a 915 MHz downlink (DL) and a 2.45 GHz uplink (UL). They have

Parts of the content of this chapter were published in [111, 112].

used an off-chip 100 nF capacitor as a storage element. Capacitors, particularly supercapacitors, are suitable storage elements, but they have two drawbacks [118]: very small energy capacity and very high self discharge. In addition, there may be long periods of time during which there is no power available from the harvesting element. Thus energy has to be harvested in a greedy manner, which requires larger energy capacities than the supercapacitors can offer. Thin-film batteries, on the other hand, have larger energy densities [123], and hence they can support a long-term energy-scavenging solution. Unfortunately, to avoid deteriorating their capacity, the discharge current is preferred to be as small as possible (~100 μA for millimeter-scale size) [118, 124]. This preferred practice maximizes the lifespan of the battery and, thereby, of the sensor node itself. In [125], an energy-autonomous millimeter-scale node is designed based on a cross-layer system-level optimization framework. It is built using both a thin-film battery and a capacitor. The battery provides the necessary energy capacity, whereas the capacitor provides the necessary peak current. However, because the proposed optimal solution is specific to a system-level cross-layer design, it cannot be standardized as an RF solution. Moreover, even though utilizing both types of storage elements is a good idea, yet this is at the expense of extra cost as well as larger nodes. Since cost is a crucial factor in the market of large-scale networks, further convenient ULP RF solutions are needed.

Because the radio section in a sensor node contributes to the overall energy consumption to a large extent [126, 127], research has focused on radio design to achieve ULP transceivers by following different approaches. One of them is to investigate the power consumption of different RF blocks to develop models for the energy consumption as, e.g., in [93, 128, 129]. Using these models, existing trade-offs can be identified, combined, and broken down to isolate their primary variables whose values are then optimized with the objective of maximizing the energy efficiency. For example, in [128], a formula for the optimal power consumption of the low-noise amplifier (LNA) is introduced for a given circuit architecture and transceiver power budget. In [93], the trade-off between the transmitter (Tx) instantaneous radiated power and the receiver (Rx) sensitivity is investigated in a duty-cycled transceiver (TRx) to find the optimal data rate. Li *et al.* in [129] have studied the conventional RF architectures of four different modulation techniques, namely, on-off keying, phase-shift keying, quadrature amplitude modulation, and frequency-shift keying. For each modulation, they have presented a model for the consumed energy per bit, and optimized the solution for different bandwidth and data rate requirements. For every such requirement and intended transmission range, they have found an optimal modulation scheme with which the energy efficiency is maximized.

In energy-scavenging-powered sensor nodes that are deployed in an ISM band, there are two main practical factors that have to be considered during the configuration of the physical layer (PHY). These factors are size constraints and emission regulations. Crystal-less design and peak-current budget are two manifestations of size constraints. Channel bandwidth and effective isotropic radiated power (EIRP) are both upper-limited by emission regulations. For a feasible and energy-efficient

RF solution, all these aforementioned practical factors have to be accounted for in the optimization of the design and operating PHY parameters (e.g., bit rate and radiated power) [130].

In this chapter, the objective is to investigate the feasibility of a UNB deployment in the 2.4 GHz ISM band in terms of energy efficiency, by determining the optimal bit rates for a wide range of deployment scenarios, in which we assess the effect of various practical factors including that of an energy-scavenging-powered sensor node. Therefore, we follow a similar approach as in [93, 128, 129] by combining different trade-offs and breaking them down to their primary variables. Then, using power consumption models of different circuit blocks in the sensor node, a comprehensive energy consumption model is developed for an asymmetric link of a star topology. Using this energy model, the optimal bit rate is calculated, at which the energy consumption is minimal. The main contribution of this chapter is building an optimization framework, in which we combine the trade-off between Rx sensitivity, Tx radiated power, and instantaneous bit rate in one analysis, while taking into account different practical factors that may stem from the deployment of an energy-scavenging-powered sensor node in the 2.4 GHz band. These practical factors are size constraints (hence, timing-frequency accuracy and peak-power budget), emission regulations (hence, radiated power and channel bandwidth), and maximum allowable path loss (hence, link budget). Finally, we apply the analysis to a numerical example to gain more insight into the optimization process.

This chapter is organized as follows. First, we start with the analysis, in which the scope, trade-offs, practical factors, and assumptions are detailed before the energy model itself is derived. Next, a numerical example is applied to the analysis, and the obtained results are discussed while examining three study cases. Finally, a conclusion is given at the end of this chapter.

2.2. ANALYSIS

In this section, we start by introducing the scope of the analysis in detail. We then explain the existing power consumption trade-offs as well as the practical factors that must be considered in the configuration of the PHY. We also outline the list of assumptions that are made throughout the analysis. Next, we develop a mathematical model of the energy consumption per transceived packet. This model is then used in the optimization process to find the optimal design and operating PHY parameters.

2.2.1. SCOPE

In the analysis, we consider the PHY of a narrowband[1] signaling scheme in an asymmetric link (i.e., star topology), focusing on Rx sensitivity, Tx radiated power,

[1] According to the emission regulations [94], a narrowband signaling scheme is any modulation that does not utilize a wideband transmission technique such as spread spectrum or orthogonal frequency-division multiplexing.

and instantaneous bit rate (R_b), while taking into account the practical factors (i.e., considerations and limitations) of an energy-scavenging-powered sensor node that is deployed in the 2.4 GHz band. The node initiates a communication link with the base station (BS) by transmitting a single packet in the UL that carries the sensing information. Then, after a predefined turnaround interval (T_{turn}), the link is terminated by the BS with a packet in the DL that carries the acknowledgement and control information, as depicted in Figure 2.1. Because of the impact of the practical factors, the outcome of the optimization process is—to a large extent—application and implementation dependent. The optimization is carried out at the node level with the objective of maximizing its energy efficiency. The latter is defined as how little energy is consumed by the node per transceived packet (E_{pkt}) for a given link budget (L_B) and a desired packet error rate (PER).

2.2.2. TRADE-OFFS

In radio design, there are multiple trade-offs in the PHY that need to be simultaneously considered to maximize the energy efficiency [111, 112]. In this analysis, we only consider the following two trade-offs.

- For a given L_B, improving the Rx sensitivity decreases the required Tx radiated power (P_{rad}) and, as a result, decreases the power consumption of the Tx. However, achieving a better Rx sensitivity needs more power to be consumed in the LNA (P_{LNA}) at the Rx to improve its noise factor (F_{LNA}). Therefore, there is a trade-off between P_{rad} and P_{LNA}. However, given the scope of an asymmetric link, in which the BS can be assumed to have unlimited resources (i.e., its energy consumption is not optimized), the aforementioned trade-off evolves to a different one. It transforms into a trade-off between P_{LNA} and the power consumption of the other Rx analog circuits of same sensor node itself. A lower R_b improves the Rx sensitivity, alleviates the requirement on F_{LNA}, and, thereby, reduces P_{LNA}, while at the same time, increases the Rx on-time and, thereby, increases the energy consumption of the rest of the analog circuits.

- To decrease the average power consumption of both the Tx and the Rx, duty cycling is usually employed. For a given offered load (i.e., average bit rate), decreasing the duty cycle reduces the average power consumption, but only to a certain point. This can be explained as follows. Because R_b is inversely proportional to the duty cycle, decreasing the latter requires in an increase in the former. To maintain a given L_B, this increase in R_b results in a greater required P_{rad}. Moreover, the required time for the startup phase (e.g., oscillator startup time) results in an associated energy consumption which increases with a higher R_b because of power dissipation in the digital circuits. As a result, at the beginning of increasing R_b (by decreasing the duty cycle), the total average power consumption begins to decrease, but later, at a certain point, it starts to increase [131]. Therefore, R_b cannot be increased arbitrarily, and it has to be traded off against duty cycle.

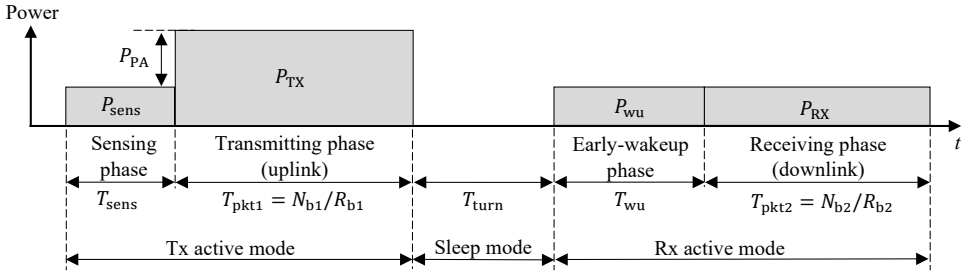

Figure 2.1: Power consumption of the sensor node per transceived packet.
Notations: N_{b1} and N_{b2} are the packet length of the UL and the DL, respectively. R_{b1} and R_{b2} are the instantaneous bit rate of the UL and the DL, respectively. During the sensing phase, the node collects the sensing information and feeds it to its digital circuits for processing before wireless transmission.

2.2.3. PRACTICAL FACTORS

In the analysis, we take into account the following practical factors (i.e., considerations and limitations) which stem from size constraints and emission regulations.

- In WSN applications with miniature-size constraints, thin-film batteries are typically used. To prolong their lifespan, an upper limit is practically put in use on the discharge current and, thereby, on the peak-power consumption [132].
- In WSN applications with miniature-size constraints, sensor nodes are required to be cheap, miniature, and highly integrated [133, 134]. Thus a crystal-less design is inevitable. Consequently, the accuracy of the timing and frequency references has to be taken into consideration.
- To cover a larger link distance and/or accommodate a larger fading margin, a larger link budget (i.e., maximum allowable path loss) is needed. This in turn requires an increase in the Tx power. However, the EIRP is upper-limited because of emission regulations, which also define the maximum channel bandwidth.

2.2.4. ASSUMPTIONS

For the sake of simplicity of the analysis, we make the following assumptions. Nevertheless, they will not significantly impact the outcome of the optimization process.

- The UL and the DL channels are modeled as AWGN channels.

- The power consumption during the sleep mode (P_{turn}) is neglected in comparison to that during the active modes. Moreover, because T_{turn} is predefined (i.e. not optimized), P_{turn} will not be considered in E_{pkt}.
- The leakage power in the digital circuits is neglected in comparison to the power consumption of the analog circuits.
- The sensor node has a sensing phase interval (T_{sens}) and an early-wakeup interval (T_{wu}), which dominate over the startup phase of the analog and the digital circuits.
- The power consumption of the BS is not considered in the optimization process since it has unlimited resources (e.g., connected to the electrical grid). However, it adheres to the emission regulations regarding EIRP and channel bandwidth [86]. Therefore, the radiated power from the BS is fixed to the maximum, i.e., to $P_{\text{rad,max}} = +10\,\text{dBm}$.
- The WSN application is given in which the link budget and the average bit rate (i.e. offered load per node) are already specified. Moreover, the latter is extremely low, e.g., several packets per day.
- The carrier frequency and the clock of the digital circuits share the same reference and, thereby, have the same accuracy.
- The link is always initiated by the sensor node.
- The modulation scheme is the same for both the UL and the DL.
- No adaptive modulation-coding scheme is implemented.

2.2.5. ENERGY MODEL

First, we start by listing the main circuit blocks in the Tx and the Rx sections. We then lay out their power consumption models. Finally, based on these models and the corresponding active intervals in Figure 2.1, we build an energy consumption model for the Tx and the Rx sections, which is used in the optimization process in the next subsection.

The analysis has not been carried out for a specific modulation format, media-access-control protocol, nor a specific circuit architecture, although it can be upgraded to become a cross-layer system-level optimization. Nevertheless, typical circuit blocks are still considered. As depicted in Figure 2.2, the circuit blocks in the Tx and the Rx sections are grouped into six main categories based on their location and power consumption model. The power consumption during the transmitting and the receiving phases that are depicted in Figure 2.1 are modeled, respectively, as

$$P_{\text{TX}} = P_{\text{FTX}} + P_{\text{DCTX}} + P_{\text{PA}} \tag{2.1}$$

$$P_{\text{RX}} = P_{\text{FRX}} + P_{\text{DCRX}} + P_{\text{LNA}} \tag{2.2}$$

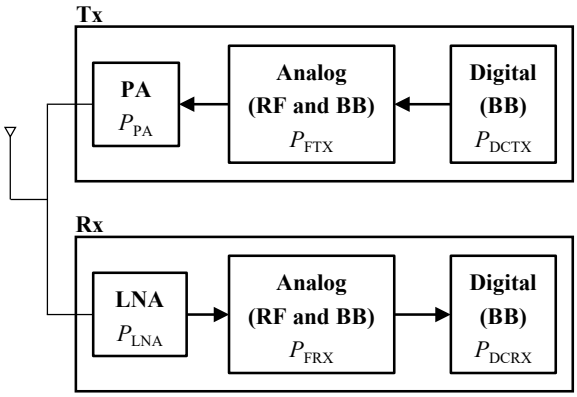

Figure 2.2: Main circuit blocks in the Tx and the Rx sections of the sensor node and their corresponding power consumption models.
Acronyms: LNA (low-noise amplifier), RF (radio frequency), BB (baseband), PA (power amplifier).

where P_{FTX} and P_{FRX} are, respectively, the aggregate power consumption of the analog circuit blocks that reside in the Tx and the Rx sections, and whose power models are independent of R_b and L_B (e.g., local oscillator, mixers, filters and low-frequency amplifiers); P_{DCTX} and P_{DCRX} are, respectively, the power consumption of the digital circuits in the Tx and the Rx sections; and P_{PA} and P_{LNA} are, respectively, the power consumption of the power amplifier (PA) and the LNA. As depicted in Figure 2.1, the PA is kept off during T_{sens} as the node collects the sensing information and feeds it to its digital circuits for processing. Additionally, the power consumption of the receiving section is the same during both the early-wakeup and receiving phases. Therefore, the power consumption during the sensing and the early-wakeup phases are modeled, respectively, as

$$P_{sens} = P_{TX} - P_{PA} = P_{FTX} + P_{DCTX} \tag{2.3}$$

$$P_{wu} = P_{RX} = P_{FRX} + P_{DCRX} + P_{LNA} \tag{2.4}$$

In the sensor node, the power consumption of the digital circuits [135, 136], the LNA [128], and the PA [137] can be modeled, respectively, as in

$$P_{DCTX} = k_{DC}\, k_{S/b1}\, R_{b1} \tag{2.5a}$$

$$P_{DCRX} = k_{DC}\, k_{S/b2}\, R_{b2} \tag{2.5b}$$

$$P_{LNA} = \frac{k_{LNA}}{F_{LNA} - 1} \tag{2.6}$$

$$P_{PA} = \frac{1}{\rho} P_{rad} = \frac{1}{\rho} k_B\, T_o\, L_B\, R_{b1}\, \gamma_{b,BS} \tag{2.7}$$

where k_{DC} is the consumed energy per IQ sample in the digital circuits expressed in joule per sample; $k_{S/b1}$ and $k_{S/b2}$ are the number of IQ samples per bit in the digital circuits of the Tx and the Rx sections, respectively; R_{b1} and R_{b2} are the instantaneous bit rate of the UL and the DL, respectively; F_{LNA} is the noise factor of the LNA; k_{LNA} is a design constant expressed in watt that indicates the required P_{LNA} to achieve $F_{LNA} = 2$; ρ is the PA drain efficiency; P_{rad} is the Tx radiated power; L_B is the link budget; $\gamma_{b,BS}$ is the minimum signal-to-noise ratio (SNR) per bit that is required at the BS to achieve a desired PER; and $k_B T_o$ is the noise power spectral density (PSD) at the standard noise temperature (T_o) with k_B being Boltzmann's constant. Equations (2.5a) and (2.5b) represent the dynamic power consumption of the digital circuits at the Tx and the Rx, respectively, whereas the static power consumption (due to leakage current) is neglected, as assumed in Section 2.2.4. The clock speed of the digital circuits linearly scales with R_{b1} and R_{b2}, depending on the resolution of the IQ samples and the complexity of the digital signal processing algorithms. Equation (2.6) is valid for LNAs that are implemented in MOSFET technology, biased in saturation, and whose specifications (e.g., gain and linearity) are fixed [128, 138]. In (2.7), L_B is defined as the maximum allowable path loss (MAPL) divided by the antenna gains of the Tx and the Rx. Moreover, since the BS has unlimited resources, it is assumed that it has zero internal noise, hence its noise factor is equal to unity in (2.7) for simplicity.

The Rx sensitivity (i.e., required minimum received signal strength, MRSS) of the sensor node is given by [137]

$$P_{MRSS} = k_B T_o F_{LNA} R_{b2} \gamma_b \tag{2.8}$$

where $k_B T_o$ is the noise PSD at the standard noise temperature (T_o) with k_B being Boltzmann's constant; F_{LNA} is the noise factor of the LNA; R_{b2} is the instantaneous bit rate of the the DL; and γ_b is the minimum SNR per bit that is required at the sensor node to achieve a desired PER. For a given L_B, the maximum radiated power from the BS ($P_{rad,max}$) and the required upper-bound F_{LNA} at the sensor node can be related together using (2.8) as in

$$F_{LNA} = \frac{1}{k_B T_o} \frac{P_{rad,max}}{L_B R_{b2} \gamma_b} \tag{2.9}$$

Equation (2.9) indicates that in order to achieve a desired PER for a given L_B, increasing R_{b2} increases the Rx bandwidth and, thereby, the total noise power. This can be alleviated to a certain extent by reducing the contribution from the Rx internal noise, i.e., by reducing F_{LNA}. However, the latter is down-limited by unity which corresponds to the ideal case of zero internal noise. This down limit on F_{LNA} creates an upper limit on R_{b2}, which can be determined by setting (2.9) to unity. Therefore, if R_{b2} exceeds its upper limit, the wireless link cannot achieve the desired PER anymore for the given L_B. In the next section, the optimization is solved numerically, and, thereby, any numerical solution with a less-than-unity F_{LNA} is simply discarded.

When the sensor node is neither transmitting nor receiving, it is normally put into sleep mode. Furthermore, the BS needs T_{turn} to detect, decode, process, and forward

the received UL packet to the cloud (e.g., for automated medical intervention) before it responds with an acknowledgement packet. So during T_{turn}, the node is put into sleep mode as well. However, because of an unavoidable timing error between the BS and the node, the latter has to wake up and listen to the channel a bit earlier to avoid missing the acknowledgement packet. Normally, the timing error in the BS is negligible compared to that in the WSN nodes. Therefore, a node with a reference accuracy of X_{ppm} has to wake up earlier for an extra time

$$T_{\text{wu}} = X_{\text{ppm}} T_{\text{turn}} \tag{2.10}$$

In the case of a crystal-less design, the local oscillator exhibits a random frequency offset, which is relatively significant for narrowband signaling. To accommodate such a frequency offset, the bandwidth of the UL channel is given by [60]:

$$\text{BW}_{\text{UL}} = \frac{1}{\eta} R_{\text{b1}} + 2 X_{\text{ppm}} f_{\text{RF}} \tag{2.11}$$

where R_{b1} is the instantaneous bit rate of the UL; η is the modulation spectral efficiency; X_{ppm} is the accuracy of the reference of the local oscillator in the sensor node; and f_{RF} is the RF frequency. A larger UL channel bandwidth can be easily tolerated in the power-hungry BS. In the DL, on the other hand, this must be accommodated in the sensor node by a larger Rx bandwidth. However, the random frequency offset in the DL of a star topology depends on the frequency-division duplexing distance (f_{FDD}) between the UL and the DL channels instead of the RF carrier itself. Therefore, at the sensor node, the Rx bandwidth—assuming a perfect frequency accuracy in the BS—must be designed following:

$$\text{BW}_{\text{DL}} = \frac{1}{\eta} R_{\text{b2}} + 2 X_{\text{ppm}} f_{\text{FDD}} \tag{2.12}$$

where R_{b2} is the instantaneous bit rate of the DL. It can be indicated from (2.12) that the Rx bandwidth and, thereby, the clock speed of the digital circuits (i.e., baseband sampling frequency) will be down-limited by the frequency offset tolerance for very low bit rates, as, e.g., in $R_{\text{b}} = 100\,\text{bit/s}$. The inherent frequency error due to a crystal-less design can be tolerated, or alternatively, its impact can be reduced. For example, complex algorithms can be implemented in the BS to extract and predict (from the UL packet) the offset and the drift of the RF carrier. The result is that a more accuracy-relaxed oscillator in the sensor node can be tolerated, or alternatively, the Rx bandwidth of the node—for very low data rates—can be reduced leading to a lower clock speed. Taking (2.12) into consideration, the number of IQ samples per bit ($k_{\text{S/b2}}$) in the sensor node that are streamed from the analog-to-digital converter to the digital circuits can be written in terms of R_{b2} and BW_{DL} as in

$$k_{\text{S/b2}} = \frac{\text{BW}_{\text{DL}}}{R_{\text{b2}}} = \frac{1}{\eta} + \frac{2 X_{\text{ppm}} f_{\text{FDD}}}{R_{\text{b2}}} \tag{2.13}$$

Based on Figure 2.1, the energy consumption per transceived packet in the sensor node can be modeled as in

$$E_{\text{pkt}} = (P_{\text{TX}} - P_{\text{PA}}) T_{\text{sens}} + P_{\text{TX}} T_{\text{pkt1}} + P_{\text{RX}} (T_{\text{wu}} + T_{\text{pkt2}}) \tag{2.14}$$

where T_{pkt1} and T_{pkt2} are the intervals of the UL and the DL packets, respectively. The power consumption models, (2.1)–(2.7), along with (2.9)–(2.13) can be substituted in (2.14) to obtain the complete formula of E_{pkt}. Additionally, for each circuit block, the energy consumption per transceived packet can be simply obtained from the multiplication of the power consumption model with its corresponding active interval, as summarized in Table 2.1 and Table 2.2. Moreover, from the standpoint of energy consumption, the energy link balance between the Tx and the Rx sections is defined as the ratio between the energy consumption per transmitted packet to the energy consumption per transceived packet. The ratio can be calculated as follows

$$\frac{E_{\text{TX}}}{E_{\text{pkt}}} = \frac{E_{\text{TX}}}{E_{\text{TX}} + E_{\text{RX}}} = \frac{1}{E_{\text{pkt}}} \left[(P_{\text{TX}} - P_{\text{PA}}) T_{\text{sens}} + P_{\text{TX}} T_{\text{pkt1}} \right] \tag{2.15}$$

where E_{TX} and E_{RX} are the energy consumption in the Tx and the Rx circuit blocks, respectively.

Table 2.1: Power consumption model per transceived packet per circuit block and corresponding active interval.

Circuit block		Energy model	Power model	Active interval
Tx	analog (RF and BB)	E_{FTX}	$P_{\text{FTX}} = \text{const.}$	$T_{\text{sens}} + T_{\text{pkt1}}$
	digital (BB)	E_{DCTX}	$P_{\text{DCTX}} = k_{\text{DC}} k_{\text{S/b1}} R_{\text{b1}}$	$T_{\text{sens}} + T_{\text{pkt1}}$
	power amplifier	E_{PA}	$P_{\text{PA}} = \frac{1}{\rho} k_{\text{B}} T_{\text{o}} L_{\text{B}} \gamma_{\text{b,BS}} R_{b1}$	T_{pkt1}
Rx	analog (RF and BB)	E_{FRX}	$P_{\text{FRX}} = \text{const.}$	$T_{\text{wu}} + T_{\text{pkt2}}$
	digital (BB)	E_{DCRX}	$P_{\text{DCRX}} = k_{\text{DC}} k_{\text{S/b2}} R_{\text{b2}}$	$T_{\text{wu}} + T_{\text{pkt2}}$
	low-noise amplifier	E_{LNA}	$P_{\text{LNA}} = k_{\text{LNA}} / (F_{\text{LNA}} - 1)$	$T_{\text{wu}} + T_{\text{pkt2}}$

Table 2.2: Energy consumption model per transceived packet per circuit block.

Circuit block		Energy model
Tx	analog (RF and BB)	$E_{\text{FTX}} = P_{\text{FTX}} T_{\text{sens}} + \frac{P_{\text{FTX}} N_{\text{b1}}}{R_{\text{b1}}}$
	digital (BB)	$E_{\text{DCTX}} = k_{\text{DC}} k_{\text{S/b1}} T_{\text{sens}} R_{\text{b1}} + k_{\text{DC}} k_{\text{S/b1}} N_{\text{b1}}$
	power amplifier	$E_{\text{PA}} = \frac{1}{\rho} k_{\text{B}} T_{\text{o}} L_{\text{B}} \gamma_{\text{b,BS}} N_{\text{b1}}$
Rx	analog (RF and BB)	$E_{\text{FRX}} = P_{\text{FRX}} X_{\text{ppm}} T_{\text{turn}} + \frac{P_{\text{FRX}} N_{\text{b2}}}{R_{\text{b2}}}$
	digital (BB)	$E_{\text{DCRX}} = k_{\text{DC}} \left(2 X_{\text{ppm}}^2 T_{\text{turn}} f_{\text{FDD}} + \frac{1}{\eta} N_{\text{b2}} \right) + \frac{1}{\eta} k_{\text{DC}} X_{\text{ppm}} T_{\text{turn}} R_{\text{b2}} + \frac{2 k_{\text{DC}} X_{\text{ppm}} f_{\text{FDD}} N_{\text{b2}}}{R_{\text{b2}}}$
	low-noise amplifier	$E_{\text{LNA}} = \frac{k_{\text{LNA}} X_{\text{ppm}} T_{\text{turn}}}{\frac{P_{\text{rad,max}}}{k_{\text{B}} T_{\text{o}} L_{\text{B}} \gamma_{\text{b}} R_{\text{b2}}} - 1} + \frac{k_{\text{LNA}} N_{\text{b2}}}{\frac{P_{\text{rad,max}}}{k_{\text{B}} T_{\text{o}} L_{\text{B}} \gamma_{\text{b}}} - R_{\text{b2}}}$

2.2.6. OPTIMIZATION PROCESS

For clarification, we first introduce the following terminology.

- f_{RF}, L_{B}, P_{peak}, X_{ppm}, $P_{\mathrm{rad,max}}$, and $\mathrm{BW}_{\mathrm{max}}$ are the *deployment parameters* whose values depend on the deployment scenario and the practical factors in Section 2.2.3. (P_{peak} is the peak-power consumption which corresponds to the upper limit on the discharge current from the battery; whereas $P_{\mathrm{rad,max}}$ and $\mathrm{BW}_{\mathrm{max}}$ are the upper limit on the EIRP and the channel bandwidth, respectively, that is imposed by emission regulations.)
- N_{b1}, N_{b2}, P_{FTX}, P_{FRX}, k_{DC}, $k_{\mathrm{S/b1}}$, k_{LNA}, ρ, γ_{b}, $\gamma_{\mathrm{b,BS}}$, η, f_{FDD}, T_{turn}, and T_{sens} are the *design constants* that mainly have to do with the circuit design.
- R_{b1} and R_{b2} are the PHY *design parameters* representing the primary variables that need to be optimized to maximize the energy efficiency given the aforementioned *deployment parameters* and *design constants*.
- F_{LNA}, $k_{\mathrm{S/b2}}$, P_{MRSS}, P_{rad}, $\mathrm{BW}_{\mathrm{UL}}$, $\mathrm{BW}_{\mathrm{DL}}$, T_{pkt1}, T_{pkt2}, and T_{wu} are the PHY *operating parameters* representing the secondary variables that can be calculated from the other aforementioned constants and/or parameters.

According to (2.14), the aforementioned trade-offs in Section 2.2.2 are broken down to the design parameters, R_{b1} and R_{b2}. In other words, the maximum energy efficiency can be achieved by optimizing the instantaneous bit rate of the UL and the DL. It can also be indicated from (2.14) or from Table 2.2 that the optimization process for the UL is independent from that for the DL.

In practice, the solution to the optimization process is mainly determined by the practical factors that are listed in Section 2.2.3. For given *design constants* and *deployment parameters*, the practical solution, $\left(R_{\mathrm{b1}}|_{\mathrm{opt,practical}}, R_{\mathrm{b2}}|_{\mathrm{opt,practical}}\right)$, of the optimal bit rates can be calculated by numerically finding the minimum of (2.14) that satisfies all of the following practical conditions (i.e., inequalities):

$$F_{\mathrm{LNA}} > 1 \tag{2.16a}$$

$$P_{\mathrm{TX}} \leq P_{\mathrm{peak}} \tag{2.16b}$$

$$P_{\mathrm{RX}} \leq P_{\mathrm{peak}} \tag{2.16c}$$

$$P_{\mathrm{rad}} \leq P_{\mathrm{rad,max}} \tag{2.16d}$$

$$\mathrm{BW}_{\mathrm{UL}} \leq \mathrm{BW}_{\mathrm{max}} \tag{2.16e}$$

$$\mathrm{BW}_{\mathrm{DL}} \leq \mathrm{BW}_{\mathrm{max}} \tag{2.16f}$$

Alternatively, the optimization process can also be solved by analytically finding the global minimum of (2.14). This minimum corresponds to the theoretical solution, $\left(R_{\mathrm{b1}}|_{\mathrm{opt,theoretical}}, R_{\mathrm{b2}}|_{\mathrm{opt,theoretical}}\right)$, of the optimal bit rates at which the first partial derivatives of (2.14) with respect to R_{b1} and R_{b2} are equal to zero, while the second

partial derivatives are positive. However, this solution is referred to as a theoretical solution since it does not take the practical conditions of (2.16a)–(2.16f) into account. The theoretical solution can be calculated as follows:

$$R_{\mathrm{b1}}\big|_{\mathrm{opt,\,theoretical}} = \sqrt{\frac{N_{\mathrm{b1}}}{T_{\mathrm{sens}}}\frac{P_{\mathrm{FTX}}}{k_{\mathrm{DC}}k_{\mathrm{S/b1}}}} \tag{2.17}$$

$$R_{\mathrm{b2}}\big|_{\mathrm{opt,\,theoretical}} = \frac{P_{\mathrm{rad,max}}}{k_{\mathrm{B}}T_{\mathrm{o}}L_{\mathrm{B}}\gamma_{\mathrm{B}}}\left(1+\sqrt{\frac{k_{\mathrm{LNA}}}{P_{\mathrm{FRX}}}}\right)^{-1} : \quad X_{\mathrm{ppm}} = 0 \tag{2.18}$$

$$R_{\mathrm{b2}}\big|_{\mathrm{opt,\,theoretical}} \approx \sqrt{\frac{\eta N_{\mathrm{b2}}}{T_{\mathrm{trun}}}\left(2f_{\mathrm{FDD}}+\frac{P_{\mathrm{FRX}}}{X_{\mathrm{ppm}}k_{\mathrm{DC}}}\right)} : \quad E_{\mathrm{LNA}} \ll E_{\mathrm{FRX}} + E_{\mathrm{DCRX}} \tag{2.19}$$

where the theoretical solution for R_{b2} is derived for two special cases as indicated. A general theoretical solution for R_{b2} is analytically complicated, not insightful, and hence disregarded. The solutions in (2.17) and (2.19) imply that the optimal bit rates for both the UL and the DL are determined—among others—by the ratio of the average power consumption of the analog circuits (P_{FTX} and P_{FRX}) in the sensor node to the energy consumption per information bit of its digital circuits (k_{DC}). For a given circuit design of a sensor node, the average power consumption of its digital circuits is typically less than that of its analog circuits. Consequently, a higher bit rate—but only up to a certain point—tends to result in a lower energy consumption, i.e., a better energy efficiency.

The practical solution which is calculated numerically is equal to the theoretical one if the latter satisfies all the practical conditions of (2.16a)–(2.16f). This case can be illustrated by Figure 2.3(a). Otherwise, the practical solution is the minimum of (2.14) that satisfies all of the practical conditions of (2.16a)–(2.16f). This case can be illustrated by Figure 2.3(b). As indicated by (2.18) and by the practical conditions of (2.16a)–(2.16f), both the link budget (L_{B}, which corresponds to the link distance and the fading margin) as well as the peak-power budget (P_{peak}, which corresponds to the peak discharge current) play a crucial role in determining the practical solution of the optimization process and, thereby, the level of the energy consumption by the sensor node. As the link distance increases and/or the fading becomes worse, more energy needs to be consumed to deliver the same payload with the same desired PER. Similarly, as the peak discharge current gets smaller, longer transmitter and/or receiver on-time is needed to deliver the same payload over the given link distance, and, thereby, more energy is consumed.

In the next section, the optimization process is carried out on a numerical example to determine the practical solutions for various study cases as well as for a wide range of L_{B} and P_{peak}.

2.3. NUMERICAL EXAMPLE

In this section, the analysis is applied to a numerical example of an asymmetric link that is deployed in the 2.4 GHz band. Therefore, the maximum EIRP and

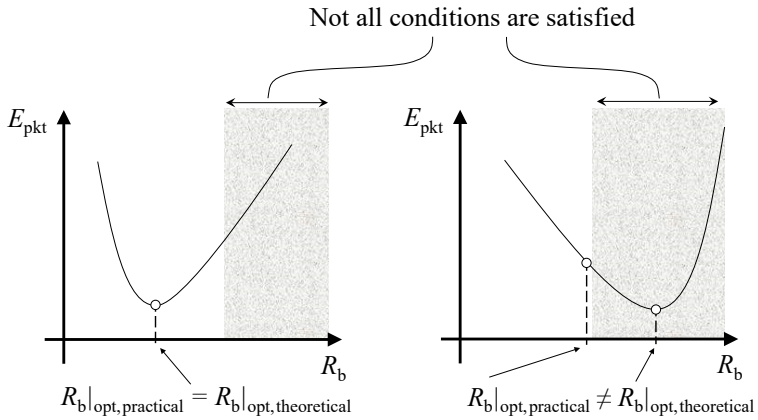

(a) (b)

Figure 2.3: Illustration of the theoretical and practical solutions of the optimal bit rate with respect to the practical conditions of (2.16a)–(2.16f). In (a), the theoretical solution satisfies all the practical conditions, whereas in (b), it does not.

the maximum channel bandwidth are upper-limited by +10 dBm and 100 MHz, respectively, according to emission regulations [86]. Moreover, the BS has unlimited resources, whereas the sensor node is powered from a thin-film battery that has a peak discharge current limitation. This can be translated into a power consumption with an upper limit, e.g., of 200 μW [118]. Nevertheless, the numerical example is carried out for a wide range of L_{B} and P_{peak} to investigate their impact on the practical solution. Due to miniature-size constraints, the sensor node is based on a crystal-less design. Consequently, the accuracy of the timing-frequency reference is badly affected, resulting in, e.g., $X_{\text{ppm}} = 2000$ ppm [139–142]. The sensor node wakes up from the sleep mode, collects the sensing information (e.g., patient's glucose level), and feeds it to its digital circuits for processing. This process lasts, e.g., for $T_{\text{sens}} = 1$ ms. Next, the node transmits the sensing information in an UL packet, whose length is, e.g., 200 bit. Then, it goes back to the sleep mode for a predefined interval, e.g., $T_{\text{turn}} = 1$ s, during which the BS decodes, processes, and forwards the received UL packet to the cloud. By the end of this predefined interval, the sensor node wakes up again from the sleep mode listening to a different frequency that is spaced, e.g., by 20 MHz to receive a DL packet, whose length is, e.g., 100 bit, which carries the acknowledgement and control information.

All the *deployment parameters* and *design constants* are summarized in Table 2.3. In the following, we examine three study cases as listed in Table 2.4. Moreover, in this thesis, any solution for the optimal bit rate that is below 2500 bit/s is referred to—by definition—as a *UNB solution*, whose Q-factor, i.e., $\frac{f_{\text{RF}}}{R_{\text{b}}}$, is above 10^6.

Table 2.3: Deployment parameters and design constants of the numerical example.

Deployment parameter	Value	Comment
f_{RF}	2.45 GHz	2.4 GHz ISM band
X_{ppm}	0 ppm 2000 ppm	Study Case I Study Case II–III [139–142]
$P_{rad,max}$	+10 dBm	emission regulations [86]
BW_{max}	100 MHz	emission regulations [86]
P_{peak}	100μ–1.0 W	-
L_B	80–140 dB	-
Design constant	**Value**	**Comment**
η	0.5 bit/s/Hz	corresponds, e.g., to discontinuous-phase BFSK with a modulation index of 1.0
γ_b	11 dB	corresponds, e.g., to 10^{-3} of bit error rate for BFSK with noncoherent detection
$\gamma_{b,Bs}$	10 dB	corresponds, e.g., to 10^{-3} of bit error rate for BFSK with coherent detection
$k_{S/b1}$	η^{-1}	-
k_{DC}	0.5×10^{-3} nJ/sample	[93]
k_{LNA}	1.52 mW	[93]
ρ	15%	[61]
f_{FDD}	20 MHz	-
T_{turn}	1 s	-
T_{sens}	1 ms	-
N_{b1}	200 bit	[21, 48]
N_{b2}	100 bit	[21, 48]
P_{FTX}	60 μW	[143–147]
P_{FRX}	90 μW	[143–147]

Table 2.4: Examined study cases of the numerical example in Table 2.3.

	Study Case I	**Study Case II**	**Study Case III**
$\boldsymbol{X_{\text{ppm}}}$	0 ppm	2000 ppm	2000 ppm
$\boldsymbol{R_{\text{b1}}}$, $\boldsymbol{R_{\text{b2}}}$	optimized	optimized	fixed (2500 bit/s)

2.3.1. STUDY CASE I

In this study case, the practical solution of the optimal bit rates of the UL and the DL is calculated numerically using (2.14) for a wide range of L_{B} and P_{peak}, while taking the practical conditions of (2.16a)–(2.16f) into account. However, a perfect timing-frequency accuracy (i.e., $X_{\text{ppm}} = 0\,\text{ppm}$) is assumed here. Figures 2.4(a) and (b) represent this practical solution for both the UL and the DL, respectively, for the numerical example in Table 2.3, Study Case I.

As depicted in Figure 2.4(a) for the UL, the wide range of L_{B} and P_{peak} can be divided into three main regions, in two of which the practical solution deviates from the theoretical one because of two practical conditions concerning the UL, as explained later below. Additionally, the energy consumption in the Tx (i.e., during the UL) dominates the total energy consumption, as specified in Figure 2.4(d). For large link budgets, i.e., $L_{\text{B}}\big|_{\text{dB}} > 100\,\text{dB}$ in particular, it is the PA that dominates the total energy consumption, as Figure 2.4(f) indicates.

For the UL, in the case of Region A in Figure 2.4(a), the theoretical solution is identical to the practical one since the former already satisfies all the practical conditions concerning the UL. This region can be illustrated by Figure 2.3(a). Moreover, the practical solution[2] in Region A is roughly constant at 346 kbit/s, which can be analytically calculated using (2.17). The corresponding optimal radiated power is depicted in Figure 2.4(e), which—in dBm—linearly scales with $L_{\text{B}}\big|_{\text{dB}}$ in Region A.

For the UL, in the case of Region B in Figure 2.4(a), P_{rad} has to be increased to achieve a larger L_{B}. However, the former is upper-limited by $P_{\text{rad,max}} = 10\,\text{dBm}$, as Figure 2.4(e) depicts, because of the practical condition of (2.16d). Therefore, the alternative to increasing P_{rad} is to lower R_{b1}, as (2.7) implies, i.e., $R_{\text{b1}}\big|_{\text{opt,practical}}$ and L_{B} become inversely proportional. Consequently, in Region B, the energy consumption in dBμJ linearly scales with $L_{\text{B}}\big|_{\text{dB}}$, as opposed to Region A, as Figure 2.4(c) indicates.

[2] ZigBee, which is a wireless technology with a focus on enabling WSNs in the 2.4 GHz band, has a bit rate of 250 kbit/s and capable of achieving a link budget of up to 110 dB using a radiated power of +10 dBm with a peak-power consumption of 30 mW [148].

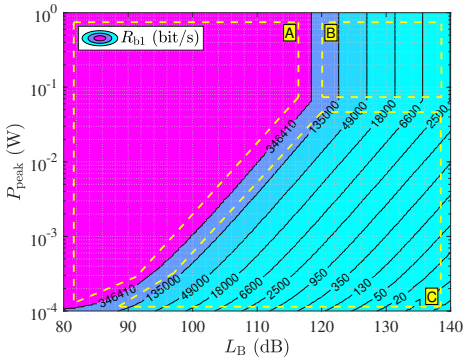

(a) Optimal bit rate of the UL.

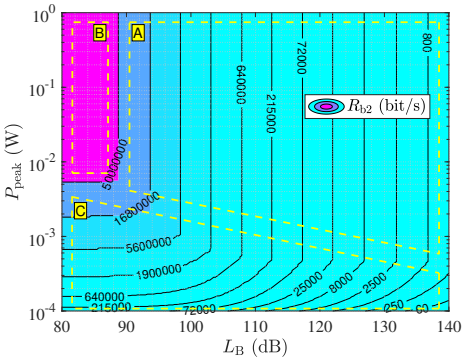

(b) Optimal bit rate of the DL.

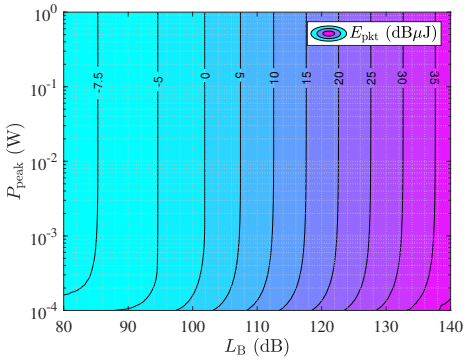

(c) Energy consumption per transceived packet.

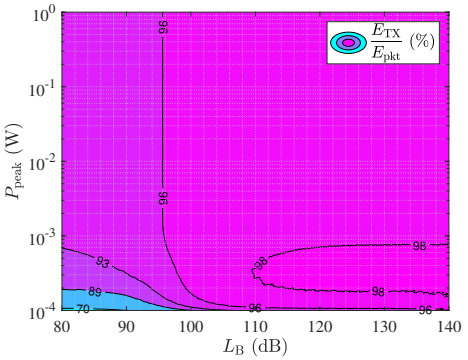

(d) Energy link balance (2.15).

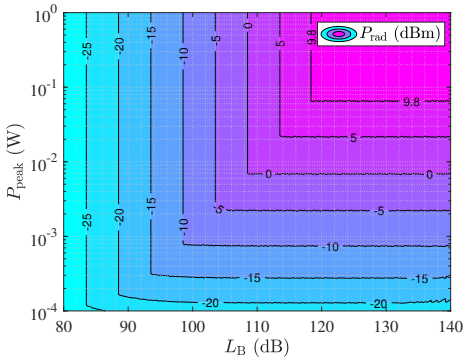

(e) Optimal radiated power in the UL.

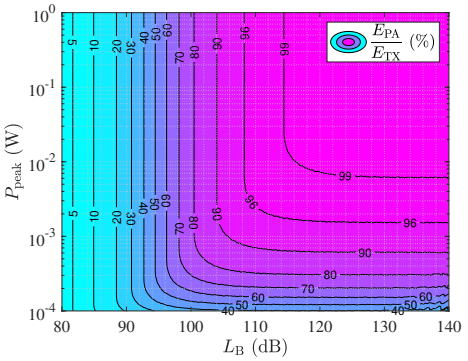

(f) Energy consumption by the PA with respect to total energy consumption in the Tx.

Figure 2.4: The outcome of the optimization process for Study Case I.

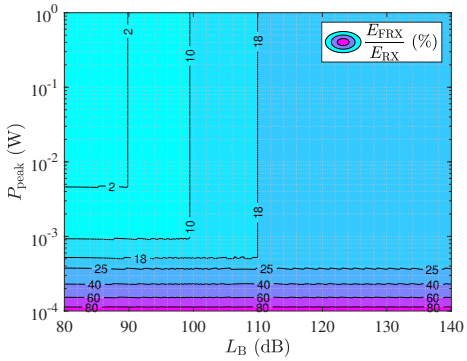

(a) Energy consumption by the analog circuits (RF and BB) in the Rx with respect to total energy consumption in the Rx.

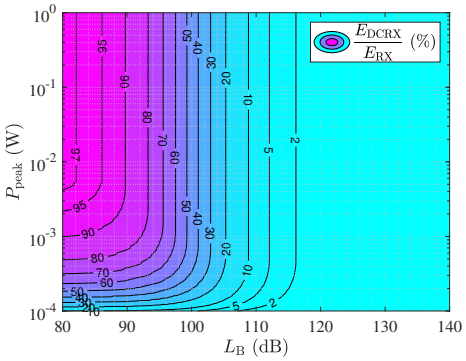

(b) Energy consumption by the digital circuits (BB) in the Rx with respect to total energy consumption in the Rx.

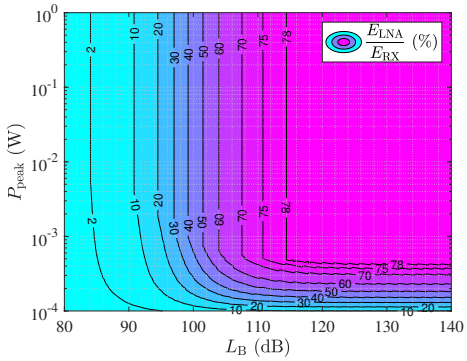

(c) Energy consumption by the LNA with respect to total energy consumption in the Rx.

Figure 2.5: (Cont.) The outcome of the optimization process for Study Case I.

For the UL, in the case of Region C in Figure 2.4(a), the practical condition of (2.16b) kicks in before that of (2.16d). Therefore, for a given upper limit on the battery peak discharge current (i.e., P_{peak}), P_{DCTX} and P_{rad} are upper-limited as well, as (2.1) and Table 2.1 imply. Consequently, for a given P_{peak}, $R_{\text{b1}}\big|_{\text{opt, practical}}$ and L_{B} follow an inverse-proportionality formula as in $R_{\text{b1}}\big|_{\text{opt, practical}} = a \div (L_{\text{B}} + b)$, where a and b depend on the *design constants*. The constant behaviour of P_{rad} with respect to P_{peak} is confirmed by Figure 2.4(e). On the other hand, for a given L_{B}, $R_{\text{b1}}\big|_{\text{opt, practical}}$ linearly scales with P_{peak}. Additionally, the aforementioned ZigBee solution of 250 kbit/s in Region A interestingly becomes a UNB solution of less than 2500 bit/s in Region C in case of $P_{\text{peak}} < 125\,\mu$W.

As depicted in Figure 2.4(b) for the DL, the wide range of L_{B} and P_{peak} can be

divided into three main regions, in two of which the practical solution deviates from the theoretical one because of two practical conditions concerning the DL, as explained later below. Moreover, the asymmetry between the practical solution of the UL and the DL is attributed to the fact that the optimization process is only concerned with minimizing the energy consumption at the sensor node, while assuming the BS has unlimited resources, as mentioned in Section 2.2.4.

For the DL, in the case of Region A in Figure 2.4(b), the theoretical solution is identical to the practical one since the former already satisfies all the practical conditions concerning the DL. This region can be illustrated by Figure 2.3(a). Moreover, $R_{b2}\big|_{opt,practical}$ and L_B are inversely proportional. Additionally, the former can be analytically calculated using (2.18). In most of Region A, the energy consumption in the Rx (i.e., during the DL) is dominated mainly by the LNA and slightly by the analog circuits, as Figures 2.5(a), (b), and (c) indicate.

For the DL, in the case of Region B in Figure 2.4(b), and as Figure 2.4(c) and (2.18) imply, achieving a lower energy consumption for a smaller L_B requires a larger $R_{b2}\big|_{opt,practical}$. However, the latter is upper-limited by 50 Mbit/s, as Figure 2.4(b) depicts, because of the practical condition of (2.16f), given $\eta = 0.5$ bit/s/Hz. Consequently, in Region B, the energy consumption in the Rx is dominated by the digital circuits, as Figure 2.5(b) indicates. Nevertheless, it only constitutes less than 10% of total energy consumption, as specified in Figure 2.4(d).

For the DL, in the case of Region C in Figure 2.4(b), the practical condition of (2.16c) kicks in before that of (2.16f). Therefore, for a given upper limit on the battery peak discharge current (i.e., P_{peak}), P_{DCRX} and P_{LNA} are upper-limited as well, as (2.2) and Table 2.1 imply. Consequently, $R_{b2}\big|_{opt,practical}$ deviates from the theoretical solution of (2.18) because of (2.16c). Moreover, for a given P_{peak}, $R_{b2}\big|_{opt,practical}$ is almost constant for $L_B\big|_{dB} < 85$ dB, in which $E_{LNA} \ll E_{FRX} + E_{DCRX}$, as Figure 2.5(c) indicates. On the other hand, for a given $L_B\big|_{dB} < 85$ dB, $R_{b2}\big|_{opt,practical}$ linearly scales with P_{peak}.

The different aforementioned regions in Figures 2.4(a) and (b) are all summarized in Table 2.5.

2.3.2. STUDY CASE II

To assess the effect of a crystal-less design on the outcome of the optimization process of the PHY parameters (i.e., bit rates and radiated power), Study Case I is repeated, but with a poor timing-frequency reference accuracy of $X_{ppm} = 2000$ ppm. Figures 2.6(a) and (b) represent the practical solution of the optimal bit rates of the the UL and the DL, respectively, for the numerical example in Table 2.3, Study Case II. As can be indicated from Study Case I and confirmed here as well, a UNB signaling scheme is the solution for deployment scenarios in which the link frequently experiences fading/obstruction (i.e., large L_B), the BS has to communicate with a sensor node over a large link distance (i.e., large L_B), or the node's battery can only tolerate a tiny peak discharge current (i.e., small P_{peak}). Moreover, since the timing-frequency accuracy only affects the outcome of the optimization process

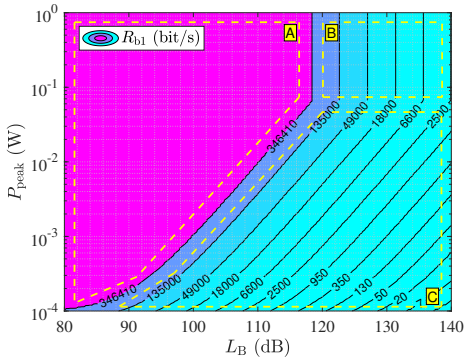

(a) Optimal bit rate of the UL.

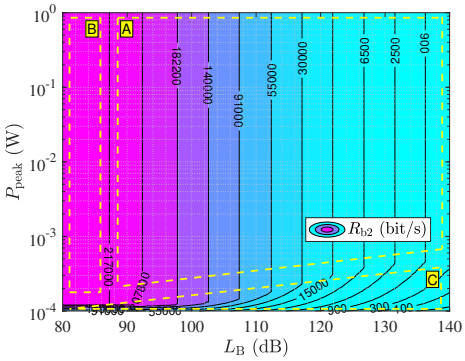

(b) Optimal bit rate of the DL.

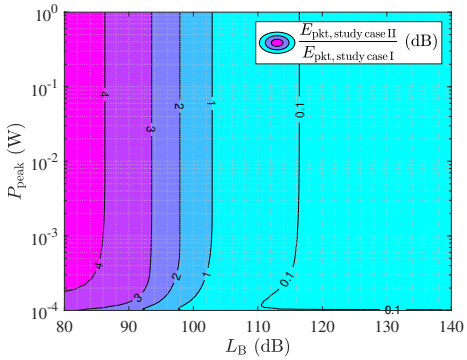

(c) Energy efficiency degradation due to a crystal-less design in Study Case II compared to Study Case I.

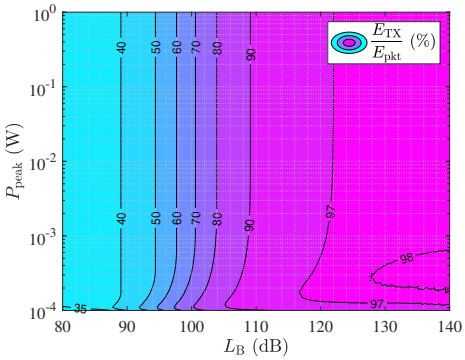

(d) Energy link balance (2.15).

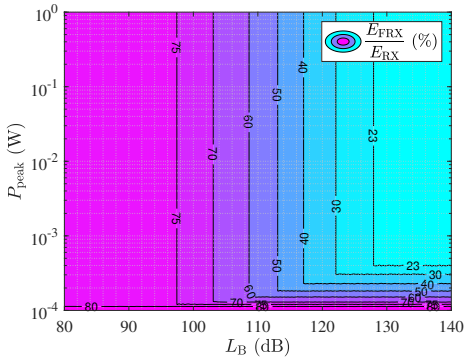

(e) Energy consumption by the analog circuits (RF and BB) in the Rx with respect to total energy consumption in the Rx.

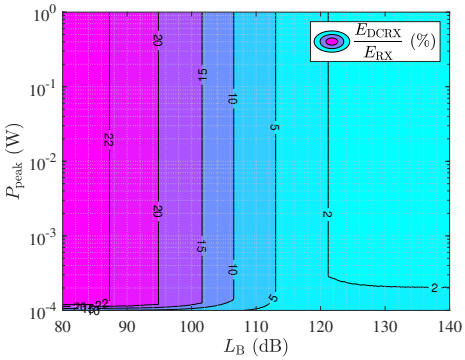

(f) Energy consumption by the digital circuits (BB) in the Rx with respect to total energy consumption in the Rx.

Figure 2.6: The outcome of the optimization process for Study Case II.

of the DL, as Table 2.2 implies, the practical solution of the UL is identical to that in Study Case I, i.e., Figures 2.4(a) and (e) are also applicable in this study case.

Considering Figures 2.6(b), (c), and (d) for $L_B|_{dB} < 100\,dB$ in comparison with Study Case I, the poor reference accuracy of $X_{ppm} = 2000\,ppm$ has a significant impact on the DL optimal bit rate (which has slowed down by a factor of up to 230), the energy efficiency (which has degraded by up to 4.3 dB), and the energy link balance (which has become almost equally balanced). As can be indicated from Figure 2.6(e) in comparison to Figure 2.6(f), the aforementioned significant impact of a crystal-less design is attributed to the extra Rx on-time (due to timing uncertainty), rather than to the extra Rx bandwidth (due to frequency uncertainty).

As depicted in Figure 2.6(b) for the DL, the wide range of L_B and P_{peak} can be divided into three main regions. In the case of Region A and Region B, the theoretical solution is identical to the practical one since the former already satisfies all the practical conditions concerning the DL. For Region B, this solution can be approximately calculated analytically using (2.19) in which $E_{LNA} \ll E_{FRX} + E_{DCRX}$, as Figures 2.6(e) and (f) indicate. In the case of Region C, on the other hand, the practical solution deviates from the theoretical one because of the practical condition of (2.16c) concerning the upper limit on the battery peak discharge current.

The different aforementioned regions in Figures 2.6(a) and (b) are all summarized in Table 2.5.

Table 2.5: Summary of the regions that are depicted in Figures 2.4(a), 2.4(b), 2.6(a), and 2.6(b) with corresponding practical condition or analytical formula.

Region	$R_{b1}\|_{opt,practical}$	$R_{b2}\|_{opt,practical}$	
	Study Case I–II	**Study Case I**	**Study Case II**
A	can be calculated analytically using (2.17)†	can be calculated analytically using (2.18)†	can be calculated analytically (formula is N.A.)†
B	deviates from the theoretical solution because of (2.16d)¶	deviates from the theoretical solution because of (2.16f)¶	can be calculated analytically using (2.19)†
C	deviates from the theoretical solution because of (2.16b)¶	deviates from the theoretical solution because of (2.16c)¶	deviates from the theoretical solution because of (2.16c)¶

†This optimal solution can be illustrated by Figure 2.3(a).
¶This optimal solution can be illustrated by Figure 2.3(b).

2.3.3. STUDY CASE III

As demonstrated by the outcome of the optimization process in Study Case II and illustrated by Figure 2.3(b), a UNB signaling scheme is an energy-efficient solution for deployment scenarios in which the sensor nodes reside, e.g., in a large building that is served by a single BS or such sensor nodes solely survive on energy scavenging while utilizing, e.g., thin-film batteries. However, to achieve the maximum energy efficiency for different deployment scenarios, a dynamic bit rate operating mode (that tracks the optimal solutions in Figures 2.6(a) and (b)) and a transmit power control mechanism (that tracks the optimal solution in Figure 2.4(e)) must both be put in use.

In this study case, on the other hand, the bit rates of the UL and the DL are not optimized. Instead, they are both fixed at 2500 bit/s, whereas a transmit power control mechanism (that tracks the minimum required radiated power in Figure 2.7(b)) is still put in use. This is to investigate the energy efficiency degradation in case of adopting a fixed UNB solution that satisfies a wide range of L_{B} and P_{peak}, rather than adopting a dynamic bit rate operating mode that tracks the optimal solutions from Study Case II.

Due to fixing the bit rates of both the UL and the DL to a non-optimal solution of 2500 bit/s, the energy efficiency is expected to degrade. For the numerical example in Table 2.3, the energy efficiency degradation is depicted in Figure 2.7(a), which indicates that a degradation of less than 3.0 dB takes place for $L_{\mathrm{B}}\big|_{\mathrm{dB}} > 111$ dB. However, this degradation is upper-limited by roughly 13.0 dB for $L_{\mathrm{B}}\big|_{\mathrm{dB}} < 80$ dB. Moreover, the white region in Figures 2.7(a) and (b) means that the wireless link using the UNB solution of 2500 bit/s cannot achieve the desired PER anymore for the given L_{B} because of the peak-discharge current limitation that is represented by the practical conditions of (2.16b) and (2.16c).

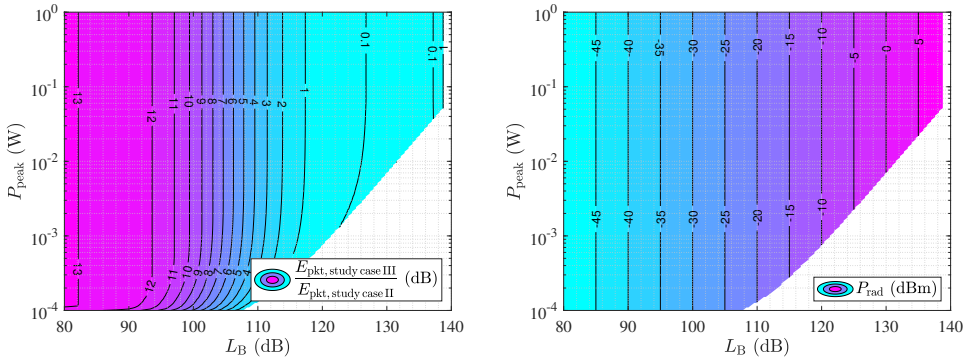

(a) Energy efficiency degradation of Study Case III compared to Study Case II.

(b) Minimum radiated power needed to achieve the desired PER.

Figure 2.7: The results of Study Case III.

2.4. CONCLUSION

In this chapter, the feasibility of a UNB deployment in the 2.4 GHz ISM band in terms of energy efficiency was investigated for star-topology-based WSNs by developing a comprehensive energy consumption model at the PHY of a sensor node. By utilizing the model, optimal bit rates for a wide range of deployment scenarios were calculated using a numerical example while taking several practical factors of different deployment scenarios into account: timing-frequency accuracy, source-power limitation, emission regulations, and link budget.

Since the investigation was dedicated for an asymmetric link (i.e., between a BS and sensor nodes), the optimization process (i.e., optimal bit rate) for the UL is independent of that for the DL. According to the analytically derived solution of the optimization framework, the optimal bit rate can be determined—among others—by the ratio of the average power consumption of the analog circuits in the sensor node to the energy consumption per information bit of its digital circuits. As the ratio increases, this optimal bit rate increases as well. However, in practice, the optimal bit rate significantly deviates from the analytical one. It is mostly determined by the practical factors of the deployment scenario, namely, the link budget and the peak-current budget.

A larger L_B and/or a lower P_{peak} significantly shifts the optimal bit rate to a lower value. This is attributed to the upper limits on the EIRP and/or on the peak-current budget. Interestingly, a narrowband/wideband solution, like, e.g., ZigBee, transforms into a UNB solution when a harsh peak-current limitation of less than, e.g., 125 μW comes into effect, as in energy-scavenging-powered sensor nodes that utilize thin-film-battery-based storage elements.

Because in our optimization framework the communication link is assumed to be always initiated by the sensor node, the accuracy of the timing-frequency reference only affects the optimal bit rate solution of the DL. A poor timing-frequency reference accuracy due to a crystal-less design shifts the optimal bit rate of the DL to a much lower value for L_B smaller than 100 dB. Compared to an ideal reference, the optimal bit rate of the DL reduces by a factor of, e.g., 230 in case of a reference accuracy $X_{ppm} = \pm 2000$ ppm. This significant impact on the optimal bit rate is attributed to the required extra on-time in the node (due to timing uncertainty), rather than to the required extra bandwidth (due to frequency uncertainty).

According to the optimization framework, for very low bit rate solutions (i.e., UNB) and regardless of the deployment scenario, the energy consumption in the sensor node is dominated by the UL circuits in general, and by the PA in particular. Moreover, in case of adopting an optimal transmit power control mechanism but fixing the bit rate of both the UL and the DL to a UNB solution of 2500 bit/s rather than adopting a dynamic bit rate operating mode, the energy efficiency of the sensor nodes would then degrade by up to 13 dB for communication links that require an L_B of less than 111 dB.

Finally, as demonstrated by the outcome of the optimization process, the UNB signaling scheme is an energy-efficient/convenient solution for the WSNs in which

the wireless link between the BS and the sensor nodes typically covers a large distance and/or frequently experiences fading/obstruction. Moreover, the UNB signaling scheme represents a convenient ULP RF solution for the WSNs whose nodes are supposed to be tiny and survive solely on energy scavenging with a harsh peak-current limitation.

3

WIRELESS COEXISTENCE

3.1. INTRODUCTION

Numerous Internet-of-Things applications and services are usually deployed as wireless sensor networks (WSNs) in the ISM bands. Consequently, the already existing problem of intra- and inter-system interference (i.e., wireless coexistence) [149–151] in these bands will grow even further in the coming few years, and the 2.4 GHz band is no exception. The regulations of the European Telecommunications Standards Institute (ETSI) have distinguished between two categories of intentional radiation in the 2.4 GHz band: the short range devices (SRDs) [86] and the wideband transmission systems [94]. The latter is meant for license-free equipment that operate specifically in the 2400 – 2483.5 MHz band, in networks following, e.g., the Wi-Fi, Bluetooth, and ZigBee communication standards. In these networks according to [94], wideband modulation schemes such as orthogonal frequency-division multiplexing (OFDM), frequency-hopping spread spectrum (FHSS), and direct-sequence spread spectrum (DSSS) are employed. On the other hand, the other category of intentional radiation is meant for license-exempt non-specific SRDs operating within the range of 1 – 40 GHz. The SRDs that operate in the 2.4 GHz band have an upper limit of +10 dBm on the effective isotropic radiated power (EIRP), and they "may use a Listen Before Talk (LBT) protocol with a preferred option of Adaptive Frequency Agility (AFA)" to share the spectrum along with other similar devices. However, for sensor nodes that maximally transmit −10 dBm of EIRP, "no access technique is specified", i.e., they do not have to adhere to any further rules regarding LBT or AFA mechanisms.

According to Chapter 2, the UNB signaling scheme is the solution for low-throughput latency tolerant WSNs in which the wireless link between the base station (BS) and the sensor nodes typically covers a large distance and/or frequently experiences fading/obstruction. Moreover, the UNB signaling scheme represents a convenient

Parts of the content of this chapter were published in [113].

ultra-low-power (ULP) RF solution for the WSNs whose nodes are supposed to be tiny and survive solely on energy scavenging. In the case of a future deployment in the 2.4 GHz band, UNB has to be friendly to pre-existing technologies, such as Wi-Fi, Bluetooth and ZigBee. Bluetooth employs adaptive frequency hopping and, thereby, can avoid interference—including that from UNB—by choosing different channels. Likewise, ZigBee employs DSSS and, thereby, can easily suppress UNB interference. However, almost all Wi-Fi versions are OFDM based and, thereby, are less immune to UNB interference compared to Bluetooth and ZigBee. Moreover, Wi-Fi networks are almost everywhere (i.e., in homes, offices, stations, public places, and even cities with free Wi-Fi), and their desirable 24/7 uninterrupted coverage may become subject to frequent outages caused by UNB interference in case of a rapid deployment of the UNB signaling scheme in the 2.4 GHz band. To that end, this chapter considers the potential impact of the UNB interference on Wi-Fi networks.

Currently, there are no UNB deployments in the 2.4 GHz band yet. Nevertheless, LoRa (by Semtech [17]) and RPMA (by Ingenu [88]), are the only signaling schemes that are deployed in the 2.4 GHz band with a low instantaneous bit rate. However, even though LoRa supports a programmable bit rate as low as 476 bit/s, it employs chirp spread spectrum while occupying a bandwidth of 203 kHz [87]. Likewise, RPMA supports a low bit rate of 1500 bit/s, yet it employs DSSS while occupying a bandwidth of 1 MHz [89]. The wireless coexistence of LoRa and Ingenu with respect to Wi-Fi is studied, e.g., in [90, 91]. There is a plenty of literature in which the resilience of Wi-Fi (as well as similar OFDM-based systems) against various sorts of interference (e.g., [152, 153]) and jamming (e.g., [154]) is studied. However, non-LBT UNB interference towards Wi-Fi has not yet been thoroughly and systematically investigated.

A sensor node, which utilizes the UNB signaling scheme, occasionally transmits data packets to a nearby base station. The size of these data packets is typically very small (e.g., 32 bytes). However, due to the very low instantaneous data rate, the packet interval probably occupies hundreds of milliseconds. For instance, a 200-bit packet transmitted, e.g., using 100 bit/s of instantaneous data rate, will fully occupy 2 s. Therefore, a single UNB packet may cause interference to hundreds and even thousands of Wi-Fi packets that are transferred by nearby Wi-Fi networks. Ideally, a 2-second transmitted UNB packet should not disrupt the connectivity of nearby Wi-Fi networks. In other words, a UNB signal should concurrently coexist (both in time and frequency) with Wi-Fi packets, so that a 20 MHz Wi-Fi channel is still efficiently utilized. Otherwise, in case of a 100 bit/s UNB signal, only around 200 Hz of bandwidth would be occupied, while the rest of the whole 20 MHz bandwidth would be vacant from Wi-Fi signals and, thereby, wasted for a period of 2 s. Therefore, an LBT mechanism in a UNB sensor is not required. Moreover, according to Chapter 2, the UNB signaling scheme can serve as a ULP RF solution, and, thereby, UNB sensors only transmit, e.g., up to −10 dBm of EIRP. In fact, they can do so without first assessing the occupancy of the channel. This is true because an LBT mechanism is not required by the emission regulations [86] for such devices with −10 dBm of EIRP. Additionally, according to Chapter 2, such UNB sensors might be tiny and, thereby, are based on crystal-less design. Nevertheless, frequency errors,

e.g., up to ±50 ppm are typically expected in crystal-based cheap sensor nodes. This corresponds to a maximum random frequency offset of ±122 kHz, meaning that a UNB packet might end up interfering with different types of Wi-Fi subcarriers. To that end, a dedicated and thorough study for the impact of the UNB signaling scheme on nearby Wi-Fi networks is necessary for a future successful deployment of the former in the 2.4 GHz band.

Because of the nature of the UNB signaling scheme with respect to Wi-Fi, it most likely has an impact similar to that from narrowband interferers and single-tone (static and slow-sweep) jammers. For example, the authors in [95–98] considered the radio-frequency interference (RFI) from the harmonics of digital clock circuits that would share the same hardware platform or at least exist in a very close proximity to Wi-Fi antennas. In [95], a methodology was proposed and used in a cabled measurement setup to empirically study the electromagnetic interference (EMI) from an LCD screen on a built-in 802.11a/b/g card of a commercial notebook. However, because of the lack of flexibility of how the LCD screen was tested, the study was only limited to the impact of a single harmonic on a specific Wi-Fi subcarrier. The authors in [96] considered the EMI from the harmonics of a 120 MHz clock signal. The measurements were conducted inside a reverberation chamber (RC), and the narrowband interference was emulated as a single tone that could reside inside or outside of an 802.11g channel and, thereby, interfere with different Wi-Fi subcarriers. However, the case of an interfered pilot subcarrier was not studied. In both [95] and [96], the measurement results were quantified in terms of throughput, but the corresponding range of the signal-to-interference ratio (SIR) was not reported. In [97], the authors studied the impact of EMI in the case of harmonics from a personal computer dithered clock as well as in the case of a single-tone interferer. The study reports the bit-error-rate performance based on a theoretical analysis and a numerical simulation. However, it assumes a simplified model of the 802.11a physical layer. In [98], a single-tone and an amplitude-modulated signal were empirically studied in the RC as potential EMI sources. They were individually injected at the center of a Wi-Fi channel as well as at the adjacent channels. The measurement results were reported in terms of a minimum required SIR to enable a Wi-Fi connection. However, the results and conclusions regarding the resilience of 802.11n were based only on one access point from a single vendor. In both [97] and [98], the interferer resided at the center of the Wi-Fi channel, and, thereby, the cases of different types of interfered subcarriers were not studied.

In the context of jamming, the authors in [99, 100] studied the impact of a narrowband jammer on different 802.11g cards in a cabled measurement setup. The jamming signal was centered at each Wi-Fi subcarrier, and packet-error-rate measurements were collected. However, like in [96], the measurement results were not reproducible because the model numbers of the tested Wi-Fi equipment were not reported. None of the studies in [95–100] follows a systematic or profound investigation of the impact of interference on the different Wi-Fi mechanisms, especially the clear-channel-assessment (CCA) mechanism in Layer 2. This is essential to correctly analyze the collected measurement results and, thereby, reach a valid conclusion. On the other hand, the authors in [101] empirically studied

both the physical (PHY) and the medium-access-control (MAC) layers jamming on various commercial 802.11b/g devices in a cabled measurement setup. The jammer generated a single-tone signal that slowly swept the whole 2.4 GHz band. However, because it was only injected in the data path which was separated from the acknowledgement path, such tested jamming scenario is not realistic. Moreover, the gained insight from the MAC layer jamming was actually based on throughput measurements of the transport layer instead of observations from the behavior of the CCA mechanism itself. Lastly, the considered Wi-Fi links in [97–101] did not represent a real-world scenario as the Wi-Fi modulation coding scheme (MCS) was fixed (i.e., not adaptive) during the simulations and/or measurement campaigns.

In this chapter, the objective is to empirically examine the feasibility of a UNB deployment in the 2.4 GHz ISM band in terms of wireless coexistence, by focusing our investigation on the impact of the interference from the ETSI-regulation-obedient non-LBT UNB signaling scheme on nearby Wi-Fi links. The main contribution of this chapter is, thereby, developing a systematic and thorough methodology for the empirical investigation of the impact of the UNB interference on the individual Wi-Fi mechanisms[1] spanning from the PHY up to the transport layer. The methodology is based on the approach of a worst-case interfering scenario and consists of three investigation steps. In the first investigation step, the impact of the UNB interference on the Wi-Fi clear-channel-assessment mechanism is studied. Next, the effect on the Wi-Fi beacon delivery rate is assessed in the second step. In the last and third step, the throughput performance of the transport layer over a Wi-Fi link is investigated. The methodology is then practically applied for a specific measurement campaign of a TCP stream over an IEEE 802.11n link that is interfered by 100 bit/s UNB signals. Multiple commercial Wi-Fi devices from different vendors are tested following the developed methodology. Two situations of single and multiple simultaneous UNB interferers are individually considered. From the standpoint of envelope constancy, two distinct modulation schemes for UNB interfering signals are individually investigated to gain a better insight: on-off-keying (OOK) and Gaussian minimum-shift-keying (GMSK). The cases of interfering with all types of Wi-Fi subcarriers are individually studied as well. Finally, based on the gained insights from the empirical investigation, spectral recommendations are proposed for a future deployment of the UNB in the 2.4 GHz band in order to reduce the potential impact on nearby Wi-Fi networks as much as possible.

This chapter is organized as follows. First, a brief background of the Wi-Fi technique is given in Section 3.2. Next, in Section 3.3, the interference analysis methodology is introduced and explained in detail. Section 3.4 presents the measurement setup, whereas the measurements results are presented and thoroughly analyzed in Section 3.5. Finally, a conclusion is given at the end of this chapter.

[1] Strictly speaking, Wi-Fi only defines the first two layers in the OSI (Open Systems Interconnection) model, namely, the physical layer and the data-link layer.

3.2. BACKGROUND

Wi-Fi is a collection of complex wireless protocols based on the IEEE 802.11 standards which are backward compatible. The IEEE 802.11 standards define extensive PHY and data-link layers [155]. Therefore, in this section, the potentially affected mechanisms in Wi-Fi by the UNB interference are briefly reviewed, as they later need to be considered while developing the methodology in Section 3.3.

Regarding the PHY in the 2.4 GHz band, the 802.11n standard is the latest widespread Wi-Fi version in the 2.4 GHz band. It does not implement a transmit power control mechanism. Its channels can be in one of two modes, 20 MHz or 40 MHz. In the 20 MHz mode in Europe, there are 13 channels, as shown in Figure 3.1. In the 802.11g/n standard, Channels 1, 5, 9 and 13 are non-overlapping, whereas Channels 1, 6 and 11 are non-overlapping in the 802.11b standard. By default, a Wi-Fi network uses one of three channels: 1, 6, or 11. However, in practice, a Wi-Fi channel configuration in access points is subject to a user manual setup as seen in Figure 3.1 (i.e., overlapping Wi-Fi channels). Therefore, from the standpoint of wireless coexistence, any primitive idea of making the UNB sensor nodes only access the guard bands between the non-overlapping Wi-Fi channels is not necessarily friendly to the nearby Wi-Fi networks.

The dominating setup of Wi-Fi networks is based on a star topology. In this setup, an access point (AP) acts as a network coordinator. It provides an Internet access service to devices such as smartphones, laptops and Wi-Fi-based sensors, all of which are usually referred to as stations (STAs). The AP itself broadcasts a beacon packet every ~100 ms by default. It carries useful information to STAs, among which is the name

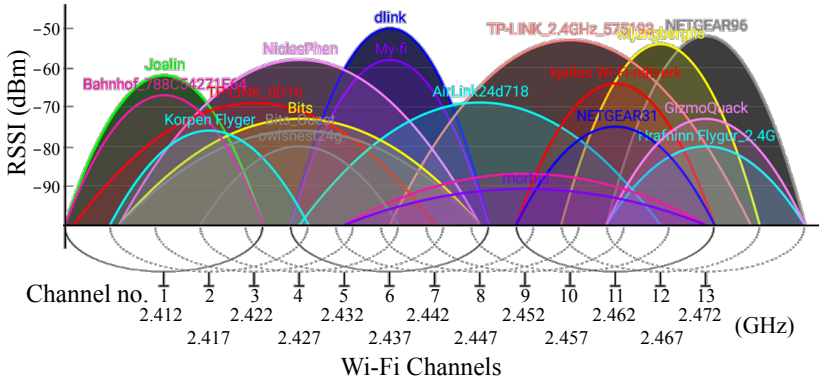

Figure 3.1: The 13 Wi-Fi channels in the 2.4 GHz ISM band and a snapshot of channel occupancy in the real world (a house case scenario taken in Gothenburg, Sweden on August 1st, 2018). Three non-overlapping channels, 1, 6, and 11 can be seen, with a guard band of 5 MHz between Channel 1 and 6 as well as between Channel 6 and 11. Names and colors in the figure are irrelevant.

of the Wi-Fi network (technically called service set identifier, i.e., SSID). By listening to these beacons, STAs can identify the network and initiate the authentication and association processes to be able to access the wireless service. Beacon packets that are broadcast by Wi-Fi APs are always sent in the 802.11b standard (for backward compatibility) at 1 Mbit/s of information bit rate using differential phase-shift-keying combined with DSSS. On the other hand, depending on the channel condition and received signal strength (i.e., momentary packet loss rate), conventional data packets are sent using different MCSs, but mostly using OFDM. Therefore, beacon packets are expected to be more robust against the UNB interference compared to data packets. OFDM is a multi-carrier modulation. In the 802.11n version, the subcarrier spacing is 312.5 kHz. Furthermore, its OFDM utilizes 64 subcarriers in total (52 for data, 4 for pilots, and the rest unused). Therefore, different types of Wi-Fi subcarriers are expected to have different vulnerabilities to the coexisting interference.

Regarding the MAC sublayer (in the data-link layer), a channel multiple-access protocol (commonly known as carrier-sense multiple access with collision avoidance, i.e., CSMA/CA) is put in use. It implements a mechanism for assessing whether the channel is idle/busy. The mechanism is called clear-channel assessment (CCA), and it has two triggering thresholds: −82 dBm for carrier sense (CCA-CS) to detect Wi-Fi packets, and −62 dBm for energy detection (CCA-ED) to detect non-Wi-Fi signals. Because the investigated UNB signaling scheme does not utilize an LBT mechanism, a transmitting UNB sensor node is expected to disrupt nearby Wi-Fi networks, if its received power is greater than the CCA-ED triggering threshold at the AP/STA.

3.3. METHODOLOGY

In this section, the three-step methodology is introduced and explained in detail. It has been developed to empirically investigate the impact of the UNB interference on nearby Wi-Fi links in a systematic reproducible step-by-step assessment. The investigation is, thereby, to be conducted in a controlled environment, e.g., in an anechoic chamber (AC) to eliminate any unintended interference.

First, the UNB and Wi-Fi parameters are identified and discussed. Different values of these parameters might significantly change the impact of the UNB interference on Wi-Fi links. Throughout this chapter, a single combination of values for the applicable UNB and Wi-Fi parameters is referred to as a *configuration*. Next, a flow graph with three priority-based investigating steps is developed. In each step, a potentially affected Wi-Fi mechanism is assessed individually, so that any impact it may endure has no effect on other mechanisms. At the end of this section, a worst-case scenario approach is motivated.

3.3.1. UNB PARAMETERS

In all of the three investigation steps, four UNB parameters need to be considered for investigation.

1. *Received power at AP/STA.* The impact of interference is not only characterized by the SIR, but it is also characterized by the signal power itself. This is explained in Section 3.3.4 when the worst-case scenario approach is motivated. Throughout this chapter, we define SIR as the total Wi-Fi average power (S) to the UNB peak power (I). Both powers are measured at the antenna port of the receiving AP/STA.

2. *Carrier frequency.* Due to large random frequency offsets, a UNB interfering signal may overlap with any of the Wi-Fi subcarriers. It may even end up between two subcarriers and, thereby, interfere with both. Moreover, different types of Wi-Fi subcarriers might have different vulnerabilities to the UNB interference [101].

3. *Modulation scheme.* From the standpoint of a Wi-Fi link, the fluctuations in the instantaneous power of a UNB signal (generated in a non-constant envelope modulation scheme) are considered very slow (e.g., a 1 ms Wi-Fi packet vs. a 10 ms UNB bit). Therefore, UNB signals with different modulation schemes might have different interfering impacts.

4. *Number of simultaneous interferers.* Multiple UNB wireless sensors could transmit data simultaneously, and, thereby, drastically interfere with the nearby Wi-Fi networks.

The four UNB parameters are summarized in Table 3.1, presenting the corresponding applicable values.

3.3.2. WI-FI PARAMETERS

There are eight Wi-Fi parameters that need to be considered in the investigation. (*i*) The received signal strength indicator (RSSI) of Wi-Fi signals at the AP/STA, and (*ii*) the offered throughput are both discussed in Section 3.3.4 when the worst-case scenario approach is motivated. (*iii*) The transport-layer protocol can be either UDP or TCP. (*iv*) Different vendors have different Wi-Fi chipsets which implement different algorithms (i.e., proprietary implementation) wherever the IEEE standard leaves it up to the vendor, or does not specify the details (e.g., adaptive MCS algorithm). The remaining Wi-Fi parameters are (*v*) the Wi-Fi standard version under investigation, (*vi*) channel bandwidth mode, (*vii*) channel number, and (*viii*) number of spatial streams.

In the next subsection, all of the eight Wi-Fi parameters are considered in the third investigation step, whereas the first two investigation steps only consider the last five Wi-Fi parameters. Table 3.1 summarizes these eight Wi-Fi parameters, presenting the corresponding applicable values.

3.3.3. THREE-STEP FLOW GRAPH

The methodology is based on three investigation steps. In the first one, the impact of the UNB interference on the Wi-Fi CCA mechanism is studied. Next, the effect

on the Wi-Fi beacon delivery rate is assessed in the second step. In the last and third step, the throughput performance of the transport layer over a Wi-Fi link is investigated.

FIRST INVESTIGATION STEP—CLEAR-CHANNEL-ASSESSMENT MECHANISM

As mentioned in Section 3.2, a non-Wi-Fi signal with a received power that is greater the −62 dBm should trigger the CCA-ED mechanism according to [155]. This causes the AP/STA to defer assuming a busy channel. However, the CCA-ED mechanism is dynamic, and its algorithm for sampling the power is vendor dependent [155]. Therefore, an initial investigation is needed to determine if—and at which *configurations*—a UNB signal would trigger the CCA-ED mechanism of the AP/STA. This initial investigation is, consequently, placed as the first step in the flow graph of the methodology, as depicted in Figure 3.2.

SECOND INVESTIGATION STEP—BEACON DELIVERY RATE

In case an STA loses multiple beacon packets due to corruption, e.g., by a 2 s UNB interfering signal, the affected STA follows a procedure that is vendor dependent. In some devices for example, when STAs lose a particular number of consecutive beacon packets, they disassociate themselves from the AP and try to roam to another one. If no other AP is available, the STAs report "Wi-Fi down" until the beacon packets can be correctly decoded. Once the latter happens, the affected STAs have to authenticate and associate themselves once again with the AP before any data packet can be transferred in between [156].

As a second step, an investigation of the impact of the UNB interference on the received beacon packets at STAs needs to be carried out (see Figure 3.2). The investigation in this step also needs to report a beacon delivery rate (BDR) with the corresponding *configurations*. The BDR is defined as the number of correctly decoded beacon packets at the considered STA divided by the total number of beacon packets broadcast by the AP that the STA is associated with.

The reason why the first investigation step has to be conducted first is to separate the *configurations* that cause an AP deferral (i.e., non-transmitted beacon packets due to a triggered CCA-ED) from those which lead to corrupted beacon packets. Therefore, the *configurations* that trigger the CCA-ED mechanism in the first step must be avoided in the next ones. Otherwise, incorrect interpretations would be made from analyzing the BDR, as both sets of *configurations* would then overlap.

THIRD INVESTIGATION STEP—TRANSPORT-LAYER THROUGHPUT

In this step, the throughput performance of the transport layer over a Wi-Fi link is assessed under the impact of interference from UNB signals. The throughput is defined as the average information bit rate of a considered case scenario which is simply the amount of data successfully delivered over the transport layer within a specified time.

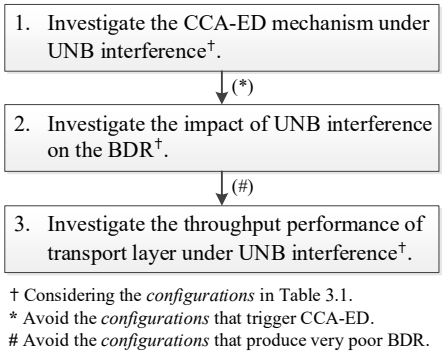

Figure 3.2: Three-step flow graph of the methodology.

Figure 3.2 depicts this investigation step as the last one to be carried out so that only the meaningful *configurations* are considered in this step. In other words, the *configurations* that trigger the CCA-ED mechanism and/or cause significant beacon losses must be avoided in this last step of the throughput performance assessment. Otherwise, the reported throughput measurements might be affected by a network disturbance/outage triggered by non-transmitted/corrupted beacons.

3.3.4. WORST-CASE SCENARIO APPROACH

The received UNB power at both sides of the Wi-Fi link (i.e., the relative position of the UNB interferer to the AP and the STA), the RSSI of Wi-Fi signals at the AP/STA, and the Wi-Fi offered throughput are three independent parameters. However, because the developed methodology has the purpose to examine only the worst-case interference scenario, only the following configuration of these three parameters is considered.

- The received UNB power is varied to obtain the same desired range of SIR at both the AP and STA. Both sides of the Wi-Fi link are then fairly impacted by interference as desirable. Such a situation represents a worst-case scenario. In practice, this would appear as if the relative position of the UNB interferer is somewhere on a perpendicular line going through the middle of the Wi-Fi link.
- The Wi-Fi link is made balanced (within ±1 dB) in terms of RSSI, i.e., both sides of the Wi-Fi link roughly report the same RSSI value. Moreover, RSSI itself is fixed at an adequately strong value. In practice, this would appear as if the the Wi-Fi link is established over a line of sight with a relatively short distance. As a result, the MCS that is automatically selected by the AP/STA has the highest data rate possible. Such an MCS (corresponding to the strongest RSSI) is the most vulnerable to interference [99] compared to those with lower data rates (i.e., lower index), hence a worst-case scenario. Consequently, throughout this chapter, any SIR value/range is reported along with the corresponding value of S itself.

Table 3.1: Wi-Fi and UNB parameters for the methodology and the measurement setup. (Empty cells are N.A.)

<table>
<tr><th colspan="2" rowspan="3"></th><th colspan="3">Methodology</th><th colspan="3">Measurement Setup</th></tr>
<tr><th rowspan="2">1st Step
(CCA-ED)</th><th rowspan="2">2nd Step
(Beacons)</th><th rowspan="2">3rd Step
(Throughput)</th><th rowspan="2">1st Step
(CCA-ED)</th><th rowspan="2">2nd Step
(Beacons)</th><th colspan="2">3rd Step
(Throughput)</th></tr>
<tr><th>Single Interferer</th><th>Multiple Interferers</th></tr>
<tr><td rowspan="5">UNB Parameters</td><td>P_{Rx} @ STA (dBm)</td><td>P_{Rx} (freq.)</td><td>range 1</td><td rowspan="2">range 2</td><td>see Figure 3.5</td><td>[−76, −49]</td><td rowspan="2">[−71, −49]</td><td rowspan="2">[−76, −65]</td></tr>
<tr><td>P_{Rx} @ AP (dBm)</td><td>P_{Rx} (freq.)</td><td></td><td>see Figure 3.5</td><td></td></tr>
<tr><td>Carrier Freq.</td><td colspan="3">coincides with any subcarrier of index −32 to +32</td><td>see Figure 3.5</td><td colspan="2">0, +16, +18, +18.5, +21, +21.5, +29</td><td>+13, +14, +15, +16, +17, +18, +19</td></tr>
<tr><td>Modulation Scheme</td><td colspan="3">constant & non-constant envelopes</td><td colspan="3">OOK, GMSK</td><td>GMSK</td></tr>
<tr><td>Num. of Interferers</td><td colspan="3">≥ 1</td><td colspan="3">1</td><td>7</td></tr>
<tr><td rowspan="7">Wi-Fi Parameters</td><td>RSSI @ STA (dBm)</td><td></td><td>fixed</td><td rowspan="2">fixed
(adequately strong)</td><td></td><td>{−40, −36}</td><td colspan="2" rowspan="2">{−40, −36}</td></tr>
<tr><td>RSSI @ AP (dBm)</td><td></td><td></td><td></td><td></td></tr>
<tr><td>Offered Throughput</td><td></td><td></td><td>max carried throughput</td><td></td><td></td><td colspan="2">≈ 54 Mbps</td></tr>
<tr><td>Transport Layer</td><td></td><td></td><td>TCP / UDP</td><td></td><td></td><td colspan="2">TCP</td></tr>
<tr><td>Device Under Test</td><td colspan="3">different brands</td><td>LogiLink WL0238
EDUP EP-AC1635
ASUS RT-AC55U
Linksys E1700-EJ
TP-Link AC600 T2UH</td><td colspan="3">Linksys E1700-EJ
TP-Link AC600 T2UH</td></tr>
<tr><td>IEEE 802.11 Ver.</td><td colspan="3">b / g / n</td><td colspan="4">n</td></tr>
<tr><td>Channel BW Mode</td><td colspan="3">20 MHz / 40 MHz (in case of 802.11n)</td><td colspan="4">20 MHz</td></tr>
<tr><td>Channel Num.</td><td colspan="3">{1, 2, 3, … , 13}</td><td colspan="4">6 (manually set in AP)</td></tr>
<tr><td>Num. of streams</td><td colspan="3">≤ 4 (in case of 802.11n)</td><td colspan="4">1</td></tr>
</table>

- If a Wi-Fi user gets temporarily and partially interfered while a small portion of the Wi-Fi channel capacity is utilized by the Wi-Fi network, then the user experience will not noticeably deteriorate. However, if the Wi-Fi network is congested (i.e., the Wi-Fi channel capacity is fully utilized), then any interference will noticeably damage the Wi-Fi user experience. Therefore, to consider a worst-case scenario, the offered Wi-Fi throughput is set to its maximum value, i.e., maximum carried throughput.

3.4. MEASUREMENT SETUP

The measurement setup in all of the three investigation steps is depicted in Figure 3.3. The AC has the dimensions of $4.5 \times 3.5 \times 3.1\,\mathrm{m}^3$, and, thereby, far fields were guaranteed at 2.4 GHz for the involved transmit and receive dipole antennas. Initial measurements were conducted to ensure that no external interference was above the noise floor in the Wi-Fi channel under test. Five commercial Wi-Fi devices from different vendors were used in the measurements and reported in Table 3.1. All of the Wi-Fi devices were kept in the default manufacturer settings, unless it is mentioned otherwise. To ensure their suitability for the measurement setup, they had to adhere to the following conditions. (*i*) They only have external antennas, i.e., no internal antennas. (*ii*) Their antennas are detachable. (*iii*) They support the 802.11n version. (*iv*) They are from popular vendors, i.e., most sold on online retailers in the Netherlands.

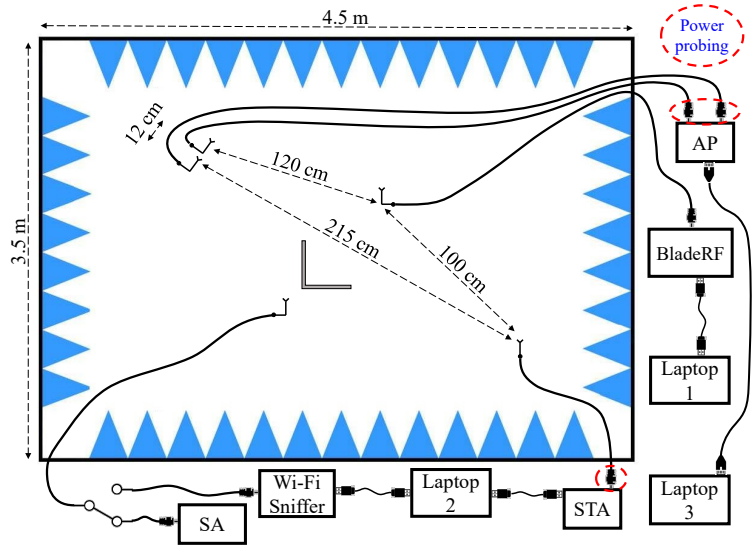

Figure 3.3: Measurement setup. (In fact, since the power probing is conducted at the antenna port of the receiver, the relative polarization, orientation, and location of transmit and receive antennas are irrelevant.)

One of the conditions for the measurement results to be easily reproducible inside the AC is that the SIR has to be measured at the antenna port of the receiver, i.e., AP/STA. This makes the relative polarization, orientation, and location of transmit and receive antennas as well as the transmit power irrelevant. Additionally, many Wi-Fi chipsets do not report the RSSI of the received Wi-Fi packets, and none of them reports the interference power. Hence, the measurement setup has to be established in such a way that both the signal and the interference are probed by the same instrument. Moreover, probing the power inside Wi-Fi devices is not always possible let alone convenient due to limited accessibility. Therefore, the conditions of external and detachable antennas are imposed.

As can be seen from Figure 3.3, a probe was located behind a corner reflector. The probe was connected through an RF switch to a spectrum analyzer (Agilent E4404B) and to a Wi-Fi sniffer (Alfa Network AWUS036NHA) for further investigations (e.g., probing the Wi-Fi channel under test in the frequency domain as well as at the packet level). According to initial measurements, the reflector provided the probe with 8 – 10 dB of effective suppression against the generated the UNB interference.

Based on the software-defined radio principle, the 100 bit/s UNB interference was built in GNU Radio software and generated using a BladeRF device. The UNB signal was generated in two different modulation schemes, namely, OOK and GMSK. The latter is a constant-envelope modulation. The 99% occupied bandwidth is 153 Hz and 93 Hz for the OOK- and the GMSK-modulated signals, respectively.

3.5. MEASUREMENT RESULTS AND ANALYSIS

Because 802.11n is the latest widespread Wi-Fi version in the 2.4 GHz band, the measurements were limited to it. Due to the time limitation of the measurement campaign, the measurements were also limited to the bandwidth mode of 20 MHz. Nevertheless, the bandwidth mode of 40 MHz is expected to produce similar trends, as it is basically a concatenation of two 20 MHz channels. The choice of the Wi-Fi channel number had no impact on the collected measurements. Moreover, the measurement setup in Section 3.4 followed the previously explained methodology in Section 3.3. Therefore, three main sets of measurement results are reported below, one for each investigation step. Table 3.1 lists the full set of values of the UNB and Wi-Fi parameters that were used in each step of the empirical investigation.

3.5.1. FIRST INVESTIGATION STEP

The CCA-ED mechanism was examined utilizing a spectrum analyzer (SA) which was set in the burst-power mode, a.k.a., time-sweeping mode. While the UNB parameters were varied, observations from the SA were taken, and the corresponding *configurations* were logged when the Wi-Fi device under test (DUT) deferred from transmission, i.e., when the CCA-ED mechanism was triggered. As mentioned in Section 3.2, APs periodically broadcast beacon packets. Therefore, if these packets (or even data packets) are observed to be missing in the SA while the interference is

present, then that is an indication of deferral. STAs, on the other hand, do not send beacon packets when they operate in the normal mode. However, there is an option in host operating systems through which they can be set in an ad hoc network mode to operate as network coordinators. One of the responsibilities of such coordinators is to periodically send beacon packets. In this first investigation step, APs and STAs were tested separately as well as in pairs, i.e., AP ⇔ STA. When an STA was tested separately, it was set to work in the ad hoc network mode. Otherwise, it operated as a normal STA.

Figure 3.4 shows a screenshot of a 10 s span on the SA in the case of a Linksys E1700-EJ access point, a TP-Link AC600 T2UH station, and a GMSK-modulated UNB interfering signal. In the figure, the UNB signal was set to coincide with the Wi-Fi data subcarrier of index +10, and a TCP traffic was initiated from the AP to the STA. As the figure depicts, the AP deferred from broadcasting the beacon packets during Period 2 due to the existence of the UNB interference. During Period 1, on the other hand, the AP did not only defer as it did in Period 2, but also both the AP and the STA deferred from sending data packets in between, i.e., all Wi-Fi traffic was halted. Therefore, in Period 1 and Period 2, it can be indicated that the CCA-ED mechanism was triggered in both Wi-Fi devices. Different *configurations* were tested and are reported in Table 3.1.

From analyzing the measurement results of different scenarios, the following observation can be made. The data traffic is always deferred whenever the received UNB interference power is above the CCA-ED triggering threshold of any side of the Wi-Fi link. The only exception, however, is when the received interference power is only above the CCA-ED triggering threshold of a UDP receiver. In this case, the UDP traffic is not deferred. This can be explained by the fact that it is only TCP that has an acknowledgment mechanism, which is basically another data traffic initiated in the opposite direction and, thereby, subject to the CCA deferral mechanism.

Five different APs and STAs from different vendors were tested regarding the CCA-ED mechanism. Their behaviors are reported in Figure 3.5 along with the −62 dBm

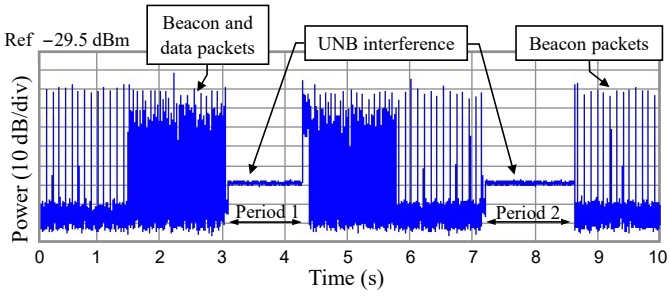

Figure 3.4: Screenshot of a 10 s span on the SA showing the deferral behavior of the beacon packets and the TCP traffic for the first investigating step. The SA was set in the burst-power mode.

triggering threshold that is specified in the IEEE standard [155]. The reported threshold is basically the UNB peak power at which the CCA-ED mechanism is supposed to be triggered. The power was measured at the antenna port of the Wi-Fi DUT. Figure 3.5 corresponds to either cases of an OOK- or a GMSK-modulated UNB signal, and this can be explained by the following. As mentioned in Section 3.3.1, from the perspective of a Wi-Fi link, the fluctuations in the instantaneous power of a UNB signal that is generated in a non-constant envelope modulation scheme (e.g., OOK) are considered very slow. In other words, the average power of a received UNB signal that is estimated by a Wi-Fi receiver is basically considered an instantaneous power by a UNB receiver (e.g., a 1 ms Wi-Fi packet vs. a 10 ms UNB bit).

It can be observed from Figure 3.5 that none of the tested Wi-Fi devices follows the −62 dBm standard. Moreover, a significant variation in behavior between the Wi-Fi devices can be observed as well. A very similar observation is reported in [101]. In fact, two STAs (LogiLink WL0238 and EDUP EP-AC1635) and one AP (ASUS RT-AC55U) have a triggering threshold that is 20 – 30 dB below the −62 dBm standard value, as can be seen from the figure. However, their thresholds become relatively less sensitive around the unused subcarriers. Nevertheless, these three Wi-Fi devices could be easily and utterly disrupted by received UNB interference that is as weak as −80 dBm.

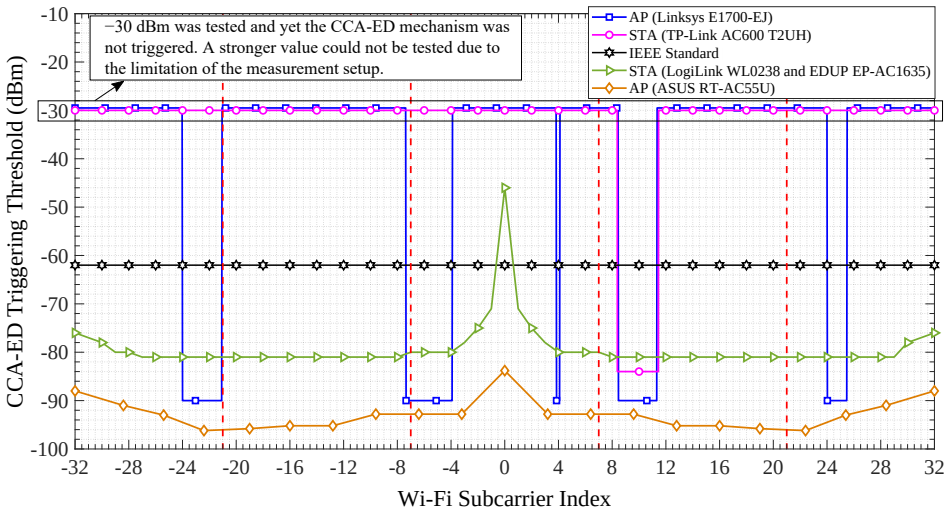

Figure 3.5: Variations of the CCA-ED triggering threshold over frequency for different Wi-Fi devices. The LogiLink WL0238 and EDUP EP-AC1635 stations had very close CCA-ED triggering thresholds (within ±4 dB), yet they are plotted here as one for simplicity. The red dashed vertical lines indicate the locations of the pilot subcarriers. (Measurement results of the first investigating step)

On the other hand, the other tested Wi-Fi devices (Linksys E1700-EJ access point and TP-Link AC600 T2UH station) have a few but very sensitive spectral windows, as can be seen in Figure 3.5. Their CCA-ED mechanism is triggered when very weak UNB interference is present inside such spectral windows. The triggering thresholds of these windows are −90 dBm and −84 dBm for the AP and the STA, respectively. The other windows of both Wi-Fi devices are virtually insensitive to the UNB interference. A UNB signal with a received power as strong as −30 dBm was tested, and yet the CCA-ED mechanism was not triggered. A stronger value could not be tested due to the limitation of the measurement setup.

The frequencies of these virtually insensitive spectral windows can be exploited to deploy UNB sensor nodes as long as the nearby Wi-Fi devices exhibit such windows. Otherwise, a sufficient distance is required to separate them from the nearby Wi-Fi devices. For example, in case of a UNB transmit power of −10 dBm and a CCA-ED triggering threshold of −62 dBm [155], a 4-meter distance (corresponding to 52 dB of free-space path loss) is required to avoid provoking a Wi-Fi network disturbance/outage. In the next investigation steps, the measurements were carried out on the Linksys E1700-EJ access point and the TP-Link AC600 T2UH station. They were also limited to the case in which the UNB interference resides inside the virtually insensitive spectral windows.

3.5.2. SECOND INVESTIGATION STEP

A Wi-Fi link was established between the Linksys E1700-EJ access point and the TP-Link AC600 T2UH station, i.e., the STA was associated with the AP. Microsoft Network Monitor™ software ran on Laptop 2. Within a specified time, the software listed—among others—all correctly decoded beacon packets along with their corresponding timestamps. These beacon packets were broadcast by the AP and received by the STA. In this investigation step, the direction of the data traffic is irrelevant since there is none in the first place.

The BDR was measured for multiple *configurations*. However, it is reported in this chapter only for the *configurations* shown in Table 3.1. These *configurations* correspond to the meaningful SIR range of 9 – 40 dB, i.e., to the range in which the throughput assumed its full dynamic range in the next investigation step. Within this SIR range, the BDR stayed at 100%, i.e., not a single beacon packet was lost as a result of the existing UNB interference. This relative robustness against UNB interference can be explained by the fact that beacon packets are always broadcast at 1 Mbit/s using the lowest MCS index as well as using DSSS. The latter is more immune to the interference under investigation compared to OFDM. A similar observation is reported in [101].

3.5.3. THIRD INVESTIGATION STEP

A Wi-Fi link was established like in the previous investigation step. Laptop 2 and Laptop 3 ran the JPerf freeware tool which reported the carried throughput of the

transport layer every second. In the JPerf tool, one laptop was configured as a server, whereas the other was configured as a client. The client sent a data stream to the server over the Wi-Fi link for a specified duration. Because TCP dominates the Internet traffic compared to UDP, all throughputs were measured at the transport layer of a TCP link in this investigation step. The TCP window size was set to 56 kbytes in the JPerf tool, whereas the maximum transfer unit (a.k.a. MTU) was set to 1500 bytes in the operating system of both Laptop 2 and Laptop 3. The maximum carried throughput was measured in the case of no interference. It was around 54 Mbit/s with a standard error less than 1.0%, as a single spatial stream was established between the STA and the AP under test.

For each tested *configuration* in Table 3.1, the instantaneous throughput was measured over a 5 min interval which is referred to as a measurement session throughout this section. During the whole session, a continuous flow of Wi-Fi data stream was set up in the JPerf tool. Every session had 21 UNB interference periods of 2 s each. This interference period was repeated every ~14.3 s. For instance, Figure 3.6(a) shows the instantaneous TCP throughput performance at the STA over half a minute in the situation of a single OOK-modulated UNB interfering signal coinciding with the Wi-Fi data subcarrier of index +16. During the interference periods in Figure 3.6(a), SIR was set at 30 dB (while S was −36 dBm).

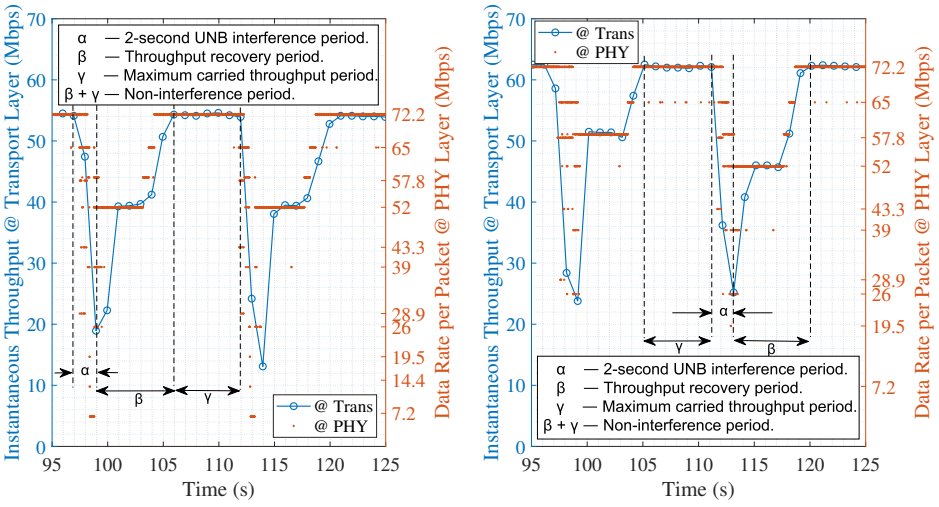

(a) TCP traffic.

(b) UDP traffic.

Figure 3.6: Example of data rate per packet at the PHY and corresponding instantaneous throughput at the transport layer for both TCP and UDP over 0.5 min. (Measured at the TP-Link AC600 T2UH station for the situation of a single OOK-modulated UNB interfering signal that coincided with the Wi-Fi subcarrier of index +16. During Period α, SIR was set at 30 dB while S was −36 dBm.)

It can be observed from the figure that after each interference period (α), there is typically a throughput recovery period (β) similar to what is reported in [157]. During this period, which lasts less than 7 s, the Wi-Fi throughput slowly rises up to its maximum value, i.e., to the maximum carried throughput. This can be initially explained by the joint impact of TCP mechanisms (flow control and congestion control) and an adaptive MCS algorithm (a.k.a. rate adaptive algorithm) that are put in use in commercial Wi-Fi devices. However, the throughput behaviour in the recovery period is in fact dominated by the adaptive MCS algorithm. This can be confirmed from Figure 3.6(b) which shows the instantaneous UDP throughput performance for the same *configuration* as of that for TCP. Both situations almost have identical behaviour where the only difference is in the maximum carried throughput, i.e., 62 Mbit/s for UDP vs. 54 Mbit/s for TCP. Moreover, Figures 3.6(a) and (b) show the data rate of each transferred packet for the same measurements which were collected from the Wi-Fi sniffer at the PHY after packet filtering, i.e., TCP/UDP packets with the appropriate IP destination. The data rate at the PHY indeed resembles the throughput behaviour at the transport layer.

A maximum carried throughput period (γ), which lasts less than 8 s, follows the recovery period, as depicted in Figure 3.6(a). It was to ensure that the Wi-Fi link settles before the next interference period. The reason is that—in a real-world scenario—the offered throughput (i.e., number of packets per day) of a UNB network would be very low. One example is to transfer some biometric data (e.g., glucose level) of a home patient to a cloud-connected BS. In such an example, data could be transmitted periodically/regularly or on an event-triggering basis. In the former case, the transfer rate could be, e.g., up to ten times a day for a diabetic patient.

From each of the 5 min measurement sessions, a single Wi-Fi throughput value was derived and reported later along with its standard error. The value was derived as follows. First, it was averaged over the period $\alpha+\beta$. Then it was averaged over 21 realizations that correspond to the 21 interference periods of the same 5 min measurement session itself.

While the traffic was set to be unidirectional in the measurement setup, acknowledgment packets at the PHY and transport layers were still generated in the opposite direction. Nevertheless, they constituted less than 5% of the total volume of the traffic according to the Wi-Fi sniffer. Therefore, when Laptop 3 was configured as a server in the JPerf tool, it was the AP that was mostly affected by the UNB interference as it received the Wi-Fi traffic from the STA. On the other hand, when Laptop 2 was configured as a server, it was the STA that was mostly affected by the UNB interference as it received the Wi-Fi traffic from the AP. Consequently, the Wi-Fi traffic (i.e., data stream) in the JPerf tool was generated in either directions of the Wi-Fi link per measurement session. One direction was from the AP to the STA, i.e., downlink (DL), as, e.g., in the case of watching a video on YouTube. The other direction was from the STA to the AP, i.e., uplink (UL), as, e.g., in the case of uploading a file to Google Drive.

The third investigation step is divided into two sub-steps as reported in Table 3.1. In the first one, a single UNB interferer was present, whereas the second sub-step was

for the situation of multiple simultaneous UNB interferers. In both sub-steps, the impact of the UNB interference on the Wi-Fi throughput performance was tested on both the AP (i.e., UL) and the STA (i.e., DL) separately.

FIRST SUB-STEP—SINGLE UNB INTERFERER

In this first sub-step, the UNB signal was generated in the two modulation schemes: OOK and GMSK. The UNB signal was also set at different frequencies inside the Wi-Fi channel under test, as reported in Table 3.1. The two Wi-Fi subcarriers of indices 0 and +29 are unused subcarriers, whereas +16 and +18 are data subcarriers. The subcarrier of index +21 is a pilot subcarrier. The two cases, in which the UNB signal resides either between two data subcarriers or between a data and a pilot subcarrier, were considered as well, i.e., +18.5 and +21.5, respectively. The choice of which subcarrier had to be tested among the 4 pilot subcarriers was irrelevant, as long as they reside inside the virtually insensitive spectral windows that were discussed in Section 3.5.1. This was also true for the 52 data subcarriers. However, 12 of them are used in the preamble of Wi-Fi packets [155], hence the subcarrier of index +16, which is one of these 12 subcarriers, was considered in the measurements as well.

Figure 3.7 and Figure 3.8 show the Wi-Fi throughput performance in the case of UL and DL, respectively, over the SIR range of 9 – 35 dB while S was −40 dBm and −36 dBm for the UL and the DL, respectively. The throughput was upper-limited by ~54 Mbit/s which corresponds to the maximum carried throughput in the case of no interference, i.e., theoretically infinite SIR. Most throughput curves in the figures can be approximately fitted by straight lines but with different slopes, i.e., an approximate linear relationship between throughput and SIR in decibel can be observed. This is similar to what is reported in [96].

Given the same UNB peak power, it can be intuitively predicted that OOK would have less interfering impact than GMSK would. This can be explained by the fact that half of the 10 ms OOK bits (i.e., nearly zero-energy bits) barely interfere with Wi-Fi packets. In fact, this can be clearly confirmed from the figures of all tested *configurations*. Given a drop to 75% of the maximum Wi-Fi throughput is acceptable, the AP in Figure 3.7 could tolerate worse SIR values (i.e., 1.5 – 6.0 dB smaller) in the case of an OOK-modulated UNB signal compared to that of GMSK. This tolerance was relatively less exhibited by the STA (only up to 1.5 dB), as can be seen in Figure 3.8. However, the friendly coexistence of OOK compared to GMSK towards the Wi-Fi link, i.e., towards both the AP and the STA, became more distinctive for worse SIR values.

Figures 3.9(a) and (b) show the same results as in Figure 3.7 and Figure 3.8 but in a different presentation. Figure 3.9(a) is dedicated for the case of an OOK-modulated UNB signal, whereas Figure 3.9(b) is for the case of GMSK. As can be indicated from both figures, the throughput performance in the case of the Wi-Fi subcarrier of index +16 was very close to that in the case of the subcarrier of index +18. That means the specific 12 data subcarriers that are used in the preamble [155] are not

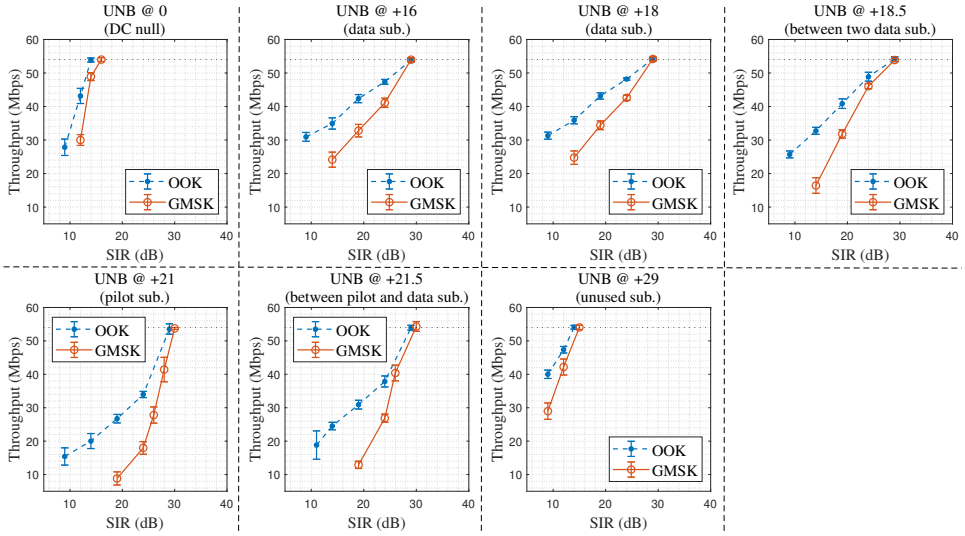

Figure 3.7: Averaged Wi-Fi throughput of the UL at the AP for the situation of a single UNB interferer. (Measurement results of the third investigating step — single UNB interferer)

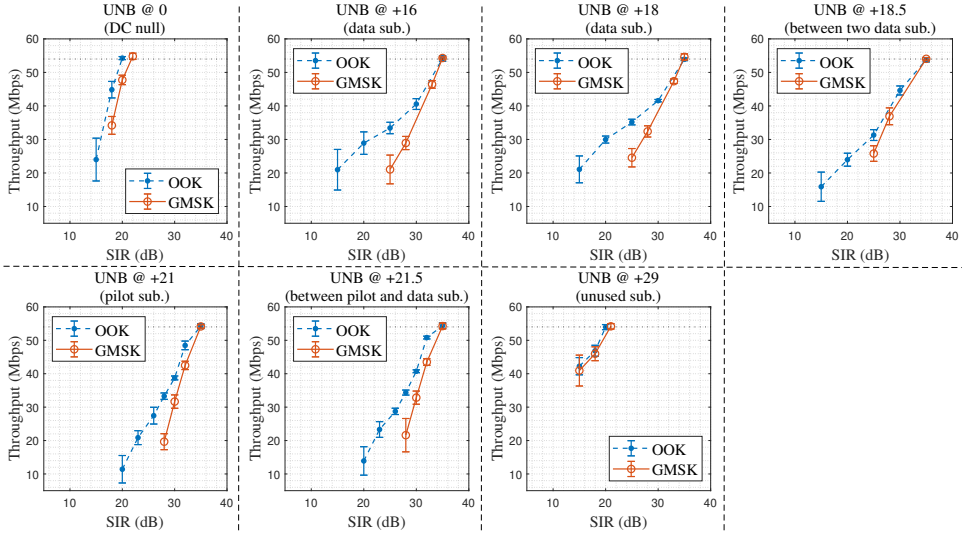

Figure 3.8: Averaged Wi-Fi throughput of the DL at the STA for the situation of a single UNB interferer. (Measurement results of the third investigating step — single UNB interferer)

more/less susceptible to UNB interference than the rest of the data subcarriers. In the case of a UNB signal residing between two data subcarriers (i.e., +18.5), the throughput performance was still close (with ±3 dB of SIR) to the previous case of data subcarriers (i.e., +16 and +18). However, it can be indicated from all tested *configurations* in both figures that the pilot subcarriers (e.g., +21) were the most vulnerable to the UNB interference, especially for poor SIR values. A similar statement is reported in [101], reasoning that such subcarriers are vital for channel estimation and frequency-offset correction processes. Moreover, the case of a UNB signal residing between a data and a pilot subcarrier (e.g., +21.5) proved such vulnerability, as the throughput performance was almost as poor as in the previous case (i.e., +21).

From Figure 3.9, comparing the UL throughput performance at the AP with that of the DL at the STA, the former was more resilient to the interference under investigation than the latter. According to the figure, while the throughput at the AP was still not impacted by interference when SIR was 30 dB, the throughput at the STA was actually 59% to 83% of its maximum value, depending on the modulation scheme and the frequency of the UNB interference. This can be attributed to a couple of reasons. (*i*) Because the AP under test has two external antennas, it receives two copies of the signal, and, thereby, twice the received power. (*ii*) Powerful decoding and detection algorithms may be implemented in the power-hungry AP compared to the STA.

The reason why the case of the unused subcarriers (i.e., 0 and +29) is not presented again in Figure 3.9 is considered later at the end of this sub-step when the 17 sub-bands are recommended. Nevertheless, it is worth noting that the throughput performance in this case was better than that when pilot and data subcarriers were subjected to interference. This is similar to what is reported in [96]. This can be explained by the fact that the unused subcarriers basically do not carry any information. Based on Figure 3.9, the throughput started degrading from its

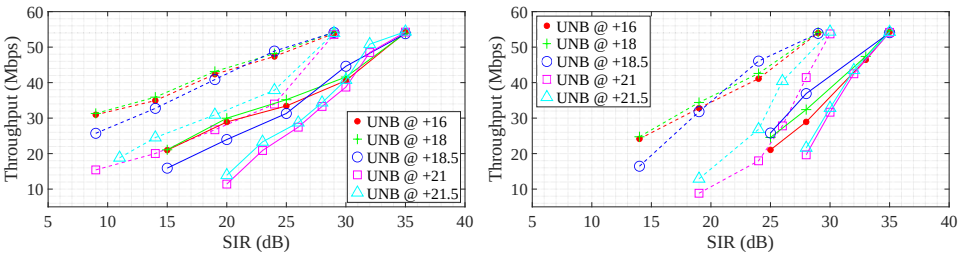

Figure 3.9: Averaged Wi-Fi throughput of the UL at the AP (dashed lines) and the DL at the STA (solid lines) for the situation of a single (a) OOK-modulated and (b) GMSK-modulated UNB signal. (Measurement results of the third investigating step — single UNB interferer)

maximum value when SIR is less than 16 dB or 22 dB, depending on the Wi-Fi DUT. This observation is somewhat in accordance with [97, 98] in which it is reported that a continuous-wave interferer at the subcarrier of index 0 caused a performance degradation when SIR is less than 20 dB.

According to Figure 3.9, by avoiding the Wi-Fi pilot subcarriers, the throughput at the AP and the STA dropped to 50% of its maximum value, as long as SIR was greater than 17 dB and 27 dB, respectively. This relatively large required SIR can be explained by the followings. (*i*) The signal power S in SIR is for the total Wi-Fi power, not for a single subcarrier. (*ii*) The duration of the UNB interference was 2 s, which means at least one Wi-Fi subcarrier was basically affected in all OFDM symbols over thousands of consecutive Wi-Fi packets. (*iii*) The developed methodology and, thereby, the measurement setup were based on the worst-case scenario, as explained earlier in Section 3.3.4.

The reason why we have only considered the throughput measurements of the Wi-Fi link between the Linksys E1700-EJ access point and the TP-Link AC600 T2UH station is because the other tested Wi-Fi devices have very low CCA-ED triggering threshold. That makes the Wi-Fi link either very weak or unable to be established, as explained in the following. The LogiLink WL0238 station was tested along with the Linksys E1700-EJ access point in terms of throughput performance. During the test, a TCP stream was initiated by the AP towards the STA, and an OOK-modulated UNB interfering signal was set to coincide with the Wi-Fi data subcarrier of index +16. Since the LogiLink WL0238 station has a CCA-ED triggering threshold of as low as −82 dBm (see Figure 3.5), the UNB signal power (I) was set in the range of −88 to −96 dBm, while the AP received signal power (S) was set at a very weak value of −80 dBm by attaching an appropriate attenuator to each antenna port of the AP and the STA. Therefore, the SIR values were in the range of 8 to 16 dB, and within which the average measured throughput was between the maximum carried throughput of 8.8 Mbit/s and a very low throughput value of less than 1 Mbit/s. On the other hand, the ASUS RT-AC55U access point was not tested in terms of throughput performance since the Wi-Fi signal power had to be as low as −91 dBm (see Figure 3.5). For such a very weak signal, the Wi-Fi link could not be established in the first place.

From the obtained measurements in the situation of a single UNB interferer, the following important insight can be derived. To reduce the impact of UNB interference on nearby Wi-Fi devices, it is strongly recommended for the UNB signals to avoid coinciding in the frequency domain with any of the pilot subcarriers of any of the 13 Wi-Fi channels. Therefore, in Figure 3.10, all of the 56 used subcarriers (i.e., 52 data and 4 pilot) of every Wi-Fi channel are plotted together in one figure. The subcarrier indices, which then are referred to as universal indices, range from 1 to 257. The universal indices 1 – 4 and 254 – 257 are never used, whereas indices 5 – 253 are occupied by either at least one data subcarrier, a pilot subcarrier, or both.

From Figure 3.10, it can be seen that in total there are 52 pilot subcarriers which correspond to all of the 13 Wi-Fi channels. As can be seen from the same figure as well, the two guard bands between the non-overlapping Wi-Fi channels (i.e., between

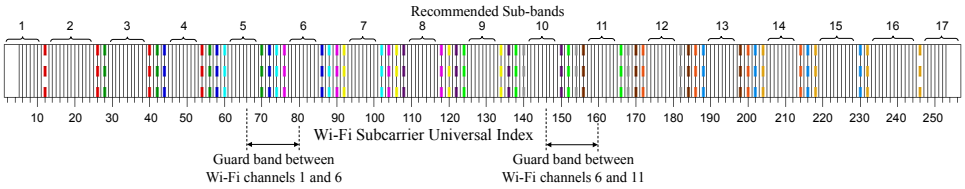

Figure 3.10: Data and pilot subcarriers of all of the 13 Wi-Fi channels in the 2.4 GHz ISM band. Black solid lines refer to the locations of data subcarriers, whereas colored dashed lines refer to the locations of pilot subcarriers. The dashed lines of the same color belong to the same Wi-Fi channel.

1 and 6, and between 6 and 11) contain pilot subcarriers of the other Wi-Fi channels. Therefore, based on the insight regarding the vulnerability of the pilot subcarriers, any idea of utilizing these two guard bands for UNB signaling is not wise, as Wi-Fi channel occupancy in the real world is not limited to the non-overlapping channels (see Figure 3.1). Alternatively, we recommend 17 sub-bands for UNB signaling—with a minimum sub-band bandwidth of 2.5 MHz—as depicted at the top of Figure 3.10. This is based on the aforementioned insight, and, thereby, these 17 sub-bands do not contain any of the 52 pilot subcarriers. Even though all of the unused subcarriers of the all 13 Wi-Fi channels reside only inside these sub-bands, a UNB signal transmitted in any of them would still definitely interfere with at least one data subcarrier of some Wi-Fi channel, as can be indicated from the figure (with the exception of sub-bands 1 and 17).

SECOND SUB-STEP—MULTIPLE UNB INTERFERERS

Multiple simultaneous UNB interferers were present in this second sub-step. Because in the developed methodology we follow the worst-case scenario approach as explained in Section 3.3.4, this sub-step only considered the combined configuration of the following four conditions. (*i*) All UNB interferers had the same modulation scheme. (*ii*) The chosen modulation scheme was GMSK because it has the most interfering impact as proven earlier. (*iii*) All UNB interferers were configured to produce the same received power at the Wi-Fi DUT. (*iv*) Each one of the simultaneous interferers affects a different data subcarrier. If multiple interferers affect the same data subcarrier, their received power will be aggregated. Consequently, we have decided in this sub-section that I in SIR refers to the peak power of only one of the simultaneous UNB interferers, given the corresponding number of the simultaneous interferers is mentioned.

In this sub-step, we have studied the throughput performance of the Wi-Fi link in the situation of 7 simultaneous and independent UNB interferers residing in sub-band 9. These interferers coincided with the data subcarriers of indices +13 to +19 of Wi-Fi channel 6 (i.e., universal indices 126 to 132), as reported in Table 3.1. They employed GMSK modulation, and they were simultaneously generated by the same BladeRF device that is depicted in the measurement setup in Figure 3.3.

Based on the *configurations* in Table 3.1, Figure 3.11 shows the throughput performance of the Wi-Fi link in the presence of such 7 UNB interferers over the SIR range of 25 – 40 dB while S was −40 dBm and −36 dBm for the UL and the DL, respectively. Comparing the UL throughput performance at the AP with that of the DL at the STA, an observation (similar to the one made previously in the case of single UNB interferer) can be made: the AP was more resilient to the interference under investigation than the STA was. According to Figure 3.11, while the throughput at the AP was still not impacted by interference when SIR was 34 dB, the throughput at the STA was actually 52% of its maximum value.

For the purpose of comparison, Figure 3.11 also presents the already-reported throughput performance in the situation of a single OOK-modulated UNB signal which coincided with the Wi-Fi subcarrier of index +16. In fact, based on the analysis of previous results, this case was the least bad in the assumed worst-case scenario. According to the figure, while the throughput at the AP in the situation of a single UNB interferer was still not impacted by interference when SIR was 29 dB, the throughput at the same AP in the other situation of 7 simultaneous UNB interferers was actually 63% of its maximum value. Similarly, while the throughput at the STA in the situation of a single UNB interferer was still not impacted by interference when SIR was 35 dB, the throughput at the same STA in the other situation of 7 simultaneous UNB interferers was actually 61% of its maximum value.

Alternatively, Figure 3.11 can be interpreted as follows. If, in any of the recommended sub-bands, there are N simultaneous UNB interferers (where $1 \leq N \leq 7$) with different modulation schemes, different received interference powers, and they interfere with

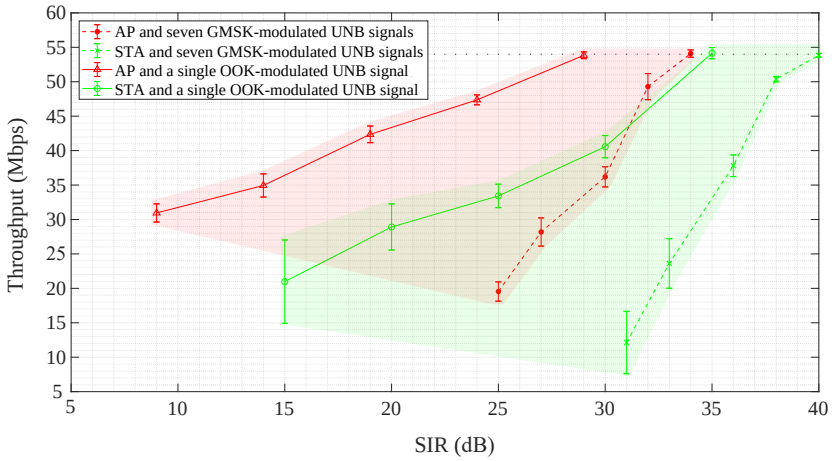

Figure 3.11: Averaged Wi-Fi throughput of the UL at the AP (red lines) and the DL at the STA (green lines) for the situation of a single OOK-modulated UNB signal (solid lines) and seven simultaneous GMSK-modulated UNB signals (dashed lines). (Measurement results of the third investigating step — multiple UNB interferers)

different subcarriers, then the throughput of the DL at the STA will be, e.g., 44%–91% of its maximum value given that at least one of the UNB interferers causes a minimum SIR value of 33 dB at the STA. In other words, the throughput performance would be anywhere in the green-shaded area in Figure 3.11 on a vertical line of SIR = 33 dB. Similarly, the throughput of the UL at the AP will be, e.g., 37%–91% of its maximum value given that at least one of the UNB interferers causes a minimum SIR value of 25 dB at the AP. In other words, the throughput performance would be anywhere in the red-shaded area on a vertical line of SIR = 25 dB.

3.6. CONCLUSION

In this chapter, the feasibility of a UNB deployment in the 2.4 GHz ISM band in terms of wireless coexistence was empirically investigated for the case of Wi-Fi networks by first developing a systematic and thorough methodology for the empirical investigation. The methodology is based on a worst-case interference scenario and consists of three investigation steps to assess the impact of the UNB interference on the CCA mechanism, the BDR, and the transport-layer throughput. The methodology was then applied to a measurement setup to practically study the case of 100 bps UNB signals interfering with an IEEE 802.11n transmission in the 2.4 GHz band. Five different Wi-Fi devices from different vendors were tested. The UNB signal was generated in two modulation schemes, namely, OOK and GMSK. Both single and multiple simultaneous UNB interferers were considered as well.

The following insights were gained regarding the interference vulnerability of different tested Wi-Fi devices and subcarriers, as well as regarding the friendly coexistence of different UNB modulation schemes. Regarding the CCA mechanism, three of the tested commercial off-the-shelf Wi-Fi devices were totally disrupted by the UNB interference that was as weak as −80 dBm, whereas the other devices only suffered in terms of carried throughput provided that their sensitive CCA-ED windows were avoided. Regarding the BDR, the beacon packets that are periodically broadcast by the AP are much more immune to the UNB interference compared to the data packets. According to the throughput measurements at the transport layer, the Wi-Fi link strived to maintain a non-zero throughput under the impact of a strong UNB interference, while at the same time the BDR maintained a perfect 100%. Moreover, the analysis of the throughput measurement results showed that an OOK-modulated UNB signal has less interfering impact than GMSK does, given both have the same peak power. Moreover, the Wi-Fi pilot subcarriers are the most vulnerable to the UNB interference compared to the other types of subcarriers, whereas the unused subcarriers are the least vulnerable.

Finally, based on the gained insights and to promote wireless coexistence, 17 sub-bands were recommended for the UNB signaling scheme in the 2.4 GHz band. If UNB signals only access these recommended sub-bands and given that a drop to 75% of the maximum Wi-Fi throughput is acceptable, then wireless coexistence is possible in the following two scenarios in which S is −36 dBm: (i) a single UNB interferer employing an OOK-modulation scheme while SIR is greater than

30 dB, or (*ii*) up-to-seven simultaneous UNB interferers interfering with different data subcarriers and employing arbitrary modulation schemes while the lowest SIR is still greater than 36 dB.

4

VIRC MEASUREMENT AND ESTIMATION METHODOLOGY

4.1. INTRODUCTION

Traditionally, reverberation chambers (RCs) use fixed, rigid metallic walls to build an overmoded rectangular resonant cavity. Such chambers are commonly known as classical reverberation chambers (CLRCs) [158]. Nevertheless, RCs with flexible but reflective fabric-based walls can also be found in the literature. The earliest design of such chambers is proposed in [106] and has been commonly known since as the Vibrating Intrinsic Reverberation Chamber (VIRC). There are two fundamental differences between the VIRC and the CLRC.

- The boundary conditions in the CLRC are altered by means of at least one rotating mechanical stirrer. On the contrary, the walls of the VIRC act as the mechanical stirrer, which vibrate and, thereby, alter the boundary conditions.
- Since the slightest vibration in the VIRC causes a significant change in the field resonance pattern (especially at high frequencies), the mode-tuning technique (a.k.a. stepping stirrers) cannot be implemented in the VIRC but is commonly adopted in the CLRC as, e.g., in [159]. On the other hand, the mode-stirring technique (a.k.a. continuously moving stirrers) is adopted in the VIRC as, e.g., in [107, 108]. The mode-stirring technique is usually implemented by means of air fans or dc motors pushing/pulling randomly on the VIRC fabric [107, 108].

Because of the second difference, the propagation channel inside the VIRC is not time invariant anymore like in the CLRC, but rather dynamic. To that end, a full characterization of the VIRC requires a measurement procedure that is substantially different from the one commonly adopted in the CLRC.

Parts of the content of this chapter were published in [114].

Initially, RCs were mainly utilized in electromagnetic compatibility (EMC) testing [104]. However, in the last couple of decades, they have attracted an increasing interest in over-the-air (OTA) testing of wireless communications [105]. Depending on which research area the RC is utilized in, a corresponding relevant characterization must first be conducted on the chamber itself before it is used in a specific application. This is to investigate the dynamic range of the chamber characteristics under interest as well as to ensure the chamber meets the different standardization requirements. The utilization of CLRCs in OTA has been vastly demonstrated in many studies as, e.g., in [103, 160–162]. A list of RC characteristics that are usually investigated from the standpoint of OTA are summarized in Table 4.1 including their equivalents from the standpoint of EMC[1].

In the worst-case scenario represented by a Rayleigh channel, the ratio of the symbol rate to the Doppler spread must roughly be as small as 100 for the wireless link to start experiencing a bit-error-rate floor/wall as high as 10^{-3} [163]. For wideband systems, as, e.g., in IEEE 802.11g [155], this translates into a Doppler spread as large as 3 kHz, which corresponds to a very high velocity of roughly 1300 km/h at a carrier frequency of 2.4 GHz. Therefore, the Doppler spread in most real-world deployments at 2.4 GHz is much less than 3 kHz. Moreover, not only most OTA use cases that are presently emulated in CLRCs are for very wideband 5G systems [105], but also CLRCs themselves cannot emulate large Doppler spreads because of their physical limitations, i.e., mechanical reasons [164]. To the best knowledge of the author, the largest Doppler spread induced by a CLRC and reported in the literature is 650 Hz at the 2.4 GHz [165]. Therefore, the impact of Doppler spreads induced by CLRCs can be neglected when testing very wideband systems [164], and, hence, the mode-tuning and mode-stirring techniques are interchangeably put in use. However, as opposed to very wideband systems, this is not the case for relatively wideband systems (as, e.g., in IEEE 802.11p [166]), narrowband (NB) systems or UNB systems (this thesis). Such systems experience the negative impact of a Doppler spread that is as low as few tens of Hz, which corresponds to many real-world deployments. To that end, before an NB system/channel can be tested/emulated in an RC (i.e., CLRC/VIRC), a second-order temporal characterization of the RC itself is necessary when the mode-stirring technique is put in use.

In recent studies, different VIRCs have been investigated in terms of various EMC and OTA characteristics [107, 108, 171–177]. However, these characteristics are either individually investigated using different VIRC frameworks or not estimated following a VIRC systematic methodology. For example, the authors in [108] claimed to devise a complete framework for the assessment of the VIRC in the frequency- and time-domains. However, they investigated and presented the spectral characteristics before the temporal ones, as opposed to the argument presented in this chapter. Moreover, the selection of sample sizes and some of the crucial settings in the vector network analyzer (VNA) is not based on a systematic approach. Thus, such a measurement procedure in [108] might lead—but not necessarily—to invalid and,

[1] A better understanding of the field properties generated in the VIRC will help utilize this unique environment for both EMC and OTA, hence yields benefits for both purposes.

Table 4.1: Summary of RC characteristics from the standpoint of OTA and EMC.

	OTA characteristic	EMC equivalent
First-order	**probability distribution function (PDF)**	
	rejection rate for Rician distribution	same as in OTA
	K-factor of Rician distribution	$Q_{\text{dB}} = -K_{\text{dB}} + C_{\text{dB}}$ [&]
	channel gain	$\text{IL}_{\text{dB}} = -G_{\text{dB}}$ [#]
Second-order spectral	**frequency correlation function (FCF)** [*]	
	power delay profile (PDP) [*]	-
	coherence bandwidth (CB)	$\Delta f_{\text{mode}} = B_{\text{coh@50\%}}$ [†]
	rms delay spread	$\tau_{\text{RC}} = \tau_{\text{rms}}$ [‡]
	maximum excess delay	-
Second-order temporal	**time correlation function (TCF)** [*]	
	Doppler spectral density (DSD) [*]	-
	coherence time (CT)	$N_{\text{ind}} \sim T_{\text{obs}} \div T_{\text{coh}}$ [††]
	Doppler spread	$e_{\text{stir}} \sim f_D$ [‡‡]
	level crossing rate	-
	average fade duration	-

[*] FCF and PDP are two equivalent representations for the same characteristic. The same thing can be said of TCF and DSD.

[&] Q_{dB} is the RC Q-factor in decibels, whereas K_{dB} is the Rician K-factor in decibels. The Q-factor is more common in EMC than the K-factor. $C_{\text{dB}} = \text{func}(V, f_c, r, D_{\text{Tx}} \times D_{\text{Rx}})$, where V is the RC volume, f_c is the CF, D_{Tx} and D_{Rx} are the antenna directivities at the Tx and the Rx, respectively, and r is the distance between them [167].

[#] IL_{dB} is the RC insertion loss in decibels, whereas G_{dB} is the channel gain in decibels (a.k.a. average power transfer level) [168].

[†] Δf_{mode} is the RC average mode bandwidth, whereas $B_{\text{coh@50\%}}$ is the CB at which the normalized frequency autocovariance function drops to 50% [169].

[‡] τ_{RC} is the RC decay time, whereas τ_{rms} is the rms delay spread [162].

[††] N_{ind} is the number of collectable independent samples in the RC, T_{coh} is the CT, and T_{obs} is the observation/measurement interval [108].

[‡‡] e_{stir} is the RC stirring efficiency, whereas f_D is the Doppler spread [170]. In [170], f_D is defined based on the autocorrelation as opposed to this methodology which adopts the autocovariance instead. Moreover, f_D is one of several methods in literature used to assess the stirring efficiency.

thereby, unreliable conclusions. Additionally, a VIRC measurement and estimation methodology for OTA testing with a systematic procedure to be followed for achieving a desired estimation accuracy is also lacking in the literature.

In this chapter, the objective is to develop a measurement procedure that is suitable for the VIRC, as an intermediate yet essential step for the next chapter in which the VIRC is empirically characterized for OTA testing of NB systems. Therefore, we have developed a measurement methodology to characterize the VIRC for use in OTA testing of wireless baseband algorithms in NB single-input single-output (SISO) systems, as in low-power wide-area networks (LPWANs) in general and UNB (this thesis) in particular. Moreover, combining the RC characteristics existing in both EMC and OTA as shown in Table 4.1, the methodology is also fully applicable for EMC. Furthermore, it is devised to be universal to any RC (i.e., VIRC and classical) independently of the antenna/loading configurations, the chamber size, structure, or stirring mechanism, as long as the mode-stirring technique is put in use. The main contribution of this chapter is, thereby, developing a systematic methodology for the empirical investigation of the channel first- and second-order temporal and spectral characteristics that is applicable for both the CLRC and the VIRC as well as for both EMC and OTA testing. Moreover, the methodology is based on a reproducible three-step procedure that takes into consideration a desired estimation accuracy as well as the effect of three variables: carrier frequency, rotational speed of the VIRC motors, and VIRC loading condition. The methodology is then used in practice to preliminarily investigate the propagation channel inside the VIRC before it is thoroughly characterized and empirically modeled in the next chapter. The preliminary investigation in this chapter is, however, only concerned with the channel first-order characteristics. Its purpose is solely to examine whether a preloading is necessary—and to what extent it is successful—so that the channel envelope histogram (CEH) resembles a theoretical Rayleigh distribution that is highly desirable for EMC and OTA testing.

This chapter is organized as follows. The proposed methodology is described in Section 4.2, in which all the three investigation steps are explained in detail. In Section 4.3, the VIRC preliminary investigation is motivated. The measurement setup and measurement results are presented and analyzed in Section 4.4 and Section 4.5, respectively. Finally, a conclusion is given at the end of this chapter.

4.2. METHODOLOGY

A schematic illustration of a universal setup that is used to develop the methodology is shown in Figure 4.1. Inside the VIRC, a SISO channel between two antennas is to be characterized. Outside, a calibrated VNA is used to measure the aggregate S_{21}-parameter of the two antennas and the propagation channel in between. The VNA is used to perform both frequency and zero-span sweeps. Moreover, for automation purposes, the VNA is controlled by a personal computer through a GPIB interface which also controls a variable DC power supply. The latter determines the

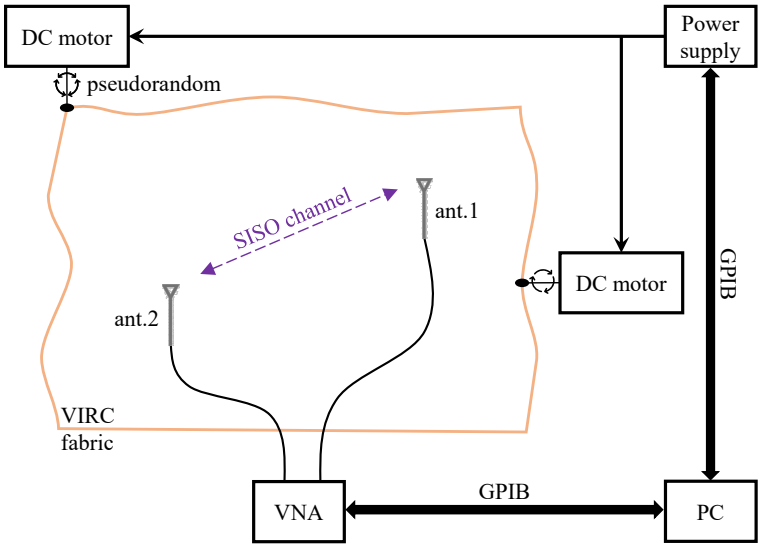

Figure 4.1: Schematic illustration of the universal measurement setup.

RS of the VIRC motors which rotate pseudo-randomly while pulling on the VIRC fabric.

Since time is the ultimate limitation of any measurement campaign, the measurement data that can be collected is limited as well. As a result, the accuracy of estimations is subject to a trade-off between bias and variability [178]. The bias in an estimate (a.k.a. trueness) is the expected difference between an estimated parameter and its true value. On the other hand, the variability among estimates (a.k.a. precision or uncertainty) is the expected confidence interval for a given confidence level. Increasing the sample size reduces both the expected bias and the expected confidence interval. However, the latter can be further reduced at the expense of the former by conducting the measurements in such a way that smaller yet more samples are collected.

In this section, the methodology is presented and explained in detail. First, the relevant channel characteristics and the VIRC variables are identified and discussed. Next, a flow graph with three priority-based investigation steps is presented taking into consideration the different possible combinations of the VIRC variables. For each of the channel first- and second-order temporal and spectral characteristics, the measurement and the estimation procedures of the methodology are individually explained.

4.2.1. OTA CHARACTERISTICS AND VIRC VARIABLES

The cumulative distribution function (CDF), the frequency correlation function (FCF), and the time correlation function (TCF) of the complex envelope can sufficiently

describe the first- and second-order temporal and spectral characteristics [55] of any SISO[2] wireless channel. Table 4.1 summarizes different RC characteristics that can be estimated from the three aforementioned functions from the stand point of OTA testing.

The effect of three independent configurable VIRC variables is considered in each of the three investigation steps since they determine the full dynamic range of the channel characteristics under interest. These variables are the carrier frequency (CF, denoted by f_c), the rotational speed (RS, denoted by ω) of the VIRC motors, and the VIRC loading condition (LC). Throughout this chapter, any unique combination of values of these variables is referred to as a *configuration*.

4.2.2. THREE-STEP FLOW GRAPH

The first step of the methodology is dedicated to the second-order temporal characteristics, namely, the normalized time autocovariance function (NTAF) and the coherence time (CT). The second step considers the normalized frequency autocovariance function (NFAF) and the coherence bandwidth (CB), which are two of the second-order spectral characteristics. In the last and third step, two of the first-order characteristics are considered. They are the rejection rate (RR) of the chi-squared (a.k.a. χ^2) goodness-of-fit (GoF) test for Rician distribution and the Rician K-factor. The three steps of the methodology are summarized in Figure 4.2.

Since each of the three investigation steps is concerned with a different order and a different category of characteristics, there is a measurement procedure and an estimation procedure dedicated to each of them. Furthermore, the reason why the channel characteristics are investigated according to the order in the flow graph of Figure 4.2, as opposed to [108], is that the measurement settings during the third step require two estimated characteristics from the previous two steps, namely, $T_{\text{coh}}\big|_{\text{max}}$ and $B_{\text{coh}}\big|_{\text{max}}$. Additionally, the measurement settings during the second step require two estimated characteristics from the first step, namely, $T_{\text{coh}}\big|_{\text{max}}$ and $T_{\text{coh}}\big|_{\text{min}}$. The three aforementioned characteristics are defined as follows.

- $T_{\text{coh}}\big|_{\text{max}}$ = longest CT of the slowest-fading case scenario which corresponds to $\left(f_c\big|_{\text{min}}, \omega\big|_{\text{min}}, \text{fully loaded}\right)$.
- $T_{\text{coh}}\big|_{\text{min}}$ = shortest CT of the fastest-fading case scenario which corresponds to $\left(f_c\big|_{\text{max}}, \omega\big|_{\text{max}}, \text{unloaded}\right)$.
- $B_{\text{coh}}\big|_{\text{max}}$ = largest CB among all possible *configurations* of $\left(f_c, \omega, \text{fully loaded}\right)$.

[2]The angular-distance correlation functions can sufficiently describe the second-order spatial characteristics of multiple-input multiple-output (MIMO) channels. A somewhat related EMC term is the field uniformity which is basically the spatial stationarity—within an accepted variation—of the maximum field strength from each probe axis inside a given working volume [179].

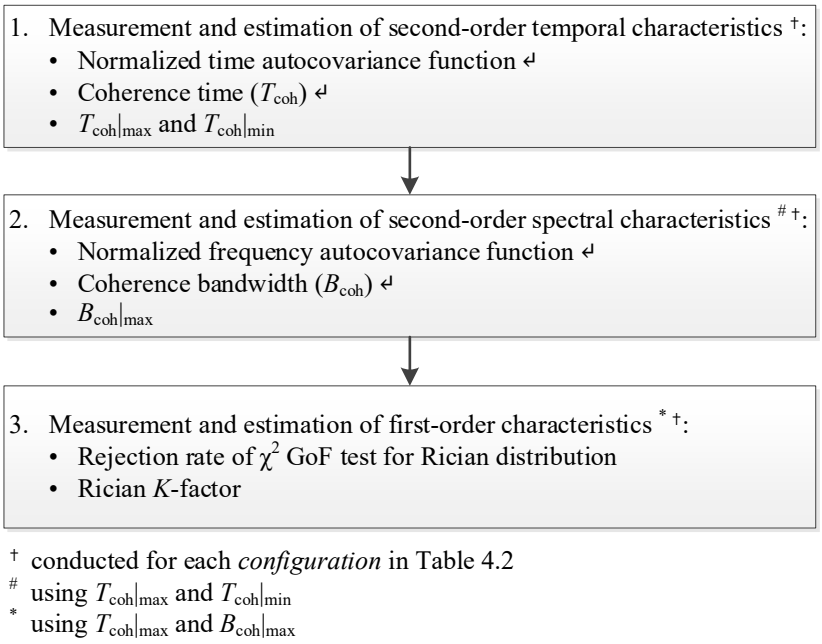

Figure 4.2: Three-step flow graph of the methodology.

4.2.3. FIRST STEP: SECOND-ORDER TEMPORAL CHARACTERISTICS

When it comes to estimating the VIRC temporal characteristics, the measurement procedure required by realization averaging is more convenient to conduct than that of ensemble averaging. Therefore, here in Section 4.2.3, the method of realization averaging over the complex S_{21}-parameter is adopted. However, the temporal ergodicity of the random process (RP), $S_{21}(t)$, must then be invoked (at least in the wide sense).

In the following, both the measurement and the estimation procedures of the NTAF and the CT are explained taking into consideration the different possible *configurations* of the three VIRC variables listed in Table 4.2.

FIRST STEP: MEASUREMENT PROCEDURE

The measurement process of the S_{21}-parameter is depicted in Figure 4.3, and the corresponding method for setting the VNA is summarized in the second column of Table 4.3. Since some VNA settings are dependent on others, they are then listed in the table in order of priority. As the figure shows, the S_{21}-parameter can be modeled as a temporal RP whose different realizations are functions of time and are collected according to the following items.

Table 4.2: Considered VIRC variables in the methodology and their configurations in the preliminary investigation.[†]

VIRC variables	**Methodology**	**VIRC preliminary investigation**		
	First—third step	**First step**	**Second step**	**Third step**
Carrier frequency	$[f_c\|_{\min}, f_c\|_{\max}]$ MHz	(670, 2740) MHz	{670, 720, 770, 820, 868, 1200, 1500, 1800, 2100, 2458, 2740} MHz	[670, 2740] MHz
Rotational speed	$[\omega\|_{\min}, \omega\|_{\max}]$ r/min	(19.4, 42.9) r/min	{19.4, 28.3, 42.9} r/min	42.9 r/min
Loading condition	different LCs	(loaded, unloaded)	loaded	unloaded

[†]Notations: (x, y) is a tuple, {1, 2, ...} is a set, and [a, b] is a finite-resolution interval (i.e., range).

- The average number of time samples (i.e., data points) per CT is given by

$$r_t = N \frac{T_{\text{coh@37\%}}}{T_{\text{swp}}} \tag{4.1}$$

where N, $T_{\text{coh@37\%}}$, and T_{swp} are defined in Table 4.3. A lower bound has to be imposed such as $r_t \geq 4$ samples per $T_{\text{coh@37\%}}$. This is to guarantee a certain degree of temporal correlation among the adjacent time samples (i.e., data points) within each realization individually since the Doppler spectrum is not expected to be strictly band-limited [165, 170, 180–182]. Otherwise, such realizations would be unreliable for TCF estimation [183].

- Since the VNA buffer size per sweep is limited, multiple realizations may need to be collected to achieve a desired estimation accuracy. Therefore, for each possible *configuration* in Table 4.2, M different realizations are collected according to Table 4.3 and as depicted in Figure 4.3. This improves the estimation accuracy in terms of variability which is quantified by ε_t. The latter is defined as the relative width of the expected confidence interval [184] of the estimated NTAF at $T_{\text{coh@37\%}}$ and is given by

$$\varepsilon_t = \pm \frac{z}{\sqrt{M}} \frac{\sigma_{\hat{\rho}_t}}{\mu_{\hat{\rho}_t}} \times 100\% \tag{4.2}$$

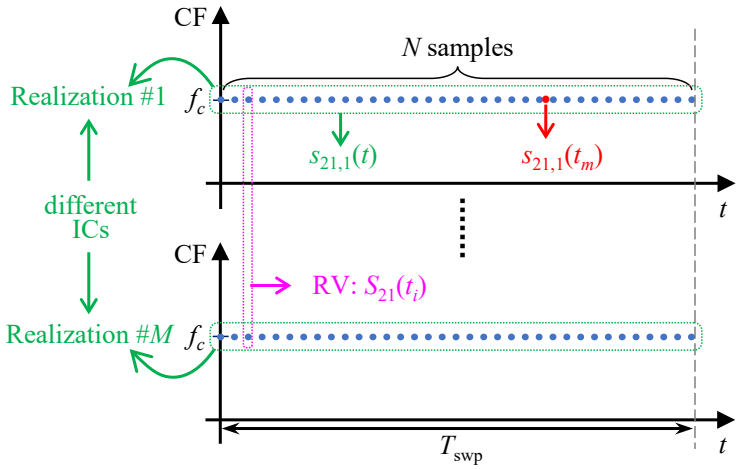

Figure 4.3: Measurement process of the S_{21}-parameter for the second-order temporal characteristics. RV, RP, and IC are abbreviations of random variable, random process, and initial condition, respectively. $s_{21,n}(t_m)$ is a time sample (i.e., data point) in the temporal RP, $S_{21}(t)$, whereas t_i and t_m are arbitrary time instants for illustration purposes. It should be noted that f_c is the CF (i.e., RF frequency) at which the S_{21}-parameter is measured.

Table 4.3: VNA settings of the 2nd-order temporal characteristics measurements.

VNA parameter (in order of priority)	**Setting**	
	Methodology	**VIRC prelim. inv.**
sweep type	zero span	
center frequency	sweep for every freq. in $[f_c\|_{\min}, f_c\|_{\max}]$ *	see the first step of VIRC prelim. inv. in Table 4.2
No. of sweeps (M)	$\geq e^2 z^2 L^{-1} \varepsilon_t^{-2} r_t$ #	4 §
No. of points (N)	$\geq e^2 z^2 M^{-1} \varepsilon_t^{-2} r_t$ #	10^4 §
sweep duration (T_{swp})	$N r_t^{-1} T_{\text{coh@37\%}}$ #	actual value depends on CF, RS, and LC ‡
IF bandwidth (IFBW)	$\gg T_{\text{coh}}^{-1}\|_{\min}$ †	1 kHz ‡

*The resolution of this frequency range can be chosen arbitrarily, i.e., independently from the rest of the VNA settings.
†IFBW is small enough to result in a negligible noise floor, but large enough to account for the maximum Doppler spread ($T_{\text{coh}}^{-1}|_{\min}$ [55]) of the VIRC.
‡A heuristic approach is followed to determine IFBW and T_{swp}.
#It follows from (4.1) and/or (4.2), where e is Euler's number, ε_t is the desired relative width of the expected confidence interval of the estimated NTAF at $T_{\text{coh@37\%}}$, z is the z-score of this confidence interval given a desired confidence level, M also indicates the number of estimates, L is the VNA buffer size, $T_{\text{coh@37\%}}$ is the CT at which the NTAF drops to e^{-1}, and r_t is the required number of samples per $T_{\text{coh@37\%}}$.
§It follows from a 95%-confidence level, $M = 4$ estimates, $z = 1.96$, $|\varepsilon_t| < 6\%$, $L = 20,001$ samples (data points), and $r_t = 4$ samples/$T_{\text{coh@37\%}}$.

where $\sigma_{\hat{\rho}_t}$ and $\mu_{\hat{\rho}_t}$ are, respectively, the expected standard deviation and the expected mean of the estimated NTAF at $T_{\text{coh@37\%}}$; and z is defined in Table 4.3. According to [66], $\mu_{\hat{\rho}_t} \approx e^{-1}|_{T_{\text{coh@37\%}} \ll T_{\text{swp}}}$ and $\sigma^2_{\hat{\rho}_t} \leq \frac{T_{\text{coh@37\%}}}{T_{\text{swp}}}$, in which the NTAF is assumed to be bounded by an exponentially decaying function with time constant $T_{\text{coh@37\%}}$.

- The collected realizations are mutually uncorrelated [179, 185–187] since they are obtained by restarting the stirring mechanism of the VIRC with different initial conditions, i.e., random initial positions of both motor arms and random fabric wrinkling. Otherwise, any correlation among the collected realizations means more redundancy in the measurement data and, thereby, less accuracy [188].

- Each realization is collected with N equidistant time samples (i.e., data points) according to Table 4.3 after M is set following previous item of (4.2).

- The value of the VNA sweep duration must satisfy the inequality,

$\frac{e^2 z^2 T_{\text{coh@37\%}}}{M\varepsilon_t^2} \leq T_{\text{swp}} \leq \frac{N T_{\text{coh@37\%}}}{r_t}$, which follows from (4.1) and (4.2). However, according to Table 4.3, T_{swp} is set to the upper bound of this inequality. This is to improve the estimation accuracy in terms of bias. The latter is the result of the windowing effect in realization averaging of time-limited realizations in case of a biased estimator [189].

- As Table 4.3 indicates, both the IF bandwidth and the sweep duration of the VNA depend on the CT, which itself needs to be first estimated by correctly choosing the VNA settings. This creates a situation similar to the "chicken-egg" problem. To break the latter, a heuristic approach is followed. In short, it is based on the following.
  1. Initial rough estimations of T_{coh} for the eight unique *configurations*: $\{f_c|_{\text{min}}, f_c|_{\text{max}}\} \times \{\omega|_{\text{min}}, \omega|_{\text{max}}\} \times \{\text{unloaded, fully loaded}\}$.
  2. A nonlinear regression utilizing the eight rough estimations in the plausible assumption that the CT is inversely proportional to the RS and to the CF.
  3. A trial-and-error method to guarantee that the inequalities and conditions in Table 4.3 are all satisfied.
- In post-processing, the realizations are up-sampled by a factor of 10 through linear interpolation, resulting in at least $10\, r_t = 40$ samples per $T_{\text{coh@37\%}}$ [190] to be used later in the estimation procedure. This is to improve the resolution of the CT estimates.
- Finally, it can be easily proved that the relative width of the expected confidence interval of the estimated CT is approximately equal to that of the estimated NTAF as long as the latter is less than 35%.

FIRST STEP: ESTIMATION PROCEDURE

For each possible *configuration* in Table 4.2, the NTAF is estimated from each of the M uncorrelated collected realizations that are depicted in Figure 4.3, resulting in the M estimates [66, 190, 191],

$$\hat{\rho}_{t,n}(m\Delta t) = \frac{\frac{1}{N}\sum_{k=0}^{N-m-1} s_{21,n}(k\Delta t)\, s_{21,n}^*((k+m)\Delta t) - |c_n|^2}{\frac{1}{N}\sum_{k=0}^{N-1} \left|s_{21,n}(k\Delta t)\right|^2 - |c_n|^2} \tag{4.3}$$

where $n \in \{1, 2, ..., M\}$; $c_n = \frac{1}{N}\sum_{k=0}^{N-1} s_{21,n}(k\Delta t)$; $s_{21,n}^*$ is the complex conjugate of $s_{21,n}$; $s_{21,n}(t)$ is the nth collected realization of $S_{21}(t)$; N is the number of time samples (i.e., data points) in $s_{21,n}(t)$; $m \in \{0, 1, ..., N-1\}$ is the time offset index at which $\hat{\rho}_t$ is evaluated; $\Delta t = T_{\text{swp}} \div N$; and T_{swp} is a variable VNA sweep duration which is dependent on the considered *configuration*. The estimated CT for a specific *configuration* is defined to be the time offset at which the estimated NTAF from

the corresponding measurement data drops to a certain desired threshold, TH. Equivalently, it is the minimum positive solution, $\hat{T}_{\text{coh@TH},n}$, of [192]

$$\left|\hat{\rho}_{t,n}(\hat{T}_{\text{coh@TH},n})\right| = \text{TH} \tag{4.4}$$

where $n \in \{1,2,...,M\}$. Finally, the sample mean (i.e., $\overline{X}$) is computed from the M estimates, (4.4), to obtain $\overline{\hat{T}}_{\text{coh@TH},n}$.

The longest CT of the slowest-fading case scenario, $T_{\text{coh}}\big|_{\text{max}}$, is defined for a TH $= e^{-1} \approx 37\%$ [187, 190] and corresponds to the following *configuration*: $\left(f_c\big|_{\text{min}}, \omega\big|_{\text{min}}, \text{fully loaded}\right)$. Since TH = 37%, $T_{\text{coh}}\big|_{\text{max}}$ guarantees a sufficient uncorrelation, which is required by the measurement settings of the next two investigation steps. On the other hand, the shortest CT of the fastest-fading case scenario, $T_{\text{coh}}\big|_{\text{min}}$, is defined for a more-conservative TH = 90% [193, 194] and corresponds to the following *configuration*: $\left(f_c\big|_{\text{max}}, \omega\big|_{\text{max}}, \text{unloaded}\right)$. Since TH = 90%, $T_{\text{coh}}\big|_{\text{min}}$ guarantees a sufficient correlation and, thereby, a nearly time-invariant channel, which is required by the measurement settings of the second investigation step.

4.2.4. SECOND STEP: SECOND-ORDER SPECTRAL CHARACTERISTICS

As mentioned in the beginning of Section 4.2, the S_{21}-parameter represents the aggregate transfer function of the two antennas and the propagation channel in between. It is used to estimate the NFAF, and from which the CB is estimated given a certain desired threshold. Because of the inherent dependence of the aggregate transfer function on frequency [188], the RP, $S_{21}(f)$, never exhibits spectral stationarity—and, thereby, nor spectral ergodicity—over a wide bandwidth (not even in the wide sense). Therefore, the NFAF and, thereby, the CB must not be estimated using realization averaging (as implemented, e.g., in [195]) since it needs the spectral ergodicity to be valid over a wide bandwidth in the first place. Even if realizations are collected with a smaller bandwidth to guarantee approximate spectral ergodicity, any estimation based on realization averaging will then suffer from a significant bias due to the windowing effect in case of a biased estimator [196].

In ensemble averaging, on the other hand, an estimation bias—due to a limited sample size and a biased estimator—can be significantly diminished by continuously increasing the number of collected realizations, i.e., sample size. Such an increase is only limited by the time limitation of the measurement campaign. Therefore, here in Section 4.2.4, instead of realization averaging, the method of ensemble averaging over the complex S_{21}-parameter [159, 161] is adopted as opposed to Section 4.2.3. This is the reason behind the contrast in the number of collected realizations between Section 4.2.3 on the one hand, and Sections 4.2.4 and 4.2.5 on the other.

In the following, both the measurement and the estimation procedures of the NFAF and the CB are explained taking into consideration the different possible *configurations* of the three VIRC variables listed in Table 4.2.

SECOND STEP: MEASUREMENT PROCEDURE

The measurement process of the S_{21}-parameter is depicted in Figure 4.4, and the corresponding method for setting the VNA is summarized in the second column of Table 4.4. Since some VNA settings are dependent on others, they are then listed in the table in order of priority. As the figure shows, the S_{21}-parameter can be modeled as a spectral RP whose different realizations are functions of frequency and are collected according to the following items.

- The collected realizations are mutually uncorrelated [108] since they are separated by $T_{\text{trig}} \geq T_{\text{coh}}\big|_{\text{max}}$ (see Figure 4.4). Like in Section 4.2.3, collecting uncorrelated realizations by applying different ICs instead of separating them by $T_{\text{coh}}\big|_{\text{max}}$ is also possible here. Yet it is inconvenient when hundreds of them are needed to be collected. In any case, the uncorrelation among the different realizations, which is a common method used to establish a weak form of independence [179, 185–187], is essential for improving the estimation accuracy in terms of both bias and variability.

- By setting the VNA sweep duration to $T_{\text{swp}} \leq T_{\text{coh}}\big|_{\text{min}}$, it is guaranteed that the propagation channel inside the VIRC is nearly time invariant during each frequency sweep as Figure 4.4 depicts.

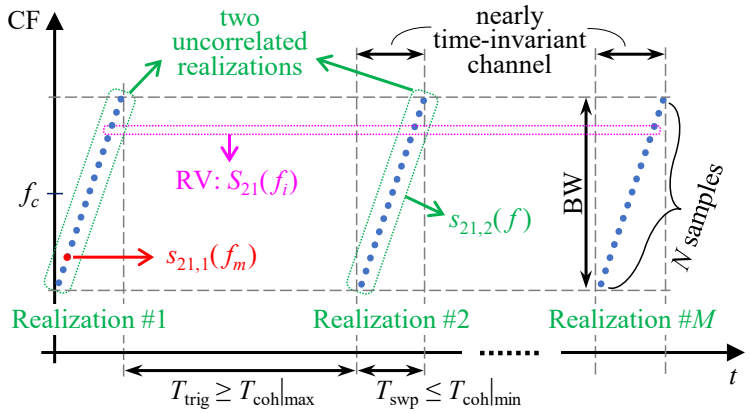

Figure 4.4: Measurement process of the S_{21}-parameter for the second-order spectral characteristics. RV and RP are abbreviations of random variable and random process, respectively. $s_{21,n}(f_m)$ is a frequency sample (i.e., data point) in the spectral RP, $S_{21}(f)$, whereas f_i and f_m are arbitrary frequencies for illustration purposes. It should be noted that f, f_i, and f_m are baseband frequencies since the S_{21}-parameter is in equivalent complex baseband representation. On the other hand, f_c is the CF (i.e., RF frequency) at which the S_{21}-parameter is measured.

Table 4.4: VNA settings of the 2nd-order spectral characteristics measurements.

VNA parameter (in order of priority)	**Setting**	
	Methodology	**VIRC prelim. inv.**
sweep type	frequency sweep	
center frequency	sweep for every freq. in $[f_c\|_{\min}, f_c\|_{\max}]$ *	see the second step of VIRC prelim. inv. in Table 4.2
trigger cycle (T_{trig})	$\geq T_{\text{coh}}\|_{\max}$	1.4 s
sweep duration (T_{swp})	$\leq T_{\text{coh}}\|_{\min}$	1.5 ms
IF bandwidth (IFBW)	min. that satisfies T_{swp} condition †	20 kHz
No. of sweeps (M)	$\geq z^2\varepsilon_f^{-2}\left(e-e^{-1}\right)^2+G$ #	500 §
span (BW)	$> B_{\text{coh}}$ ¶	30 MHz ‡
No. of points (N)	$\geq \text{BW}B_{\text{coh@37\%}}^{-1} r_f$ & #	27 ‡§

*The resolution of this frequency range can be chosen arbitrarily, i.e., independently from the rest of the VNA settings

†A smaller value to further lower the noise floor would automatically result in a VNA sweep duration longer than accepted.

&N is small enough to satisfy T_{swp} condition, but large enough to satisfy (4.6).

¶For CB estimation, a span that is greater than B_{coh} itself is sufficient.

‡A heuristic approach (like in Table 4.3) is followed to determine BW and N.

#It follows from (4.5) and/or (4.6), where e is Euler's number, ε_f is the desired relative width of the expected confidence interval of the estimated NFAF at $B_{\text{coh@37\%}}$, z is the z-score of this confidence interval given a desired confidence level, G is the number of groups that M is split into (i.e., number of estimates), $B_{\text{coh@37\%}}$ is the CB at which the NFAF drops to e^{-1}, and r_f is the required number of samples per $B_{\text{coh@37\%}}$.

§It follows from a 95%-confidence level, $G=4$ estimates, $z=1.96$, $|\varepsilon_f|<25\%$, and $r_f=4$ samples/$B_{\text{coh@37\%}}$.

- For each possible *configuration* in Table 4.2, M uncorrelated realizations are collected as depicted in Figure 4.4. Increasing M improves the estimation accuracy in terms of both bias and variability. To further increase the latter, yet at the expense of the former, the total M collected realizations are split into G groups, and from each of which the NFAF is estimated. The variability among the estimates is quantified by ε_f, which is defined as the relative width of the expected confidence interval [184] of the estimated NFAF at $B_{\text{coh@37\%}}$ and is given by

$$\varepsilon_f = \pm\frac{z}{\sqrt{G}}\frac{\sigma_{\hat{\rho}_f}}{\mu_{\hat{\rho}_f}}\times 100\% \tag{4.5}$$

where $\sigma_{\hat{\rho}_f}$ and $\mu_{\hat{\rho}_f}$ are, respectively, the expected standard deviation and

the expected mean of the estimated NFAF at $B_{\text{coh@37\%}}$; whereas z and G are defined in Table 4.4. According to [197, 198] and assuming the NFAF is bounded by an exponentially decaying function with frequency constant $B_{\text{coh@37\%}}$, then $\mu_{\hat{\rho}_f} = e^{-1}\left(1 - \frac{1}{2}\frac{1-e^{-2}}{D-1}\right) \approx e^{-1}\big|_{D>45}$ and $\sigma^2_{\hat{\rho}_f} = \left(1-e^{-2}\right)^2 (D-1)^{-1}$, where $D = M \div G$ is the number of collected realizations per group that M is split into.

- For CB estimation in NB systems, the VNA sweeps the frequency axis over a bandwidth that is greater than the CB itself according to Table 4.4. Moreover, when setting the VNA span (BW), it is worthwhile noting that the CB depends on the considered *configuration* in Table 4.2. For example, the CB is expected to increase as a result of loading the VIRC [159, 161, 199].

- The average number of frequency samples (i.e., data points) per CB is given by

$$r_f = N\frac{B_{\text{coh@37\%}}}{\text{BW}} \tag{4.6}$$

where N, $B_{\text{coh@37\%}}$, and BW are defined in Table 4.4. A lower bound has to be imposed such as $r_f \geq 4$ samples per $B_{\text{coh@37\%}}$. This is to guarantee a certain degree of spectral correlation among the adjacent frequency samples (i.e., data points) within each realization individually. Otherwise, such realizations would be meaningless [183] and, thereby, unreliable for FCF estimation.

- Like the aforementioned "chicken-egg" problem in CT estimation, a similar heuristic approach is followed here as well since both BW and N of the VNA depend on the CB as discussed in the previous two items.

- Similar to CT post-processing, the spectral realizations are up-sampled by a factor of 10 through linear interpolation, resulting in at least $10\,r_f = 40$ samples per $B_{\text{coh@37\%}}$ [190] to be used later in the estimation procedure. This is to improve the resolution of the CB estimates.

- Finally, it can be easily proved that the relative width of the expected confidence interval of the estimated CB is approximately equal to that of the estimated NFAF as long as the latter is less than 35%.

SECOND STEP: ESTIMATION PROCEDURE

For each possible *configuration* in Table 4.2, the NFAF is estimated from the corresponding G groups of uncorrelated collected realizations that are depicted in Figure 4.4, resulting in the G estimates[188, 197, 198],

$$\hat{\rho}_{f,n}(\Delta f) = \frac{\hat{\mathbb{C}}\left[s_{21,a_n:b_n}\left(-\frac{\text{BW}}{2}\right), s_{21,a_n:b_n}\left(-\frac{\text{BW}}{2}+\Delta f\right)\right]}{\hat{\mathbb{S}}\left[s_{21,a_n:b_n}\left(-\frac{\text{BW}}{2}\right)\right]\hat{\mathbb{S}}\left[s_{21,a_n:b_n}\left(-\frac{\text{BW}}{2}+\Delta f\right)\right]} \tag{4.7}$$

where $n \in \{1,2,...,G\}$; $\Delta f \in [0,\text{BW}]$ is the frequency offset at which $\hat{\rho}_f$ is evaluated; $a_n = 1+(n-1)D$; $b_n = nD$, $s_{21,a_n:b_n}(f)$ is the nth group of D collected realizations of

$S_{21}(f)$; BW is the VNA span; and the two unbiased estimators, $\hat{\mathbb{C}}$ and $\hat{\mathbb{S}}$, are the sample covariance and the sample standard deviation, respectively. The estimated CB for a specific *configuration* is defined to be the frequency offset at which the estimated NFAF from the corresponding measurement data drops to a certain desired threshold, TH. Equivalently, it is the minimum positive solution, $\hat{B}_{\text{coh@TH},n}$, of [192]

$$\left|\hat{\rho}_{f,n}(\hat{B}_{\text{coh@TH},n})\right| = \text{TH} \tag{4.8}$$

where $n \in \{1,2,...,G\}$. Finally, the sample mean (i.e., $\overline{X}$) is computed from the G estimates, (4.8), to obtain $\overline{\hat{B}}_{\text{coh@TH},n}$.

In EMC, a TH = 50% is commonly used [169] since $\hat{B}_{\text{coh@50\%}}$ represents the estimated average mode bandwidth of an RC under investigation [159, 161]. In this methodology, however, a TH $= e^{-1} \approx 37\%$ [187] is used to determine the frequency step setting, $B_{\text{coh}}|_{\text{max}}$, in the frequency-stirring (FS) technique that is adopted in the third investigation step. By definition, $B_{\text{coh}}|_{\text{max}}$ is the largest CB among all possible *configurations* of $(f_c,\ \omega,$ fully loaded$)$ in Table 4.2.

4.2.5. THIRD STEP: FIRST-ORDER CHARACTERISTICS

The FS technique, which is adopted in this investigation step, is commonly used in RCs as, e.g., in [168, 182] to improve the estimation accuracy [200], given the condition that the frequency samples (i.e., data points) within the same spectral realization are mutually uncorrelated [201]. According to the bias-variance trade-off [178], the improvement in the estimation accuracy can be obtained in terms of either variability [201] (in case of averaging) or bias [202] (in case of bundling). In this methodology, the former is opted in for by utilizing a moving-average filter (MAF).

In the following, both the measurement and the estimation procedures of the RR of the χ^2 GoF test for Rician distribution and the Rician K-factor are explained taking into consideration the different possible *configurations* of the three VIRC variables listed in Table 4.2. The adopted FS technique consists of two main steps: the first one has to do with the measurement procedure, whereas the second one has to do with the estimation procedure.

THIRD STEP: MEASUREMENT PROCEDURE

The measurement process of the S_{21}-parameter is depicted in Figure 4.5, and the corresponding method for setting the VNA is summarized in the second column of Table 4.5. Since some VNA settings are dependent on others, they are then listed in the table in order of priority. As the figure shows, this process is similar to that of the second-order spectral characteristics (see Figure 4.4). However, it is different in the following four items.

- The VNA sweeps the entire CF range from $f_c|_{\text{min}}$ to $f_c|_{\text{max}}$ in one go according to Table 4.5 and Figure 4.5.

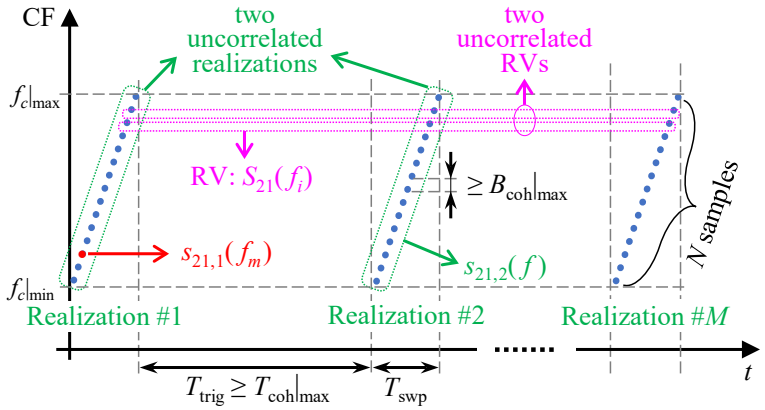

Figure 4.5: Measurement process of the S_{21}-parameter for the first-order characteristics. RV and RP are abbreviations of random variable and random process, respectively. $s_{21,n}(f_m)$ is a frequency sample (i.e., data point) in the spectral RP, $S_{21}(f)$, whereas f_i and f_m are arbitrary frequencies for illustration purposes. It should be noted that f, f_i, and f_m are baseband frequencies since the S_{21}-parameter is in equivalent complex baseband representation. On the other hand, f_c is the CF (i.e., RF frequency) at which the S_{21}-parameter is measured.

Table 4.5: VNA settings of the 1st-order characteristics measurements.

VNA parameter (in order of priority)	**Setting**	
	Methodology	**VIRC prelim. inv.**
sweep type	frequency sweep	
start frequency	$f_c\|_{\min}$	670 MHz ¶
stop frequency	$f_c\|_{\max}$	2740 MHz ¶
No. of points (N)	$(f_c\|_{\max} - f_c\|_{\min})\, B_{\text{coh}}^{-1}\|_{\max}$	100 ¶
trigger cycle (T_{trig})	$\geq T_{\text{coh}}\|_{\max}$	1.4 s
IF bandwidth (IFBW)	minimum VNA setting	20 kHz †
sweep duration (T_{swp})	set by IFBW	5.5 ms
No. of sweeps (M)	see Figure 4.6	10^4 §

¶See the third step of VIRC preliminary investigation in Table 4.2.
†A smaller value could have been used to further lower the noise floor.
§Given an unknown true K-factor = −35 dB and a 4-tap FS MAF, it follows from a 1.5 dB upper-limit on the expected bias of the estimated K-factor and from a 6.5 dB upper-limit on the width of the expected 95%-confidence interval of the estimated K-factor (see Third Step: Estimation Procedure of Rician K-Factor in Section 4.2.5).

- Since the estimation procedure in this step makes use of the FS technique, each spectral realization is then collected with N equidistant frequency samples (i.e., data points) that are separated by $B_{\text{coh}}\big|_{\text{max}}$ according to Table 4.5 and Figure 4.5. This is to guarantee the mutual uncorrelation among the spectral RVs.
- Since the frequency samples (i.e., data points) within the same realization are mutually uncorrelated (as a consequence of the previous item), the VNA sweep duration relative to the channel CT is irrelevant.
- Since the adopted K-factor estimator [186] is anticipated to suffer from a possibly significant expected bias, the considered CF range is then swept to extensively collect M realizations per *configuration*, as depicted in Figure 4.5 and justified later (when the estimation procedure of Rician K-factor is discussed). This is to improve the estimation accuracy in terms of bias before any attempt at improving it in terms of variability.

THIRD STEP: ESTIMATION PROCEDURE OF ALL FIRST-ORDER CHARACTERISTICS

The estimation procedure shares the following three items, the first two of which have been depicted in Figure 4.5 and justified earlier in the measurement procedure of Section 4.2.4.

- All collected realizations are mutually uncorrelated.
- All first-order characteristics are estimated from the complex S_{21}-parameter using ensemble averaging over the M collected realizations.
- After all estimates of the first-order characteristics are calculated, an FS MAF is applied over the adjacent frequency samples (i.e., data points). Thanks to the FS technique, this MAF improves the estimation accuracy in terms of variability within the FS bandwidth.

THIRD STEP: ESTIMATION PROCEDURE OF REJECTION RATE

Since the Rician channel represents the general case that encompasses both AWGN channels (K-factor $\rightarrow \infty$, i.e., no fading) and Rayleigh channels (K-factor $\rightarrow 0$, i.e., worst-case fading scenario), many theoretical studies of different wireless baseband algorithms (e.g., demodulators and decoders) are derived assuming a theoretical Rician distribution. Moreover, it is frequently reported in the literature (e.g., [67, 203–206]) that the CEH, in both urban (residential/forest-park) and suburban environments with both fixed and high-speed mobile wireless links, follows a theoretical Rician distribution for the frequency range 0.9 – 1.8 GHz. Additionally, a poor resemblance of the CEH with a theoretical Rayleigh distribution could be the result of a skew, a large K-factor, or a combination of both. Therefore, the investigation in this methodology regarding the CEH is performed in two steps. First, we consider whether—and to what extent—it resembles a theoretical Rician distribution, instead of Rayleigh. Then, we consider how small its K-factor is.

Miscellaneous GoF tests are available in the literature to quantify the aforementioned resemblance. For example, the Kolmogorov-Smirnov test is commonly used, however, it is not appropriate for RC measurements [185]. In [203], the Cramér-von Mises (CvM) test is used in the study case of an urban/suburban environment to investigate the resemblance of the measured CEH with the theoretical Rician, Rayleigh, Nakagami, and lognormal distributions. The Anderson-Darling (AD) test, on the other hand, is more sensitive to the extreme values of the distribution compared to the CvM test [185] since the former provides equal sensitivity at the tails as at the median [207]. This AD test is based on comparing a CDF with a hypothetical one [208], relying on a critical value that is analytically determined from the hypothetical CDF itself and from a desired significance level. Very recently, this test is used in [108] for the study case of a VIRC to investigate the resemblance of the CEH with a theoretical Rayleigh distribution.

Another GoF test that is commonly used is the χ^2 test, which is based on calculating an error function and comparing it to a hypothetical χ^2 distribution [207]. For example, this test is used for the study cases of CLRC and VIRC [107], in which the CEH is tested against a theoretical Rayleigh distribution. In [185], it is mentioned that the χ^2 test is not well adapted to the case of a continuous distribution, which is the case of RC measurements. However, the authors in [209] argued that the performance of the χ^2 test depends crucially on the way the data is binned. By proposing a binning method, they demonstrated that it is generally competitive and sometimes even superior to other tests, including the AD test. Additionally, in practical measurements, since the parameters of the estimated CDF are not known a priori, the χ^2 test is more suitable compared to the AD test since the latter requires the CDF to be completely specified [208].

To that end, the RR of the χ^2 GoF test for Rician distribution is adopted in this methodology along with the settings that are listed in Table 4.6. The RR is defined as the number of rejected null hypotheses to the total number of tests per *configuration* and is estimated from

$$\hat{R} = \left\langle \frac{1}{\eta} \sum_{n=0}^{\eta-1} D_{H_0}\{s_{21,a_n}, \ldots, s_{21,b_n}\} \right\rangle_{\text{FS}} \tag{4.9}$$

where $\langle\cdot\rangle_{\text{FS}}$ is the output of the FS MAF over the adjacent frequency samples

Table 4.6: Settings of the rejection rate and the χ^2 GoF test.

$\alpha = 5\%$ significance level, i.e., 95%–confidence level
$\eta = 10$ tests per *configuration*
$\gamma = M \div \eta = 1000$ data points per test per *configuration*
$\delta = 1 + \log_2 \gamma \approx 11$ bins for data pooling [209, 210]
$\gamma \div \delta \approx 91 \gg 5 =$ minimum expected count per bin [207]

(i.e., data points); $a_n = 1 + n\gamma$; $b_n = (1+n)\gamma$; η and γ are defined in Table 4.6; and D_{H_0} is the outcome of the test decision for the null hypothesis, H_0, that the measurement data set, $\{s_{21,a_n}, ..., s_{21,b_n}\}$, is drawn from a theoretical Rician distribution whose parameters are first estimated from the same data set itself using maximum-likelihood estimation.

THIRD STEP: ESTIMATION PROCEDURE OF RICIAN K-FACTOR

Several estimators are available in the literature to quantify the Rician K-factor of measured channels (e.g., [211–215]). Most of them rely solely on either the envelope, the phase, or the power of the received signal. They can be categorized into either Rician PDF fitting or moment-based estimators. On the other hand, the commonly used complex-envelope-based estimator [186, eq. (31)] is adopted in this methodology since it outperforms the other estimators in terms of both bias and variability [216, 217]. This is especially true for very small values of the K-factor.

That being said, however, the expected bias between the estimated K-factor (denoted by $\hat{K}$) and the true one (denoted by K) can be as large as multiple decibels if the sample size, M, is not large enough, as Figure 4.6(a) indicates [186]. Therefore, to be able to estimate an unknown K-factor as low as, e.g., -35 dB with an expected bias, e.g., smaller than 1.5 dB, a sample size of $M = 10^4$ is required.

Increasing the sample size also improves the estimation accuracy in terms of variability [186]. However, given $M = 10^4$ and $K\big|_{\text{dB}} = -35$ dB, the width of the expected 95%-confidence interval (denoted by $\text{CI}_{95\%}$) of the estimated bias is shown in Figure 4.6(b) to be much larger than 10 dB. Therefore, after the estimation accuracy has been mainly addressed in terms of bias, a further much-needed improvement in terms of variability is considered as follows. The FS technique is put in use with a 4-tap MAF resulting in an expected confidence interval whose width is less than 6.5 dB for $K\big|_{\text{dB}} \geq -35$ dB, as Figure 4.6(c) indicates. A MAF with a number of taps greater then 4 is not recommended as the channel true statistics would then not stay approximately constant within the FS bandwidth [182, 188].

The K-factor is estimated using the following adopted biased estimator [186, eq. (31)]:

$$\hat{K} = \left\langle \frac{|\overline{S_{21}}|^2}{|S_{21} - \overline{S_{21}}|^2} \right\rangle_{\text{FS}} \tag{4.10}$$

where $\langle\cdot\rangle_{\text{FS}}$ is the output of the FS MAF over the adjacent frequency samples (i.e., data points) and $\overline{S_{21}}$ is the sample mean of S_{21}. Equation (4.10) assumes a noiseless channel[3] with no prior knowledge about the stirred/unstirred components. It is worth mentioning that since the autocovariance function is used in the estimation of the CT instead of the autocorrelation, $\overline{\hat{T}}_{\text{coh@TH}}$ is independent from $\hat{K}$.

[3] In Section 4.3 as well as in Chapter 5, this assumption is approximately valid since the average signal-to-noise ratio of all of the conducted measurements is greater than 30 dB.

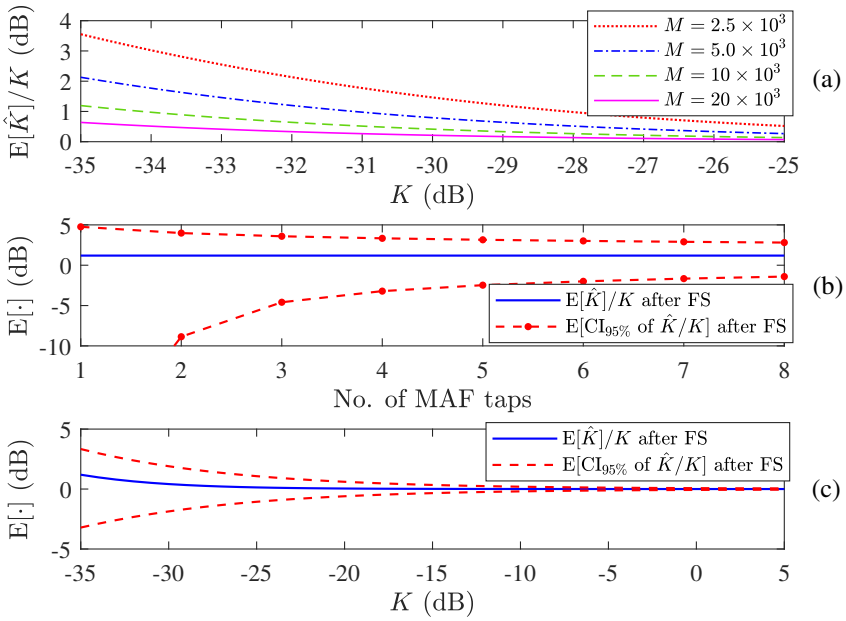

Figure 4.6: Performance of the adopted K-factor estimator [186]. (a) The expected bias versus the true K-factor for different sample sizes before FS. (b) The expected bias and the expected 95%-confidence interval of the estimated bias versus the number of taps of the FS MAF given $M = 10^4$ and $K\big|_{\text{dB}} = -35\,\text{dB}$. (c) The expected bias and the expected 95%-confidence interval of the estimated bias versus the true K-factor after FS given $M = 10^4$ and a 4-tap FS MAF.

4.3. PURPOSE OF PRELIMINARY INVESTIGATION

To increase the modal overlap in the RC [218], the practice of adding an absorber (i.e., slight loading) is commonly followed. Moreover, an RC calibration (as, e.g., in [219]) is sometimes necessary before the RC itself is utilized in a measurement application. Such calibration and loading procedures may impact the dynamic range of the OTA characteristics under investigation. Thus, before a thorough VIRC characterization is carried out in the next chapter, a preliminary investigation which involves a slight preloading of the VIRC is first conducted in the following sections. Therefore, the same framework (i.e., channel and VIRC setups) is used in the preliminary investigation of this chapter and later in the thorough characterization of Chapter 5.

By following the proposed methodology as described in Section 4.2, measurements of the S_{21}-parameter are collected. Next, estimations of the first-order characteristics,

namely, $\hat{R}$ and $\hat{K}$, are calculated for two cases: before and after the VIRC preloading. The objective of the preliminary investigation is to examine whether this slight preloading is necessary—and to what extent it is successful—so that the CEH of the propagation channel inside the VIRC resembles a theoretical Rayleigh distribution.

In the following sections, the structure of the VIRC under investigation as well as the components of the channel inside are described and justified. Additionally, the settings of the measurement setup of both the VIRC variables and the VNA are also listed. Next, the measurement results of the preliminary investigation (i.e., before and after the preloading) are presented and analyzed.

4.4. MEASUREMENT SETUP

A schematic illustration of the framework (i.e., channel and VIRC setups) is shown in Figure 4.1, which depicts a SISO channel between two antennas inside the VIRC. An Agilent N5230A is used to measure the aggregate S_{21}-parameter of the two antennas and the channel in between.

In the following subsections, the structure of the VIRC under investigation as well as the components of the channel inside are described and justified. Additionally, the settings of the measurement setup of both the VIRC variables and the VNA are also listed.

4.4.1. VIRC SETUP

The VIRC is located at the lab of the Power Electronics & EMC research group at the University of Twente. An exterior view of the VIRC with dimensions 1.0 m × 1.2 m × 1.5 m is shown in Figure 4.7. Its walls are made of a copper fabric which delimits the volume of the chamber. Moreover, its front wall is fixed to a metal frame to which a hatch is attached. The rest of the fabric is tied only with strings and springs to the frame. Their purpose is to maintain the rectangular geometry while providing enough flexibility to ensure unrestrained operation of the dc motors shown in Figure 4.7.

Each motor has an arm that pulls the flexible fabric, causing it to wrinkle on the whole surface. As a result, different boundary conditions for the resonant field within the chamber are continuously created. One of the motors is attached to the corner of the VIRC. In this way, all of the three walls are directly engaged in the stirring while maintaining the average volume of the chamber. This motor also pseudo-randomly changes its direction every 0.2–2.0 s. This causes the fabric to wrinkle differently each time. Along with a continuously rotating second motor, such a VIRC setup ensures that all five walls simultaneously vibrate. This positively contributes to the effectiveness of the stirring mechanism by continuously creating unpredictably new boundary conditions for a long time [107, 108].

Since motors with no position tracking are used, and the fabric wrinkles unpredictably due to momentum and air pressure, the exact boundary conditions are not directly

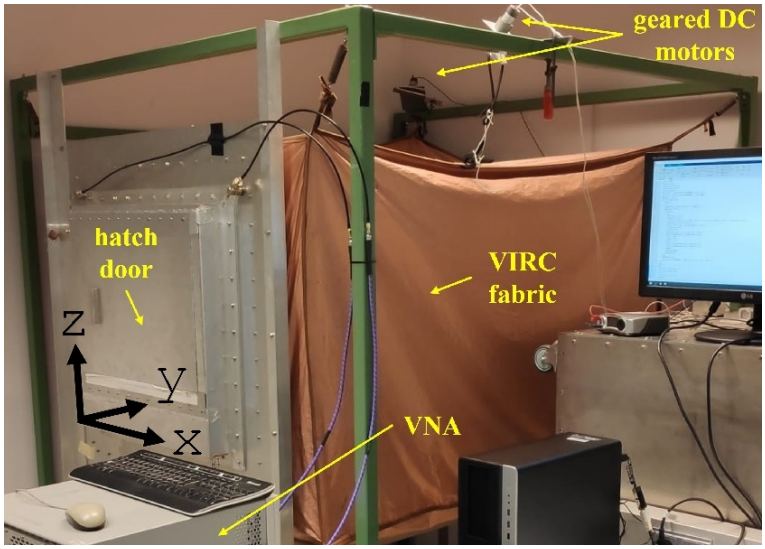

Figure 4.7: Measurement setup.

reproducible at will, but only in a statistical sense. Therefore, due to this ignorance, the stirring of the electromagnetic (EM) fields inside the VIRC seems random to the observer. The source of randomization can be attributed to the following three factors: the pseudo-randomly rotating motor, the random initial positions of both motor arms, and the random fabric wrinkling.

The RS of the motors is controlled by a variable DC power supply. The peak-to-peak displacement of the VIRC walls along the surface norm (a.k.a. shaking amplitude [173, 220]) depends on the RS of the DC motors due to the inertia effect. The maximum shaking amplitude at the center of the wobbling walls is measured to be roughly 10 cm and 13 cm for 19.4 r/min and 42.9 r/min, respectively.

4.4.2. CHANNEL SETUP

An interior view of the VIRC is shown in Figure 4.8. Two identical broadband omni-directional antennas are adopted. They comprise an intrinsic part of the propagation channel to be characterized. As the figure shows, they are carried on a polystyrene foam testbed, which itself is attached solely to the front wall. The matching efficiency of the two identical antennas is plotted in Figure 4.10. Furthermore, two LCs are considered: unloaded and loaded. For the latter case, the VIRC can be seen loaded with two 1×6 pyramidal carbon foam absorbers whose dimensions are $30\,\text{cm} \times 10\,\text{cm} \times 60\,\text{cm}$ (H × W × L).

The top and side views of the layout inside the VIRC are depicted in Figure 4.9. Mainly two unstirred components (UCs) are anticipated and denoted by UC_1 and UC_2. The former is the line-of-sight (LoS) component, whereas the latter is a static

Figure 4.8: Channel setup inside the VIRC.

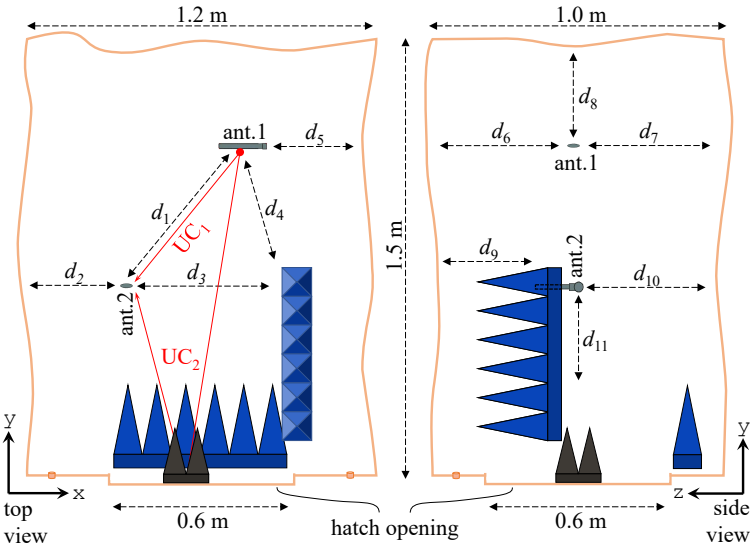

Figure 4.9: Top and side views of the layout inside the VIRC in the loaded condition.

reflection from the hatch. To achieve a very small K-factor in RCs, the direct coupling (i.e., UC_1) between the two antennas has to be minimized as well as their separation distance has to be maximized [159, eq. (13)]. For the former case, the two antennas are cross-polarized [159, 167]. For the latter case, however, a minimum distance of a quarter wavelength between each antenna and a nearby boundary condition should still be respected. In this framework, we opt in for a separation

distance of at least a half wavelength for all cases, i.e., $d_i \geq d_{\min} = \frac{1}{2} c/f_c|_{\min}$.

Thanks to the structure and the stirring mechanism of the VIRC, the adoption of such non-directional antennas will still produce the highly desirable well-stirred EM fields. This is true since all walls of the VIRC (except for the front wall) vibrate and, thereby, contribute to the stirring process. On the contrary, utilizing a CLRC with non-directional antennas would result in up to seven relatively significant unstirred components (one from each wall plus the LoS component) and, thereby, severely degrade the overall stirring effectiveness.

4.4.3. VIRC VARIABLES AND VNA SETTINGS

The objective of the next chapter is to characterize the VIRC for OTA testing of NB systems by following the methodology proposed in Section 4.2. Therefore, since this section is part of a preliminary investigation for the next chapter, the VIRC variables that are considered in the first two investigation steps in this chapter are determined accordingly[4], as listed in Table 4.2. Moreover, since the preliminary investigation is only concerned with estimating the RR and the K-factor, the focus of the preliminary investigation during the first and the second investigation steps is limited to estimating only $T_{\text{coh}}|_{\max}$, $T_{\text{coh}}|_{\min}$, and $B_{\text{coh}}|_{\max}$ (see Figure 4.2).

The VNA settings during each of the three investigation steps are given in the third column of Tables 4.3, 4.4, and 4.5 in accordance with the measurement procedures explained in Sections 4.2.3, 4.2.4, and 4.2.5, respectively.

4.5. MEASUREMENT RESULTS AND ANALYSIS

Before the preloading, the measurements of the S_{21}-parameter are conducted to estimate the RR of the channel inside the VIRC for 11 CFs in the frequency band of 670 – 2740 MHz. As a reference, a simulation-based Rician distribution generator (with the same $\hat{K}$ and the same estimation procedure of the RR as of the channel under investigation) has an $\hat{R}$ of up to 20%.

As can be seen in Figure 4.11 (before the preloading), all CFs below 1500 MHz have a high $\hat{R}$ that is well above the 20% reference. A further investigation performed by plotting the empirical PDF and CDF (at 868 MHz and 1055 MHz) in Figure 4.13 reveals a deviation from the fit to the theoretical Rician distribution whose parameters are estimated from the corresponding measurement data using maximum-likelihood estimation. This deviation can be attributed to a limited mode density [221], but also to imperfections of the channel setup, i.e., the low matching efficiency of the utilized antennas [222].

In [107], it is shown that slightly loading a VIRC with an absorber decreases its Q-factor and, thereby, broadens the resonance bandwidths. This consequently

[4] In Chapter 5, the considered VIRC variables are [670 – 2740] MHz, [19.4 – 42.9] r/min, and {unloaded, loaded} for CF, RS, and LC, respectively. This CF range contains the two ISM bands, namely, 868 MHz and 2.4 GHz, which makes it beneficial to LPWANs as well.

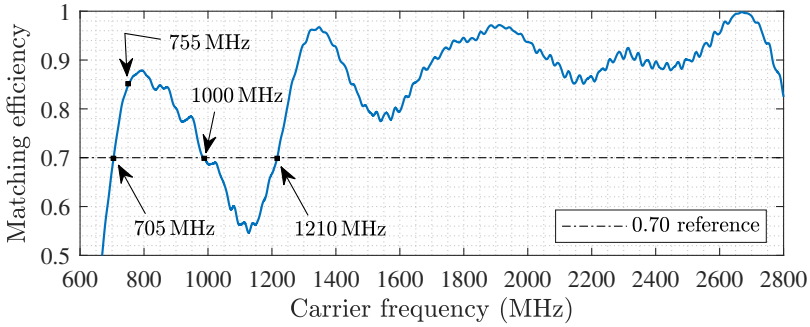

Figure 4.10: Matching efficiency of the utilized antennas measured in the anechoic chamber. It is defined as $1-|S_{11}|^2$ according to [159, 223], where S_{11} is the antenna return loss.

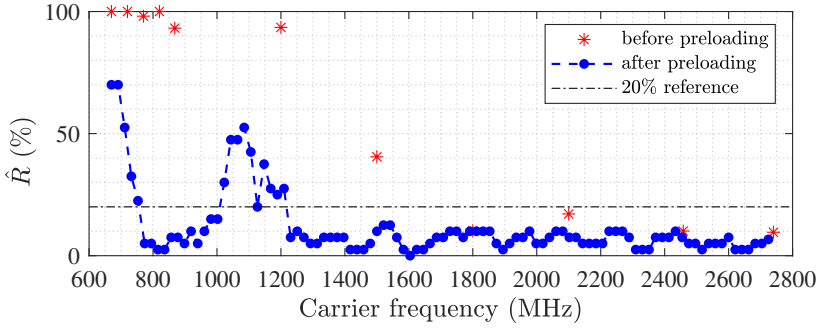

Figure 4.11: Estimated rejection rate versus carrier frequency for the unloaded VIRC before and after the slight preloading.

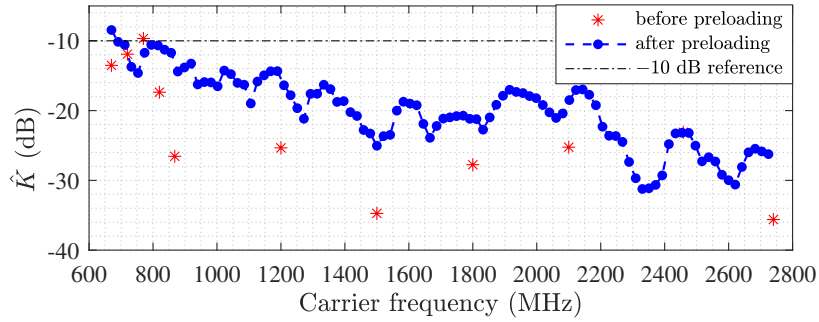

Figure 4.12: Estimated K-factor versus carrier frequency for the unloaded VIRC before and after the slight preloading.

increases the modal overlap and ensures a better fit to the theoretical Rician distribution [224], i.e., a lower RR. On the other hand, care needs to be taken

not to overload the chamber with absorbers, which can have negative effects on its reverberation properties [225]. To that end, the VIRC is slightly preloaded by mounting an absorber on the internal side of the hatch (as can be seen in Figure 4.15 and depicted in Figure 4.9) while respecting the aforementioned minimum distance, d_{min}, from the antennas.

The reason behind choosing the hatch to mount the absorber on can be justified as follows. It is well established [167] that loading an RC causes its K-factor to become larger. Moreover, as depicted in Figure 4.9, the non-LoS unstirred component, UC_2, contributes to the K-factor increase. Hence, mounting an absorber on the hatch (where UC_2 is reflected from) lowers the RR [224] as can be seen from Figure 4.11 (after the preloading). At the same time, this will—to a large extent—not sacrifice the K-factor of the channel (see Figure 4.12). It should be noted that in this preliminary investigation, the aforementioned slight preloading is not referred to as "loaded" in the context of LC.

After the preloading, the measurements of the S_{21}-parameter are repeated following the VIRC variables listed in Table 4.2, as well as following the VNA settings listed in Tables 4.3, 4.4, and 4.5. The measurement results of the first two investigation steps are summarized in Table 4.7. They are mainly used for the measurement settings of the last investigation step concerning the estimation of the RR and the K-factor (see Figure 4.2). It is worth noting that the relative width of the estimated confidence

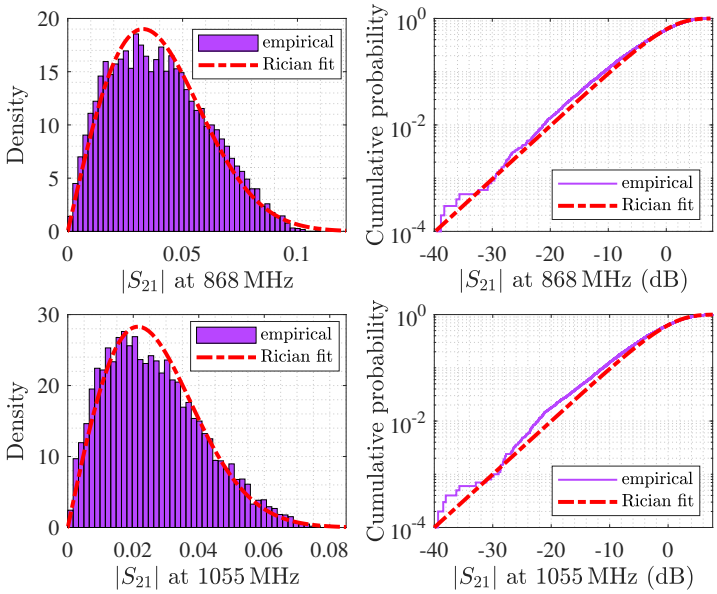

Figure 4.13: Empirical PDF and CDF of $|S_{21}|$ for the unloaded VIRC at 868 MHz and 1055 MHz before the slight preloading.

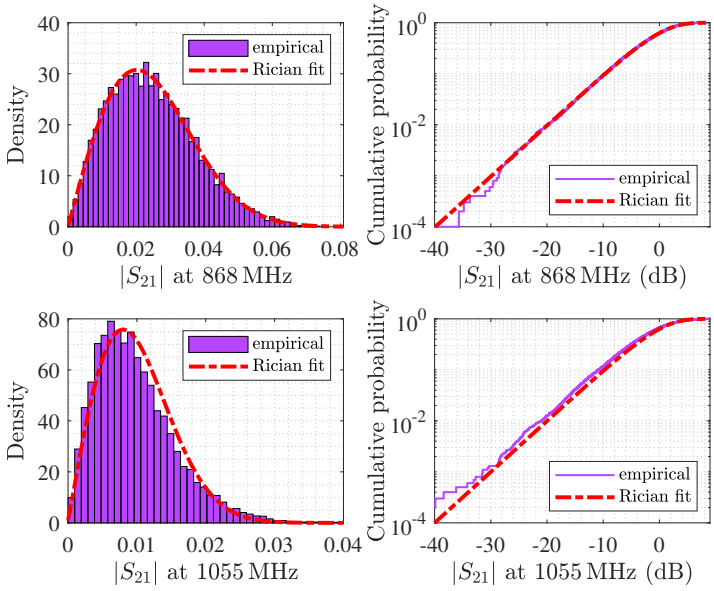

Figure 4.14: Empirical PDF and CDF of $|S_{21}|$ for the unloaded VIRC at 868 MHz and 1055 MHz after the slight preloading.

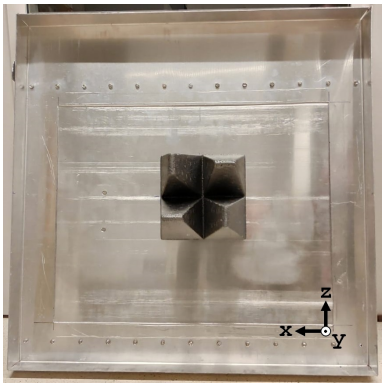

Figure 4.15: RF absorber mounted on the internal side of the VIRC hatch as a slight preloading. It is a 2 × 2 pyramidal carbon foam absorber whose dimensions are 20 cm × 16 cm × 16 cm (H × W × L).

Table 4.7: Measurement results of the first two investigation steps after the slight pre-loading.

	First step		**Second step**
Configuration	(670 MHz, 19.4 r/min, loaded)	(2740 MHz, 42.9 r/min, unloaded)	(f_c, ω, loaded)
Characteristic	$T_{\text{coh}}\big\|_{\text{max}}$	$T_{\text{coh}}\big\|_{\text{min}}$	$B_{\text{coh}}\big\|_{\text{max}}$
Estimation	330 ms	5.7 ms	20.7 MHz
$\hat{\varepsilon}$ †	±1.5%	±4.3%	±9.9%

†The relative width of the estimated confidence interval of the estimated coherence time (or coherence bandwidth).

intervals (reported in the last row of Table 4.7) are all below their corresponding desired expected values, which are mentioned in Tables 4.3 and 4.4.

Because of the preloading, a K-factor increase of up to 12 dB can be observed at 868 MHz in Figure 4.12. Nevertheless, in most of the CF range under interest (i.e., above 820 MHz), $\hat{K}$ is still well below −10 dB. However, the CF range 1000 – 1210 MHz has a very high $\hat{R}$ even after the preloading (see Figure 4.11), which is evident from the visible persistent skewness at 1055 MHz compared to 868 MHz (see Figure 4.14). As reasoned in [222], this can be attributed to the two utilized antennas of the measurement setup since they have a matching efficiency less than 0.70 within the said frequency range, as Figure 4.10 shows. Moreover, the low CFs up to 755 MHz also exhibit an $\hat{R}$ above 20%, which in fact is mainly due to a limited mode density, as reasoned in [221], since the matching efficiency of the two antennas is above 0.70 within the frequency range 705 – 755 MHz (see Figure 4.10).

4.6. CONCLUSION

In this chapter, a systematic measurement and estimation methodology was developed for the empirical investigation of the first- and second-order temporal and spectral characteristics of an NB SISO channel inside the VIRC. The methodology was devised to be universal to any RC as long as the mode-stirring technique is put in use. It was also devised to take into consideration a desired estimation accuracy as well as the effect of different CFs, RSs, and LCs. As a proof-of-concept for the proposed methodology and before the VIRC itself is fully characterized, and a preliminary investigation following the procedures described in this chapter was carried out to estimate the RR and the K-factor before and after a slight preloading of a VIRC under investigation.

It was shown that the measurement accuracy of the CT and the CB are in agreement with the expected values from theory. Moreover, by analyzing the measurement results of the preliminary investigation, a considerable skewness was demonstrated between the theoretical Rician distribution and the CEH before preloading. Additionally, it was demonstrated that the suggested slight preloading of the VIRC, by mounting an RF absorber on the internal side of the hatch, significantly decreases $\hat{R}$ without increasing $\hat{K}$ above −10 dB over the frequency range 755 – 2740 MHz. However, the frequency range 1000 – 1210 MHz, in which the matching efficiency of the utilized antennas is below is 0.7, has an $\hat{R}$ that is above 20% in spite of the slight preloading. Therefore, after the suggested slight preloading, a near-Rayleigh channel could indeed be achieved inside the VIRC under investigation with a Rician K-factor below −11 dB in the frequency range 755 – 1000 MHz and 1210 – 2740 MHz in general, and with a Rician K-factor below −23 dB in the 2.4 GHz band in particular.

In the next chapter, various characteristics of the propagation channel inside the VIRC are thoroughly and jointly investigated with respect to the VIRC operating variables with emphasis on the 2.4 GHz band.

5

VIRC CHARACTERIZATION AND MODELING

5.1. INTRODUCTION

Typically, over-the-air (OTA) testing and electromagnetic compatibility (EMC) measurements are performed in shielded rooms to isolate them from the ambient interference. Furthermore, especially at high frequencies, such rooms are modified to create an environment suitable for the desired test. On the one hand, lining the room with absorbers creates an anechoic chamber that emulates a free-space environment necessary, e.g., for the measurement setups of antenna characterization [226] and wireless coexistence [113]. On the other hand, a resonating and electrically large room creates a reverberation chamber (RC) that emulates a rich multipath environment. Such a chamber has been used mainly in EMC to conduct radiated immunity and radiated emission measurements [104]. In the last two decades, RCs have become an indispensable OTA-testing tool in research and development as well as in the certification of wireless devices [105].

Because the RC is a controlled experimental environment with well defined propagation characteristics, using it to conduct OTA testing guarantees the bare-minimum requirement for repeatability [102]. This is contrary to RF drive/walk testing in real-world environments, which—in addition to being not repeatable—is labor intensive, time consuming, and costly [102]. From the standpoint of OTA, the work in the literature concerning the RC can be categorized into two main groups.

- *The characterization of the propagation channel inside the RC* is considered, e.g., in [159, 161, 162, 167, 227–229]. Table 5.1 summarizes the first- and second-order temporal and spectral characteristics of the wireless propagation channel. It also gives examples of why these characteristics are crucial for wireless system design.

Parts of the content of this chapter are in submission [115].

- *The testing of the wireless system performance metrics in the RC* includes, e.g., bit-error-rate, packet-error-rate, and throughput measurements; total isotropic sensitivity, average fading sensitivity, and total radiated power measurements; and antenna radiation and total efficiency measurements [230]. Moreover, this group can be further categorized into three sub-groups.
  - *OTA testing of wireless baseband algorithms.* See, e.g., [164, 231, 232].
  - *OTA-based antenna measurements.* See, e.g., [233–235].
  - *OTA testing of wireless devices* (i.e., wireless baseband algorithms and antennas combined). See, e.g., [71, 98, 160, 236].

Traditionally, RCs have been classically designed as rectangular cuboids with rigid metallic walls, which are commonly known as classical reverberation chambers (CLRCs). Instead, we focus here on a variation of the RC, known as the Vibrating Intrinsic Reverberation Chamber (VIRC) [106]. In addition to the advantages of *in-situ* testing as well as cost efficiency, it has been shown that the VIRC can exhibit a performance comparable to that of the CLRC of a similar size [107, 173, 237]. Also, it may even offer a shorter measurement time and a larger number of uncorrelated samples [107, 108], e.g., to empirically estimate the extreme field strengths. Additionally, it potentially provides a better field uniformity that is useful for EMC testing according to [179]. To that end, it is considered a potentially attractive alternative for OTA as well.

The investigation of the VIRC has been conducted in several studies in terms of various characteristics [107, 108, 171–177]: field uniformity, lowest usable frequency, field statistical distribution, Q-factor, Rician K-factor, frequency autocorrelation function, average mode bandwidth, time autocorrelation function, decorrelation time, and number of collectable independent samples. However, the aforementioned work in the literature concerning the VIRC has—at least—one of the following drawbacks.

- The investigation of the VIRC characteristics does not follow a systematic measurement methodology, as argued in—and hence the objective of—the previous chapter. Therefore, the estimation of the VIRC characteristics might exhibit significant inaccuracies in terms of both bias and variability.
- The VIRC characteristics are not jointly and/or thoroughly investigated with respect to the VIRC variables: carrier frequency (CF), rotational speed (RS) of the VIRC motors (or other stirring mechanism), and VIRC loading condition (LC). Therefore, the relative behaviour of the VIRC characteristics cannot be reliably deduced.
- Because of the previous point, no mathematical models that describe the joint behaviour of the VIRC characteristics with respect to the VIRC variables are available. Such models are essential to correctly configure the VIRC variables in order to accurately emulate a desired channel characteristic under interest.

Table 5.1: Summary of propagation channel characteristics and their relevance to wireless system design.

		Channel characteristic [¶]	Example of its impact on system design
First-order		**probability distribution function (PDF)**	
	✓	rejection rate for Rician distribution	-
	✓	K-factor of Rician distribution	fading margin in narrowband systems [192]
	✓	channel gain	link budget calculations [192]
Second-order spectral	✓	**frequency correlation function (FCF)**	
		power delay profile (PDP)	channel equalizer design in wideband systems [192]
	✓	coherence bandwidth (CB)	maximum signaling rate in narrowband systems [192]
		rms delay spread	pilot spacing in OFDM systems [196]
		maximum excess delay	cyclic prefix interval in OFDM systems [238]
Second-order temporal		**time correlation function (TCF)**	
	✓	Doppler spectral density (DSD)	-
	✓	coherence time (CT)	how often pilot signals are sent [189]
	✓	Doppler spread	subcarrier spacing in OFDM systems [164]
		level crossing rate	buffer depth of adaptive modulation schemes [67]
		average fade duration	frame length in coded packetized systems [67]

[¶]Only the ticked characteristics in this table are considered in this chapter.

In this chapter, the objective is to investigate the feasibility of using the VIRC as a channel emulator that is capable of accurately and easily emulating a wide dynamic range for the Doppler spread (or coherence time) and the Rician K-factor. The scope of the investigation is for the OTA testing[1] of wireless baseband algorithms in narrowband (NB) single-input single-output (SISO) systems, as in low-power wide-area networks (LPWANs) in general and UNB (this thesis) in particular. Therefore, as a basis for the development of the aforementioned channel emulator, a simple and cost-effective framework[2] is assembled which is capable of both providing a near-Rayleigh channel as well as supporting the 868 MHz and 2.4 GHz ISM bands. The main contribution of this chapter is, thereby, applying the systematic methodology proposed in the previous chapter in a thorough, joint and empirical characterization of the VIRC in terms of the channel first- and second-order temporal and spectral characteristics (see Table 5.1) with respect to the VIRC variables: CF, RS, and LC. Next, we propose a number of mathematical models to fit the behavior of the following characteristics: coherence time on the one hand versus CF and RS on the other, Doppler spectrum, frequency autocovariance function, K-factor versus RS, and channel gain versus CF. Then, we demonstrate the generality of the aforementioned models as well as briefly illustrate their potential usability for both EMC and OTA testing. Finally, based on the gained insights, we examine the feasibility of using the VIRC as a channel emulator for the deployment of the UNB signaling scheme in the 2.4 GHz band.

This chapter is organized as follows. The methodology and the measurement setup are briefly described in Section 5.2. In Section 5.3, the measurement results are presented, analyzed and discussed, in which various mathematical fitting models are proposed. Section 5.4 discusses the validity of the statistical method as well as demonstrates the generality and the potential usability of these models. The feasibility of using the VIRC as a UNB channel emulator is examined in Section 5.5. Finally, a conclusion is given at the end of this chapter.

5.2. METHODOLOGY AND MEASUREMENT SETUP

The empirical characterization in this chapter follows the measurement and estimation methodology as well as the measurement setup presented in Chapter 4. Therefore, to avoid repetition, the following subsections will mostly discuss the additional characteristics, estimations, concepts, and settings that are further needed for the thorough characterization of the VIRC in this chapter.

[1] Given the equivalence between EMC and OTA characteristics in Table 4.1, the investigation is also fully applicable for EMC. This is useful to better understand the statistical properties as well as to fully utilize the potential capabilities of this unique environment for both EMC and OTA testing.

[2] The framework is comprised of both the VIRC setup and the channel setup inside it.

5.2.1. MEASUREMENT AND ESTIMATION PROCEDURES[3]

The methodology is comprised of three investigation steps, each of which is concerned with a different order and/or category of channel characteristics. Each of these steps considers the effect of three VIRC variables: CF (denoted by f_c), RS (denoted by ω), and LC (loaded/unloaded). Throughout this chapter, any unique combination of values of these variables is referred to as a *configuration*. They are summarized in Table 5.2 for each of the three investigation steps individually.

FIRST INVESTIGATION STEP: SECOND-ORDER TEMPORAL CHARACTERISTICS

For each possible *configuration* in Table 5.2, the normalized time autocovariance function (NTAF) and the coherence time (CT) are estimated from M uncorrelated realizations using (4.3) and (4.4), respectively, resulting in M estimates for both. Using the estimated CT ($\hat{T}_{\text{coh@37\%},n}$) from (4.4), the Doppler spread is estimated as follows [55, 163]:

$$\hat{\nu}_{D,n} = 1/\hat{T}_{\text{coh@37\%},n} \tag{5.1}$$

where $n \in \{1,2,...,M\}$. Similarly, for each possible *configuration* in Table 5.2, the Doppler spectrum is estimated using Bartlett's method (a.k.a. method of averaged periodograms) from M uncorrelated realizations, resulting in the M estimates [181]:

$$\hat{\mathcal{L}}_n(\nu) = \frac{1}{L}\sum_{i=1}^{L}\left|\sum_{k=0}^{\frac{N}{L}-1} s_{21,n,i}(k\Delta t)\exp(-j2\pi\nu k)\right|^2 \tag{5.2}$$

where $n \in \{1,2,...,M\}$, ν is the Doppler frequency; $L = 5$ is a segmentation factor; $\Delta t = T_{\text{swp}} \div N$; T_{swp} is a variable VNA sweep duration which depends on the considered *configuration*; N is the number of time samples (i.e., data points) in $s_{21,n}(t)$; and $s_{21,n,i}(t)$ is the ith segment of the nth collected realization, $s_{21,n}(t)$, of the temporal random process, $S_{21}(t)$. Finally, the sample mean (i.e., $\overline{X}$) is computed from (4.4), (5.1), and (5.2) using M estimates to obtain $\overline{\hat{T}}_{\text{coh@37\%}}$, $\overline{\hat{\nu}}_D$, and $\overline{\hat{\mathcal{L}}}(\nu)$, respectively.

The longest CT of the slowest-fading case scenario, $T_{\text{coh}}|_{\text{max}}$, is defined for a threshold $= e^{-1} \approx 37\%$ and corresponds to the following configuration: $(f_c|_{\text{min}}, \omega|_{\text{min}},$ fully loaded VIRC). On the other hand, the shortest CT of the fastest-fading case scenario, $T_{\text{coh}}|_{\text{min}}$, is defined for a more-conservative threshold $= 90\%$ and corresponds to the following configuration: $(f_c|_{\text{max}}, \omega|_{\text{max}},$ unloaded VIRC). In the next two investigation steps, $T_{\text{coh}}|_{\text{min}}$ and/or $T_{\text{coh}}|_{\text{max}}$ are essential (see Figure 4.2).

[3] To avoid repetition, the reader is encouraged to refer to Section 4.2

Table 5.2: VIRC variables and their considered *configurations*.

Section	Carrier frequency (MHz)	Rotational speed (r/min)	Loading condition
5.3.1	{868, 2458}	{19.4, 21.4, 24.8, 28.3, 32.1, 35.9, 39.5, 42.9}	unloaded
	{670, 720, 770, 820, 868, 1200, 1500, 1800, 2100, 2458, 2740}	{19.4, 28.3, 42.9}	unloaded
	{868, 2458}	{19.4, 28.3, 42.9}	loaded
5.3.2	{670, 720, 770, 820, 868, 1200, 1500, 1800, 2100, 2458, 2740}	{19.4, 28.3, 42.9}	unloaded
	{670, 720, 770, 820, 868, 1200, 1500, 1800, 2100, 2458, 2740}	{19.4, 28.3, 42.9}	loaded
5.3.3	[670–2740]	{19.4, 21.4, 24.8, 28.3, 32.1, 35.9, 39.5, 42.9}	unloaded
	[670–2740]	{19.4, 28.3, 42.9}	loaded

SECOND INVESTIGATION STEP: SECOND-ORDER SPECTRAL CHARACTERISTICS

For each possible *configuration* in Table 5.2, the normalized frequency autocovariance function (NFAF) and the coherence bandwidth (CB) are estimated from $G = (M \div D)$ groups of uncorrelated realizations using (4.7) and (4.8), respectively, resulting in G estimates for both, where M is the total number of collected realizations whereas D is the number of realizations per group that M is split into. Finally, the sample mean (i.e., $\overline{X}$) is computed from (4.7) and (4.8) using G estimates to obtain $\overline{\hat{\rho}}_f$ and $\overline{\hat{B}}_{\text{coh@37\%}}$, respectively.

The largest CB, $B_{\text{coh}}\big|_{\text{max}}$, among all possible *configurations* of $(f_c,\ \omega,$ fully loaded VIRC$)$ is defined for a threshold $= e^{-1} \approx 37\%$. $B_{\text{coh}}\big|_{\text{max}}$ is essential for the frequency-stirring (FS) moving-average filter (MAF) in the next investigation step. On the other hand, the smallest CB, $B_{\text{coh}}\big|_{\text{min}}$, among all possible *configurations* of $(f_c,\ \omega,$ unloaded VIRC$)$ is defined for a more-conservative threshold $= 90\%$. Given the scope of this chapter, $B_{\text{coh}}\big|_{\text{min}}$ is used to determine the upper limit on the signaling rate of NB systems for OTA testing in the VIRC. By definition, an NB system experiences flat fading when it is deployed in an intended real-world environment. Thus, such an NB system will experience the desired flat fading when it is tested in the VIRC as long as its signaling rate is less than $B_{\text{coh}}\big|_{\text{min}}$.

THIRD INVESTIGATION STEP: FIRST-ORDER CHARACTERISTICS

For each possible *configuration* in Table 5.2, the rejection rate (RR) of the chi-squared (a.k.a. χ^2) goodness-of-fit test for the Rician distribution and the Rician K-factor are estimated from M uncorrelated realizations using (4.9) and (4.10), respectively. Similarly, for each possible *configuration* in Table 5.2, the channel gain (a.k.a. average power transfer level) is estimated from M uncorrelated realizations using the following unbiased estimator [168]:

$$\hat{G} = \left\langle \overline{|S_{21}|^2} \right\rangle_{\text{FS}} \tag{5.3}$$

where $\langle\cdot\rangle_{\text{FS}}$ is the output of the FS MAF over the adjacent frequency samples (i.e., data points) and $\overline{S_{21}}$ is the sample mean of S_{21}.

5.2.2. VIRC SETUP AND CHANNEL SETUP[4]

The VIRC under investigation is depicted in Figure 4.1 and shown in Figure 4.8. According to the preliminary investigation in Section 4.3 in the previous chapter, the VIRC under investigation is slightly preloaded to lower the RR of its channel envelope histogram (CEH). As can be seen in Figure 4.15, the interior side of the hatch carries a 2×2 pyramidal carbon foam absorber whose dimensions are $20\,\text{cm} \times 16\,\text{cm} \times 16\,\text{cm}$ (H × W × L). It should be noted that this slight preloading is not referred to as "loaded" in the context of LC. The matching efficiency of the utilized antennas is depicted in Figure 5.1.

[4]To avoid repetition, the reader is encouraged to refer to Section 4.4

5.2.3. VIRC VARIABLES AND VNA SETTINGS

To investigate the dynamic range of the VIRC characteristics under investigation, different *configurations* of the VIRC variables (i.e., CF, RS, and LC) are considered. They are summarized in Table 5.2 for each of the three investigation steps individually. When it comes to several different combinations of RSs and LCs, the focus is mainly placed on two CFs, namely, 868 MHz and 2458 MHz. An RS below 19.4 r/min severely degrades the effectiveness of the stirring mechanism. Two LCs are considered: unloaded and loaded. For the latter case, the VIRC is loaded with two 1×6 absorbers as depicted in Figure 5.2.

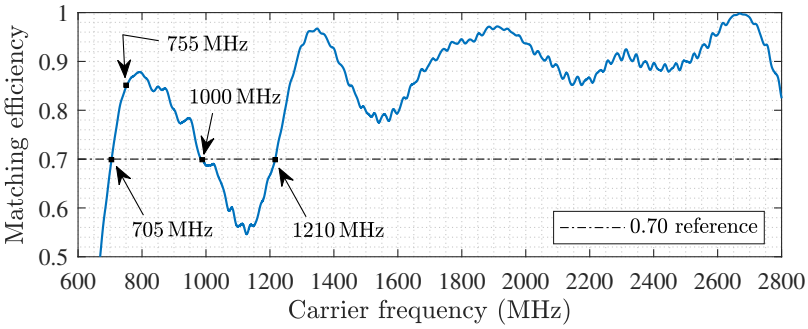

Figure 5.1: Matching efficiency $(1-|S_{11}|^2)$ of the utilized identical antennas measured in the anechoic chamber, where S_{11} is the antenna return loss.

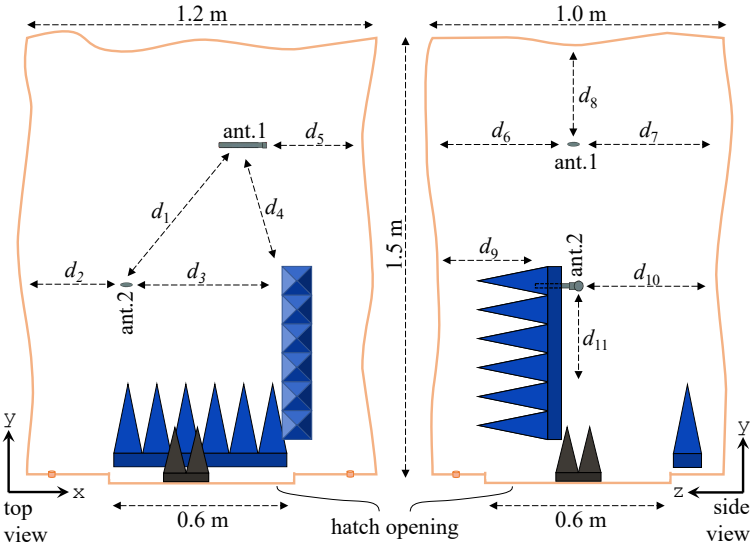

Figure 5.2: Top and side views of the layout inside the VIRC in the loaded condition.

Table 5.3 summarizes the VNA settings for the measurement setups of each of the three investigation steps. The estimation results of $T_{\text{coh}}|_{\text{min}}$, $T_{\text{coh}}|_{\text{max}}$, and $B_{\text{coh}}|_{\text{max}}$ are summarized in Table 5.4. According to the argument of the proposed methodology in the previous chapter, these three primary characteristics are essential—among others—for determining part of the VNA settings.

Table 5.3: VNA settings.

VNA parameter	Section		
	5.3.1 †	5.3.2 ‡	5.3.3 §
sweep type	zero span	freq. sweep	freq. sweep
center frequency	see CF in Table 5.2	see CF in Table 5.2	-
span (BW)	-	(15, 30) MHz #	-
start frequency	-	-	670 MHz
stop frequency	-	-	2740 MHz
sweep time (T_{swp})	$\geq 2500\,T_{\text{coh@37\%}}$ ¶	1.5 ms	5.5 ms
No. of points (N)	10^4	27	100
IF bandwidth (IFBW)	1 kHz	20 kHz	20 kHz
trigger cycle	-	1.4 s	1.4 s
No. of sweeps (M)	4	500	10^4

†The settings follow from the measurement setup of Chapter 4: a 95%-confidence level, a less-than-6% desired accuracy in the coherence time estimation, and a VNA buffer size of 20,001 data points.
‡The settings follow from the measurement setup of Chapter 4: a 95%-confidence level and a less-than-25% desired accuracy in the coherence bandwidth estimation.
§The settings follow from the measurement setup of Chapter 4: a 1.5 dB upper-limit on the expected bias of the estimated K-factor and from a 6.5 dB upper-limit on the width of the expected 95%- confidence interval of the estimated K-factor, given an unknown true K-factor as low as −35 dB and a four-tap frequency-stirring moving-average filter.
¶Actual value depends on the considered *configuration*, i.e., on CF, RS, and LC.
#Corresponds to (unloaded, loaded) VIRC.

Table 5.4: Estimation of the essential VIRC characteristics.

Characteristic	Configuration	Estimation
$T_{\text{coh}}\|_{\text{min}}$	(2740 MHz, 42.9 r/min, unloaded)	5.7 ms
$T_{\text{coh}}\|_{\text{max}}$	(670 MHz, 19.4 r/min, loaded)	330 ms
$B_{\text{coh}}\|_{\text{max}}$	$(f_c, \omega,$ loaded$)$	20.7 MHz

5.3. MEASUREMENT RESULTS, ANALYSIS, AND MODELING

The measurement data is collected according to Section 5.2, and from which the estimations are calculated using (4.3), (4.4), (5.1), (5.2), (4.7), (4.8), (4.9), (4.10), and (5.3). The measurement results are presented, analyzed, and discussed in detail in the following three subsections. Each of them is dedicated to a different order and/or category of channel characteristics. Moreover, various mathematical fitting models (both theoretical and empirical) are proposed.

5.3.1. SECOND-ORDER TEMPORAL CHARACTERISTICS

COHERENCE TIME

For all the considered *configurations* listed in Table 5.2, $\overline{\hat{T}}_{\text{coh@37\%}}$ is plotted as a function of the CF and the RS in Figures 5.3(a) and (b), respectively. As the figures indicate, the achievable dynamic range of the CT is 25–250 ms for the VIRC under investigation, which can be tuned to by setting the VIRC *configurations* accordingly.

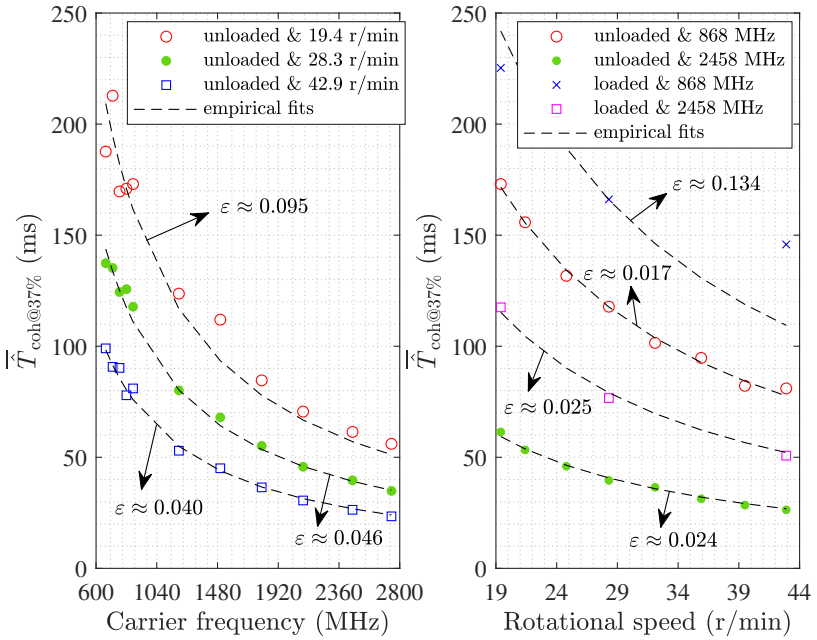

Figure 5.3: Estimated coherence time versus (a) the carrier frequency and (b) the rotational speed, where ε is the coefficient of variation of the root-mean-square error between $\overline{\hat{T}}_{\text{coh@37\%}}$ and empirical fits.

Moreover, the expected trend of an inverse-proportionality relation between the CT and the CF can be observed in Figure 5.3(a). Additionally, a similar trend with respect to the RS can also be observed in Figure 5.3(b). Consequently, the CT of the VIRC can be empirically modeled as in

$$T_{\text{coh@37\%}} = \frac{k_1}{f_c} \tag{5.4}$$

$$T_{\text{coh@37\%}} = \frac{k_2}{\omega} \tag{5.5}$$

where $T_{\text{coh@37\%}}$ and f_c are expressed in ms and MHz, respectively; k_1 is a unitless constant whose value depends on the RS and the LC; ω is the RS expressed in r/min; and k_2 is a constant expressed in ms$\cdot$r/min and whose value depends on the CF and the LC.

The nonlinear least-squares (NLS) regression method is used to fit (5.4) and (5.5) with $\overline{\hat{T}}_{\text{coh@37\%}}$ of each of the 7 scenarios considered in Figures 5.3(a) and (b). All the empirical fits are shown in the same figures. It is worth observing that both (5.4) and (5.5) produce good fits as long as the CF and the RS are above 868 MHz and 28.3 r/min, respectively, for the VIRC under investigation. Additionally, the CT increases as a result of loading, which is in accordance with [108], causing both fitting constants to increase. Moreover, since the propagation channel is time variant, increasing the RS causes k_1 to decrease. On the other hand, k_2 decreases when the CF increases, which is typical of wireless channels [55].

DOPPLER SPECTRUM AND DOPPLER SPREAD

Four examples of $\overline{\hat{\mathcal{L}}}(\nu)$ are shown in Figures 5.4(a)–(d). They correspond to four different *configurations*, representing—in order—the worst empirical fit, the best empirical fit, and the effect of low and high CFs on the deformation of the Doppler spectrum. As the figures depict, the unstirred component manifests itself as a spike in the middle. This is an indication of zero-mean Doppler shift as expected since both antennas are static. Moreover, the magnitude of this spike relative to the skirt is an indication of how large/small the K-factor is [181] for the considered *configuration*. On the other hand, the stirred components are represented by the skirt whose width is proportional to the Doppler spread. Given the latter is defined in this chapter according to (5.1), it has been found that 98% of the average power in the *stirred components* is roughly contained within $2 \times \overline{\hat{\nu}}_D$ around the middle of the Doppler spectrum. Additionally, the symmetric feature of the Doppler spectrum of the unloaded VIRC in Figures 5.4(a) and (b) is an indication that the stirred components arrive uniformly from all directions. However, the two harmonics that can be observed in Figure 5.4(a) are an indication of a poor stirring efficiency. This can be attributed to the combined effect of a limited mode density at a low CF of 770 MHz as well as an imperfection in the stirring mechanism at a very slow RS of 19.4 r/min. The latter effect is discussed further in Section 5.3.3 when the results of the K-factor are analyzed.

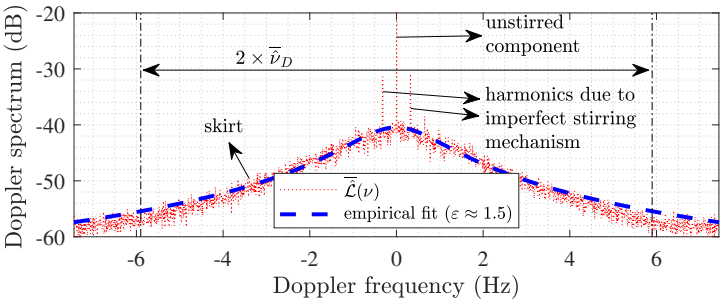

(a) (770 MHz, 19.4 r/min, unloaded)

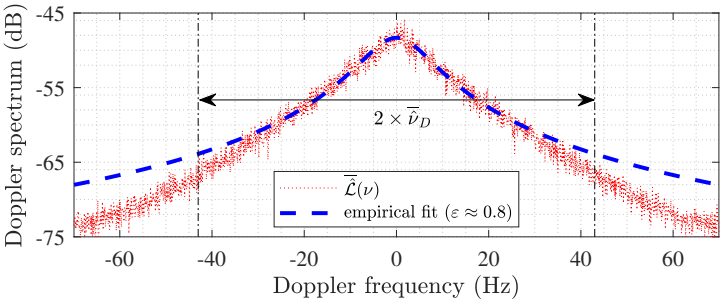

(b) (2740 MHz, 42.9 r/min, unloaded)

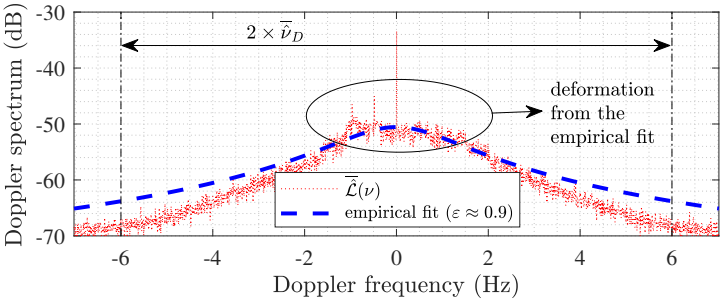

(c) (868 MHz, 28.3 r/min, loaded)

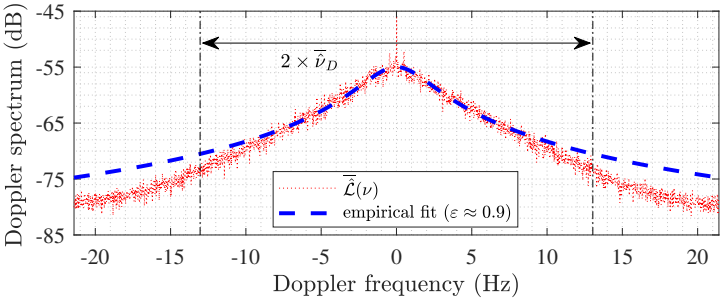

(d) (2458 MHz, 28.3 r/min, loaded)

Figure 5.4: Estimated Doppler spectrum for four distinct *configurations*.

According to [239], the Bell shape (a.k.a. inverted-V shape in decibel scale) is proposed as a channel model for the Doppler spectrum of IEEE 802.11 fixed indoor SISO links. When the mode-stirring technique is adopted in CLRCs, the inverted-V shape emerges in many scenarios [165, 170, 180–182]. This trend is also true for the VIRC as, e.g., Figures 5.4(a)–(d) show. Consequently, considering the *stirred components* exclusively, the Doppler spectrum of the VIRC can be empirically modeled in linear values as in [239]

$$\mathcal{L}(\nu) = \frac{k_3}{1 + 35\left(\frac{\nu}{k_4}\right)^2} \tag{5.6}$$

where ν is expressed in Hz; k_3 is a unitless constant whose value mainly depends on the CF and LC; whereas k_4 is a constant expressed in Hz and whose value depends on all the three VIRC variables.

The NLS regression method is used to fit (5.6) with $\overline{\hat{\mathcal{L}}}(\nu)$ of the *stirred components*. The empirical fits are shown in the same corresponding figures of $\overline{\hat{\mathcal{L}}}(\nu)$, i.e., Figures 5.4(a)–(d). To compare the goodness-of-fit among the considered *configurations*, the coefficient of variation, ε, of the root-mean-square error between $\overline{\hat{\mathcal{L}}}(\nu)$ and (5.6) is used. The coefficient is calculated by normalizing the root-mean-square error to the mean, i.e., to the power of the *stirred components*. This normalization guarantees a fair comparison. For all the considered *configurations* listed in Table 5.2, ε is calculated in linear values and graphically presented in Figures 5.5(a) and (b) as a function of the CF and the RS, respectively. Considering the unloaded VIRC, most of the *configurations* have a good fit whose ε is in the range 0.8–1.1. However, for low CFs and very slow RSs, ε becomes greater than 1.4. The worst (i.e., $\varepsilon \approx 1.5$) and the best (i.e., $\varepsilon \approx 0.8$) fits are shown in Figures 5.4(a) and (b), respectively. In the former case, the bad fit can be attributed to the aforementioned two harmonics. Considering the loaded VIRC, on the other hand, it is worth

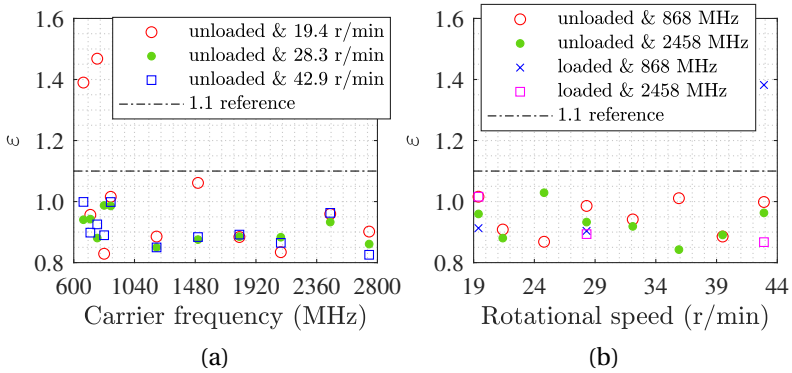

Figure 5.5: Goodness-of-fit of (5.6) versus (a) the carrier frequency and (b) the rotational speed.

mentioning that the validity of (5.6) is questionable for low CFs regardless of the RS or how small ε is. A deformation from the empirical fit can be observed in Figure 5.4(c), which corresponds to the *configuration* (868 MHz, 28.3 r/min, loaded) whose $\varepsilon \approx 0.9$. However, a good fit can still be achieved in the case of high CFs such as in Figure 5.4(d), which corresponds to the *configuration* (2458 MHz, 28.3 r/min, loaded) whose $\varepsilon \approx 0.9$.

The fitting constants, k_3 and k_4, of (5.6) are graphically presented in Figures 5.6(a) and (b) as a function of the CF and the RS, respectively, for all the considered *configurations* listed in Table 5.2. As the figures show, k_4 overlaps with $\overline{\nu}_D$ since the former is directly proportional to the latter [239]. The constant of this proportionality is empirically set to unity by using a scaling factor of 35 in (5.6) for the VIRC under investigation. Moreover, both k_4 and $\overline{\nu}_D$ closely resemble a straight line as anticipated from (5.1), (5.4) and (5.5). However, as k_4 in Figure 5.6(b) indicates, one exception is the *configuration* of 868 MHz and loaded VIRC, regardless of the RS. This is the result of the aforementioned deformation in the VIRC under investigation. On the other hand, considering Figure 5.6(a), k_3 decreases when the CF increases as anticipated from the gain of a typical propagation channel. This is true because k_3 is directly proportional to the power of the *stirred components* as

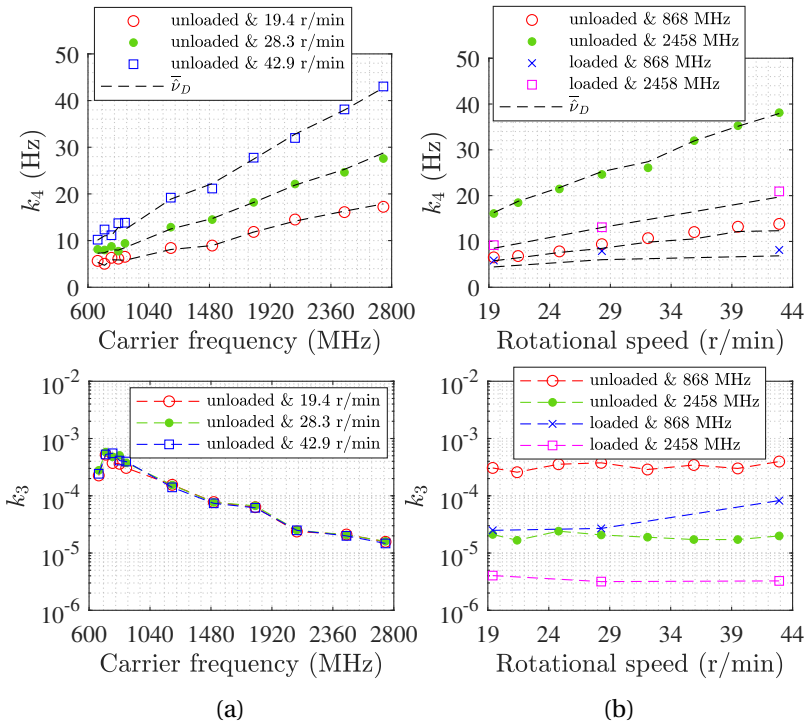

Figure 5.6: Fitting constants, k_3 and k_4, of (5.6) versus (a) the carrier frequency and (b) the rotational speed.

can be indicated from (5.6). Furthermore, considering k_3 as a function of the RS in Figures 5.6(a) and (b), the former is roughly constant and, thereby, not dependent on the latter. This is true because the RS affects the stirring efficiency, rather than the channel gain, as explained later in Section 5.3.3 when the results of the channel gain are analyzed.

5.3.2. SECOND-ORDER SPECTRAL CHARACTERISTICS

NORMALIZED FREQUENCY AUTOCOVARIANCE FUNCTION

For all the considered *configurations* listed in Table 5.2, $\left|\overline{\hat{\rho}}_f\right|$ is plotted in Figures 5.7(a) and (b) for the unloaded and the loaded VIRC, respectively. According to the theory [240] and the measurements [231], the linearly scaled power delay profile (PDP) of CLRCs is commonly modeled as an exponentially decaying pulse

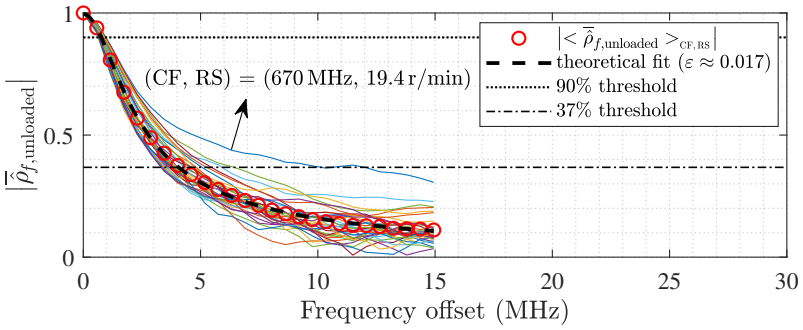

(a)

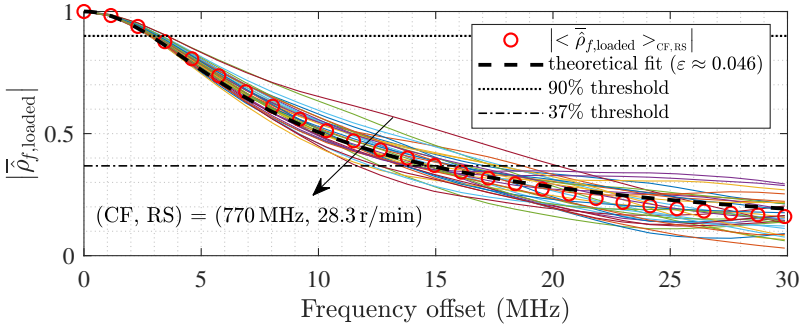

(b)

Figure 5.7: Estimated normalized frequency autocovariance function for (a) the unloaded and (b) the loaded VIRC, where ε is the coefficient of variation of the root-mean-square error between $\left|\left\langle\overline{\hat{\rho}}_f\right\rangle\right|$ and empirical fits. The different *configurations* are represented by solid lines with different colors.

with a specific time constant that describes how quickly the energy dissipates in the chamber. Moreover, a Fourier-transform pair between the NFAF and the PDP exists [55, 192]. Consequently, the NFAF of the VIRC can be theoretically/empirically modeled as in

$$\left|\rho_f\right| = \frac{1}{\left|1 + j2\pi\frac{\Delta f}{k_5}\right|} \tag{5.7}$$

where k_5 is a frequency constant whose value depends on the LC and the considered CF range.

Before fitting (5.7) with $\overline{\hat{\rho}}_f$, the latter is first averaged over the considered CFs (i.e., $\langle\cdot\rangle_{\text{CF}}$), then over the considered RSs (i.e., $\langle\cdot\rangle_{\text{RS}}$), resulting in the two averages, $\left|\left\langle\overline{\hat{\rho}}_{f,\text{unloaded}}\right\rangle_{\text{CF,RS}}\right|$ and $\left|\left\langle\overline{\hat{\rho}}_{f,\text{loaded}}\right\rangle_{\text{CF,RS}}\right|$, for the unloaded and the loaded VIRC, respectively. Next, the NLS regression method is used to fit (5.7) with each of these two resulted averages individually. Both fits are shown in Figure 5.7. It is worth observing that (5.7) produces a good fit as long as the CF and the RS are above 770 MHz and 28.3 r/min, respectively, for the VIRC under investigation. Moreover, loading the VIRC causes k_5 to increase, which is in accordance with [159], since it is directly proportional to the average mode bandwidth.

5

Coherence Bandwidth

For all the considered *configurations* listed in Table 5.2, both $\overline{\hat{B}}_{\text{coh@37\%}}$ and $\overline{\hat{B}}_{\text{coh@90\%}}$ are plotted in Figures 5.8(a) and (b), respectively, as a function of the CF. As can be observed in the figures, the CB increases as a result of loading, which is in accordance with [161, 199]. Additionally, it is roughly flat over the CFs above 820 MHz for the VIRC under investigation. It also has no well-defined behavior when it comes to the RS. This is generally in accordance with [161, 199] in which the measurements are smoothed using an FS MAF resulting an approximately flat behaviour. Moreover, for the VIRC under investigation, the upper limit on the signaling rate of NB systems is $B_{\text{coh}}\big|_{\text{min}} \approx 0.5$ MHz, which can be determined from the unloaded VIRC in Figure 5.8(b).

5.3.3. First-Order Characteristics

Rejection Rate

The estimated RR of the unloaded and the loaded VIRC are denoted by $\hat{R}_{\text{unloaded}}$ and $\hat{R}_{\text{loaded}}$, respectively. For all the considered RSs listed in Table 5.2, both $\hat{R}_{\text{unloaded}}$ and $\hat{R}_{\text{loaded}}$ are plotted in Figures 5.9(a) and (b), respectively, as a function of the CF. For both LCs, the CFs below 770 MHz have a high RR that is well above a 20% reference for the VIRC under investigation. This is due to the limited mode density, as reasoned in [221]. Moreover, for the unloaded VIRC specifically, the CF range 930–1220 MHz also has a high $\hat{R}_{\text{unloaded}}$. However, on the contrary to the CFs below 770 MHz, this high RR is due to the matching efficiency of the utilized antennas that is less than 0.7 within the said frequency range, as reasoned in [222].

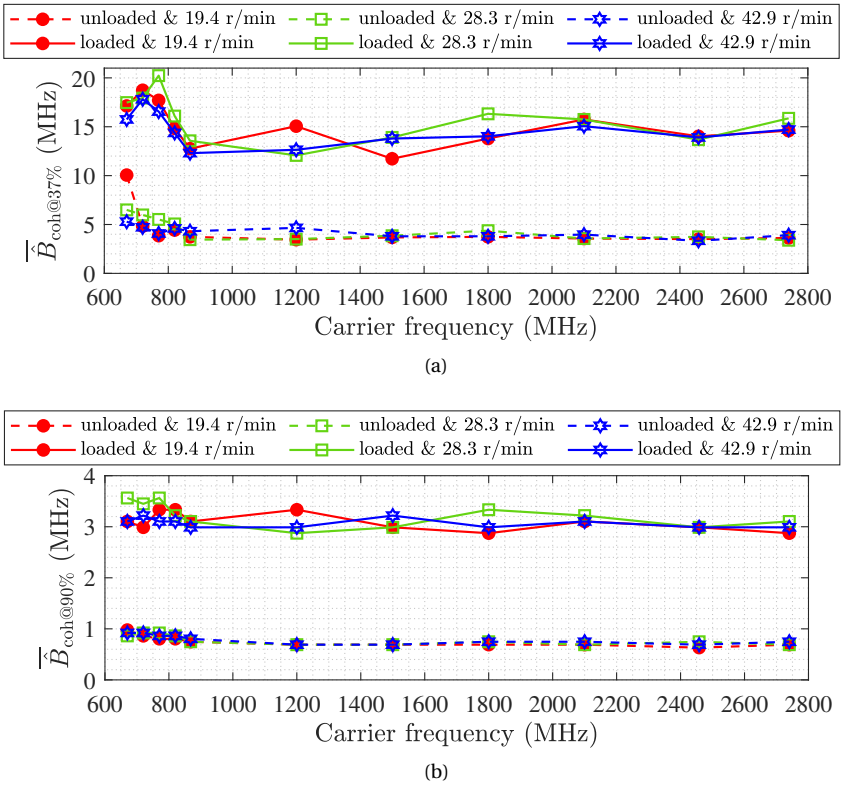

Figure 5.8: Estimated coherence bandwidth defined at (a) 37% and (b) 90% versus the carrier frequency.

The high $\hat{R}$ for the two previous cases is true regardless of the RS. Yet in the case of the loaded VIRC, the same CF range 930–1220 MHz has an $\hat{R}_{\text{loaded}}$ below 20% due the increase in the modal overlap after loading [218]. On the other hand, in the case of low CFs and very slow RSs, loading will not help at lowering its RR as can be indicated from Figure 5.9(b) for CFs below 1000 MHz for the VIRC under investigation. Nevertheless, the typical VIRC trend of a low RR that is below 20% for high CFs [107, 108] can be observed in Figures 5.9(a) and (b) regardless of the RS or the LC. Additionally, another trend of an RR decrease as the RS increases can be observed in Figure 5.10(b), which is interestingly not true for the unloaded VIRC, as Figure 5.10(a) indicates.

K-FACTOR

The estimated K-factor of the unloaded and the loaded VIRC are denoted by $\hat{K}_{\text{unloaded}}$ and $\hat{K}_{\text{loaded}}$, respectively. For all the considered RSs listed in Table 5.2, both $\hat{K}_{\text{unloaded}}$ and $\hat{K}_{\text{loaded}}$ are plotted in Figures 5.11(a) and (b), respectively, as a function of the CF. For the unloaded VIRC under investigation, $\hat{K}_{\text{unloaded}}$ in most of the CF

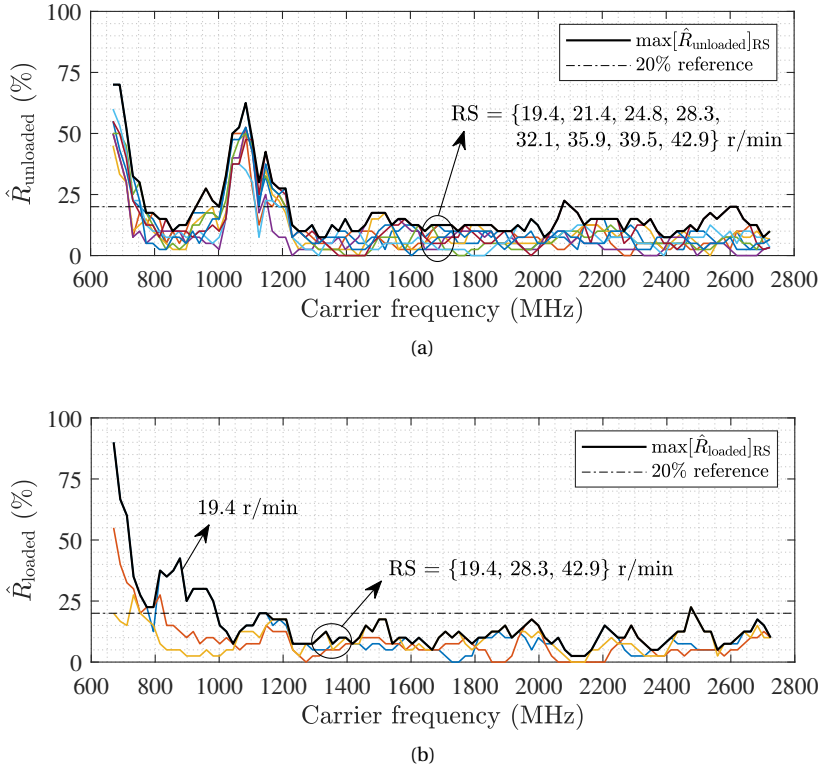

Figure 5.9: Estimated rejection rate versus the carrier frequency for (a) the unloaded and (b) the loaded VIRC. The different rotational speeds are represented by solid lines with different colors.

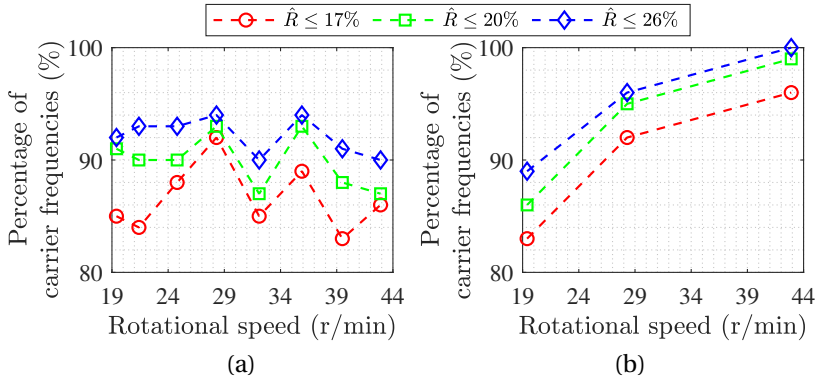

Figure 5.10: Percentage of the carrier frequencies at which the estimated rejection rate is below some upper limit versus the rotational speed for (a) the unloaded and (b) the loaded VIRC.

range above 820 MHz is well below −10 dB. For the loaded VIRC, on the other hand, $\hat{K}_{\text{loaded}}$ in most of the CF range above 1000 MHz is well below −7 dB, whereas it is only well below −10 dB for most of the CF range above 1800 MHz. Moreover, a trend of a K-factor decrease as the CF increases can be clearly seen in the figures for both LCs, which is in accordance with [107], since the VIRC is good at stirring the high CFs. However, there is no simple relation that can be observed between $\hat{K}$ and the CF. This is true because the theoretical formula of the K-factor [159, eq. (13)] depends—among others—on two variables: the directivities of the utilized antennas in the direction of each other (which themselves depend on the CF) and the average mode bandwidth (which depends on the LC). The latter itself has a complicated relation with respect to the CF [159, eq. (7)], which further explains the rapid spectral variations in $\hat{K}$ that can be seen in Figures 5.11(a) and (b). Additionally, $\hat{K}$ of different RSs do not overlap, as the figures clearly show. This can be attributed to an imperfection in the stirring mechanism, as explained in the next paragraph. Nevertheless, a compelling correlation between the curves in terms of their behavior

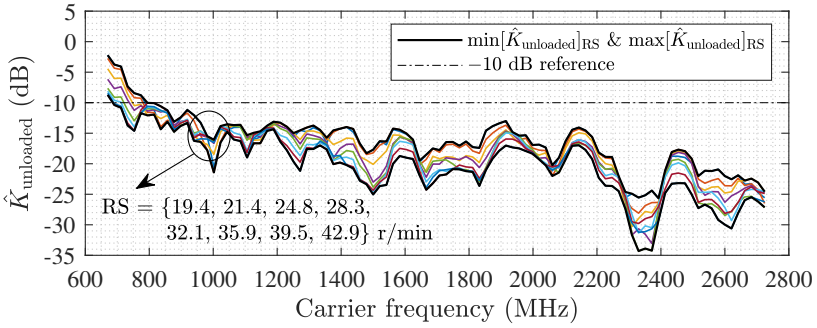

(a)

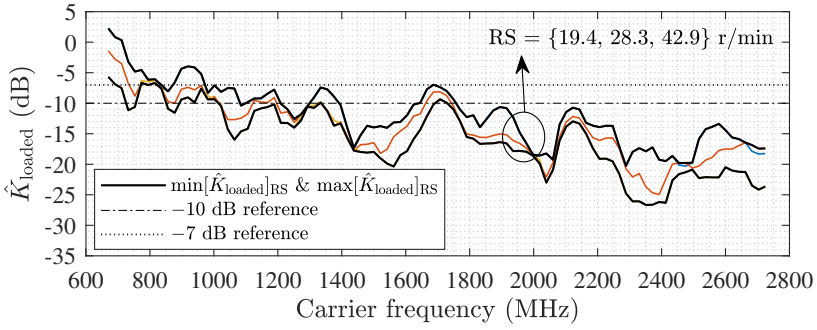

(b)

Figure 5.11: Estimated K-factor versus the carrier frequency for (a) the unloaded and (b) the loaded VIRC. The different rotational speeds are represented by solid lines with different colors.

with respect to the CF can be observed for both LCs in Figure 5.11.

According to the theory [159, eqs. (7) and (13)], the K-factor of an RC depends on the chamber volume, the directivities of the utilized antennas in the direction of each other, the distance between them, the average mode bandwidth, the effectiveness of the stirring mechanism, the CF, and the LC. In this chapter, we define an intrinsic K-factor, $K_{\text{intrinsic}}$, that is independent of the effectiveness of the stirring mechanism. In other words, the actual K-factor of an RC matches its $K_{\text{intrinsic}}$ if its stirring mechanism is ideal, hence the latter is a conceptual metric. This concept of $K_{\text{intrinsic}}$ can be applied to the VIRC as follows. Considering any point on the VIRC wrinkled fabric, the peak-to-peak displacement along the surface norm depends on the RS because of the inertia effect. This displacement is also known as the shaking amplitude according to [173, 220]. That means at faster RSs, the VIRC fabric vibrates more significantly. However, at a certain fast RS, the displacement reaches its maximum value because of the physical limitation of the VIRC fabric. Therefore, fast RSs create new uncorrelated boundary conditions and, thereby, cause the actual K-factor of the VIRC to decrease while approaching its $K_{\text{intrinsic}}$. At very slow RSs, on the other hand, the displacement reaches its minimum, creating new yet partially correlated boundary conditions and, thereby, causing the actual K-factor to rather increase above $K_{\text{intrinsic}}$.

For the whole range of the CF considered in Table 5.2, both $\hat{K}_{\text{unloaded}}$ and $\hat{K}_{\text{loaded}}$ are plotted in Figures 5.12(a) and (b), respectively, as a function of the RS. The concept of $K_{\text{intrinsic}}$ can be used to explain why $\hat{K}$ of different RSs do not overlap (see Figure 5.11), but rather decrease as the RS increases (see Figure 5.12). Consequently, after the K-factor of the VIRC is averaged over the considered CFs, it can be

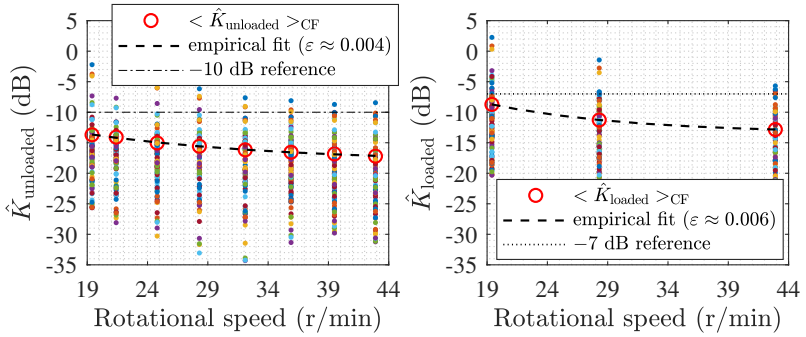

Figure 5.12: Estimated K-factor versus the rotational speed for (a) the unloaded and (b) the loaded VIRC. The different carrier frequencies are represented by solid points with different colors, where ε is the coefficient of variation of the root-mean-square error between $\left|\langle \hat{K} \rangle\right|_{\text{dB}}$ and empirical fits.

empirically modeled in decibel as in

$$\left|\langle K\rangle_{\mathrm{CF}}\right|_{\mathrm{dB}} = k_6 + k_7 \times \exp\left(-\frac{\omega}{k_8}\right) \tag{5.8}$$

where ω is the RS expressed in r/min; k_6 is a constant expressed in dB and represents an asymptote which can be thought of as $K_{\mathrm{intrinsic}}$ averaged over the considered CFs, i.e., $k_6 = \left|\langle K_{\mathrm{intrinsic}}\rangle_{\mathrm{CF}}\right|_{\mathrm{dB}}$; k_7 is a constant expressed in dB and whose value is an indicator of how much the stirring efficiency degrades at very slow RSs; and k_8 is a constant expressed in r/min and whose value describes to what degree the stirring efficiency depends on the RS. An RC with a near-ideal stirring mechanism has very small k_7 and k_8. Moreover, the values of all the three fitting constants of (5.8) depend on the LC and the considered CF range. Additionally, according to (5.8), when the RS is very slow, $\left|\langle K\rangle_{\mathrm{CF}}\right|_{\mathrm{dB}}$ approaches $k_6 + k_7$. On the other hand, $\left|\langle K\rangle_{\mathrm{CF}}\right|_{\mathrm{dB}}$ becomes approximately k_6 when the RS is fast.

After $\hat{K}$ is averaged over the considered CFs (i.e., $\langle\cdot\rangle_{\mathrm{CF}}$) for each of the two LCs individually, it is converted into decibel, then the NLS regression method is used to fit (5.8) with each of the two resulted decibel-scaled averages, $\left|\langle \hat{K}_{\mathrm{unloaded}}\rangle_{\mathrm{CF}}\right|_{\mathrm{dB}}$ and $\left|\langle \hat{K}_{\mathrm{loaded}}\rangle_{\mathrm{CF}}\right|_{\mathrm{dB}}$. Both fits are shown in Figures 5.12(a) and (b) for the unloaded and the loaded VIRC, respectively. In both LCs, the stirring efficiency degrades when decreasing the RS, which is in accordance with [173, 220]. Moreover, the lower the CF range and/or the more loaded the VIRC, the larger the fitting constants of (5.8) become. This in turn results in a worse stirring efficiency (see Figure 5.11), which is in accordance with [159, 167].

CHANNEL GAIN

The estimated channel gain of the unloaded and the loaded VIRC are denoted by $\hat{G}_{\mathrm{unloaded}}$ and $\hat{G}_{\mathrm{loaded}}$, respectively. For all the considered RSs listed in Table 5.2,

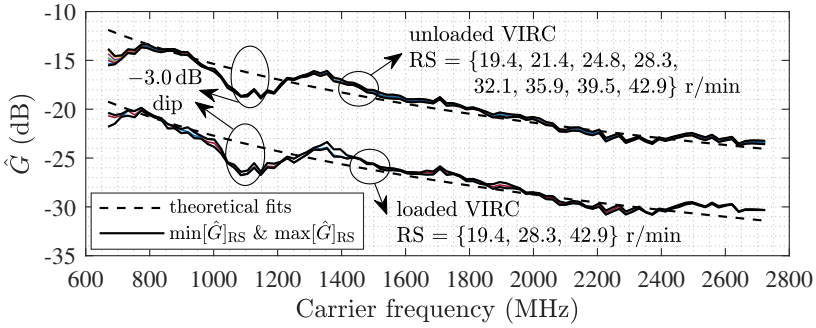

Figure 5.13: Estimated channel gain versus the carrier frequency for both loading conditions. The different rotational speeds are represented by solid lines with different colors.

both $\hat{G}_{\text{unloaded}}$ and $\hat{G}_{\text{loaded}}$ are plotted in Figure 5.13 as a function of the CF. As the figure shows, the RS has almost no impact on $\hat{G}$. This is similar to the trend in Figure 5.6(b) regarding k_3 versus the RS. Moreover, the typical RC trends of a channel gain decline as a result of increasing the CF and/or loading [201] can be observed in the same figure as well. Additionally, a clear resemblance with k_3 in Figure 5.6(a) can be observed. Yet contrary to $\hat{G}$, it should be emphasized that k_3 carries no information about the unstirred component because the empirical fit of (5.6) exclusively takes the *stirred components* into consideration.

According to the theory [159, eq. (6)], the gain of a propagation channel inside an RC can be expressed as in

$$G = \frac{c^3 e_1 e_2}{16\pi^2 V \Delta f_{\text{mode}}} \times \frac{1}{f_c^2} \tag{5.9}$$

where c is the speed of light; V is the chamber volume; Δf_{mode} is the average mode bandwidth; and e_1 and e_2 are the total efficiencies of the utilized antennas (i.e., both matching and radiation efficiencies combined). The left fraction of the expression on the right side of (5.9) can be averaged over the considered CFs, i.e., $\langle G f_c^2 \rangle_{\text{CF}}$, resulting in a constant denoted in decibel by k_9. Consequently, the gain of the propagation channel inside the VIRC can be theoretically modeled in decibel as in

$$G_{\text{dB}} = k_9 - 20 \times \log_{10}(f_c) \tag{5.10}$$

where f_c is expressed in MHz; whereas k_9 is a constant expressed in dBMHz^2 and whose value depends on $e_1 \times e_2$, V, and Δf_{mode}, hence the LC [159, eq. (7)].

After $\hat{G}$ is averaged over the considered RSs (i.e., $\langle\cdot\rangle_{\text{RS}}$) for each of the two LCs individually, it is multiplied by f_c^2, averaged over the considered CFs (i.e., $\langle\cdot\rangle_{\text{CF}}$), then converted into decibel, resulting in two values for k_9 for both LCs. These two values are then used to fit (5.10) with $\left|\langle \hat{G}_{\text{unloaded}} \rangle_{\text{RS}}\right|_{\text{dB}}$ and $\left|\langle \hat{G}_{\text{loaded}} \rangle_{\text{RS}}\right|_{\text{dB}}$. Both fits are shown in Figure 5.13, which is in accordance with [201]. For the VIRC under investigation, k_9 decreases by roughly 7 dB due to loading. Moreover, a considerable deviation of up to −3 dB between the estimated channel gains and the theoretical fits of (5.10) can be observed in the CF range 1000–1210 MHz. This is an indication that the utilized antennas have low total efficiencies within the said CF range (see (5.9)), which is confirmed by the matching efficiency that is less than 0.7 (see Figure 5.1).

5.4. FURTHER INVESTIGATION AND DISCUSSION

In the following, we discuss the validity of the statistical method as well as we demonstrate the generality and the potential usability of these models.

5.4.1. VALIDITY OF PROPOSED METHODOLOGY

According to [179], a 3-decibel standard deviation is the tolerance requirement of the field uniformity for CFs above 400 MHz. Moreover, the lowest usable frequency (LUF) is practically defined in [179] as the lowest frequency above which the specified

field uniformity requirement is achieved for a given working volume. According to [172, Fig. 7], the LUF is roughly 600 MHz for the VIRC under investigation that is depicted in Figure 4.7. This is in accordance with the observations from the previous section (see Figures 5.3(a), 5.5(a), 5.7(a), and 5.9(a)), in which most of the proposed models break down for CFs below 750 MHz. This can be attributed to the significant decrease in the VIRC mode density, which invalidates the invoked temporal stationarity and, thereby, the temporal ergodicity in [114] for CFs below the LUF. However, for high CFs, the mode density is high enough (i.e., enough modal overlap) and, thereby, the invoked stationarity as well as the statistical method itself are still applicable. The consistency between the obtained estimations and the proposed models in the previous section is a strong indication of the validity of the statistical method (proposed in the previous chapter) for CFs well above the LUF.

5.4.2. GENERALITY OF PROPOSED MODELS

In the previous section, it has been shown that the proposed models provide good fits for the corresponding characteristics of the VIRC as long as the CF is sufficiently above the LUF. In this section, to demonstrate the generality of these models, the investigation is repeated but after adequately modifying the framework (i.e., the setups of the channel and the VIRC), as depicted in Figure 5.14. First, a table is inserted beneath the VIRC to cease its bottom wall from vibrating and, thereby, to modify its stirring mechanism. Moreover, the channel setup has been modified to consider log-periodic directional antennas, a different antenna location and orientation, a different LC, and a different CF range. The matching efficiency of the utilized antennas is presented in Figure 5.15 for the considered CF range. According to Figures 5.16–5.20, the proposed models, namely, (5.4)–(5.8) and (5.10), still provide good fits despite the substantial modification to the framework. This is a strong indication of the generality of such models for comparable VIRCs.

Several fitting models, namely, (5.4)–(5.7), are required in case of developing a VIRC-based channel emulator that is capable of conducting OTA testing of wireless baseband algorithms, as, e.g., in [167, 231, 238, 241, 242]. In particular, the proposed models can be used to predict (through interpolation and—to a certain degree—extrapolation) the channel characteristics of the VIRC with a certain accuracy. This is to correctly configure the VIRC variables in order to accurately emulate, e.g., a desired B_{coh}, T_{coh}, and $\mathcal{L}(v)$. The predictive accuracy of the proposed models, (5.4)–(5.7), is assessed using the aforementioned *modified framework* as follows. In Figure 5.16(a), six CT estimations are carried out. However, based on (5.4), an empirical fit to the estimated CT with respect to the CF is generated only from three of the six estimations. These three estimations are referred to as "utilized estimations" in the figure. The empirical fit is then used to predict the other three estimations, which are referred to as "unutilized estimations" in the same figure. Moreover, a similar approach based on (5.5) is applied to the estimated CT with respect to the RS in Figure 5.16(b). In all predictions, the percent error (δ) is less than 6% in absolute value. Additionally, a similar approach to Figure 5.16 for the fitting constants of (5.6) is also applicable. This can be done, however, by utilizing

the trends in Figures 5.6(a) and (b), which were discussed in Section 5.3.1. Finally, a somewhat similar approach based on (5.7) is applied to the estimated NFAF in Figures 5.17(a) and (b). In all predictions at a threshold = 37%, the percent error satisfies: $-23\% < \delta < +9\%$.

5.4.3. USABILITY OF PROPOSED MODELS

SYSTEMATIC EVALUATION OF VIRC STIRRING MECHANISM

The fitting constants, k_7 and k_8, of the proposed model in (5.8) can be used in EMC characterization as a systematic method for evaluating the effectiveness of the stirring mechanism of different VIRCs. The smaller the constants, the less dependent the K-factor is on the RS, and the better the stirring effectiveness becomes. It is worth repeating that the K-factor is actually dependent on the shaking amplitude, which itself depends on the RS because of the inertia effect, as explained earlier in Section 5.3.3. This dependence is conditional on the type of the implemented stirring mechanism. Generally speaking, however, given the same channel and VIRC setups (i.e., same framework), the K-factor becomes less dependent on the RS when considering a higher CF range. In the specific case of the *modified framework* in Figure 5.14 in comparison to the unloaded framework in Figure 5.2, k_8 has almost doubled in value because of the combined effect of fixing the VIRC bottom wall as well as loading. This combined effect has negatively impacted the stirring efficiency. However, the net effect of the higher CF range and the utilization of directional antennas have resulted in smaller values for k_6 and k_7. This has positively improved

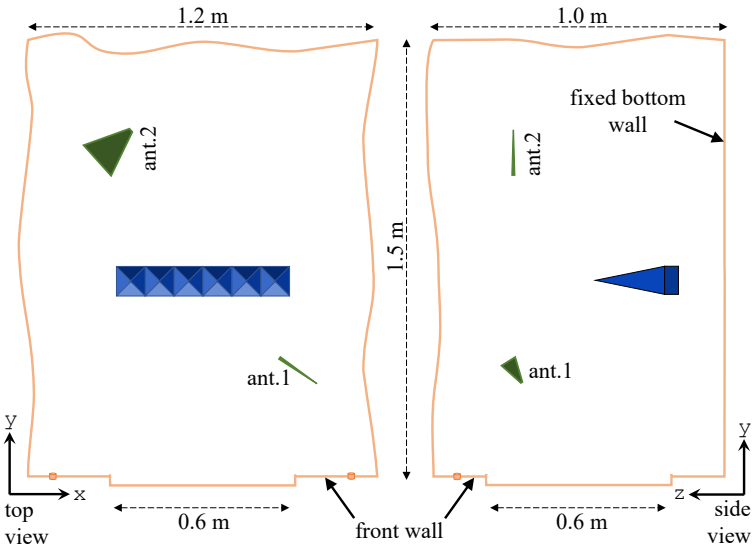

Figure 5.14: Top and side views of the layout inside the VIRC for the *modified framework*. Ant.1 and Ant.2 are two identical log-periodic antennas.

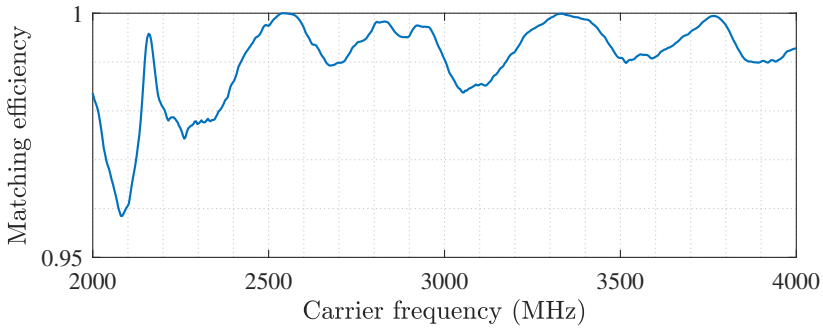

Figure 5.15: Matching efficiency of the utilized identical antennas (measured in the anechoic chamber) for the *modified framework*.

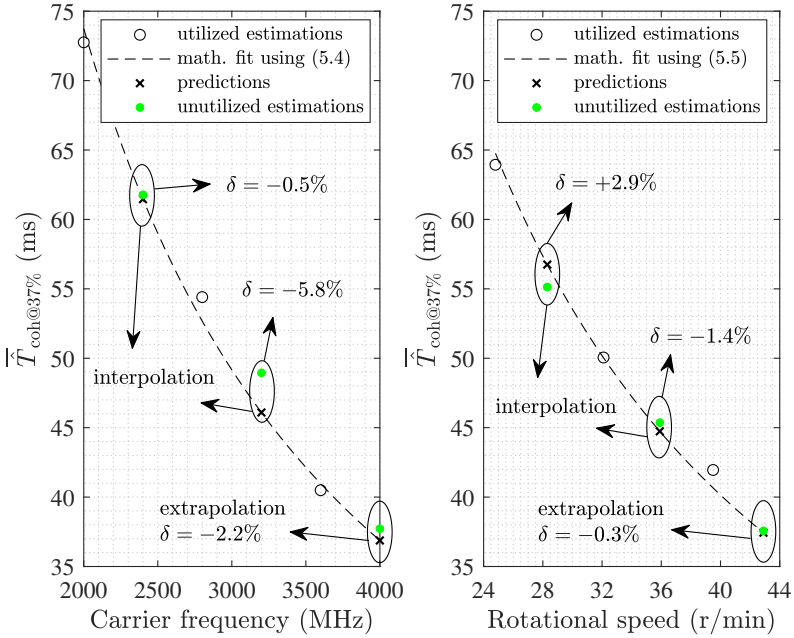

Figure 5.16: Estimated coherence time versus (a) the carrier frequency and (b) the rotational speed for the *modified framework*. The rotational speed and the carrier frequency for (a) and (b) are 39.5 r/min and 3600 MHz, respectively.

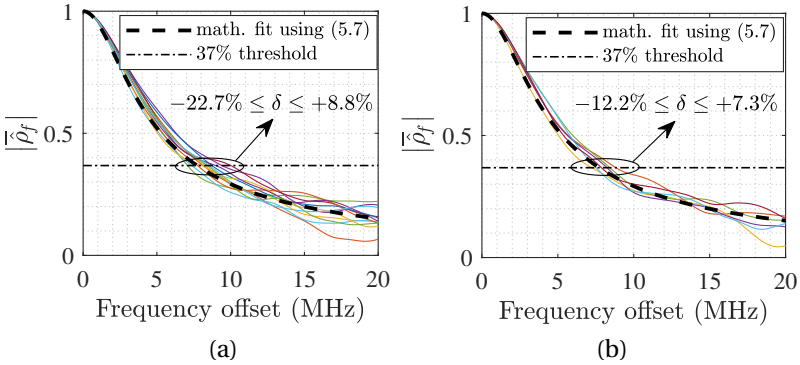

Figure 5.17: Estimated normalized frequency autocovariance function for the *modified framework*. The solid lines with different colors represent:
(a) {2400, 3200} MHz × {24.8, 28.3, 32.1, 35.9, 39.5, 42.9} r/min and
(b) {4000} MHz × {24.8, 28.3, 32.1, 35.9, 39.5, 42.9} r/min.
In both (a) and (b), the mathematical fit is the same and is generated using {2000, 2800, 3600} MHz × {24.8, 28.3, 32.1, 35.9, 39.5, 42.9} r/min.

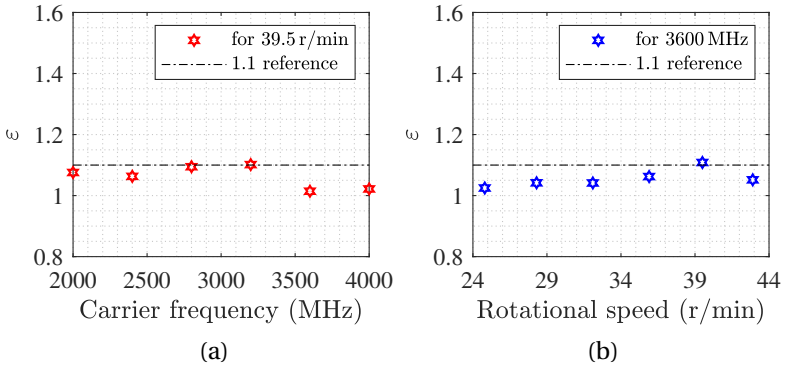

Figure 5.18: Goodness-of-fit of (5.6) versus (a) the carrier frequency and (b) the rotational speed for the *modified framework*.

the total stirring efficiency, which can be observed in Figure 5.19 in comparison to Figure 5.12(a).

Cost-Efficient Assessment of Antenna Radiation Efficiency

According to [107, 108], the VIRC can offer a shorter measurement time and a larger number of uncorrelated samples compared to the CLRC. Therefore, it may offer a potentially attractive alternative for OTA-based antenna measurements, which are conducted in CLRCs as, e.g., in [233, 234, 243]. The mathematical model in (5.10) can be useful for preliminarily assessing the radiation efficiency of an antenna

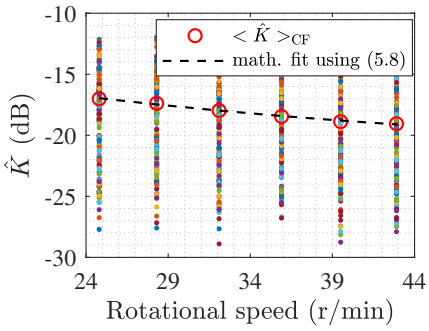

Figure 5.19: Estimated K-factor versus the rotational speed for the *modified framework*. The different carrier frequencies (2000–4000 MHz) are represented by solid points with different colors.

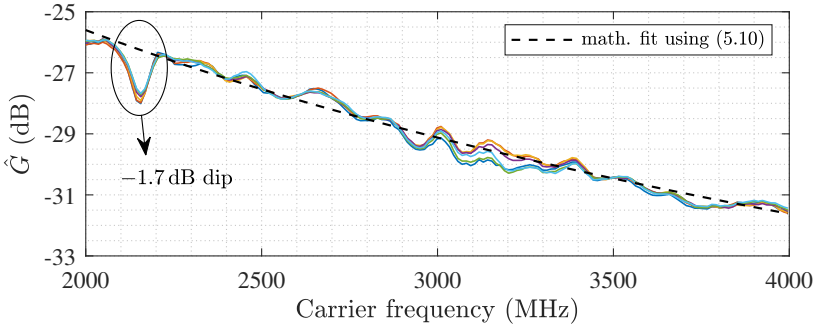

Figure 5.20: Estimated channel gain versus the carrier frequency for the *modified framework*. The different rotational speeds (24.8, 28.3, 32.1, 35.9, 39.5, 42.9 r/min) are represented by solid lines with different colors.

under test as long as its matching efficiency is known. This is advantageous since measuring the total efficiency using antenna positioners in anechoic chambers is expensive and time consuming. Thanks to (5.10), a significant dip (i.e., deviation) below the theoretical fit is an indication of a low total efficiency. However, this can be attributed to either the matching efficiency, the radiation efficiency, or both. The 3-decibel dip in Figure 5.13 is an example in which the dip is mainly attributed to the low matching efficiency, as argued in the previous section (see Figure 5.1). On the other hand, the 1.7-decibel dip in Figure 5.20 is another example in which the dip is mainly attributed to the low radiation efficiency since the corresponding matching efficiency is above 0.95 (see Figure 5.15).

5.5. UNB CHANNEL EMULATION

A cost-efficient channel emulator would be useful for further developing and testing the PHY of the UNB signaling scheme, such as carrier- and timing-synchronization algorithms [64], frequency-offset tolerant modulation/demodulation techniques [62, 63], and interleaver-based channel-coding schemes [76]. Therefore, regarding the two UNB potential deployment scenarios in the 2.4 GHz band, the characteristics of interest of the corresponding propagation channels from the literature are summarized. Moreover, the feasibility of a VIRC-based channel emulator for the UNB signaling scheme in the 2.4 GHz band is examined.

5.5.1. UNB CHANNEL CHARACTERISTICS

According to Chapter 2, there are potentially two main deployment scenarios for the UNB signaling scheme as an energy-efficient/convenient physical layer (PHY) for low-throughput latency-tolerant wireless sensor networks (WSNs) in the 2.4 GHz band.

- The first one is that the UNB is an energy efficient solution for the WSNs whose nodes reside, e.g., in a large building that is served by a single base station (BS). Moreover, the wireless link between the BS and the nodes typically covers a large distance and/or frequently experiences fading/obstruction. One example is a campus indoor environment [244], which is a public place inhabited by pedestrians. In such an environment, the measured CEH matches the theoretical Rician distribution very well with K-factors roughly ranging from +3 dB to +20 dB [244]. Moreover, the NTAF is modeled as a sum of two exponentially decaying terms with a CT ranging from 0.5 to 5 s [244]. Nevertheless, the Doppler spectrum [239, 244] still roughly resembles an inverted-V shape in decibel scale.

- The UNB also represents a convenient ultra-low-power RF solution for the WSNs whose nodes are supposed to be tiny with very harsh peak-power limitations. One example is the body-area networks [245, 246], in which an off-body BS communicates in an indoor environment with, e.g., an on-body energy-scavenging-powered sensor node. In such a deployment, the measured CEH better fits the Gamma and the Log-normal theoretical distributions with an equivalent K-factor roughly ranging from −32 dB to +33 dB [245, 246], that corresponds to several scenarios: the sensor node is either attached to the chest or the wrist, the person is standing still or walking, and the BS is 1 to 4 meters away. However, the Doppler spectrum does not match a specific model [247]. Nevertheless, depending on the everyday activity of the person, the measured CT can reach up to one second, but also can drop to between 70 ms and 25 ms with significant continuous movement. [248]

Due to the nature of the UNB signaling scheme, its bandwidth is less than 10 kHz, i.e., ultra narrow, hence the name. Moreover, since in indoor deployments at 2.4 GHz, the rms delay spread is reported [245, 249] to be in the order of a few

tens of ns, the corresponding CB [55, 192] is much larger than the bandwidth of UNB signals. Consequently, UNB indoor communications in the 2.4 GHz band will definitely experience flat fading.

5.5.2. VIRC-BASED CHANNEL EMULATOR

Given the gained insights from analyzing the measurement results in Sections 5.3 and 5.4.2, the VIRC can certainly mimic the desired flat fading since $B_{\text{coh}}\big|_{\text{min}}$ is 0.5 MHz. Moreover, it can mimic a near-Rayleigh channel with a Rician K-factor below −17 dB. Therefore, with an appropriate external setup of attenuators, similar to the one in [186, Fig. 12], it is capable of emulating a wide range of the K-factor. The accuracy and the width of this range depends on how low the K-factor of the VIRC itself is. Additionally, the Doppler spectrum of the propagation channel inside the VIRC matches the Bell model with a CT that can be easily tuned in the range 30–120 ms by changing the RS and the LC accordingly. Furthermore, given the channel characteristics of the two aforementioned deployment scenarios in the previous subsection, the feasibility of utilizing the VIRC as a UNB channel emulator with ascribed first- and second-order temporal characteristics can be summarized as follows.

- For the UNB's first potential deployment scenario of a campus indoor environment, a VIRC-based channel emulator is capable of closely mimicking the desired models of the first- and second-order temporal characteristics, but with an upper limit on the emulated CT of 120 ms.
- For the UNB's second potential deployment scenario of a WBAN on-body to off-body channel, a VIRC-based channel emulator is not capable of closely emulating the desired models of the CEH or the Doppler spectrum.

Therefore, it can be concluded that the VIRC is most suitable for the first deployment scenario, but with a limited emulation capability on how slow the emulated fading can be. The reason is that the VIRC stirring efficiency degrades at very slow RSs because of the implemented stirring mechanism, as explained in Section 5.3.3, hence an aspect to further improvement.

5.6. CONCLUSION

After a framework, that is composed of the setups of the VIRC and the propagation channel inside it, is assembled, a thorough empirical characterization of the channel was conducted. Various channel first- and second-order temporal and spectral characteristics were measured, analyzed and discussed. Moreover, the effects of different rotational speeds of the VIRC motors, two loading conditions, and the frequency range 670–2740 MHz were considered for the sake of determining the dynamic range of the studied characteristics.

For the VIRC under investigation, based on $B_{\text{coh}}\big|_{\text{min}}$, 0.5 MHz is the maximum signaling rate of NB systems that can be tested. Furthermore, the achievable dynamic

range of the Doppler spread is 4–40 Hz (or 25–250 ms for the CT), which corresponds to the following *configurations*: (670 MHz, 19.4 r/min, loaded)–(2740 MHz, 42.9 r/min, unloaded). Additionally, for the unloaded VIRC, the framework can provide a near-Rayleigh channel (Rician with a K-factor below −11 dB) as long as the CF is in the range 850–930 MHz or 1220–2740 MHz. For the loaded VIRC, on the other hand, the framework provides a Rician channel with a K-factor below −7 dB as long as the CF and the RS are above 840 MHz and 24.8 r/min, respectively.

Many behavioral trends were observed while analyzing the measurement results. Consequently, a number of mathematical models were proposed to fit the behavior of various of these characteristics. The consistency between the models and the corresponding estimations is a strong indication of the validity of the statistical method. This is true as long as the CF is sufficiently above the LUF where the invoked stationarity is valid. Otherwise, the models break down for CFs near or below the LUF. Furthermore, the generality as well as the predictive accuracy of the proposed models were assessed using a substantially modified framework. Additionally, the potential usability of these models for both EMC and OTA testing was briefly demonstrated: the evaluation of the effectiveness of a VIRC stirring mechanism and the assessment of the radiation efficiency of an antenna under test.

It was shown that the model of the inverse-proportionality between the CT and the CF (or the RS) provides a good empirical fit. Additionally, the Bell model was found to be a good empirical fit for the Doppler spectrum. Furthermore, for both LCs, the model of the deviated one-sided exponential decay in (5.8) was found to provide a good empirical fit for the decibel-scaled K-factor with respect to the RS. Moreover, the linear function model in (5.10) was found to be a good theoretical fit for the decibel-scaled channel gain with respect to the logarithmically scaled CF. Finally, considering the NFAF, it was found that the model of the inverse-Fourier transform of the exponentially decaying pulse, i.e., (5.7), provides a good fit for both LCs.

Finally, given the channel characteristics of the two UNB potential deployment scenarios in the 2.4 GHz band, it was shown that a VIRC-based channel emulator can certainly mimic the desired flat fading since $B_{\text{coh}}\big|_{\text{min}}$ is 0.5 MHz. Moreover, regarding the CEH, the propagation channel inside the VIRC can mimic a near-Rayleigh channel with a Rician K-factor as low as −17 dB, and thereby—with an appropriate external setup of attenuators—it is capable of supporting a wide range of the K-factor. Additionally, the Doppler spectrum of the propagation channel inside the VIRC matches the Bell model with a CT that can be easily tuned to any value in the range 30–120 ms by changing the RS and the LC. However, for the UNB second potential deployment scenario of a WBAN on-body to off-body channel, a VIRC-based channel emulator is not capable of accurately emulating the CEH or the Doppler spectrum. Moreover, for the UNB first potential deployment scenario of a campus indoor environment, the VIRC-based channel emulator is capable of mimicking the desired models of the first- and second-order temporal characteristics, but with a lower limit on how slow the emulated fading can be. Therefore, it can be concluded that the VIRC can roughly be used as a UNB channel emulator in general, with a limited emulation capabilities in particular.

6

CONCLUSIONS AND FUTURE WORK

The majority of the wireless sensor network (WSN) applications within the Low-Power Wide-Area Networks (LPWANs) are characterized by latency tolerance, low throughput, and low cost, for which the Ultra-Narrowband (UNB) signaling scheme has emerged as one of the main contenders. The 868 MHz license-free band is currently shared by several LPWAN technologies including the UNB signaling scheme. However, the emission regulations of this band impose a harsh upper limit on the duty cycle, resulting in a severe cap on the carried throughput, i.e., number of messages a sensor node can send per day. On the other hand, the 2.4 GHz ISM band does not have such a limit. Besides, it offers a much larger bandwidth. Therefore, as one of the work packages in the Slow Wireless project, this thesis investigated the feasibility of alternatively deploying the UNB signaling scheme in the 2.4 GHz band. The investigation was carried out in terms of energy efficiency and wireless coexistence. The thesis also investigated the potentiality of utilizing the Vibrating Intrinsic Reverberation Chamber (VIRC) as an experimental environment in which proposed solutions to the potential challenges of this deployment can be investigated.

In this chapter, we summarize the research questions as well as the corresponding contributions and the main conclusions. Moreover, recommendations for future research are also suggested. The main goal of the Slow Wireless project is to investigate the feasibility of—and ultimately accomplish—a deployment of the UNB signaling scheme in the 2.4 GHz ISM band. Therefore, this thesis has considered the following research goals.

6.1. INVESTIGATION OF UNB ENERGY EFFICIENCY

To maximize the energy efficiency of the sensor nodes in a WSN, the design of the communication link between the nodes and the base station typically involves optimizing the instantaneous data rate while solely considering the distribution of the power consumption among the different circuit blocks in the sensor node itself. In practice, however, the operating data rate must deviate from the theoretically optimized one to take into account several practical factors that stem from a deployment scenario

under interest, e.g., emission regulations and size constraints of the sensor node. Consequently, the feasibility of a UNB deployment—and thereby its potentially suitable deployment scenarios—in the 2.4 GHz band must then be investigated in terms of energy efficiency. Therefore, the first research question was formulated as follows.

- *When it comes to feasibility in terms of energy efficiency, what are the suitable deployment scenarios for the UNB signaling scheme in the 2.4 GHz band?*

In Chapter 2, we investigated the feasibility of a UNB deployment in the 2.4 GHz band in terms of energy efficiency, by determining the optimal bit rates for a wide range of deployment scenarios, i.e., link budgets and peak-power budgets. A comprehensive energy consumption model of the physical layer of the sensor node was developed for an asymmetric link in a star topology. Several power consumption models of different circuit blocks in the sensor node were combined and broken down into their primary variables. The main contribution of this chapter was developing an energy-efficiency optimization framework that takes into account several practical factors of different deployment scenarios in the 2.4 GHz band, including that of an energy-scavenging-powered sensor node. These practical factors are maximum allowable path loss (hence, link budget), size constraints (hence, timing-frequency accuracy and source-power limitation) and emission regulations (hence, radiated power and channel bandwidth). Finally, we applied the analysis to a numerical example of typical deployment parameters and design constants to gain more insight into the optimization process.

According to the analytically derived solution of developed optimization framework, the optimal bit rate can be determined—among others—by the ratio of the average power consumption of the analog circuits in the sensor node to the energy consumption per information bit of its digital circuits. As the ratio increases, this optimal bit rate increases as well. This is in agreement with the literature. However, based on our analysis, it was shown that in practice (i.e., by taking into account the practical factors) the optimal bit rate significantly deviates from the analytical one. It is mostly determined by the practical factors of the deployment scenario, namely, the link budget and the peak-power budget. Moreover, a large link budget and/or a very low limit on the peak-power consumption significantly shifts the optimal bit rate to a much lower value.

Finally, as demonstrated by the outcome of the developed optimization process, the UNB signaling scheme is an energy-efficient/convenient solution for two potential deployment scenarios of the low-throughput latency-tolerant WSNs. In the first one, the sensor nodes, e.g., reside in a large building that is served by a single base station. Moreover, the wireless link between the base station and the nodes typically covers a large distance and/or frequently experiences fading/obstruction. In the second one, the UNB represents a convenient ultra-low-power RF solution for the WSNs whose nodes are supposed to be tiny with a very harsh peak-power consumption limitation as, e.g., in energy-scavenging-powered sensor nodes.

DIRECTIONS FOR FURTHER RESEARCH

In this thesis, the optimization framework was not designed for a specific modulation scheme or media-access-control protocol. Moreover, it was dedicated to an asymmetric link of a star topology in which the link is always initiated by the sensor node. Additionally, an AWGN channel was assumed, and environmental interference was not considered. Therefore, it would be interesting to extend the optimization framework to consider a symmetric link of a multi-hop topology, as well as to limit its scope to a specific modulation-coding scheme and a suitable media-access-control protocol given the relevant models of the interference and the temporal-fading available in the literature. As such, this might lead to other potentially useful deployment scenarios for UNB in the 2.4 GHz band. Moreover, considering the UNB's second potential deployment scenario of an on-body to off-body link with energy-scavenging-powered sensors, an energy budget calculation is required to investigate the limitations and, thereby, the practicality of such a UNB application.

6.2. INVESTIGATION OF UNB WIRELESS COEXISTENCE

For the UNB signaling scheme to be widely adopted in the 2.4 GHz band, UNB has to be friendly to the pre-existing technologies. Bluetooth and Zigbee can overcome UNB interference by employing adaptive frequency hopping and spread spectrum technique, respectively. However, most Wi-Fi versions are OFDM based and, thereby, are less immune to UNB interference. Moreover, Wi-Fi networks are almost everywhere, and their desirable 24/7 uninterrupted coverage may become subject to frequent outages caused by UNB interference in case of rapid deployment of the UNB signaling scheme in the 2.4 GHz band. For instance, a 200-bit packet transmitted, e.g., using 100 bit/s of instantaneous data rate, will fully occupy 2 s. Therefore, a single UNB packet may cause interference to thousands of Wi-Fi packets transferred by nearby Wi-Fi networks. Consequently, the feasibility of a UNB deployment in the 2.4 GHz band must then be investigated in terms of wireless coexistence towards Wi-Fi networks. Therefore, the second research question was formulated as follows.

- *In the case of a future deployment in the 2.4 GHz band, how friendly is the UNB signaling scheme to the IEEE 802.11-based networks (a.k.a. Wi-Fi)?*

In Chapter 3, we investigated the feasibility of a UNB deployment in the 2.4 GHz band in terms of wireless coexistence, by focusing our investigation on the impact of the interference from an emission regulation-obedient UNB signaling scheme on nearby Wi-Fi links. The main contribution of this chapter was developing a systematic and thorough methodology for the empirical investigation of the UNB interference on the individual Wi-Fi mechanisms spanning from the physical layer up to the transport layer. The methodology is based on the approach of a worst-case interfering scenario, and it follows three investigation steps. The first step is dedicated to studying the impact of the UNB interference on the Wi-Fi clear-channel-assessment (CCA) mechanism. Next, the effect on the Wi-Fi beacon delivery rate is assessed in the second step. The last and third step is dedicated to investigating the throughput performance of the

transport layer over a Wi-Fi link under the UNB interference. The methodology was then practically applied for a specific measurement campaign of a TCP stream over an IEEE 802.11n link that was interfered by 100 bit/s UNB signals. Multiple commercial Wi-Fi devices from different vendors were tested following the developed methodology. Two situations of single and multiple simultaneous UNB interferers were individually considered. From the standpoint of envelope constancy, two distinct modulation schemes for UNB interfering signals were individually accounted for: on-off-keying (OOK) and Gaussian minimum-shift-keying (GMSK). The cases of interfering with all types of Wi-Fi subcarriers were individually studied as well.

Based on the gained insights that the Wi-Fi pilot subcarriers are the most vulnerable to the UNB interference, and to promote wireless coexistence, 17 sub-bands were recommended for the UNB signaling scheme in the 2.4 GHz band. If UNB communications only utilize these recommended sub-bands and given that a drop to 75% of the maximum Wi-Fi throughput is acceptable, then wireless coexistence is possible in the following two scenarios in which the received Wi-Fi power is −36 dBm: (*i*) a single UNB interferer employing an OOK-modulation scheme while SIR is greater than 30 dB, or (*ii*) up-to-seven simultaneous UNB interferers interfering with different data subcarriers and employing arbitrary modulation schemes while the lowest SIR is still greater than 36 dB.

6

DIRECTIONS FOR FURTHER RESEARCH

In this thesis, the methodology was limited to conducting the investigation inside the anechoic chamber, in which the multipath components are ideally removed. The obtained results shall, therefore, be considered as offering an upper bound of the performance for single-input single-output (SISO) Wi-Fi links. However, multipath propagation is typically expected in real-world environments. As such, it would be interesting to carry out the investigation in such environments. However, this requires designing a reproducible and interference-free environment as well as developing another systematic methodology to consider multiple-input multiple-output (MIMO) based systems.

The investigation in real-world deployments has to consider two aspects. The first one is the practical propagation channel between the UNB interfering nodes and nearby single-antenna/multi-antenna Wi-Fi devices. The second aspect is that the techniques that are implemented in MIMO-based Wi-Fi devices have to be investigated from two perspectives regarding wireless coexistence in general, but also regarding the impact of the UNB interference in particular. The first perspective is that the performance of the MIMO techniques that are designed to combat interference has to be investigated on how good they are in doing so against the UNB interference. The second perspective is that the impact of the UNB interference on the performance of the MIMO techniques that are designed to combat/exploit multipath propagation has to be investigated as well. Having said that, however, the IEEE 802.11n version that was considered in our empirical study does not implement interference nulling, and most vendors opted out of the optional transmit beamforming. On the other hand, the other MIMO techniques in the 802.11n version, namely, diversity and multiplexing, are not intended

for interference mitigation. Instead, they are for combating and exploiting multipath propagation. Therefore, it would be indeed beneficial to investigate the behavior of the CCA mechanism and the throughput performance of Wi-Fi links while utilizing such MIMO techniques when the UNB interfering signal is deeply faded at least at one of the receiving antennas of Wi-Fi device.

6.3. DEVELOPMENT OF A UNB CHANNEL EMULATOR

The investigation of the challenges facing the UNB deployment in the 2.4 GHz band, along with any corresponding proposed solutions, can be conducted in controlled experimental environments, which guarantee the bare-minimum requirement for repeatability as opposed to real-world environments. One such controlled environment is the Vibrating Intrinsic Reverberation Chamber (VIRC) which—compared to classical reverberation chambers—is more cost effective, has a simpler structure to assemble/disassemble, is a more efficient environment at generating multipath conditions, and is capable of producing more uncorrelated samples. Therefore, the VIRC can serve as a cost-effective channel emulator for the UNB signaling scheme in the 2.4 GHz band. However, a relevant characterization must first be conducted on the chamber itself to investigate whether it can closely mimic the wireless propagation channel of the real-world environment under interest. Therefore, the third research question was formulated as follows.

- *Considering the potential UNB deployment scenarios, to what extent can the VIRC be used to emulate the wireless propagation channel that a UNB-based sensor node would experience?*

In Chapter 4, we developed a measurement procedure for the empirical characterization of the propagation channel inside the VIRC for the testing of wireless baseband algorithms of narrowband SISO systems. The main contribution of this chapter was developing a systematic and accuracy-driven measurement and estimation methodology for the empirical investigation of the channel first- and second-order temporal and spectral characteristics that is applicable for both the classical and VIRC chambers as well as for both electromagnetic compatibility (EMC) and over-the-air (OTA) testing. Moreover, the methodology takes into consideration the effect of three VIRC variables: carrier frequency (CF), rotational speed (RS) of the VIRC motors, and VIRC loading condition (LC, i.e., loading the chamber with RF absorbers). Before a thorough VIRC characterization, the methodology was then used in practice to preliminarily examine whether a VIRC preloading is necessary—and to what extent it is successful—so that the channel envelope histogram (CEH) resembles a theoretical Rician distribution.

By analyzing the measurement results of the preliminary investigation, a considerable skewness was demonstrated between the theoretical Rician distribution and the CEH before preloading. However, by mounting an RF absorber on the internal side of the VIRC hatch, this slight preloading was successful in getting the CEH to closely resemble a near-Rayleigh distribution with a Rician K-factor below -23 dB in the 2.4 GHz band.

Therefore, with an appropriate external setup of attenuators as part of future work, it is capable of supporting a wide range of the Rician K-factor.

In Chapter 5, we investigated the feasibility of using the VIRC in the 2.4 GHz band as a UNB channel emulator that is capable of accurately and easily emulating a wide dynamic range for the Doppler spread (or coherence time) and the Rician K-factor. The main contribution of this chapter was applying the systematic methodology proposed in the previous chapter in a thorough, joint and empirical characterization of the VIRC in terms of various channel first- and second-order temporal and spectral characteristics with respect to the VIRC variables. The investigated characteristics that are relevant to UNB were—among others—the coherence time, Doppler spectrum, coherence bandwidth, Rician K-factor, and channel gain. Next, we proposed a number of mathematical models to fit the behavior of various of the investigated characteristics. These models are essential to correctly configure the VIRC variables in order to accurately emulate a desired UNB channel characteristic of interest.

Finally, based on the gained insights from analyzing the measurement results and the proposed models, we examined the feasibility of using the VIRC as a UNB channel emulator. It was shown that a VIRC-based channel emulator can certainly mimic the desired flat fading. Moreover, regarding the CEH, the VIRC can mimic a near-Rayleigh channel with a Rician K-factor below -17 dB. Additionally, the Doppler spectrum of the VIRC propagation channel matches the Bell model with a coherence time that can be tuned in the range 30–120 ms. However, given the channel characteristics of the two UNB potential deployment scenarios in the 2.4 GHz band, a VIRC-based channel emulator is most suitable for the first potential deployment scenario. Moreover, it was concluded that the VIRC can be used as a rough UNB channel emulator in general, with limited emulation capabilities in particular.

DIRECTIONS FOR FURTHER RESEARCH

Based on the proposed fitting models and by utilizing an external set of attenuators, a channel emulator for the testing of wireless baseband algorithms of narrowband SISO systems will be developed using the assembled framework described in this thesis. Moreover, to accomplish a complete experimental framework for LPWAN in general and UNB (this thesis) in particular, it would be beneficial to investigate the feasibility of developing a standalone modular (i.e., embedded SDR-based) RF transceiver in terms of cost and power budgets.

The developed measurement and estimation methodology in this thesis was limited to investigating narrowband SISO propagation channels inside the VIRC. Therefore, yet beyond the scope of this thesis, it would be interesting to expand the methodology to consider wideband as well as MIMO channels. Moreover, it would also be interesting to extend the VIRC empirical characterization and modeling to consider much higher frequency bands.

REFERENCES

[1] S. B. Baker, W. Xiang, and I. Atkinson. “Internet of Things for Smart Healthcare: Technologies, Challenges, and Opportunities”. In: *IEEE Access* 5 (2017), pp. 26521–26544. DOI: 10.1109/ACCESS.2017.2775180.

[2] P. Rizwan, K. Suresh, and M. R. Babu. “Real-time smart traffic management system for smart cities by using Internet of Things and big data”. In: *2016 International Conference on Emerging Technological Trends (ICETT)*. 2016, pp. 1–7. DOI: 10.1109/ICETT.2016.7873660.

[3] M. Chui, M. Loffler, and R. Roberts. *The internet of things*. Tech. rep. McKinsey Quarterly, 2010, pp. 1–9.

[4] *IoT Analytics website*. Accessed on Feb. 10, 2023. URL: https://iot-analytics.com/number-connected-iot-devices.

[5] J. M. Kahn, R. H. Katz, and K. S. Pister. “Next century challenges: mobile networking for "Smart Dust"”. In: *Proceedings of the 5th annual ACM/IEEE international conference on Mobile computing and networking*. 1999, pp. 271–278.

[6] A. Ali, Y. Ming, S. Chakraborty, and S. Iram. “A Comprehensive Survey on Real-Time Applications of WSN”. In: *Future Internet* 9.4 (2017). DOI: 10.3390/fi9040077.

[7] L. M. Borges, F. J. Velez, and A. S. Lebres. “Survey on the Characterization and Classification of Wireless Sensor Network Applications”. In: *IEEE Communications Surveys and Tutorials* 16.4 (2014), pp. 1860–1890. DOI: 10.1109/COMST.2014.2320073.

[8] M. Majid, S. Habib, A. R. Javed, M. Rizwan, G. Srivastava, T. R. Gadekallu, and J. C.-W. Lin. “Applications of Wireless Sensor Networks and Internet of Things Frameworks in the Industry Revolution 4.0: A Systematic Literature Review”. In: *Sensors* 22.6 (2022). DOI: 10.3390/s22062087.

[9] P. Prasad. “Recent trend in wireless sensor network and its applications: a survey”. In: *Sensor Review* 35.2 (2015), pp. 229–236. DOI: 10.1108/SR-08-2014-683.

[10] W. Dargie and C. Poellabauer. *Fundamentals of wireless sensor networks: theory and practice*. John Wiley & Sons, 2010.

[11] M. Vaezi, A. Azari, S. R. Khosravirad, M. Shirvanimoghaddam, M. M. Azari, D. Chasaki, and P. Popovski. “Cellular, Wide-Area, and Non-Terrestrial IoT: A Survey on 5G Advances and the Road Toward 6G”. In: *IEEE Communications Surveys and Tutorials* 24.2 (2022), pp. 1117–1174. DOI: 10.1109/COMST.2022.3151028.

[12] R. Sanchez-Iborra and M.-D. Cano. “State of the Art in LP-WAN Solutions for Industrial IoT Services”. In: *Sensors* 16.5 (2016). ISSN: 1424-8220. DOI: 10.3390/s16050708.

[13] S. Phoha, T. F. La Porta, and C. Griffin. *Sensor network operations*. John Wiley & Sons, 2007.

[14] B. S. Chaudhari, M. Zennaro, and S. Borkar. “LPWAN Technologies: Emerging Application Characteristics, Requirements, and Design Considerations”. In: *Future Internet* 12.3 (2020). DOI: 10.3390/fi12030046.

[15] S. Persia and L. Rea. “Next generation M2M Cellular Networks: LTE-MTC and NB-IoT capacity analysis for Smart Grids applications”. In: *2016 AEIT International Annual Conference (AEIT)*. 2016, pp. 1–6. DOI: 10.23919/AEIT.2016.7892789.

[16] J. Gozalvez. “New 3GPP Standard for IoT [Mobile Radio]”. In: *IEEE Vehicular Technology Magazine* 11.1 (2016), pp. 14–20. DOI: 10.1109/MVT.2015.2512358.

[17] *LoRa Alliance website*. Accessed on Feb. 10, 2023. URL: https://lora-alliance.org/about-lorawan/.

[18] M. Aref and A. Sikora. “Free space range measurements with Semtech Lora technology”. In: *2014 2nd International Symposium on Wireless Systems within the Conferences on Intelligent Data Acquisition and Advanced Computing Systems*. 2014, pp. 19–23. DOI: 10.1109/IDAACS-SWS.2014.6954616.

[19] *Sigfox website*. Accessed on Feb. 10, 2023. URL: https://www.sigfox.com/en/what-sigfox/technology.

[20] G. Margelis, R. Piechocki, D. Kaleshi, and P. Thomas. “Low Throughput Networks for the IoT: Lessons learned from industrial implementations”. In: *Proc. IEEE World Forum on Internet of Things (WF-IoT)*. 2015, pp. 181–186.

[21] U. Raza, P. Kulkarni, and M. Sooriyabandara. “Low Power Wide Area Networks: An Overview”. In: *IEEE Communications Surveys and Tutorials* 19.2 (2017), pp. 855–873. DOI: 10.1109/COMST.2017.2652320.

[22] K. Mekki, E. Bajic, F. Chaxel, and F. Meyer. “A comparative study of LPWAN technologies for large-scale IoT deployment”. In: *ICT Express* 5.1 (2019), pp. 1–7. ISSN: 2405-9595. DOI: 10.1016/j.icte.2017.12.005.

[23] K. E. Nolan, W. Guibene, and M. Y. Kelly. “An evaluation of low power wide area network technologies for the Internet of Things”. In: *Proc. Int. Wireless Communications and Mobile Computing Conference (IWCMC)*. Sept. 2016, pp. 439–444.

[24] C. Gomez, J. C. Veras, R. Vidal, L. Casals, and J. Paradells. “A Sigfox Energy Consumption Model”. In: *Sensors* 19.3 (2019). ISSN: 1424-8220. DOI: 10.3390/s19030681.

[25] R. S. Sinha, Y. Wei, and S.-H. Hwang. “A survey on LPWA technology: LoRa and NB-IoT”. In: *ICT Express* 3.1 (2017), pp. 14–21. DOI: 10.1016/j.icte.2017.03.004.

[26] F. Adelantado, X. Vilajosana, P. Tuset-Peiro, B. Martinez, J. Melia-Segui, and T. Watteyne. “Understanding the Limits of LoRaWAN”. In: *IEEE Communications Magazine* 55.9 (2017), pp. 34–40. DOI: 10.1109/MCOM.2017.1600613.

[27] C. B. Mwakwata, H. Malik, M. Mahtab Alam, Y. Le Moullec, S. Parand, and S. Mumtaz. “Narrowband Internet of Things (NB-IoT): From Physical (PHY) and Media Access Control (MAC) Layers Perspectives”. In: *Sensors* 19.11 (2019). DOI: 10.3390/s19112613.

[28] K. Mekki, E. Bajic, F. Chaxel, and F. Meyer. “Overview of Cellular LPWAN Technologies for IoT Deployment: Sigfox, LoRaWAN, and NB-IoT”. In: *2018 IEEE International Conference on Pervasive Computing and Communications Workshops (PerCom Workshops)*. 2018, pp. 197–202. DOI: 10.1109/PERCOMW.2018.8480255.

[29] F. J. Oppermann, C. A. Boano, and K. Römer. “A decade of wireless sensing applications: Survey and taxonomy”. In: *The Art of Wireless Sensor Networks* (2014), pp. 11–50. DOI: 10.1007/978-3-642-40009-4_2.

[30] H. Wang and A. O. Fapojuwo. “A Survey of Enabling Technologies of Low Power and Long Range Machine-to-Machine Communications”. In: *IEEE Communications Surveys and Tutorials* 19.4 (2017), pp. 2621–2639.

[31] Q. Du, W. Zhao, W. Li, X. Zhang, B. Sun, H. Song, P. Ren, L. Sun, and Y. Wang. “Massive access control aided by knowledge-extraction for co-existing periodic and random services over wireless clinical networks”. In: *Journal of Medical Systems* 40.171 (2016), pp. 1–8. DOI: 10.1007/s10916-016-0506-5.

[32] J. Suhonen, M. Kohvakka, M. Hännikäinen, and T. D. Hämäläinen. “Design, implementation, and experiments on outdoor deployment of wireless sensor network for environmental monitoring”. In: *SAMOS*. Springer. 2006, pp. 109–121.

[33] Y.-J. Chong, S.-J. You, M.-S. Kang, M.-S. Song, and S.-H. Oh. “A frequency offset compensation method for ultra narrowband digital wireless modems”. In: *2004 IEEE 15th International Symposium on Personal, Indoor and Mobile Radio Communications (IEEE Cat. No.04TH8754)*. Vol. 2. 2004, pp. 1370–1374. DOI: 10.1109/PIMRC.2004.1373922.

[34] L. Boucher, Y. Jolly, J. Lodge, and S. Dery. “A narrowband tactical ratio for the VHF and UHF frequency bands”. In: *IEEE Conference on Military Communications*. Vol. 3. 1990, pp. 1271–1275. DOI: 10.1109/MILCOM.1990.117613.

[35] M.-T. Do, C. Goursaud, and J.-M. Gorce. “Interference Modelling and Analysis of Random FDMA scheme in Ultra Narrowband Networks”. In: *AICT 2014*. Paris, France, 2014. URL: https://hal.science/hal-01096493.

[36] M. Anteur, V. Deslandes, N. Thomas, and A.-L. Beylot. “Modeling and performance analysis of ultra narrow band system for M2M”. In: *2016 8th Advanced Satellite Multimedia Systems Conference and the 14th Signal Processing for Space Communications Workshop (ASMS/SPSC)*. 2016, pp. 1–6. DOI: 10.1109/ASMS-SPSC.2016.7601549.

[37] M.-T. Do, C. Goursaud, and J.-M. Gorce. “On the benefits of random FDMA schemes in ultra narrow band networks”. In: *2014 12th International Symposium on Modeling and Optimization in Mobile, Ad Hoc, and Wireless Networks (WiOpt)*. 2014, pp. 672–677. DOI: 10.1109/WIOPT.2014.6850364.

[38] M. Anteur, V. Deslandes, N. Thomas, and A.-L. Beylot. “Ultra Narrow Band Technique for Low Power Wide Area Communications”. In: *2015 IEEE Global Communications Conference (GLOBECOM)*. 2015, pp. 1–6. DOI: 10.1109/GLOCOM.2015.7417420.

[39] C. Goursaud and Y. Mo. “Random unslotted time-frequency ALOHA: Theory and application to IoT UNB networks”. In: *2016 23rd International Conference on Telecommunications (ICT)*. 2016, pp. 1–5. DOI: 10.1109/ICT.2016.7500489.

[40] B. Reynders, W. Meert, and S. Pollin. “Range and coexistence analysis of long range unlicensed communication”. In: *2016 23rd International Conference on Telecommunications (ICT)*. 2016, pp. 1–6. DOI: 10.1109/ICT.2016.7500415.

[41] Y. Mo, C. Goursaud, and J. M. Gorce. “Theoretical analysis of UNB-based IoT networks with path loss and random spectrum access”. In: *Proc. IEEE Int. Symp. on Personal, Indoor and Mobile Radio Comm. (PIMRC)*. 2016, pp. 1–6.

[42] R. Kalfus and T. Hégr. “Ultra narrow band radio technology in high-density built-up areas”. In: *Communications in Computer and Information Science* 639 (2016), pp. 663–676. DOI: 10.1007/978-3-319-46254-7_54.

[43] Y. Mo, M.-T. Do, C. Goursaud, and J.-M. Gorce. “Optimization of the predefined number of replications in a Ultra Narrow Band based IoT network”. In: *2016 Wireless Days (WD)*. 2016, pp. 1–6. DOI: 10.1109/WD.2016.7461514.

[44] C. Goursaud and J.-M. Gorce. “Dedicated networks for IoT: PHY / MAC state of the art and challenges”. In: *EAI endorsed transactions on Internet of Things* (2015). DOI: 10.4108/eai.26-10-2015.150597.

[45] *Telensa website*. Accessed on Feb. 10, 2023. URL: https://info.telensa.com/hubfs/Resources%5C%20page%5C%20files/datasheet_telensa_planet_network.pdf.

[46] *Weightless Alliance website*. Accessed on Feb. 10, 2023. URL: https://www.weightless-alliance.org/technology.

[47] *Waviot website*. Accessed on Feb. 10, 2023. URL: https://waviot.com/technology/nb-fi-specification.

[48] *Low Throughput Networks (LTN); Protocols and Interfaces*, Group Specification, ETSI GS LTN 003 V1.1.1. 2014.

[49] *Electromagnetic compatibility and Radio spectrum Matters (ERM)*, ETSI Std. EN 300 220-1 V2.4.1. 2012.

[50] CEPT, ECC. *Relating to the use of Short Range Devices (SRD)*. ERC Recommendation 70-03, 2018.

[51] C. Fourtet and B. Ponsard. “An introduction to Sigfox radio system”. In: *LPWAN Technologies for IoT and M2M Applications*. Ed. by B. S. Chaudhari and M. Zennaro. Academic Press, 2020, pp. 103–118. DOI: 10.1016/B978-0-12-818880-4.00005-3.

[52] M. Centenaro, L. Vangelista, A. Zanella, and M. Zorzi. “Long-range communications in unlicensed bands: the rising stars in the IoT and smart city scenarios”. In: *IEEE Wireless Communications* 23.5 (2016), pp. 60–67. DOI: 10.1109/MWC.2016.7721743.

[53] K. Mikhaylov, M. Stusek, P. Masek, R. Fujdiak, R. Mozny, S. Andreev, and J. Hosek. “Communication Performance of a Real-Life Wide-Area Low-Power Network Based on Sigfox Technology”. In: *ICC 2020 - 2020 IEEE International Conference on Communications (ICC)*. 2020, pp. 1–6. DOI: 10.1109/ICC40277.2020.9148645.

[54] S. Haykin and M. Moher. *An Introduction to Analog and Digital Communications*. Wiley, 2007.

[55] T. S. Rappaport. *Wireless Communications: Principles and Practice*. 2nd ed. Upper Saddle River, NJ, USA: Prentice-Hall, 2002.

[56] *ZERO project: Towards Energy Autonomous Systems for IoT*. Accessed on Feb. 10, 2023. URL: https://www.nwo.nl/en/researchprogrammes/perspectief/previous-awards/zero-towards-energy-autonomous-systems-iot.

[57] *Green Sensors project*. Accessed on Feb. 10, 2023. URL: https://www.4tu.nl/greensensors/.

[58] Y. Mo, M. T. Do, C. Goursaud, and J.-M. Gorce. “Up-link capacity derivation for ultra-narrow-band IoT wireless networks”. In: *International Journal of Wireless Information Networks* 24 (2017), pp. 300–316. DOI: 10.1007/s10776-017-0361-4.

[59] *Mordor Intelligence website*. Accessed on Feb. 10, 2023. URL: https://www.mordorintelligence.com/industry-reports/global-crystal-oscillator-market-industry.

[60] S. Hellan. “CC11xx Sensitivity versus Frequency Offset and Crystal Accuracy”. In: *Design Note DN005, Texas Instruments, Dallas, Texas* (2009).

[61] D. Lachartre, F. Dehmas, C. Bernier, C. Fourtet, L. Ouvry, F. Lepin, E. Mercier, S. Hamard, L. Zirphile, S. Thuries, and F. Chaix. “7.5 A TCXO-less 100Hz-minimum-bandwidth transceiver for ultra-narrow-band sub-GHz IoT cellular networks”. In: *2017 IEEE International Solid-State Circuits Conference (ISSCC)*. 2017, pp. 134–135. DOI: 10.1109/ISSCC.2017.7870297.

[62] S. Safapourhajari and A. B. J. Kokkeler. “Frequency offset tolerant demodulation for low data rate and narrowband wireless sensor node”. In: *2017 11th International Conference on Signal Processing and Communication Systems (ICSPCS)*. 2017, pp. 1–8. DOI: 10.1109/ICSPCS.2017.8270451.

[63] S. Safapourhajari and A. B. J. Kokkeler. “Demodulation of Double Differential PSK in Presence of Large Frequency Offset and Wide Filter”. In: *2018 IEEE 87th Vehicular Technology Conference (VTC Spring)*. 2018, pp. 1–5. DOI: 10.1109/VTCSpring.2018.8417526.

[64] S. Safapourhajari and A. B. J. Kokkeler. “Low Complexity Synchronization for Offset Tolerant DFT-Based BFSK Demodulator”. In: *2019 IEEE 20th International Workshop on Signal Processing Advances in Wireless Communications (SPAWC)*. 2019, pp. 1–5. DOI: 10.1109/SPAWC.2019.8815394.

[65] S. Safapourhajari and A. B. J. Kokkeler. “On the Low Complexity Implementation of the DFT-Based BFSK Demodulator for Ultra-Narrowband Communications”. In: *IEEE Access* 8 (2020), pp. 146666–146682. DOI: 10.1109/ACCESS.2020.3013986.

[66] L. Ahumada, R. Feick, R. Valenzuela, and C. Morales. “Measurement and characterization of the temporal behavior of fixed wireless links”. In: *IEEE Transactions on Vehicular Technology* 54.6 (2005), pp. 1913–1922. DOI: 10.1109/TVT.2005.858189.

[67] A. Abdi, K. Wills, H. Barger, M.-S. Alouini, and M. Kaveh. “Comparison of the level crossing rate and average fade duration of Rayleigh, Rice and Nakagami fading models with mobile channel data”. In: *52nd Vehicular Technology Conference*. Vol. 4. 2000, pp. 1850–1857. DOI: 10.1109/VETECF.2000.886139.

[68] G. Zhou, Y. Kim, and G. Giannakis. “Estimation and equalization of time-selective fading channels”. In: *Conference Record of the Thirty-Third Asilomar Conference on Signals, Systems, and Computers (Cat. No.CH37020)*. Vol. 1. IEEE. 1999, pp. 248–252. DOI: 10.1109/ACSSC.1999.832331.

[69] K. Yoshida, S. Kameda, and N. Suematsu. “Effect of Estimation Timing Error on Pre-TDE for Narrowband Uplink NOMA”. In: *2020 23rd International Symposium on Wireless Personal Multimedia Communications (WPMC)*. 2020, pp. 1–6. DOI: 10.1109/WPMC50192.2020.9309481.

[70] J. Petäjäjärvi, K. Mikhaylov, M. Pettissalo, J. Janhunen, and J. Iinatti. “Performance of a low-power wide-area network based on LoRa technology: Doppler robustness, scalability, and coverage”. In: *International Journal of Distributed Sensor Networks* 13.3 (2017), p. 1550147717699412. DOI: 10.1177/1550147717699412.

[71] I. Rodriguez, M. Lauridsen, K. Arvidsson, J. Kvarnstrand, M. Andersson, and P. Mogensen. “Testing of low-power wide-area technologies in controlled propagation environments”. In: *IET Conference Proceedings* (2017). DOI: 10.1049/cp.2017.0271.

[72] Y. Watanabe and Y. Shoji. “A Study on Packet Repetition Format for Advertising-Based IoT Data Transmission System”. In: *2017 IEEE Globecom Workshops (GC Wkshps)*. 2017, pp. 1–7. DOI: 10.1109/GLOCOMW.2017.8269113.

[73] M. Anteur, N. Thomas, V. Deslandes, and A.-L. Beylot. “On the performance of UNB for machine-to-machine low earth orbit (LEO) satellite communications”. In: *International Journal of Satellite Communications and Networking* 37.1 (2019), pp. 56–71. DOI: 10.1002/sat.1285.

[74] S.-Y. Wang, J.-E. Chang, H. Fan, and Y.-H. Sun. “Comparing the performance of NB-IoT, LTE Cat-M1, Sigfox, and LoRa for IoT end devices moving at high speeds in the air”. In: *Journal of Signal Processing Systems* 94 (2022), pp. 81–99. DOI: 10.1007/s11265-021-01660-4.

[75] L. Oliveira, J. J. Rodrigues, S. A. Kozlov, R. A. Rabêlo, and V. Furtado. “Performance assessment of long-range and Sigfox protocols with mobility support”. In: *International Journal of Communication Systems* 32.13 (2019), e3956. DOI: 10.1002/dac.3956.

[76] S. Safapourhajari and A. B. J. Kokkeler. “Offset Tolerant Demodulator for Frequency/Phase Modulation in Time-Varying Channel”. In: *2019 IEEE Wireless Communications and Networking Conference (WCNC)*. 2019, pp. 1–6. DOI: 10.1109/WCNC.2019.8886086.

[77] Y. Mo, C. Goursaud, and J.-M. Gorce. “Multiple Base Stations Diversity for UNB Systems: Theoretical Analysis and Performances”. In: *2018 International Symposium on Networks, Computers and Communications (ISNCC)*. 2018, pp. 1–6. DOI: 10.1109/ISNCC.2018.8531010.

[78] Y. MO, C. GOURSAUD, and J.-M. GORCE. “Uplink Multiple Base Stations Diversity for UNB based IoT networks”. In: *2018 IEEE Conference on Antenna Measurements and Applications (CAMA)*. 2018, pp. 1–4. DOI: 10.1109/CAMA.2018.8530530.

[79] M. J. Farooq and Q. Zhu. “Optimal dynamic contract for spectrum reservation in mission-critical UNB-IoT systems”. In: *2018 16th International Symposium on Modeling and Optimization in Mobile, Ad Hoc, and Wireless Networks (WiOpt)*. 2018, pp. 1–6. DOI: 10.23919/WIOPT.2018.8362861.

[80] H. Mroue, A. Nasser, S. Hamrioui, B. Parrein, E. Motta-Cruz, and G. Rouyer. “MAC layer-based evaluation of IoT technologies: LoRa, SigFox and NB-IoT”. In: *2018 IEEE Middle East and North Africa Communications Conference (MENACOMM)*. 2018, pp. 1–5. DOI: 10.1109/MENACOMM.2018.8371016.

[81] Y. Wang, G. Li, H. Yousaf, and G. Lyu. “A Study of the Collision Probability for R-FTMA Ultra-Narrowband IoT Networks”. In: *2018 IEEE 4th International Conference on Computer and Communications (ICCC)*. 2018, pp. 845–851. DOI: 10.1109/CompComm.2018.8780809.

[82] G. Hattab and D. Cabric. “Spectrum Sharing Protocols based on Ultra-Narrowband Communications for Unlicensed Massive IoT”. In: *Proc. IEEE International Symposium on Dynamic Spectrum Access Networks (DySPAN)*. Oct. 2018, pp. 1–10.

[83] Y. Mo, C. Goursaud, and J.-M. Gorce. “On the benefits of successive interference cancellation for ultra narrow band networks: Theory and application to IoT”. In: *2017 IEEE International Conference on Communications (ICC)*. 2017, pp. 1–6. DOI: 10.1109/ICC.2017.7996900.

[84] M. Lauridsen, B. Vejlgaard, I. Z. Kovacs, H. Nguyen, and P. Mogensen. “Interference Measurements in the European 868 MHz ISM Band with Focus on LoRa and SigFox”. In: *2017 IEEE Wireless Communications and Networking Conference (WCNC)*. 2017, pp. 1–6. DOI: 10.1109/WCNC.2017.7925650.

[85] M. A. Ben Temim, G. Ferré, and R. Tajan. “Analysis of the Coexistence of Ultra Narrow Band and Spread Spectrum Technologies in ISM Bands”. In: *Ubiquitous Networking*. Ed. by O. Habachi, V. Meghdadi, E. Sabir, and J.-P. Cances. Cham: Springer International Publishing, 2020, pp. 56–67. DOI: 10.1007/978-3-030-58008-7_5.

[86] *Harmonized European Standard*, ETSI Std. EN 300 440 v2.2.1. 2018.

[87] *Semtech Corporation, "SX1280/SX1281/SX1282 Long Range Low Power 2.4 GHz Transceiver with Ranging Capability,"* Accessed on Feb. 10, 2023. URL: https://www.semtech.com/products/wireless-rf/lora-connect/sx1280.

[88] *Ingenu website*. Accessed on Feb. 10, 2023. URL: https://www.ingenu.com/technology/.

[89] *Ingenu, "How RPMA Works. A White Paper by Ingenu,"* Accessed on Feb. 10, 2023. URL: https://www.ingenu.com/wp-content/uploads/dlm_uploads/2015/08/How-RPMA-Works.pdf.

[90] L. Polak and J. Milos. “Performance analysis of LoRa in the 2.4 GHz ISM band: coexistence issues with Wi-Fi”. In: *Telecommunication Systems* 74.3 (2020), pp. 299–309. DOI: 10.1007/s11235-020-00658-w.

[91] K. Yamamoto and T. Sugiyama. “Separation Distance Performances between Ingenu and Wi-Fi Systems with Concatenated FEC”. In: *2021 International Conference on Information and Communication Technology Convergence (ICTC)*. 2021, pp. 413–415. DOI: 10.1109/ICTC52510.2021.9620764.

[92] N. Naik. “LPWAN Technologies for IoT Systems: Choice Between Ultra Narrow Band and Spread Spectrum”. In: *2018 IEEE International Systems Engineering Symposium (ISSE)*. 2018, pp. 1–8. DOI: 10.1109/SysEng.2018.8544414.

[93] R. Dutta, R. v. d. Zee, M. J. Bentum, and A. B. J. Kokkeler. “Choosing optimum noise figure and data rate in wireless sensor network radio transceivers”. In: *2011 IEEE International Conference on Communications (ICC)*. 2011, pp. 1–5. DOI: 10.1109/icc.2011.5963069.

[94] *Harmonized European Standard*, ETSI Std. EN 300 328 v2.2.2. 2019.

[95] S. Jin, A. Bettner, G. Chinn, K. Slattery, and D. Xiaopeng. “A study of platform EMI from LCD panels: Impact on wireless, root causes and mitigation methods”. In: *Proc. IEEE International Symposium on Electromagnetic Compatibility (EMC USA)*. Aug. 2006, pp. 626–631.

[96] J. Lee, H. H. Hsu, P. Davuluri, Y. Ho, and J. Chen. “Impact of broadband and out-of-band radio frequency interference (RFI) noise on WiFi performance”. In: *Proc. IEEE International Symposium on Electromagnetic Compatibility (EMC USA)*. Aug. 2017, pp. 453–457.

[97] T. Shimizu, Y. Matsumoto, K. Fujii, and A. Sugiura. “Performance evaluation of IEEE802.11a WLAN interfered by spread spectrum noises from a PC clock system”. In: *Proc. IEEE 2005 International Symposium on Microwave, Antenna, Propagation and EMC Technologies for Wireless Communications (MAPE'2005)*. Aug. 2005, pp. 1534–1537.

[98] R. Recanatini, F. Moglie, and V. Mariani Primiani. “Performance and immunity evaluation of complete WLAN systems in a large reverberation chamber”. In: *IEEE Transactions on Electromagnetic Compatibility* 55.5 (2013), pp. 806–815.

[99] K. Pietikäinen, A. Silvennoinen, M. Hall, and S. G. Häggman. “IEEE 802.11G tolerance to narrowband jamming”. In: *Proc. IEEE Military Communications Conference (MILCOM)*. Oct. 2005, pp. 1825–1830.

[100] T. Karhima, A. Silvennoinen, M. Hall, and S. G. Häggman. “IEEE 802.11b/g WLAN tolerance to jamming”. In: *Proc. IEEE Military Communications Conference (MILCOM)*. Oct. 2004, pp. 1364–1370.

[101] I. Harjula, J. Pinola, and J. Prokkola. “Performance of IEEE 802.11 based WLAN devices under various jamming signals”. In: *Proc. IEEE Military Communications Conference (MILCOM)*. Nov. 2011, pp. 2129–2135.

[102] W. Fan, I. Carton, P. Kyösti, and G. F. Pedersen. “Emulating Ray-Tracing Channels in Multiprobe Anechoic Chamber Setups for Virtual Drive Testing”. In: *IEEE Transactions on Antennas and Propagation* 64.2 (2016), pp. 730–739. DOI: 10.1109/TAP.2015.2498951.

[103] C. Lötbäck, A. Skårbratt, and C. Orlenius. “Extending the reverberation chamber using a channel emulator for characterisation of over-the-air performance of multiple-input- multiple-output wireless devices”. In: *IET Science, Measurement and Technology* 9.5 (2015), pp. 555–562. DOI: 10.1049/iet-smt.2014.0290.

[104] P. Corona, J. Ladbury, and G. Latmiral. “Reverberation-chamber research—then and now: A review of early work and comparison with current understanding”. In: *IEEE Transactions on Electromagnetic Compatibility* 44.1 (2002), pp. 87–94. DOI: 10.1109/15.990714.

[105] X. Chen, J. Tang, T. Li, S. Zhu, Y. Ren, Z. Zhang, and A. Zhang. “Reverberation Chambers for Over-the-Air Tests: An Overview of Two Decades of Research”. In: *IEEE Access* 6 (2018), pp. 49129–49143. DOI: 10.1109/ACCESS.2018.2867228.

[106] F. Leferink, J.-C. Boudenot, and W. van Etten. “Experimental results obtained in the vibrating intrinsic reverberation chamber”. In: *IEEE International Symposium on Electromagnetic Compatibility*. Vol. 2. 2000, pp. 639–644. DOI: 10.1109/ISEMC.2000.874695.

[107] R. Vogt-Ardatjew. “Electromagnetic fields in reverberant environments”. PhD thesis. the Netherlands: University of Twente, Nov. 2017. DOI: 10.3990/1.9789036544245.

[108] G. Andrieu, N. Meddeb, C. Jullien, and N. Ticaud. “Complete Framework for Frequency and Time-Domain Performance Assessment of Vibrating Intrinsic Reverberation Chambers”. In: *IEEE Transactions on Electromagnetic Compatibility* 62.5 (2020), pp. 1911–1920. DOI: 10.1109/TEMC.2020.2966741.

[109] D. M. Davenport, B. Deb, and F. J. Ross. “Wireless Propagation and Coexistence of Medical Body Sensor Networks for Ambulatory Patient Monitoring”. In: *2009 Sixth International Workshop on Wearable and Implantable Body Sensor Networks*. 2009, pp. 41–45. DOI: 10.1109/BSN.2009.8.

[110] A. Hithnawi, V. Kulkarni, S. Li, and H. Shafagh. “Controlled Interference Generation for Wireless Coexistence Research”. In: *Proceedings of the 2015 Workshop on Software Radio Implementation Forum*. SRIF ’15. New York, NY, USA: Association for Computing Machinery, 2015, pp. 19–24. DOI: 10.1145/2801676.2801682.

[111] M. Z. Mahfouz, A. Meijerink, and M. J. Bentum. “Optimum Design Parameters for Ultra-Low-Power RF Transceivers in Wireless Sensor Networks”. In: *2016 IEEE Global Communications Conference (GLOBECOM)*. 2016, pp. 1–7. DOI: 10.1109/GLOCOM.2016.7842112.

[112] M. Z. Mahfouz, A. Meijerink, and M. J. Bentum. “Ultra-Narrowband for Energy-Scavenging-Powered Wireless Sensor Networks”. In: *2017 IEEE 28th Annual International Symposium on Personal, Indoor, and Mobile Radio Communications (PIMRC)*. 2017, pp. 1–7. DOI: 10.1109/PIMRC.2017.8292562.

[113] M. Z. Mahfouz, A. B. J. Kokkeler, A. Meijerink, and A. A. Glazunov. “Impact of Ultra-Narrowband Interference on Wi-Fi Links: An Experimental Study”. In: *IEEE Transactions on Wireless Communications* 20.5 (2021), pp. 3016–3030. DOI: 10.1109/TWC.2020.3046765.

[114] M. Z. Mahfouz, R. Vogt-Ardatjew, A. B. J. Kokkeler, and A. A. Glazunov. “Measurement and Estimation Methodology for EMC and OTA Testing in the VIRC”. In: *IEEE Transactions on Electromagnetic Compatibility* 65.1 (2023), pp. 3–16. DOI: 10.1109/TEMC.2022.3218413.

[115] M. Z. Mahfouz, R. Vogt-Ardatjew, A. B. J. Kokkeler, and A. A. Glazunov. "Empirical Characterization and Modeling of the Propagation Channel inside the VIRC". *IEEE Access*, [in submission].

[116] T. Cuzanauskas, A. Medeisis, Y. Haddad, A. Anskaitis, L. C. Cremene, J. Sydor, O. D. Holland, and M. Nekovee. “Interference-aware power coordination game for ISM bands”. In: *2014 9th International Conference on Cognitive Radio Oriented Wireless Networks and Communications (CROWNCOM)*. 2014, pp. 389–394. DOI: 10.4108/icst.crowncom.2014.255367.

[117] I. Stojmenovic. *Handbook of sensor networks: algorithms and architectures*. Vol. 49. John Wiley & Sons, 2005.

[118] P. P. Mercier and A. P. Chandrakasan. *Ultra-low-power Short-range Radios*. Springer Cham, 2015. DOI: 10.1007/978-3-319-14714-7.

[119] J. R. Long, W. Wu, Y. Dong, Y. Zhao, M. Sanduleanu, J. Gerrits, and G. van Veenendaal. "Energy-efficient wireless front-end concepts for ultra lower power radio". In: *2008 IEEE Custom Integrated Circuits Conference*. 2008, pp. 587–590. DOI: 10.1109/CICC.2008.4672154.

[120] M. Honda, T. Sakurai, and M. Takamiya. "Wireless temperature and illuminance sensor nodes with energy harvesting from insulating cover of power cords for building energy management system". In: *2015 IEEE PES Asia-Pacific Power and Energy Engineering Conference (APPEEC)*. 2015, pp. 1–5. DOI: 10.1109/APPEEC.2015.7381080.

[121] Y. Syed, B. G. Hegde, T. V. Prabhakar, M. Manjunath, and K. J. Vinoy. "RF energy harvesting chip powered sensor node". In: *2016 IEEE International Conference on Electronics, Circuits and Systems (ICECS)*. 2016, pp. 748–751. DOI: 10.1109/ICECS.2016.7841310.

[122] G. Papotto, F. Carrara, A. Finocchiaro, and G. Palmisano. "A 90-nm CMOS 5-Mbps Crystal-Less RF-Powered Transceiver for Wireless Sensor Network Nodes". In: *IEEE Journal of Solid-State Circuits* 49.2 (2014), pp. 335–346. DOI: 10.1109/JSSC.2013.2285371.

[123] D. Pech, M. Brunet, H. Durou, P. Huang, V. Mochalin, Y. Gogotsi, P.-L. Taberna, and P. Simon. "Ultrahigh-power micrometre-sized supercapacitors based on onion-like carbon". In: *Nature nanotechnology* 5.9 (2010), pp. 651–654. DOI: 10.1038/nnano.2010.162.

[124] G. Chen, M. Fojtik, D. Kim, D. Fick, J. Park, M. Seok, M.-T. Chen, Z. Foo, D. Sylvester, and D. Blaauw. "Millimeter-scale nearly perpetual sensor system with stacked battery and solar cells". In: *2010 IEEE International Solid-State Circuits Conference - (ISSCC)*. 2010, pp. 288–289. DOI: 10.1109/ISSCC.2010.5433921.

[125] Y. Chen, N. Chiotellis, L.-X. Chuo, C. Pfeiffer, Y. Shi, R. G. Dreslinski, A. Grbic, T. Mudge, D. D. Wentzloff, D. Blaauw, and H. S. Kim. "Energy-Autonomous Wireless Communication for Millimeter-Scale Internet-of-Things Sensor Nodes". In: *IEEE Journal on Selected Areas in Communications* 34.12 (2016), pp. 3962–3977. DOI: 10.1109/JSAC.2016.2612041.

[126] J. Rabaey, J. Ammer, T. Karalar, S. Li, B. Otis, M. Sheets, and T. Tuan. "PicoRadios for wireless sensor networks: the next challenge in ultra-low power design". In: *2002 IEEE International Solid-State Circuits Conference. Digest of Technical Papers (Cat. No.02CH37315)*. Vol. 1. 2002, 200–201 vol.1. DOI: 10.1109/ISSCC.2002.993005.

[127] M. Srivastava. *Power-Aware Communication Systems*. Boston, MA: Springer US, 2002, pp. 297–334. DOI: 10.1007/0-306-48139-1_11.

[128] B. Cook, A. Molnar, and K. Pister. "Low power RF design for sensor networks". In: *2005 IEEE Radio Frequency integrated Circuits (RFIC) Symposium - Digest of Papers*. 2005, pp. 357–360. DOI: 10.1109/RFIC.2005.1489809.

[129] Y. Li, D. Qiao, Z. Xu, D. Xu, F. Miao, and Y. Zhang. “Energy-Model-Based Optimal Communication Systems Design for Wireless Sensor Networks”. In: *International Journal of Distributed Sensor Networks* 8.12 (2012), p. 861704. DOI: 10.1155/2012/861704.

[130] S. Drago, F. Sebastiano, L. J. Breems, D. M. W. Leenaerts, K. A. A. Makinwa, and B. Nauta. “Impulse-Based Scheme for Crystal-Less ULP Radios”. In: *IEEE Transactions on Circuits and Systems I: Regular Papers* 56.5 (2009), pp. 1041–1052. DOI: 10.1109/TCSI.2009.2015208.

[131] D. C. Daly and A. P. Chandrakasan. “An Energy-Efficient OOK Transceiver for Wireless Sensor Networks”. In: *IEEE Journal of Solid-State Circuits* 42.5 (2007), pp. 1003–1011. DOI: 10.1109/JSSC.2007.894323.

[132] M. Pedram and Q. Wu. “Design considerations for battery-powered electronics”. In: *Proceedings 1999 Design Automation Conference (Cat. No. 99CH36361)*. 1999, pp. 861–866. DOI: 10.1109/DAC.1999.782166.

[133] H. Bhamra *et al.* “A 24 μW, Batteryless, Crystal-free, Multinode Synchronized SoC "Bionode" for Wireless Prosthesis Control”. In: *IEEE Journal of Solid-State Circuits* 50.11 (2015), pp. 2714–2727.

[134] F. Sun, Z. Zhao, Z. Fang, Y. Shi, X. Chen, and Y. Xuan. “A design of a band-aid like health monitoring node for body sensor network”. In: *Proc. Int. Conference on Measurement, Information and Control (ICMIC)*. May 2012, pp. 34–39.

[135] N. Kim, T. Austin, D. Blaauw, T. Mudge, K. Flautner, J. Hu, M. Irwin, M. Kandemir, and V. Narayanan. “Leakage current: Moore’s law meets static power”. In: *Computer* 36.12 (2003), pp. 68–75. DOI: 10.1109/MC.2003.1250885.

[136] T. Cordell Randall. “A low-power, reconfigurable, pipelined ADC with automatic adaptation for implantable bioimpedance applications”. PhD thesis. The United States: University of Tennessee, Dec. 2014. URL: https://trace.tennessee.edu/utk_graddiss/3162.

[137] L. S. Gordon. *Principles of Mobile Communication*. Spinger, 2017.

[138] T. Tran. “Ultra low power low noise amplifier designs for 2.4 GHz ISM band applications”. PhD thesis. Singapore: Nanyang Technological University, July 2012.

[139] P. Greiner, J. Grosinger, J. Schweighofer, C. Steffan, S. Wilfling, G. Holweg, and W. Bösch. “A System-on-Chip Crystal-Less Wireless Sub-GHz Transmitter”. In: *IEEE Transactions on Microwave Theory and Techniques* 66.3 (2018), pp. 1431–1439. DOI: 10.1109/TMTT.2017.2748130.

[140] M. Song, M. Ding, E. Tiurin, K. Xu, E. Allebes, G. Singh, P. Zhang, S. Traferro, H. Korpela, N. Van Helleputte, R. B. Staszewski, Y.-H. Liu, and C. Bachmann. “30.8 A 3.5mm×3.8mm Crystal-Less MICS Transceiver Featuring Coverages of ±160ppm Carrier Frequency Offset and 4.8-VSWR Antenna Impedance for Insertable Smart Pills”. In: *2020 IEEE International Solid- State Circuits Conference - (ISSCC)*. 2020, pp. 474–476. DOI: 10.1109/ISSCC19947.2020.9063083.

[141] T. Chang, T. Watteyne, B. Wheeler, F. Maksimovic, D. C. Burnett, and K. Pister. “Surviving the Hair Dryer: Continuous Calibration of a Crystal-Free Mote-on-Chip”. In: *IEEE Internet of Things Journal* 9.6 (2022), pp. 4737–4747. DOI: 10.1109/JIOT.2021.3108077.

[142] I. Suciu, F. Maksimovic, B. Wheeler, D. C. Burnett, O. Khan, T. Watteyne, X. Vilajosana, and K. S. J. Pister. “Dynamic Channel Calibration on a Crystal-Free Mote-on-a-Chip”. In: *IEEE Access* 7 (2019), pp. 120884–120900. DOI: 10.1109/ACCESS.2019.2937689.

[143] S. J. Kim, D. Lee, K.-Y. Lee, and S.-G. Lee. “A 2.4-GHz Super-Regenerative Transceiver With Selectivity-Improving Dual Q-Enhancement Architecture and 102-μW All-Digital FLL”. In: *IEEE Transactions on Microwave Theory and Techniques* 65.9 (2017), pp. 3287–3298. DOI: 10.1109/TMTT.2017.2664826.

[144] D. Ye, R. van der Zee, and B. Nauta. “A 915 MHz 175 μW Receiver Using Transmitted-Reference and Shifted Limiters for 50 dB In-Band Interference Tolerance”. In: *IEEE Journal of Solid-State Circuits* 51.12 (2016), pp. 3114–3124. DOI: 10.1109/JSSC.2016.2602943.

[145] Y.-L. Tsai, C.-Y. Lin, B.-C. Wang, and T.-H. Lin. “A 330-μW 400-MHz BPSK Transmitter in 0.18- μm CMOS for Biomedical Applications”. In: *IEEE Transactions on Circuits and Systems II: Express Briefs* 63.5 (2016), pp. 448–452. DOI: 10.1109/TCSII.2015.2505080.

[146] C.-S. A. Gong, C.-H. Chang, and Y.-L. Tsou. “Fully integrated 2.45-GHz OOK receiver for wireless sensor networks”. In: *International Journal of Circuit Theory and Applications* 44.11 (2016), pp. 1926–1941. DOI: 10.1002/cta.2202.

[147] E. T. Armas, D. Ramos-Valido, S. L. Khemchandani, and J. del Pino. “A 40.9 µW high sensitivity wake-up radio for wireless sensor networks using uncertain-IF architecture”. In: *2015 Conference on Design of Circuits and Integrated Systems (DCIS)*. 2015, pp. 1–6. DOI: 10.1109/DCIS.2015.7388585.

[148] *Atmel Corporation*. AVR Low Power 2.4 GHz Transceiver for ZigBee, IEEE 802.15.4, 6LoWPAN, RF4CE and ISM Applications, AT86RF230 Spec. Sheet, 5131E-MCU Wireless-02/09, 2009.

[149] O. Carhacioglu, P. Zand, and M. Nabi. “Time-domain cooperative coexistence of BLE and IEEE 802.15.4 networks”. In: *Proc. IEEE Int. Symp. on Personal, Indoor and Mobile Radio Comm. (PIMRC)*. Oct. 2017, pp. 1–7.

[150] H. Lieske, G. Kilian, M. Breiling, S. Rauh, J. Robert, and A. Heuberger. “Decoding Performance in Low-Power Wide Area Networks with Packet Collisions”. In: *IEEE Transactions on Wireless Communications* 15.12 (2016), pp. 8195–8208.

[151] H. Zhang, X. Chu, W. Guo, and S. Wang. “Coexistence of Wi-Fi and heterogeneous small cell networks sharing unlicensed spectrum”. In: *IEEE Communications Magazine* 53.3 (2015), pp. 158–164.

[152] S. Zinno, G. Di Stasi, S. Avallone, and G. Ventre. “On a fair coexistence of LTE and Wi-Fi in the unlicensed spectrum: A Survey”. In: *Computer Communications* 115 (2018), pp. 35–50.

[153] D. Yang, Y. Xu, and M. Gidlund. “Wireless coexistence between IEEE 802.11- and IEEE 802.15.4-based networks: A survey”. In: *International Journal of Distributed Sensor Networks* 2011 (2011).

[154] C. Shahriar *et al.* “PHY-Layer Resiliency in OFDM Communications: A Tutorial”. In: *IEEE Communications Surveys and Tutorials* 17.1 (2015), pp. 292–314.

[155] *IEEE Standard for Information Technology-Telecommunications and Information Exchange Between Systems Local and Metropolitan Area Networks-Specific Requirements—Part 11: Wireless LAN Medium Access Control (MAC) and Physical Layer (PHY) Specifications*, IEEE Standard 802.11-2016. Dec. 2016.

[156] P. Machan and J. Wozniak. “On the fast BSS transition algorithms in the IEEE 802.11r local area wireless networks”. In: *Telecommunication Systems* 52.4 (2013), pp. 2713–2720.

[157] G. Noubir, R. Rajaraman, B. Sheng, and B. Thapa. “On the robustness of IEEE 802.11 Rate adaptation algorithms against smart jamming”. In: *Proc. 4th ACM WiSec Conf.* June 2011, pp. 97–108.

[158] J. Yousaf, W. Nah, M. I. Hussein, J. G. Yang, A. Altaf, and M. Elahi. “Characterization of Reverberation Chamber - A Comprehensive Review”. In: *IEEE Access* 8 (2020), pp. 226591–226608. DOI: 10.1109/ACCESS.2020.3045028.

[159] P.-S. Kildal, X. Chen, C. Orlenius, M. Franzen, and C. S. L. Patane. “Characterization of Reverberation Chambers for OTA Measurements of Wireless Devices: Physical Formulations of Channel Matrix and New Uncertainty Formula”. In: *IEEE Transactions on Antennas and Propagation* 60.8 (2012), pp. 3875–3891. DOI: 10.1109/TAP.2012.2201125.

[160] V. M. Primiani, M. Barazzetta, L. Bastianelli, D. Micheli, E. Moglie, R. Diamanti, and G. Gradoni. “Reverberation chambers for testing wireless devices and systems”. In: *IEEE Electromagnetic Compatibility Magazine* 9.2 (2020), pp. 45–55. DOI: 10.1109/MEMC.2020.9133241.

[161] X. Chen, P.-S. Kildal, C. Orlenius, and J. Carlsson. “Channel Sounding of Loaded Reverberation Chamber for Over-the-Air Testing of Wireless Devices: Coherence Bandwidth Versus Average Mode Bandwidth and Delay Spread”. In: *IEEE Antennas and Wireless Propagation Letters* 8 (2009), pp. 678–681. DOI: 10.1109/LAWP.2009.2025149.

[162] C. L. Holloway, H. A. Shah, R. J. Pirkl, K. A. Remley, D. A. Hill, and J. Ladbury. “Early Time Behavior in Reverberation Chambers and Its Effect on the Relationships Between Coherence Bandwidth, Chamber Decay Time, RMS Delay Spread, and the Chamber Buildup Time”. In: *IEEE Transactions on Electromagnetic Compatibility* 54.4 (2012), pp. 714–725. DOI: 10.1109/TEMC.2012.2188896.

[163] M. K. Simon and M.-S. Alouini. *Digital communication over fading channels*. New York: Wiley, 2001.

[164] X. Chen, P.-S. Kildal, and M. Gustafsson. “Characterization of Implemented Algorithm for MIMO Spatial Multiplexing in Reverberation Chamber”. In: *IEEE Transactions on Antennas and Propagation* 61.8 (2013), pp. 4400–4404. DOI: 10.1109/TAP.2013.2259459.

[165] J.-H. Choi, J.-H. Lee, and S.-O. Park. “Characterizing the Impact of Moving Mode-Stirrers on the Doppler Spread Spectrum in a Reverberation Chamber”. In: *IEEE Antennas and Wireless Propagation Letters* 9 (2010), pp. 375–378. DOI: 10.1109/LAWP.2010.2049331.

[166] K. Karlsson, X. Chen, J. Carlsson, and A. Skårbratt. “On OTA Test in the Presence of Doppler Spreads in a Reverberation Chamber”. In: *IEEE Antennas and Wireless Propagation Letters* 12 (2013), pp. 886–889. DOI: 10.1109/LAWP.2013.2272716.

[167] C. L. Holloway, D. A. Hill, J. M. Ladbury, P. F. Wilson, G. Koepke, and J. Coder. “On the Use of Reverberation Chambers to Simulate a Rician Radio Environment for the Testing of Wireless Devices”. In: *IEEE Transactions on Antennas and Propagation* 54.11 (2006), pp. 3167–3177. DOI: 10.1109/TAP.2006.883987.

[168] A. Gifuni, L. Bastianelli, M. Migliaccio, F. Moglie, V. M. Primiani, and G. Gradoni. “On the Estimated Measurement Uncertainty of the Insertion Loss in a Reverberation Chamber Including Frequency Stirring”. In: *IEEE Transactions on Electromagnetic Compatibility* 61.5 (2019), pp. 1414–1422. DOI: 10.1109/TEMC.2018.2870073.

[169] Q. Xu, L. Xing, Y. Zhao, Z. Tian, and Y. Huang. “Wiener-Khinchin Theorem in a Reverberation Chamber”. In: *IEEE Transactions on Electromagnetic Compatibility* 61.5 (2019), pp. 1399–1407. DOI: 10.1109/TEMC.2018.2863297.

[170] Z. Tian, Y. Huang, and Q. Xu. “Stirring effectiveness characterization based on Doppler spread in a reverberation chamber”. In: *2016 10th European Conference on Antennas and Propagation (EuCAP)*. 2016, pp. 1–3. DOI: 10.1109/EuCAP.2016.7481108.

[171] E. Cheng, P. Wang, Q. Xu, C. Meng, R. Jia, *et al.* “Design and Measurement of a Vibrating Intrinsic Reverberation Chamber Working in Tuned Mode”. In: *International Journal of Antennas and Propagation* 2023 (2023). DOI: 10.1155/2023/3466400.

[172] D. Mandaris, R. Vogt-Ardatjew, E. Suthau, and F. Leferink. “Simultaneous multi-probe measurements for rapid evaluation of reverberation chambers”. In: *2018 IEEE International Symposium on Electromagnetic Compatibility and 2018 IEEE Asia-Pacific Symposium on Electromagnetic Compatibility (EMC/APEMC)*. 2018, pp. 590–594. DOI: 10.1109/ISEMC.2018.8393847.

[173] M. Hara, Y. Takahashi, R. Vogt-Ardatjew, and F. Leferink. “Statistical Analysis for Reverberation Chamber with Flexible Shaking Walls with Various Amplitudes”. In: *2018 International Symposium on Electromagnetic Compatibility (EMC EUROPE)*. 2018, pp. 694–698. DOI: 10.1109/EMCEurope.2018.8485107.

[174] G. Ferrara, A. Gifuni, M. Migliaccio, and A. Sorrentino. “Probability density function for the quality factor of vibrating reverberation chambers”. In: *2015 IEEE Metrology for Aerospace (MetroAeroSpace)*. 2015, pp. 230–234. DOI: 10.1109/MetroAeroSpace.2015.7180659.

[175] R. Vogt-Ardatjew, S. van de Beek, and F. Leferink. “Influence of reverberation chamber loading on extreme field strength”. In: *2014 International Symposium on Electromagnetic Compatibility, Tokyo*. 2014, pp. 685–688.

[176] R. Vogt-Ardatjew, S. van de Beek, and F. Leferink. “Experimental extreme field strength investigation in reverberant enclosures”. In: *2014 International Symposium on Electromagnetic Compatibility*. 2014, pp. 332–336. DOI: 10.1109/EMCEurope.2014.6930927.

[177] R. Vogt-Ardatjew and F. Leferink. “Observation of maximal and average field values in a Reverberation chamber”. In: *2013 International Symposium on Electromagnetic Compatibility*. 2013, pp. 508–513.

[178] A. Hero, J. Fessler, and M. Usman. “Exploring estimator bias-variance tradeoffs using the uniform CR bound”. In: *IEEE Transactions on Signal Processing* 44.8 (1996), pp. 2026–2041. DOI: 10.1109/78.533723.

[179] *Electromagnetic Compatibility (EMC) Part 4-21: Testing and Measurement Techniques - Reverberation Chamber Test Methods*, IEC 61000-4-21, Int. Electrotechnical Commission. Geneva, Switzerland, 2011.

[180] M. Jeong, B.-Y. Park, J. Choi, and S.-O. Park. “Doppler Spread Spectrum of a Circularly Moving Receiver in an Anechoic and a Reverberation Chamber”. In: *Progress In Electromagnetics Research C* 48 (2014). Accessed on Feb. 10, 2022, pp. 125–132. DOI: 10.2528/PIERC13122601. URL: http://www.jpier.org/PIERC/pier.php?paper=13122601.

[181] A. Sorrentino, A. Gifuni, G. Ferrara, and M. Migliaccio. “Mode-stirred reverberating chamber Doppler spectra: Multi-frequency measurements and empirical model”. In: *IET Microwaves, Antennas and Propagation* 8.15 (2014), pp. 1356–1362. DOI: 10.1049/iet-map.2014.0140.

[182] X. Chen. “Evaluation and measurement of the Doppler spectrum in a reverberation chamber”. In: *Progress In Electromagnetics Research M* 26 (2012). Accessed on Feb. 10, 2022, pp. 267–277. DOI: 10.2528/PIERM12091808. URL: http://www.jpier.org/PIERM/pier.php?paper=12091808.

[183] J. Xu, Y. Zhao, and Q. Xu. “On the Time Domain Error Caused By the Frequency Domain Sampling Rate in a Reverberation Chamber”. In: *IEEE Access* 7 (2019), pp. 78223–78227. DOI: 10.1109/ACCESS.2019.2921997.

[184] R. T. O’neill. “On sample sizes to estimate the protective efficacy of a vaccine”. In: *Statistics in Medicine* 7.12 (1988), pp. 1279–1288. DOI: 10.1002/sim.4780071208.

[185] C. Lemoine, P. Besnier, and M. Drissi. “Investigation of Reverberation Chamber Measurements Through High-Power Goodness-of-Fit Tests”. In: *IEEE Transactions on Electromagnetic Compatibility* 49.4 (2007), pp. 745–755. DOI: 10.1109/TEMC.2007.908290.

[186] C. Lemoine, E. Amador, and P. Besnier. “On the K-Factor Estimation for Rician Channel Simulated in Reverberation Chamber”. In: *IEEE Transactions on Antennas and Propagation* 59.3 (2011), pp. 1003–1012. DOI: 10.1109/TAP.2010.2103003.

[187] P. Hallbjorner. “Estimating the number of independent samples in reverberation chamber measurements from sample differences”. In: *IEEE Transactions on Electromagnetic Compatibility* 48.2 (2006), pp. 354–358. DOI: 10.1109/TEMC.2006.873866.

[188] R. J. Pirkl, K. A. Remley, and C. S. L. Patane. “Reverberation Chamber Measurement Correlation”. In: *IEEE Transactions on Electromagnetic Compatibility* 54.3 (2012), pp. 533–545. DOI: 10.1109/TEMC.2011.2166964.

[189] A. Chelli and M. Pätzold. “An Improved Method for Estimating the Time ACF of a Sum of Complex Plane Waves”. In: *2010 IEEE Global Telecommunications Conference GLOBECOM*. 2010, pp. 1–6. DOI: 10.1109/GLOCOM.2010.5683495.

[190] R. Dana. *Statistics of sampled Rician fading*. Mission Res. Corporation, Santa Barbara, CA, USA, Tech. Rep. DNA-TR-92-98, Feb. 1993.

[191] P. Stoica and R. L. Moses. *Spectral Analysis of Signals*. Upper Saddle River, NJ, USA: Pearson Prentice Hall, 2005.

[192] A. F. Molisch. *Wireless communications*. John Wiley & Sons, 2012.

[193] H.-J. Körber, H. Wattar, and G. Scholl. “Modular Wireless Real-Time Sensor/Actuator Network for Factory Automation Applications”. In: *IEEE Transactions on Industrial Informatics* 3.2 (2007), pp. 111–119. DOI: 10.1109/TII.2007.898451.

[194] X. Xie, X. Zhang, and K. Sundaresan. “Adaptive feedback compression for MIMO networks”. In: *Proceedings of the 19th annual international conference on Mobile computing & networking*. 2013, pp. 477–488. DOI: 10.1145/2500423.2500446.

[195] J. Gutiérrez, Ó. González, J. Pérez, D. Ramírez, L. Vielva, J. Ibáñez, and I. Santamaría. “Frequency-Domain Methodology for Measuring MIMO Channels Using a Generic Test Bed”. In: *IEEE Transactions on Instrumentation and Measurement* 60.3 (2011), pp. 827–838. DOI: 10.1109/TIM.2010.2082432.

[196] A. Chelli and M. Pätzold. “An improved method for estimating the frequency correlation function”. In: *2012 IEEE Wireless Communications and Networking Conference (WCNC)*. 2012, pp. 1054–1059. DOI: 10.1109/WCNC.2012.6213930.

[197] R. A. Fisher. “Frequency Distribution of the Values of the Correlation Coefficient in Samples from an Indefinitely Large Population”. In: *Biometrika* 10.4 (1915), pp. 507–521. ISSN: 00063444. DOI: 10.2307/2331838. URL: http://www.jstor.org/stable/2331838 (visited on 09/21/2022).

[198] G. Shieh. “Estimation of the simple correlation coefficient”. In: *Behavior Research Methods* 42.4 (2010), pp. 906–917. DOI: 10.3758/BRM.42.4.906.

[199] M. I. Andries, P. Besnier, and C. Lemoine. “On the prediction of the average absorbing cross section of materials from coherence bandwidth measurements in reverberation chamber”. In: *International Symposium on Electromagnetic Compatibility - EMC EUROPE*. 2012, pp. 1–6. DOI: 10.1109/EMCEurope.2012.6396685.

[200] *Universal Mobile Telecommunications System (UMTS); LTE; Universal Terrestrial Radio Access (UTRA) and Evolved Universal Terrestrial Radio Access (E-UTRA); Verification of Radiated Multi-Antenna Reception Performance of User Equipment(UE)*, ETSI TR 137 977 V12.1.0. Oct. 2014.

[201] U. Carlberg, P.-S. Kildal, and J. Carlsson. “Numerical Study of Position Stirring and Frequency Stirring in a Loaded Reverberation Chamber”. In: *IEEE Transactions on Electromagnetic Compatibility* 51.1 (2009), pp. 12–17. DOI: 10.1109/TEMC.2008.2011818.

[202] X. Chen. “On Statistics of the Measured Antenna Efficiency in a Reverberation Chamber”. In: *IEEE Transactions on Antennas and Propagation* 61.11 (2013), pp. 5417–5424. DOI: 10.1109/TAP.2013.2276920.

[203] A. A. Glazunov, H. Asplund, and J.-E. Berg. “Statistical analysis of measured short-term impulse response functions of 1.88 GHz radio channels in Stockholm with corresponding channel model”. In: *50th Vehicular Technology Conference*. Vol. 1. 1999, pp. 107–111. DOI: 10.1109/VETECF.1999.797058.

[204] R. Bultitude and G. Bedal. “Propagation characteristics on microcellular urban mobile radio channels at 910 MHz”. In: *IEEE Journal on Selected Areas in Communications* 7.1 (1989), pp. 31–39. DOI: 10.1109/49.16841.

[205] R. He, Z. Zhong, B. Ai, G. Wang, J. Ding, and A. F. Molisch. “Measurements and Analysis of Propagation Channels in High-Speed Railway Viaducts”. In: *IEEE Transactions on Wireless Communications* 12.2 (2013), pp. 794–805. DOI: 10.1109/TWC.2012.120412.120268.

[206] J. C. R. Dal Bello, G. Siqueira, and H. Bertoni. “Theoretical analysis and measurement results of vegetation effects on path loss for mobile cellular communication systems”. In: *IEEE Transactions on Vehicular Technology* 49.4 (2000), pp. 1285–1293. DOI: 10.1109/25.875242.

[207] G. Cirrone, S. Donadio, S. Guatelli, A. Mantero, B. Mascialino, S. Parlati, M. Pia, A. Pfeiffer, A. Ribon, and P. Viarengo. “A goodness-of-fit statistical toolkit”. In: *IEEE Transactions on Nuclear Science* 51.5 (2004), pp. 2056–2063. DOI: 10.1109/TNS.2004.836124.

[208] M. A. Stephens. “EDF Statistics for goodness of fit and some comparisons”. In: *Journal of the American Statistical Association* 69.347 (1974), pp. 730–737. DOI: 10.1080/01621459.1974.10480196.

[209] W. Rolke and C. G. Gongora. “A Chi-square goodness-of-fit test for continuous distributions against a known alternative”. In: *Computational Statistics* 36 (2021), pp. 1885–1900. DOI: 10.1007/s00180-020-00997-x.

[210] H. A. Sturges. “The choice of a class interval”. In: *Journal of the American Statistical Association* 21.153 (1926), pp. 65–66. DOI: 10.1080/01621459.1926.10502161.

[211] A. A. Glazunov, A. Razavi, R. Maaskant, and J. Yang. “Semi-analytical model of the Rician K-factor”. In: *Radio Science* 55.11 (2020), pp. 1–13. DOI: 10.1029/2020RS007099.

[212] A. Sorrentino, G. Ferrara, A. Gifuni, and M. Migliaccio. “An Alternative Technique for Estimating the K-Factor from the Phase of the Electromagnetic Field Within a Reverberating Chamber”. In: *Progress In Electromagnetics Research C* 44 (2013). Accessed on Feb. 10, 2022, pp. 27–40. DOI: 10.2528/PIERC13080202. URL: http://www.jpier.org/PIERC/pier.php?paper=13080202.

[213] K. E. Baddour and T. J. Willink. “Improved estimation of the Ricean K-factor from I/Q fading channel samples”. In: *IEEE Transactions on Wireless Communications* 7.12 (2008), pp. 5051–5057. DOI: 10.1109/T-WC.2008.070972.

[214] L. Lauwers, K. Barbe, W. Van Moer, and R. Pintelon. “Estimating the parameters of a Rice distribution: A Bayesian approach”. In: *2009 IEEE Instrumentation and Measurement Technology Conference*. 2009, pp. 114–117. DOI: 10.1109/IMTC.2009.5168426.

[215] L. Greenstein, D. Michelson, and V. Erceg. “Moment-method estimation of the Ricean K-factor”. In: *IEEE Communications Letters* 3.6 (1999), pp. 175–176. DOI: 10.1109/4234.769521.

[216] M. I. Andries, P. Besnier, and C. Lemoine. “Rician channels in a RC: Statistical uncertainty of K estimations versus K fluctuations due to unstirred paths”. In: *Proceedings of the 5th European Conference on Antennas and Propagation (EUCAP)*. 2011, pp. 1758–1762.

[217] C. Tepedelenlioglu, A. Abdi, and G. Giannakis. “The Ricean K factor: Estimation and performance analysis”. In: *IEEE Transactions on Wireless Communications* 2.4 (2003), pp. 799–810. DOI: 10.1109/TWC.2003.814338.

[218] L. L. Bars, J.-F. Rosnarho, P. Besnier, J. Sol, F. Sarrazin, and E. Richalot. “Geometry and Loading Effects on Performances of Mode-Stirred Reverberation Chambers: An Experimental Study”. In: *2019 International Symposium on Electromagnetic Compatibility - EMC EUROPE*. 2019, pp. 163–168. DOI: 10.1109/EMCEurope.2019.8872134.

[219] D. Izzo, A. Rommel, M. Aidam, R. Vogt-Ardatjew, and F. Leferink. “A Cosed-Loop Calibration Method for the Vibrating Intrinsic Reverberation Chamber”. In: *2020 International Symposium on Electromagnetic Compatibility - EMC EUROPE*. 2020, pp. 1–6. DOI: 10.1109/EMCEUROPE48519.2020.9245656.

[220] M. Hara, Y. Takahashi, R. Vogt-Ardatjew, and F. Leferink. “Validation of Vibrating Intrinsic Reverberation Chamber using Computational Electromagnetics”. In: *2019 Joint International Symposium on Electromagnetic Compatibility, Sapporo and Asia-Pacific International Symposium on Electromagnetic Compatibility (EMC Sapporo/APEMC)*. 2019, pp. 593–596. DOI: 10.23919/EMCTokyo.2019.8893677.

[221] G. Orjubin, E. Richalot, S. Mengue, and O. Picon. “Statistical model of an undermoded reverberation chamber”. In: *IEEE Transactions on Electromagnetic Compatibility* 48.1 (2006), pp. 248–251. DOI: 10.1109/TEMC.2006.870705.

[222] C. Lemoine, P. Besnier, and M. Drissi. “Effect of the size of the antenna on measurements distribution in reverberation chamber”. In: *2007 18th International Zurich Symposium on Electromagnetic Compatibility*. 2007, pp. 461–464. DOI: 10.1109/EMCZUR.2007.4388295.

[223] A. G. García, J. Rubio, J. L. Masa-Campos, J. Córcoles, Y. C. Roca, and R. G. Alcalá. “A Novel Design of a SIW-Fed Antenna Array Using an Accelerated Full-Wave Methodology”. In: *IEEE Transactions on Antennas and Propagation* (2022). DOI: 10.1109/TAP.2022.3177505.

[224] V. Rajamani, C. F. Bunting, and J. C. West. “Effects of loading on independent samples and uniformity of a reverberation chamber”. In: *2013 IEEE International Symposium on Electromagnetic Compatibility*. 2013, pp. 217–221. DOI: 10.1109/ISEMC.2013.6670412.

[225] C. L. Holloway, D. A. Hill, J. M. Ladbury, and G. Koepke. “Requirements for an effective reverberation chamber: Unloaded or loaded”. In: *IEEE Transactions on Electromagnetic Compatibility* 48.1 (2006), pp. 187–194. DOI: 10.1109/TEMC.2006.870709.

[226] S. Ohm, E. Kang, T. H. Lim, and H. Choo. “Design of a Dual-Polarization All-Metal Vivaldi Array Antenna Using a Metal 3D Printing Method for High-Power Jamming Systems”. In: *IEEE Access* 11 (2023), pp. 35175–35181. DOI: 10.1109/ACCESS.2023.3262463.

[227] X. Chen, P.-S. Kildal, and S.-H. Lai. “Estimation of Average Rician K-Factor and Average Mode Bandwidth in Loaded Reverberation Chamber”. In: *IEEE Antennas and Wireless Propagation Letters* 10 (2011), pp. 1437–1440. DOI: 10.1109/LAWP.2011.2179910.

[228] K. A. Remley, J. Dortmans, C. Weldon, R. D. Horansky, T. B. Meurs, C.-M. Wang, D. F. Williams, C. L. Holloway, and P. F. Wilson. “Configuring and Verifying Reverberation Chambers for Testing Cellular Wireless Devices”. In: *IEEE Transactions on Electromagnetic Compatibility* 58.3 (2016), pp. 661–672. DOI: 10.1109/TEMC.2016.2549031.

[229] A. A. Glazunov, S. Prasad, and P. Handel. “Experimental characterization of the propagation channel along a very large virtual array in a reverberation chamber”. In: *Progress in Electromagnetics Research B* 59 (2014), pp. 205–217. DOI: 10.2528/PIERB14031203.

[230] Q. Xu and Y. Huang. *Anechoic and Reverberation Chambers: Theory, Design, and Measurements*. John Wiley & Sons, 2019.

[231] E. Genender, C. L. Holloway, K. A. Remley, J. M. Ladbury, G. Koepke, and H. Garbe. "Simulating the Multipath Channel With a Reverberation Chamber: Application to Bit Error Rate Measurements". In: *IEEE Transactions on Electromagnetic Compatibility* 52.4 (2010), pp. 766–777. DOI: 10.1109/TEMC.2010.2044578.

[232] P.-S. Kildal and K. Rosengren. "Correlation and capacity of MIMO systems and mutual coupling, radiation efficiency, and diversity gain of their antennas: simulations and measurements in a reverberation chamber". In: *IEEE Communications Magazine* 42.12 (2004), pp. 104–112. DOI: 10.1109/MCOM.2004.1367562.

[233] C. L. Holloway, H. A. Shah, R. J. Pirkl, W. F. Young, D. A. Hill, and J. Ladbury. "Reverberation Chamber Techniques for Determining the Radiation and Total Efficiency of Antennas". In: *IEEE Transactions on Antennas and Propagation* 60.4 (2012), pp. 1758–1770. DOI: 10.1109/TAP.2012.2186263.

[234] A. Hubrechsen, K. A. Remley, R. D. Jones, D. F. Williams, D. Gu, A. B. Smolders, and L. A. Bronckers. "The Effect of Noise on Reverberation-Chamber Measurements of Antenna Efficiency". In: *IEEE Transactions on Antennas and Propagation* 69.12 (2021), pp. 8744–8752. DOI: 10.1109/TAP.2021.3083822.

[235] A. Hussain, A. A. Glazunov, B. Einarsson, and P.-S. Kildal. "Antenna Measurements in Reverberation Chamber Using USRP". In: *IEEE Transactions on Antennas and Propagation* 64.3 (2016), pp. 1152–1157. DOI: 10.1109/TAP.2016.2518211.

[236] D. Micheli, M. Barazzetta, R. Diamanti, P. Obino, R. Lattanzi, L. Bastianelli, V. M. Primiani, and F. Moglie. "Over-the-Air Tests of High-Speed Moving LTE Users in a Reverberation Chamber". In: *IEEE Transactions on Vehicular Technology* 67.5 (2018), pp. 4340–4349. DOI: 10.1109/TVT.2018.2795650.

[237] D. Izzo, A. Rommel, R. Vogt-Ardatjew, and F. Leferink. "Validation and Use of a Vibrating Intrinsic Reverberation Chamber for Radiated Immunity Tests". In: *2020 IEEE International Symposium on Electromagnetic Compatibility & Signal/Power Integrity (EMCSI)*. 2020, pp. 56–60. DOI: 10.1109/EMCSI38923.2020.9191603.

[238] A. B. Kihero, M. Karabacak, and H. Arslan. "Emulation Techniques for Small Scale Fading Aspects by Using Reverberation Chamber". In: *IEEE Transactions on Antennas and Propagation* 67.2 (2019), pp. 1246–1258. DOI: 10.1109/TAP.2018.2883571.

[239] V. Erceg. "TGn channel models". In: *IEEE Tech. Rep. 802.11-03/940r4*. May 2004.

[240] D. A. Hill. *Electromagnetic theory of reverberation chambers*. Dept. Radio-Freq. Technol. Division Electron. Elect. Eng., Lab. Natl. Inst. Stand. Technol., Boulder, CO, USA, Tech. Note 1506, Dec. 1998, p. 60.

[241] I. Rodriguez, M. Lauridsen, K. Arvidsson, J. Kvarnstrand, M. Andersson, and P. Mogensen. “Testing of low-power wide-area technologies in controlled propagation environments”. In: (2017). DOI: 10.1049/cp.2017.0271.

[242] G. Ferrara, M. Migliaccio, and A. Sorrentino. “Characterization of GSM Non-Line-of-Sight Propagation Channels Generated in a Reverberating Chamber by Using Bit Error Rates”. In: *IEEE Transactions on Electromagnetic Compatibility* 49.3 (2007), pp. 467–473. DOI: 10.1109/TEMC.2007.903040.

[243] W. Xue, X. Chen, M. Zhang, L. Zhao, A. Zhang, and Y. Huang. “Statistical Analysis of Antenna Efficiency Measurements With Non-Reference Antenna Methods in a Reverberation Chamber”. In: *IEEE Access* 8 (2020), pp. 113967–113980. DOI: 10.1109/ACCESS.2020.3003530.

[244] R. Feick, L. Ahumada, and H. Carrasco. “Effect of pedestrian traffic on fade statistics of fixed wireless links in public spaces”. In: *IET communications* 5.16 (2011), pp. 2285–2290. DOI: 10.1049/iet-com.2011.0037.

[245] A. Celik, K. N. Salama, and A. M. Eltawil. “The Internet of Bodies: A Systematic Survey on Propagation Characterization and Channel Modeling”. In: *IEEE Internet of Things Journal* 9.1 (2022), pp. 321–345. DOI: 10.1109/JIOT.2021.3098028.

[246] D. B. Smith, L. W. Hanlen, J. Zhang, D. Miniutti, D. Rodda, and B. Gilbert. “First- and second-order statistical characterizations of the dynamic body area propagation channel of various bandwidths”. In: *annals of telecommunications-annales des télécommunications* 66.3-4 (2011), pp. 187–203. DOI: 10.1007/s12243-010-0233-8.

[247] S. L. Cotton, R. D’Errico, and C. Oestges. “A review of radio channel models for body centric communications”. In: *Radio Science* 49.6 (2014), pp. 371–388. DOI: 10.1002/2013RS005319.

[248] D. B. Smith, D. Miniutti, T. A. Lamahewa, and L. W. Hanlen. “Propagation Models for Body-Area Networks: A Survey and New Outlook”. In: *IEEE Antennas and Propagation Magazine* 55.5 (2013), pp. 97–117. DOI: 10.1109/MAP.2013.6735479.

[249] A. Fort, C. Desset, P. Wambacq, and L. Biesen. “Indoor body-area channel model for narrowband communications”. In: *IET microwaves, antennas & propagation* 1.6 (2007), pp. 1197–1203. DOI: 10.1049/iet-map:20060215.

LIST OF MY PUBLICATIONS

1. M. Z. Mahfouz, R. Vogt-Ardatjew, A. B. J. Kokkeler, and A. A. Glazunov. "Empirical Characterization and Modeling of the Propagation Channel inside the VIRC". *IEEE Access*, [in submission]

2. M. Z. Mahfouz, R. Vogt-Ardatjew, A. B. J. Kokkeler, and A. A. Glazunov. "Measurement and Estimation Methodology for EMC and OTA Testing in the VIRC". in: *IEEE Transactions on Electromagnetic Compatibility* 65.1 (2023), pp. 3–16. DOI: 10.1109/TEMC.2022.3218413

3. M. Z. Mahfouz, A. B. J. Kokkeler, A. Meijerink, and A. A. Glazunov. "Impact of Ultra-Narrowband Interference on Wi-Fi Links: An Experimental Study". In: *IEEE Transactions on Wireless Communications* 20.5 (2021), pp. 3016–3030. DOI: 10.1109/TWC.2020.3046765

4. M. Z. Mahfouz, A. Meijerink, and M. J. Bentum. "Ultra-Narrowband for Energy-Scavenging-Powered Wireless Sensor Networks". In: *2017 IEEE 28th Annual International Symposium on Personal, Indoor, and Mobile Radio Communications (PIMRC)*. 2017, pp. 1–7. DOI: 10.1109/PIMRC.2017.8292562

5. M. Z. Mahfouz, A. Meijerink, and M. J. Bentum. "Optimum Design Parameters for Ultra-Low-Power RF Transceivers in Wireless Sensor Networks". In: *2016 IEEE Global Communications Conference (GLOBECOM)*. 2016, pp. 1–7. DOI: 10.1109/GLOCOM.2016.7842112